



UNIL | Université de Lausanne

Unicentre

CH-1015 Lausanne

<http://serval.unil.ch>

Year : 2017

THE PHOTOREDUCTION OF δ -MnO₂

Marafatto Francesco Femi

Marafatto Francesco Femi, 2017, THE PHOTOREDUCTION OF δ -MnO₂

Originally published at : Thesis, University of Lausanne

Posted at the University of Lausanne Open Archive <http://serval.unil.ch>

Document URN : urn:nbn:ch:serval-BIB_44B7D24679B40

Droits d'auteur

L'Université de Lausanne attire expressément l'attention des utilisateurs sur le fait que tous les documents publiés dans l'Archive SERVAL sont protégés par le droit d'auteur, conformément à la loi fédérale sur le droit d'auteur et les droits voisins (LDA). A ce titre, il est indispensable d'obtenir le consentement préalable de l'auteur et/ou de l'éditeur avant toute utilisation d'une oeuvre ou d'une partie d'une oeuvre ne relevant pas d'une utilisation à des fins personnelles au sens de la LDA (art. 19, al. 1 lettre a). A défaut, tout contrevenant s'expose aux sanctions prévues par cette loi. Nous déclinons toute responsabilité en la matière.

Copyright

The University of Lausanne expressly draws the attention of users to the fact that all documents published in the SERVAL Archive are protected by copyright in accordance with federal law on copyright and similar rights (LDA). Accordingly it is indispensable to obtain prior consent from the author and/or publisher before any use of a work or part of a work for purposes other than personal use within the meaning of LDA (art. 19, para. 1 letter a). Failure to do so will expose offenders to the sanctions laid down by this law. We accept no liability in this respect.



UNIL | Université de Lausanne

Faculté des géosciences et de l'environnement

Institut des dynamiques de la surface terrestre

THE PHOTOREDUCTION OF δ -MnO₂

Thèse de Doctorat

à l'Institut des dynamiques de la surface terrestre

en géosciences et environnement mention "Sciences de l'environnement"

Presentée à la faculté des géosciences et de l'environnement de l'Université de

Lausanne par

Francesco Femi Marafatto

Titulaire d'une *Laurea Magistrale in Geoscienze* délivrée par l'université de Trieste

Jury:

Prof. Jasquelin Peña, Université de Lausanne (Suisse); directrice de thèse

Prof. Stephan Kraemer, Université de Vienne (Autriche); expert externe

Docteur Benjamin Gilbert, Lawrence Berkeley National Laboratory (Etats Unis); expert externe

Prof. Torsten Vennemann, Université de Lausanne (Suisse); expert interne

Sous la présidence de Prof. Michel Jaboyedoff, Université de Lausanne (Suisse)

Lausanne, 2017

IMPRIMATUR

Vu le rapport présenté par le jury d'examen, composé de

Président de la séance publique :	M. le Professeur Michel Jaboyedoff
Président du colloque :	M. le Professeur Michel Jaboyedoff
Directrice de thèse :	Mme la Professeure Jasquelin Peña
Expert interne:	M. le Professeur Torsten Vennemann
Expert externe :	M. le Professeur Stephan M. Krämer
Expert externe :	M. le Docteur Benjamin Gilbert

Le Doyen de la Faculté des géosciences et de l'environnement autorise l'impression de la thèse de

Monsieur Francesco MARAFATTO

Titulaire d'une
Maîtrise ès Sciences en Géosciences
de l'Université de Trieste

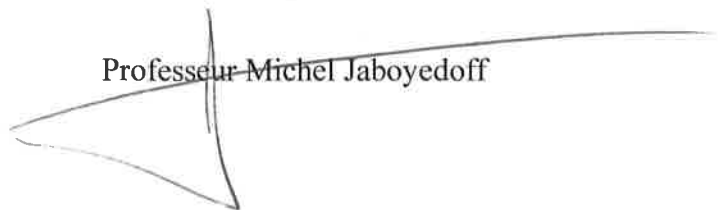
intitulée

The photoreduction of δ -MnO₂

Lausanne, le 21 avril 2017

Pour le Doyen de la Faculté des géosciences et
de l'environnement

Professeur Michel Jaboyedoff



ACKNOWLEDGEMENTS

I would like to thank my parents for allowing and motivating me to pursue my education, leading me to where I am today, my brothers for being amazing, all my friends past and present for being there such as the incredible people that I met in this Lausanne adventure, with a particular mention to those met at Géopolis between ISTE, IDYST, IGD and other (i.e. Zelig). The list is long, I genuinely love you all !

I would like to thank Jackie, for having trained me to be a scientist, and for having had a hands-on approach without which I would have had a hard time getting to this point. A big thanks for your advising and supervising during these 4 years ! A big thank you also goes to all members of the LGE, past and present : Julia, Naomi, Anna, Case, Sassi, Yuheng and Debra, for their help during my dissertation and also simply for the time shared (some more some less) during my time here in Lausanne. With some there were also, aside from scientific discussions, really good discussions of varying degrees of seriousness from politics and society (Julia) to just plain stupidity :-) (Case).

A thank you goes to Ben Gilbert, for his scientific insight during our collaborations in this work, I was always impressed by the brilliance of your observations on the results, which came very quickly while I was still trying to understand what the points on the graphs even meant.

I thank the entirety of my Thesis Jury (Jackie Peña, Benjamin Gilbert, Stephan Kraemer, Torsten Vennemann, Michel Jaboyedoff) for the time invested in reading my dissertation and giving their comments as well as judging my work, as well as the Swiss National Fund for the funding of my PhD, and the Société Académique Vaudoise for integrating the funding at the end of my contract. Also, Sci-hub for facilitating bibliographic searches.

I would like to thank Zelig for existing and being the amazing place it is, especially during the end of my dissertation work, where it became a place to change my mind for a brief moment. The ACIGE for the time I spent in its committee from it's birth and seeing it grow in time.

So then the difficult part, names, because I am afraid to forget some. This is completely not a full list, those not in here I love you too! Thank you Giulia (indescrivibile, <3), Benji (rouais gros !), Gab (c'est quoi ton animal totem ?), Mikey (love you cockney bear), Vjeran (we were between two ferns), Erica (« j'ai perdu mon mari »), Kiki (l'as de la grimpe, ou bien du matos), Alexis (hugs !!!), Mor1 (machine de fete!), Nath (ou Mathalie ou Nagalie, je sais plus), Anders (petit poussin), Maga (le feste quinquennali patriarcali...Magma o Mathalie o Nagalie), Zozo (Amazon man !), Stephane (et l'experience des gendarmes dans le Vercors, aussi plein de clopes taxées !), Guinness (toujours la plus jeune en cœur), Elfie (des discussions toujours geniales, la Zen par definition), Seb (tranquilo, maquina !), Mert'(et la musique de

tunnel, DJ Had), Manu (Incroyable energie positive), Nico (grande DJ coi capelli blu), Camille (je t'ai connu tards mais c'était quand meme pire bien), Myriam (l'achat du banjo chez toi complètement sous), Antoine (et les grosses discussions sur la politique et la societ  ainsi que les moustiques en camargue), Kristel (et ta preparation du voyage a velo, ainsi que des discussions sur les ONG), Boris (des randos et du punk, t'es incroyable bob), Case (and the office garden, the couch, the petit pois and your super heavy bike, and talking about science and stupid stuff), Julia (faut regonfler le requin), Naomi (on a commenc  ensemble et on a l'anniversaire le meme jour, c' tait drole de le decouvrir comme ca random !), Anna (fun to share lab work and discussions on manganese, and also discussions at barbecues with Sophia and Roman), Sassi (c' tait cool l'echange de responsabilit s du projet, l'ACS – avec ton reveil toute la nuit - et le beamtime), Yuheng (des discussions interessantes de science et de la Chine), Debra (a lot of info exchange for your establishment here in Lausanne, keep me up to date about your van-project so I can follow), Luc (et tes films absurdes), Iacopo (grazie per lo script ICP !!!), Georgina (we shared an office, and biking, and you saw me saying no to science and then again yes), Alexandra (on a eu des discussions incroyables meme si on s'est connu tres recemment, t'es trop trop trop cool et une personne incroyable !), Marga (abbiamo condiviso molto), Federica (la sorella acquisita), Evelyne (on a partag  la fin de these, ainsi que des discussions plus profondes, merci pour toutes les clopes que je t'ai tax s !), Leanne (we share dangerous childish attitudes with fire), J rg (thanks for the schtroumpf readings), Renske and Maarten (with Lise and Espen, Maarten old schoolmate from Kenya!), Ehsan (goat master flying eagle), Gustavo, Mathieu, Inigo et Benoit (bien de discussions   la cafet Idyst), Claire (energie positive incroyable, keep on psytrancing !), les deux Francois (et les discussions - et vols en parapente), Pascal (Ma-qui-na), Meri (sempre agonismo), Riky (pazzo scatenato), and, well, also Ramona. To all you and those that I may have forgotten to list, I love you all !

Dedicated to you all!

Donkeys Rule!

ABSTRACT

Layer manganese(III,IV) oxides are amongst the most reactive transition metal oxides in surface environments. The high reactivity of these minerals towards sorption and oxidation of many organic and inorganic compounds arises from their high specific surface area and density of sorption sites, as well as from the high redox potential of the Mn(III,IV)/Mn(II) couples. Because of these mineral properties, Mn is linked to the biogeochemical cycle of carbon and many trace elements.

The reactivity of birnessite essentially depends on its structural and chemical stability. In particular, the dissolution of these minerals occurs through the reduction of Mn(III,IV), with the potential to mobilize associated compounds. One of the pathways for Mn oxide reduction in surface environments is photoreductive dissolution, a process in which sunlight initiates the electron transfer that leads to reductive dissolution of the mineral. Although this process is predicted to occur, it has never been observed in a system without components that themselves react to light. Therefore, the intrinsic photoreactivity of birnessite minerals in an environmental system lacks experimental evidence.

The objective of this dissertation was to identify the effect of visible light irradiation on the stability of δ -MnO₂, a fully oxidized synthetic birnessite. The rate and mechanism of photoreduction in aqueous mineral suspensions were determined by combining the rates measured on laboratory-based photoreactors with the molecular scale insights on electron transfer dynamics provided by pump-probe optical and synchrotron based techniques. The experiments were initially carried out in simple system containing only the mineral and water at a fixed pH. We then included the effect of environmentally relevant parameters, such as solution pH and the presence of the redox-inactive trace metal Ni(II) adsorbed onto the surface, on the photoreduction of birnessites. Our results show that irradiation of δ -MnO₂ results in the formation of Mn(III), which is stabilized against chemical re-oxidation by migrating in the interlayer. The migration of Mn(III) to the interlayer is pH dependent, with a greater rate at lower pH. Furthermore, the higher amount of Mn(III) stabilized at low pH is also able to compete with Ni(II) adsorbed onto the surface by driving previously adsorbed Ni to solution.

The results from this dissertation provide experimental evidence to the thermodynamic predictions on the intrinsic photoreactivity of birnessite minerals, allowing us to predict the stability of Mn oxides in sunlit surface environments even in the absence of organic and inorganic electron donors. Furthermore, birnessite minerals have been studied recently as viable cost-effective candidates in water oxidation photocatalysis. Our results on the role of Mn(III) may be relevant to the material sciences community, providing better constraints for the design of efficient photoelectrocatalysts for water oxidation.

RÉSUMÉ

Les oxydes de manganèse (III, IV) sont parmi les plus réactifs des oxydes de métaux de transition présents dans les écosystèmes de surface. La birnessite, qui est un oxyde de manganèse lamellaire, en est la phase prédominante. Elle est formée principalement via une oxydation du Mn (II) médiée par des microorganismes. Ces minéraux sont caractérisés par une réactivité élevée à l'adsorption et à la dégradation de nombreux composés organiques et inorganiques, due à une surface spécifique et une densité des sites d'adsorption très importante (au niveau des bords des particules et des sites vacants), ainsi qu'au potentiel redox élevé des couples Mn (III, IV) / Mn (II). Ces propriétés de la birnessite font que le Mn se retrouve en interaction avec le cycle biogéochimique du carbone et de nombreux oligo-éléments.

La grande capacité d'adsorption de la birnessite dépend essentiellement de sa stabilité structurale et chimique. En particulier, sa dissolution se produit par la réduction de Mn (III, IV), qui peut mobiliser les composés associés. Une des voies de réduction de l'oxyde de Mn est la dissolution photoréductive, un processus dans lequel la lumière initie le transfert d'électrons qui conduit à une dissolution réductrice du minéral. Bien que ce processus soit connu en théorie, il n'a jamais été observé dans un système sans éléments réactifs à la lumière. Par conséquent, la photoréactivité intrinsèque de la birnessite n'a pas encore été démontrée expérimentalement.

L'objectif de cette thèse a été d'identifier l'effet de l'irradiation sur la stabilité de la δ -MnO₂, une birnessite synthétique, en déterminant le taux et le mécanisme de sa photoréduction intrinsèque. Pour ce faire, des mesures de taux de photoréduction ont été prises en laboratoire à l'aide de photoréacteurs. Puis, elles ont été combinées avec des mesures portant sur le mécanisme de photoréduction à l'échelle moléculaire obtenues par des techniques de type "pump-probe" optiques et de synchrotron. Les expériences ont été initialement réalisées dans un système simplifié à pH fixe contenant une solution aqueuse de birnessite. Ensuite, le pH a été modifié et un métal inactif d'un point de vue redox a été ajouté, le Ni (II), pour observer leur influence sur la photoréduction du Mn ainsi que sur la spéciation de Mn et Ni entre la surface minérale et la solution. Les résultats montrent que l'irradiation de δ -MnO₂ mène à la formation de Mn(III) qui, lorsqu'il migre au niveau des sites vacants, se retrouve stabilisé chimiquement évitant ainsi d'être oxydé à nouveau. La migration de Mn(III) s'intensifie avec une diminution de pH. A faible pH, le Mn(III) formé entre en compétition avec le Ni(II) qui après désorption se retrouve en solution.

Ces résultats confirment les prédictions thermodynamiques sur la photoréactivité intrinsèque de la birnessite. Aussi, ils permettent de prédire la stabilité des oxydes de Mn dans des écosystèmes de surface irradiés par le soleil même en l'absence de donneurs d'électrons organiques ou inorganiques. De plus, les minéraux de birnessite sont des candidats rentables pour créer des énergies renouvelables par photocatalyse de l'eau. Nos résultats sur le rôle de Mn (III) dans la photoréduction fournissent des contraintes supplémentaires pour la conception de photoélectrocatalyseurs utilisés pour l'oxydation de l'eau en sciences des matériaux.

Chapter 1. Introduction.....	1
1.1. The natural abundance of manganese and its applications in human activities.....	1
1.2. Speciation of Mn between soluble and insoluble species.....	2
1.3. The sunlight-dependent distribution of Mn in surface waters.....	4
1.4. Theoretical background on the photochemistry of transition metal oxides.....	5
1.5. Photochemistry of Fe oxides in environmental science: state of the art.....	8
1.6. Photochemistry of Mn oxides in materials science: state of the art.....	9
1.7. Dissertation objectives and research questions.....	11
1.8. Dissertation organization.....	12
1.9. References.....	15
Chapter 2. Experimental approach.....	21
2.1. Photoreactor design.....	21
2.2. Identification and quantification of photoreduced Mn.....	25
2.3. Photoexcitation mechanism.....	27
2.3.1. Ultrafast (transient absorption) pump-probe optical spectroscopy.....	28
2.3.2. Time resolved X-ray absorption spectroscopy (TRXAS).....	31
2.4. References.....	33
Chapter 3. Controlled synthesis of δ -MnO ₂ : an in-depth characterization of the synthesis products.....	35
3.1. Abstract.....	35
3.2. Introduction.....	35
3.3. Materials and methods.....	38
3.3.1. Background.....	38

TABLE OF CONTENTS

3.3.2. Mineral synthesis	39
3.3.3. Chemical analyses.....	41
3.3.4. Structural characterization of the synthesis products.....	42
3.4. Results.....	44
3.4.1. Physical-chemical characterization.....	44
3.4.2. Structural characterization	45
3.5. Discussion	50
3.6. Conclusions.....	52
3.7. Acknowledgements.....	53
3.8. References.....	53
Chapter 4. The mechanism and rate of δ -MnO ₂ photoreduction in a simplified system	59
4.1. Abstract.....	59
4.2. Significance Statement.....	60
4.3. Introduction.....	60
4.4. Materials and methods	62
4.5. Results.....	66
4.6. Discussion	71
4.7. Environmental implications	76
4.8. Acknowledgements.....	76
4.9. References.....	77
Chapter 5. The pH-dependent photoreduction of δ -MnO ₂ : increased surface protonation leads to greater rates of irreversible Mn(III) photogeneration.....	81
5.1. Abstract.....	81

TABLE OF CONTENTS

5.2. Introduction.....	82
5.3. Materials and methods	84
5.4. Results.....	88
5.5. Discussion	92
5.6. Environmental implications	96
5.7. Acknowledgements.....	97
5.8. References.....	97
 Chapter 6. Photoreactivity of Ni-doped MnO ₂ : pH dependent metal release reflects stabilization of photogenerated Mn(III) in the mineral structure	 101
6.1. Abstract.....	101
6.2. Introduction.....	101
6.3. Materials and methods	104
6.4. Results.....	109
6.5. Discussion	128
6.6. Environmental implications	131
6.7. Acknowledgements.....	132
6.8. References.....	132
 Chapter 7. Conclusions.....	 137
7.1. Directions of future research.....	140
7.2. References.....	151
 ANNEX 1. Photoreactor design	 155
ANNEX 2. Supporting information for Chapter 3	163
ANNEX 3. Supporting information for Chapter 4	167

TABLE OF CONTENTS

7.3. SI Materials and methods.....	168
7.4. SI Results and discussion.....	170
7.5. SI Figures.....	175
7.6. References.....	182
ANNEX 4. Supporting information to Chapter 5.....	184
7.7. SI Text.....	185
7.8. SI Figures and tables.....	188
7.9. References.....	191
ANNEX 5. Supporting Information to Chapter 6.....	193
7.10. References.....	201
ANNEX 6. Chapter 4 as published in PNAS without modifications.....	203
ANNEX 7. Raw data from the flow through photoreduction experiments in Chapters 3 through 6.....	219

Chapter 1. Introduction

1.1. The natural abundance of manganese and its applications in human activities

Manganese is the fifth most abundant element in the Earth's crust, with an average concentration of 11 g/kg (Morgan, 2000). It is an essential micronutrient for many organisms (Tebo et al., 2004) and plants (Armstrong, 2008; Hocking et al., 2011; Hsu et al., 2012; Wiechen et al., 2012b), and can be found in natural waters as dissolved Mn at concentration levels that range from nano- to millimolar (Post, 1999). As a solid species, Mn is mostly found as Mn oxides in surface environments, with concentrations that can reach up to 324 g/kg in ocean sediments (Morgan, 2000). The primary sources of Mn to the Earth's surface are igneous and metamorphic rocks as well as Mn bearing carbonates and silicates, which weather both physically (erosion) and chemically (redox reactions) and release Mn to soils and freshwaters. The release of Mn to the environment from human activities (secondary sources) is even greater. In fact, the anthropogenic mobilization factor for Mn, defined as the mass of element extracted by human activities divided by the mass released from weathering or volcanic activity, is equal to 10 (Sposito, 2008). The total Mn delivered to soils and freshwaters then eventually accumulates in the oceans (Post, 1999). The oceans are also supplied with Mn through hydrothermal vents from oceanic ridges, where Mn co-precipitates with Fe in oceanic ferromanganese nodules (Elderfield, 1976; Morgan, 2000). These nodules, being often associated with trace metals, have been considered in the past as an economically exploitable minable resource (Chung, 1994).

Manganese has found various economic applications in the past and present, ranging from an agent to decolorize glass since the Roman age (Maltoni et al., 2016) to a component in metallurgical products that increase strength (Nurnberger, 1978; Dalai et al., 2014; Ma et al., 2016) as well as reduce corrosion (Al-Negheimish et al., 2014) in steel alloys. Manganese oxides have also found many technological applications, for example as the cathode material of choice in alkaline batteries (Daley, 1961; Greenwood and Earnshaw, 1984; Kordesch and Weissenbacher, 1994) as well as more recently in the development of Li/Mg ion batteries in the pursuit of cost-effective energy storage (Ghoury et al., 2016; Lee et al., 2016; Lu et al., 2016). Because of the strong redox potential of the Mn(IV)/Mn(II) and Mn(III)/Mn(II) couples,

CHAPTER 1

Mn oxides have also been applied as catalysts in many industrial processes (Ching et al., 2016; Delmondo et al., 2016; Dinh et al., 2016). Their redox properties, together with their high sorption affinity, makes them well suited for remediation strategies (e.g. decontamination of polluted water both through the oxidative decomposition of organic compounds (Dang et al., 2016; Peng et al., 2016; Periyasamy et al., 2016) or by sorption and oxidation or precipitation of potentially toxic transition elements (Al Abdullah et al., 2016; Bai et al., 2016; Kim et al., 2016)). Recognizing Mn oxides as semiconductors and the importance of Mn at the core of the water oxidation center (WOC) of photosystem II (Armstrong, 2008), many studies have focused on the potential application of Mn oxides to create efficient and inexpensive photocatalysts for the splitting of water into hydrogen and oxygen for renewable energy generation (Hocking et al., 2011; Wiechen et al., 2012a; Wiechen et al., 2012b; Robinson et al., 2013), as well as in the photocatalytic degradation of organic pollutants (Liu et al., 2016) and inorganic contaminants (Shumlas et al., 2016).

1.2. Speciation of Mn between soluble and insoluble species

In natural environments, Mn is stable in several different oxidation states: Mn(II), Mn(III) and Mn(IV). The cycle of this element is a function of redox conditions and oxygen availability, with the oxidized species, Mn(IV), forming insoluble oxides at oxic, alkaline conditions and the reduced species, Mn(II), mostly present as dissolved ions in acidic, oxygen limited conditions (Morgan, 2000; Tebo et al., 2007). Mn(III), on the other hand, can occur in both solid form (e.g., Mn(III/IV) oxides) as well as a soluble species if complexed by ligands (Morgan, 2000; Madison et al., 2013).

Soluble (aqueous) Mn is found mainly as the free divalent ion, Mn(II). It can be oxidized by molecular oxygen to form Mn oxides, but this process is known to be kinetically limited at the pH of natural waters if uncatalyzed. In fact, the half-life of Mn(II) in oxic seawater is 350 days in the absence of catalysts for its oxidation (Morgan, 2005). Microorganisms (bacteria and fungi) serve as the main catalysts for Mn(II) oxidation (Tebo et al., 2004). The precipitated oxide then catalyzes further oxidation of Mn(II) on its surface (Spiro et al., 2010; Droz et al., 2015). Manganese oxidation can also be catalyzed on mineral surfaces (Wilson, 1980) as well as by reactive oxygen species (Hansel et al., 2012). Because of its widespread occurrence and the range of stable oxidation states, Mn is also known to play

an important role in biological systems. In fact, it is an essential component of the oxygen evolution center in Photosystem II to yield O₂ from the oxidation of water in photosynthesis (Armstrong, 2008; Hocking et al., 2011; Hsu et al., 2012; Wiechen et al., 2012b), as well as an important component of many enzymatic processes that protect cells from reactive oxygen species (Morgan, 2000; Tebo et al., 2007). Another soluble species of Mn that has recently gained importance is aqueous Mn(III), although it is not stable as a free ion. In fact, Mn(III) requires complexation by natural organic or inorganic ligands in order to remain stable in solution (Madison et al., 2013). In the absence of such ligands, Mn(III) disproportionates rapidly into Mn(II) and Mn(IV) in solution. The presence of soluble Mn(III) has recently been found to be a major component of the sedimentary redox system, accounting for up to 90% of the soluble manganese present in suboxic porewaters up to 20 cm of depth (Madison et al., 2013). Recently, it has been shown that aqueous Mn(III) is also stable in oxic conditions, complexed by humic ligands (Oldham et al., 2016). Therefore, in natural environments where Mn(III) complexing ligands are present, aqueous Mn(III) may be a non-negligible aqueous Mn species.

Insoluble Mn, on the other hand, is found primarily as Mn oxides, which in nature contain Mn(IV) and Mn(III) in varying proportions (Post, 1999). The majority of Mn oxides form layer or tunnel type structures. The most environmentally relevant structures are the layer Mn oxides, also known as birnessites. These minerals occur as randomly stacked sheets of MnO₆ edge sharing octahedra containing Mn in both the Mn(III) and Mn(IV) states. Birnessites are the predominant natural Mn oxide as they form through microbially catalyzed Mn(II) oxidation (Villalobos et al., 2003; Jurgensen et al., 2004). During biogenic Mn(II) oxidation the first oxidation product is a fully oxidized phase (only Mn(IV) present), which subsequently accumulates Mn(III) within its structure (Spiro et al., 2010). Birnessite minerals have a set of properties that make them important players in the biogeochemical cycle of many other elements, including trace metals and carbon. The first property is their particle size: natural birnessites are characterized as nanoparticles with a high specific surface area. A consequence of their size and layer-type structure is the high density of sorption sites (i.e., sites in the octahedral sheet that lack a Mn octahedron), situated both on particle edges and Mn octahedral vacancies, (Ruetschi, 1984). Finally, the Mn(IV)/Mn(II) and Mn(III)/Mn(II) redox couples are amongst the most potent in nature, rendering them powerful oxidants of many

organic and inorganic compounds (Stumm and Morgan, 1996; Sposito, 2008). Given these properties, birnessite minerals, together with Fe oxides, play an important role in governing numerous biogeochemical cycles. Furthermore, the greater sorptive and redox reactivity per unit mass of Mn oxides (relative to Fe oxides) makes them at least as important as these ubiquitous Fe oxides even though the average concentration of Mn oxides in soils and sediments is 10 times lower than that of Fe oxides (Tebo et al., 2007). A schematic representation of the Mn cycle is shown in **Figure 1**.

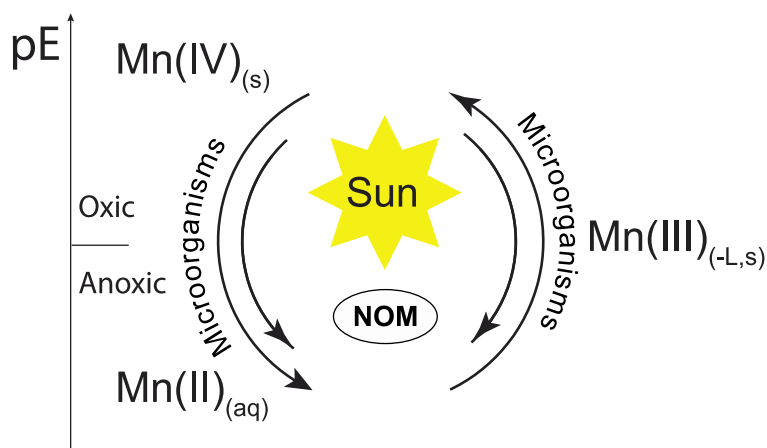


Figure 1. Mn cycle showing the oxidation and reduction of Mn by microorganisms and the reduction of Mn by sunlight and natural organic matter. The position of aqueous Mn(II), ligand-bound and solid Mn(III) and solid Mn(IV) on the vertical is related to the redox potential of the system, as well as the oxic/anoxic conditions in the absence of reducing and oxidizing forces.

1.3. The sunlight-dependent distribution of Mn in surface waters

In oxygen-rich environments, manganese forms oxides through the catalyzed oxidation of Mn(II). Therefore, aqueous Mn is generally absent in surface waters characterized by high dissolved oxygen concentrations and in the presence of Mn-oxidizing bacteria. In contrast to thermodynamic predictions, however, the vertical profile of Mn in a multitude of oceanic and lacustrine water columns shows dissolved Mn(II) in surface waters reaching nanomolar concentrations (Klinkhammer and Bender, 1980; Landing and Bruland, 1987; Sunda and Huntsman, 1990; Davison, 1993; Statham et al., 1998). The Mn profile contrasts that of most trace metals, which are depleted at the surface due to biological scavenging (Morgan, 2000). A gradual decrease in the concentration of aqueous Mn is observed with depth, becoming

negligible below the photic zone, where particulate Mn (Mn(IV/III) oxides) predominate (Sunda et al., 1983).

The anomaly of Mn speciation with depth is attributed to the fact that Mn oxides are transition metal oxides, and like many transition metal oxides, they are semiconductors. Therefore, visible light can initiate electronic transitions in the mineral. Manganese oxides are known to undergo photoreductive dissolution whereby light can mediate the transfer of electrons from surface sorbed species (Stone, 1983; Waite, 1990; Sunda and Huntsman, 1994). Although semiconduction theory and thermodynamic calculations predict that Mn oxides should react to light (Sherman, 2005), few experimental studies have investigated the mechanism and environmental controls on the photoreduction of these oxides. Among these studies, the most complete are those of Sunda et al. (1983); Sunda and Huntsman (1990, 1994). These studies propose that photoreductive dissolution is caused either by a ligand to metal charge transfer process involving organics, or by reduction of the oxide by photochemically generated H_2O_2 and/or photoinhibition of biogenic Mn oxidation. These hypotheses support the low occurrence of Mn oxides in the surface of oceanic waters and the presence of modest concentrations of aqueous, reduced Mn.

1.4. Theoretical background on the photochemistry of transition metal oxides

Before introducing the objectives of this dissertation, I first outline the theoretical basis behind photochemical processes in semiconducting transition metal oxides. Photochemical processes at the mineral-water interface can follow three main processes: i) light absorption in the bulk mineral, which leads to electron transfer by a semiconduction mechanism; ii) light absorption by surface species which leads to electron transfer between the mineral and the surface species (i.e., ligand to metal charge transfer – LMCT - or metal to ligand charge transfer – MLCT) which often involves the formation of radical species; and iii) light absorption by surface species, which does not lead to electron transfer between the mineral and the surface species (Waite, 1990).

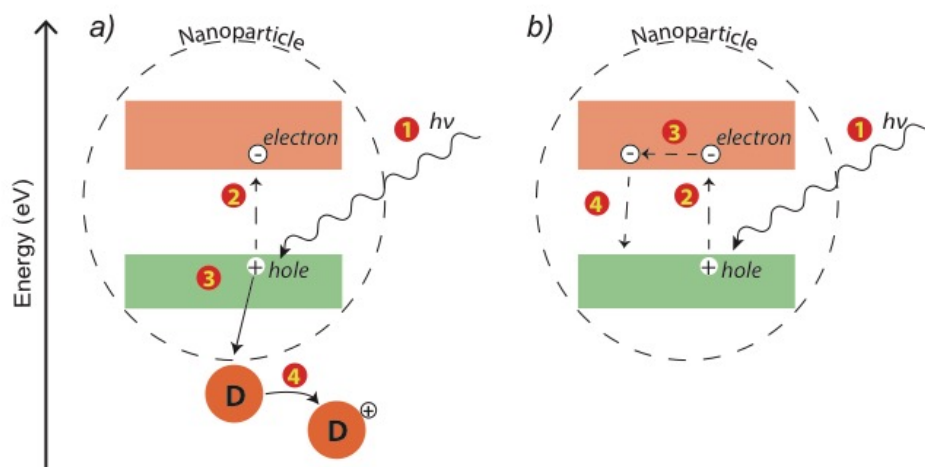


Figure 2. Schematic outlining a) the steps in the photocorrosion (~photoreduction) process of a semiconductor nanoparticle: 1) photon absorption, 2) electron excitation from valence band to conduction band with creation of a valence hole, 3) hole scavenging (equivalent to electron injection) from a surface sorbed hole scavenger (~electron donor), 4) desorption of the hole scavenger as an oxidized species. The nanoparticle then re-equilibrates through a valence change, in this case a reduction of the metal atoms (~conduction band); b) band gap excitation of a semiconducting nanoparticle that does not lead to photoreduction. Steps are identical to the photocorrosion, except that: 3) photoexcited electron may or may not move by conduction in the conduction band until 4) it recombines with the valence band hole, terminating the photexcitation process. Usually during photoexcitation of semiconductors with surface sorbed hole scavengers, a combination of the two processes occurs. Diagram adapted from Gilbert and Banfield (2005).

The basis for all of the photochemical processes described is the semiconduction mechanism, of which a schematic representation in relation to a metal to ligand charge transfer mechanism is shown in **Figure 2**. Semiconduction can be described more precisely using band theory, which treats the photoexcitation from an energetic perspective. The energy separation between the valence band, which is equivalent to the “filled” electronic orbitals, and the conduction band, which is equivalent to the “unoccupied” electronic orbitals, is such that visible light may promote/excite a valence band electron into the conduction band. These bands are separated by a band gap, with the Fermi level found in the middle of the band gap and can be considered the electrochemical potential of the mineral. The band gap can be either direct or indirect (i.e., the electrons and holes in the conduction and valence bands have the same or opposite momentum, respectively). Upon absorption of visible light, a photoexcited electron is promoted to the conduction band and an electron hole is formed in the valence band. If the band gap is indirect, additional energy is required for the electron to transfer momentum to the material. Once excited into the conduction band, the electron can relax in three different ways:

i) it may recombine with the hole emitting heat (non-radiative degradation), thereby terminating the photoexcited state without any change to the mineral; ii) it can be temporarily trapped into various intra- or interband states or receive additional energy from a second photon absorption, then relax into the valence band hole emitting one or more photons of higher or lower energy (luminescence – radiative degradation); or iii) it may move by conduction within the conduction band until it, or the valence hole, are scavenged by a surface species. In this last scenario the mineral will have a deficiency or excess of electrons, thereby resulting in a chemical change that is termed photo-oxidation or photo-reduction (Waite, 1990; Gilbert and Banfield, 2005; Balzani et al., 2014).

The semiconducting properties of many transition metal oxides including Mn and Fe oxides originate from their partially filled *d* orbitals, by which the absorption of light leads to *d-d* transitions (Sakai et al., 2005). In the case of Mn oxides, the transitions occur from Mn $3d_{t_2g}$ orbitals, which lie at the top of the valence band, to Mn $3d_{e_g}$ orbitals, which lie at the bottom of the conduction band. Usually the conduction band states are localized in the metal (3d) orbitals, whereas the valence band states are localized in the O (2p) orbitals. However, M-O bonds are partially covalent, since electrons are shared between the metal and oxygen orbitals. Therefore, the Mn atom has some O (2p) character, which allows the top of the valence band to be localized on Mn atoms (Sakai et al., 2005).

The semiconducting properties of minerals are also influenced by surface impurities, defects (such as vacancies), and finite size (Waite, 1990; Gilbert and Banfield, 2005). Surface impurities, for example, may introduce electrons in the conduction band by underbonded atoms, mediate charge transfer between adsorbates and the mineral surface, and modify the lifetime of the photoexcited electron and hole (Gilbert and Banfield, 2005). For example, since electron/hole recombination is size independent, while electron transit to a surface is directly size dependent, electron or hole escape before recombination may be enhanced in smaller particles with respect to larger particles. An opposite effect occurs when a nanoparticle small enough to be comparable to the Bohr radius (the distance for the lowest energy attraction between an electron-hole pair) is irradiated. In this case, additional energy for band gap excitation is required to overcome the electron-hole interaction, which results in an overall increase in the band gap (Gilbert and Banfield, 2005).

CHAPTER 1

Different band gap values have been measured for birnessite due to the effect of size, impurities and defects on semiconducting properties. For example, Sherman (2005) measured a band gap between 1.8 and 1.0 eV in triclinic Na-birnessite with oxygen X-ray absorption (valence band sensitive) and emission (conduction band sensitive) spectroscopy, respectively, and Kwon et al. (2009) showed an increase in vacancies from 0 to 12.5 % reduced the band gap in the mineral from 1.3 eV to 0.3 eV when estimating the effect of vacancies on the band gap of hexagonal K-birnessite with density of states (DOS) studies. Furthermore, with an increase in vacancies to 12.5 % the band gap changes from indirect to direct. Hsu et al. (2012), on the other hand, measured a band gap of 2.1 eV for birnessite nanosheets synthesized through electrochemical oxidation of MnSO_4 . Finally, Sakai et al. (2005) estimated an indirect band gap of 2.23 eV for atom-thick birnessite nanosheets by correlating the incident photon to electron conversion efficiency (IPCE) with the photon energy. These band gap values, being lower than 3.1 eV (i.e., the highest energy obtainable by visible light (400 nm)), confirm that birnessite minerals are susceptible to band gap excitations by visible light.

1.5. Photochemistry of Fe oxides in environmental science: state of the art

Most transition metal oxides undergo photoreductive processes due to their semiconducting nature. However, even though the photoreduction of Mn oxides strongly affects the distribution of Mn in the ocean water column, this process has not been well-studied experimentally (Sunda et al., 1983; Waite et al., 1988; Sunda and Huntsman, 1994; Kim et al., 2012). The environmental chemistry literature has primarily focused on the photoreduction of Fe oxides (Siffert and Sulzberger, 1991; Karametaxas et al., 1995; Sulzberger and Laubscher, 1995; Voelker et al., 1997; Emmenegger et al., 2001; Borer et al., 2005; Borer et al., 2007; Borer et al., 2009b, c; Sulzberger and Laubscher, 2009). In particular, the photochemistry of Fe oxides has been studied in the presence and absence of organic compounds such as citrate and siderophores (Borer et al., 2005; Borer et al., 2009b) and as a function of pH and irradiation wavelength (Borer et al., 2009a; Borer et al., 2009c). These studies show that the photoreduction of Fe oxides depends on wavelength, where lower wavelengths lead to higher photoreduction rates due to the wavelength-dependent photolysis of photoreduced Fe(II)-hydroxo groups. Photoreduction is pH dependent, where lower pH leads to greater photoreduction because of the pH dependence of Fe(II) stability against re-oxidation by

oxygen. Fe photoreduction is also highly dependent on the presence of organic compounds to complex and scavenge photoreduced Fe(II) from the Fe oxide mineral surface as Fe(II) rapidly re-oxidizes on the surface of the oxide under oxic conditions. Furthermore, the authors observe that photoreduction of Fe(III) to Fe(II) is coupled to the generation of hydroxyl radicals (OH[•]), where the combination of 2 hydroxyl radical molecules eventually results in the formation of H₂O₂. In their studies, the authors also observed that the pH dependence of the reaction is largely due to the pH-dependent reoxidation kinetics of Fe(II) on the mineral surface. Finally, the authors calculate apparent quantum yields (Fe(II) formed per photon absorbed) for the photoreduction process, which were on the order of $\sim 10^{-5}$ for the highest rate conditions (low pH) in the absence of organic compounds.

The few studies on Mn photoreduction were carried out in natural systems and investigated the photoreductive process in seawater in the presence of organic compounds and microorganisms. Organic compounds and microorganisms are also known to react separately with the oxides in the presence of sunlight. A LMCT mechanism between organics and the mineral, reduction by reaction of photoproduct H₂O₂ with the oxides, or photoinhibition of Mn oxidizing microorganisms was invoked to explain the photoreductive dissolution of Mn oxides (Sunda et al., 1983; Sunda and Huntsman, 1994). However, H₂O₂ is also known to oxidize Mn(II) (Hansel et al., 2012) and photoinhibition of Mn oxidizing bacteria has only been observed indirectly. Furthermore, no experiments have been carried out to decouple the photoreduction mechanism of the Mn mineral from the photoreactivity of other components present in the natural system, and advanced techniques providing molecular scale information were at the initial stage of development at the time of those studies. Therefore, the Mn oxide photoreduction mechanism has not yet been confirmed experimentally.

1.6. Photochemistry of Mn oxides in materials science: state of the art

In the last two decades Mn oxides have emerged as a promising technology to harvest sunlight, both as a catalyst for water oxidation and in the design of novel solar cells for electricity generation (Sakai et al., 2005; Hocking et al., 2011; Young et al., 2011; Hsu et al., 2012; Kolling et al., 2012; Takashima et al., 2012; Wiechen et al., 2012b; Birkner et al., 2013; Robinson et al., 2013; Zhou et al., 2013). A review of the main findings of a selection of these

CHAPTER 1

studies provides some information to constrain the controlling processes of Mn photochemistry.

Recent water oxidation studies have shown that the layer structure and bonding of birnessite minerals mimicks the water oxidation center (WOC) of photosystem II (Hocking et al., 2011; Hsu et al., 2012; Wiechen et al., 2012b). In fact, the WOC is the only established system that efficiently catalyzes water oxidation (Hocking et al., 2011), a process that is otherwise demanding both kinetically and thermodynamically. The WOC is constituted of CaMn_4O_5 in which 3 Mn ions and Ca form a cubane and the fourth Mn is bound with ligands. Hocking et al. (2011) studied the catalysis of water oxidation by a Mn containing molecule similar to the WOC incorporated onto a Nafion[®] polymer matrix. This molecule was shown to convert to a Mn(III/IV) phase similar in structure to birnessite after electro-oxidation, which then was able to generate oxygen upon irradiation. Similarly, Deibert et al. (2015) have shown that under photocatalytic conditions their initial Mn based photocatalysts convert to a layer phase similar to birnessite, with varying amounts of Mn(III). The final layer-type phase and not the initial WOC-mimicking molecule was responsible for the high photocatalytic activity, since the final phases retained the activity over various photoelectrochemical cycles.

Wiechen et al. (2012b) confirmed that the birnessite structure is a good mimic of the WOC because of Mn-Mn distances, Mn oxidation state and Mn-Ca connectivities. Their studies also show that Ca is necessary for water oxidation, which derives from both a biological and structural role in the WOC. These observations were also confirmed by Lucht and Mendoza-Cortes (2015); Rong et al. (2016). Interestingly, also the microbial oxidation of Mn(II) requires the presence of calcium (Webb et al., 2005). The nature of interlayer cations, in particular the charge, also affects the frustration of water molecules coordinated to them in the interlayer (Remsing et al., 2015). Frustration defines the complex structures that arise because of conflicting inter-atomic forces. An increased cation charge leads to greater water molecule frustration, which potentially enhances the water oxidation capacity in birnessite minerals (Remsing et al., 2015).

The role of Mn(III) in the photocatalytic activity of Mn oxides is also important. The presence of up to 50 % mol Mn(III) mol⁻¹ Mn_{total}⁻¹ and its crystallographic location have been shown to strongly enhance the photocatalytic activity of the materials (Maitra et al., 2013;

Robinson et al., 2013; Lucht and Mendoza-Cortes, 2015). In particular, Maitra et al. (2013) have shown that the photocatalytic activity occurs due to Mn(III) having a single electron in a e_g^1 degeneracy which facilitates electron transfer during the electrochemical water oxidation reaction and Lucht and Mendoza-Cortes (2015) have shown that the presence of Mn(III) lowers the band gap in the mineral. Finally, Robinson et al. (2013) showed that the Jahn-Teller distortion of Mn(III) imparts greater structural flexibility to the mineral, and suggested this to be important for the catalytic activity of the oxides.

The effect of mineral size has been observed in studies investigating the potential applications of Mn oxides to harvest light for direct production of electricity in solar cells. For example, photocurrent generation by birnessite nanosheets was studied by Hsu et al. (2012) and Sakai et al. (2005). Hsu et al. (2012) observed a modest current generation (7% incident photon to current efficiency – IPCE) when irradiating these oxides with visible light. In Sakai et al. (2005), the authors showed that only the topmost layer is photoactive, whereas the lower layers are characterized by recombinative processes. Therefore, these studies show that nanostructures are important in designing an efficient Mn oxide-based solar cell.

In summary, the reactivity of Mn oxides in the oxidation of water depends on the interlayer cation, where Ca has a strong effect on the catalytic activity of the oxides relative to other cations, and on the amount and structural location of Mn(III). Therefore, these parameters are likely to affect Mn oxide photoreactivity in environmental systems. The small particle size of these oxides was also shown to enhance their photoreactivity in a solar cell circuit. Therefore, the nanoscale of environmentally occurring birnessite minerals will play an important role in their photoreactivity, where smaller particles will likely be more reactive than larger particles (within the physical limit set by the Bohr radius as previously described).

1.7. Dissertation objectives and research questions

This PhD dissertation aims to identify the mechanism and environmental controls on the photoreduction of Mn oxides independent of the interference of microorganisms and organic compounds on the process. A simple model will be initially studied, to which layers of complexity will be gradually added. The experimental design builds on information obtained in the Mn oxide photocatalysis and photoelectrochemistry studies, combined with the

CHAPTER 1

information from the Fe oxide environmental photochemistry studies. These studies also provide a reference basis to frame the obtained results, bridging an important knowledge gap in the environmental science community and providing new insights for the material science community. The objectives of this dissertation will be achieved by attempting to answer the following research questions:

- What is the rate and mechanism of birnessite photoreduction?
- How does pH affect the rate and mechanism of birnessite photoreduction?
- How does the photoreduction of birnessite affect the fate of surface-sorbed trace metals?

We will focus particularly on the key parameters identified by the material sciences studies, such as interlayer cations, Mn(III) content and particle size. The interpretation of our results will be linked with the environmental studies on Fe oxide photochemistry, in particular the photoreduction mechanism resulting in OH radical generation and the pH dependence of the photoreduction rates.

1.8. Dissertation organization

This dissertation begins with an initial chapter introducing the analytical techniques that were key to obtaining the results presented throughout this thesis. The following four chapters describe the experimental work carried out during the duration of this PhD project. Each chapter addresses a system of increasing complexity. The final chapter summarizes the conclusions obtained in the previous chapters and presents future research directions that can be addressed to further advance the knowledge on the photoreduction of birnessite minerals. A summary of the motivation, objectives and main results of the different chapters is provided below.

Chapter 2 provides a description of the analytical techniques that were used in this dissertation, in particular the techniques that were either key to results obtained in this work or that are uncommon in the geochemistry community, including: the average Mn oxidation number determination by potentiometric titration, the Mn(III) extraction protocol with sodium pyrophosphate, the photoreactor design and characterization, the transient absorption pump-probe spectroscopy, and the X-ray absorption spectroscopy.

Chapter 3 describes the synthesis of the mineral used for the photoreduction studies, δ -MnO₂. This mineral is the synthetic analog to naturally occurring birnessites, in particular those precipitated by microorganisms in surface environments (Spiro et al., 2010). The motivation for this study arose from variations in the published physicochemical properties of δ -MnO₂. In addition, the initial synthesis of this mineral in our laboratory gave products with differing physicochemical properties including Na content, particle size, and specific surface area. This chapter therefore addresses these issues, showing that the pH of the synthesis is directly proportional to the Na content and inversely proportional to specific surface area. Furthermore, an in-depth characterization of the mineral phase used in all subsequent photoreduction experiments is provided.

Chapter 4 investigates the rates and photoreduction mechanism for δ -MnO₂ in a simplified system containing only water at circumneutral pH and a background electrolyte (either CaCl₂, NaCl, or sodium pyrophosphate). The advantage of obtaining molecular scale information allows us to constrain the effects of sunlight to the mineral alone, and not to the components of the natural system that are often associated with the mineral (e.g. redox-active and photoactive organic compounds) as well as transition metals that may enhance or reduce the (photo)reactivity of the mineral. In this study we combined hour to day time resolution experiments on photoreactors to evaluate the Mn(IV) photoreduction rates with ultrafast transient absorption spectroscopy (both all optical and optical/X-ray) to investigate the photoexcitation mechanism on the femto- to microsecond timescale. The results show that photoreduction occurs with the progressive accumulation of Mn(III) in the mineral in a different crystallographic location compared to the initial Mn(IV). Furthermore, the amount of photogenerated Mn(III) is much lower than the actual number of atoms that are photoexcited in the mineral, as evidenced by the apparent quantum yield of the process (defined as the amount of Mn(III) generated per photon absorbed) on the order of $\sim 10^{-4}$, which is one order of magnitude greater than that of Fe oxides. By extrapolating from the Fe oxide photoreduction studies and the simplicity of our studied system, we predict that Mn(IV) photoreduction is coupled to partial water oxidation, leading to the formation of OH radical species. However, these species still have to be determined experimentally.

Chapter 5 expands the previous model for δ -MnO₂ photoreduction to include the effect of the master variable controlling most environmental systems: solution pH. In this chapter, the photoreduction rates and mechanism were investigated at pH values of 4.0, 6.5 and 8.0 using either sodium pyrophosphate as a pH buffer or using HCl and NaOH adjustment by automatic titrators in the presence of a NaCl electrolyte. The experiments were carried out as outlined in the previous chapter with lab-based photoreactors and transient absorption all optical spectroscopy. The results show that although photoreduction rates vary as a function of pH, the photoexcitation mechanism remains the same. In particular, we relate the greater photoreduction at lower pH to increased protonation of the mineral surface, which leads to a weakening of Mn-O bonds and enhances the probability for the migration of photogenerated Mn(III) to the stable structural site identified in **Chapter 3**.

Chapter 6 investigates the effect of mineral irradiation on the mobility of Ni previously adsorbed onto δ -MnO₂ in suspensions at pH 4.0 and 8.0, as well as on the photoreduction rates of δ -MnO₂ with and without Ni on the surface. Toward this end, we combine the knowledge gained from **Chapters 4** on the photoreduction rate and mechanism for δ -MnO₂ and **Chapter 5** on the effect of pH on the photoreduction rate with the well understood sorption mechanism of Ni, a redox-inactive transition metal, on δ -MnO₂. The results show that at pH 4.0, irradiation leads to a 50% release of Ni from the mineral surface, and the remaining Ni is sorbed primarily on particle edges and not on vacancy sites as occurs in the dark. At pH 8.0, on the other hand, there is no Ni release. There is, however, a slight change in the sorption geometry of Ni, where irradiation leads to a small increase in Ni incorporation into the nanosheets with respect to Ni adsorbed onto vacancy sites. These results have important implications for a wide range of trace metal dynamics in surface environments (e.g. lakes, streams and ocean waters), where diel variations in sunlight irradiation may modify the speciation of Ni and other similar trace metals through the formation of Mn(III) on the mineral surface. Furthermore, these results give an indirect indication that photogenerated Mn(III) is preferentially located above layer vacancies confirming the model developed in **Chapter 3**.

1.9. References

- Al-Negheimish, A., Alhozaimy, A., Hussain, R.R., Al-Zaid, R., Singh, J.K., Singh, D.D.N., **2014**. Role of Manganese Sulfide Inclusions in Steel Rebar in the Formation and Breakdown of Passive Films in Concrete Pore Solutions. *Corrosion-Us* 70, 74-86.
- Al Abdullah, J., Al Lafi, A.G., Al Masri, W., Amin, Y., Alnama, T., **2016**. Adsorption of Cesium, Cobalt, and Lead onto a Synthetic Nano Manganese Oxide: Behavior and Mechanism. *Water Air Soil Poll* 227.
- Armstrong, F.A., **2008**. Why did Nature choose manganese to make oxygen? *Philos Trans R Soc Lond B Biol Sci* 363, 1263-1270; discussion 1270.
- Bai, Y.H., Yang, T.T., Liang, J.S., Qu, J.H., **2016**. The role of biogenic Fe-Mn oxides formed in situ for arsenic oxidation and adsorption in aquatic ecosystems. *Water Res* 98, 119-127.
- Balzani, V., Ceroni, P., J., A., **2014**. *Photochemistry and Photophysics: Concepts, Research, Applications*, Weinheim, Germany.
- Birkner, N., Nayeri, S., Pashaei, B., Najafpour, M.M., Casey, W.H., Navrotsky, A., **2013**. Energetic basis of catalytic activity of layered nanophase calcium manganese oxides for water oxidation. *Proc Natl Acad Sci U S A* 110, 8801-8806.
- Borer, P., Hug, S.J., Sulzberger, B., Kraemer, S.M., Kretzschmar, R., **2007**. Photolysis of citrate on the surface of lepidocrocite: An in situ attenuated total reflection infrared spectroscopy study. *J Phys Chem C* 111, 10560-10569.
- Borer, P., Kraemer, S.M., Sulzberger, B., Hug, S.J., Kretzschmar, R., **2009a**. Photodissolution of lepidocrocite (γ -FeOOH) in the presence of desferrioxamine B and aerobactin. *Geochim Cosmochim Acta* 73, 4673-4687.
- Borer, P., Sulzberger, B., Hug, S.J., Kraemer, S.M., Kretzschmar, R., **2009b**. Photoreductive dissolution of iron(III) (hydr)oxides in the absence and presence of organic ligands: experimental studies and kinetic modeling. *Environ Sci Technol* 43, 1864-1870.
- Borer, P., Sulzberger, B., Hug, S.J., Kraemer, S.M., Kretzschmar, R., **2009c**. Wavelength-Dependence of Photoreductive Dissolution of Lepidocrocite (γ -FeOOH) in the Absence and Presence of the Siderophore DFOB. *Environ Sci Technol* 43, 1871-1876.
- Borer, P.M., Sulzberger, B., Reichard, P., Kraemer, S.M., **2005**. Effect of siderophores on the light-induced dissolution of colloidal iron(III) (hydr)oxides. *Mar Chem* 93, 179-193.
- Ching, S., Carmichael, J.R., Eichelberger, L.A., Kriz, D.A., Alley, K.A., Jackvony, S.E., **2016**. Influence of Fe, Cu, V, and Ce doping on morphology and catalytic activity of amorphous manganese oxide hollow spheres. *Polyhedron* 114, 205-212.
- Chung, J.S., **1994**. Deep-Ocean Cobalt-Rich Crust Mining System Concepts. *Mts 94 - Challenges and Opportunities in the Marine Environment, Proceedings*, 95-101.
- Dalai, R.P., Das, S., Das, K., **2014**. Development of TiC reinforced austenitic manganese steel. *Can Metall Quart* 53, 317-325.
- Daley, J.L.S., **1961**. Alkaline Manganese Dioxide-Zinc Batteries. *J Electrochem Soc* 108, C162-C163.
- Dang, T.D., Banerjee, A.N., Tran, Q.T., Roy, S., **2016**. Fast degradation of dyes in water using manganese-oxide-coated diatomite for environmental remediation. *J Phys Chem Solids* 98, 50-58.
- Davison, W., **1993**. Iron and Manganese in Lakes. *Earth-Sci Rev* 34, 119-163.

CHAPTER 1

- Deibert, B.J., Zhang, J.M., Smith, P.F., Chapman, K.W., Rangan, S., Banerjee, D., Tan, K., Wang, H., Pasquale, N., Chen, F., Lee, K.B., Dismukes, G.C., Chabal, Y.J., Li, J., **2015**. Surface and Structural Investigation of a MnOx Birnessite-Type Water Oxidation Catalyst Formed under Photocatalytic Conditions. *Chem-Eur J* 21, 14218-14228.
- Delmondo, L., Salvador, G.P., Munoz-Tabares, J.A., Sacco, A., Garino, N., Castellino, M., Gerosa, M., Massaglia, G., Chiodoni, A., Quaglio, M., **2016**. Nanostructured Mn_xO_y for oxygen reduction reaction (ORR) catalysts. *Appl Surf Sci* 388, 631-639.
- Dinh, M.T.N., Giraudon, T.M., Vandenbroucke, A.M., Morent, R., De Geyter, N., Lamonier, J.F., **2016**. Manganese oxide octahedral molecular sieve K-OMS-2 as catalyst in post plasma-catalysis for trichloroethylene degradation in humid air. *J Hazard Mater* 314, 88-94.
- Droz, B., Dumas, N., Duckworth, O.W., Pena, J., **2015**. A Comparison of the Sorption Reactivity of Bacteriogenic and Mycogenic Mn Oxide Nanoparticles. *Environ Sci Technol* 49, 4200-4208.
- Elderfield, H., **1976**. Manganese fluxes to the oceans. *Mar Chem* 4, 103-132.
- Emmenegger, L., Schonenberger, R.R., Sigg, L., Sulzberger, B., **2001**. Light-induced redox cycling of iron in circumneutral lakes. *Limnol Oceanogr* 46, 49-61.
- Ghour, Z.K., Zahoor, A., Barakat, N.A.M., Alsoufi, M.S., Bawazeer, T.M., Mohamed, A.F., Kim, H.Y., **2016**. The (2 x 2) tunnels structured manganese dioxide nanorods with alpha phase for lithium air batteries. *Superlattice Microst* 90, 184-190.
- Gilbert, B., Banfield, J.F., **2005**. Molecular-scale processes involving nanoparticulate minerals in biogeochemical systems. *Molecular Geomicrobiology* 59, 109-155.
- Greenwood, N.N., Earnshaw, A., **1984**. Chemistry of the elements. *Pergamon Press*.
- Hansel, C.M., Zeiner, C.A., Santelli, C.M., Webb, S.M., **2012**. Mn(II) oxidation by an ascomycete fungus is linked to superoxide production during asexual reproduction. *Proc Natl Acad Sci U S A* 109, 12621-12625.
- Hocking, R.K., Brimblecombe, R., Chang, L.Y., Singh, A., Cheah, M.H., Glover, C., Casey, W.H., Spiccia, L., **2011**. Water-oxidation catalysis by manganese in a geochemical-like cycle. *Nat Chem* 3, 461-466.
- Hsu, Y.K., Chen, Y.C., Lin, Y.G., Chen, L.C., Chen, K.H., **2012**. Birnessite-type manganese oxides nanosheets with hole acceptor assisted photoelectrochemical activity in response to visible light. *J Mater Chem* 22, 2733-2739.
- Jurgensen, A., Widmeyer, J.R., Gordon, R.A., Bendell-Young, L.I., Moore, M.M., Crozier, E.D., **2004**. The structure of the manganese oxide on the sheath of the bacterium *Leptothrix discophora*: An XAFS study. *Am Mineral* 89, 1110-1118.
- Karametaxas, G., Hug, S., Sulzberger, B., **1995**. Photodegradation of EDTA in the presence of lepidocrocite. *Environ Sci Technol* 29, 2992-3000.
- Kim, D.G., Nhung, T.T., Ko, S.O., **2016**. Enhanced adsorption of heavy metals with biogenic manganese oxide immobilized on zeolite. *Ksce J Civ Eng* 20, 2189-2196.
- Kim, K., Yoon, H.I., Choi, W., **2012**. Enhanced dissolution of manganese oxide in ice compared to aqueous phase under illuminated and dark conditions. *Environ Sci Technol* 46, 13160-13166.
- Klinkhammer, G.P., Bender, M.L., **1980**. The Distribution of Manganese in the Pacific-Ocean. *Earth Planet Sc Lett* 46, 361-384.

- Kolling, D.R., Cox, N., Ananyev, G.M., Pace, R.J., Dismukes, G.C., **2012**. What Are the Oxidation States of Manganese Required To Catalyze Photosynthetic Water Oxidation? *Biophys J* 103, 313-322.
- Kordesch, K., Weissenbacher, M., **1994**. Rechargeable Alkaline Manganese-Dioxide Zinc Batteries. *J Power Sources* 51, 61-78.
- Kwon, K.D., Refson, K., Sposito, G., **2009**. On the role of Mn(IV) vacancies in the photoreductive dissolution of hexagonal birnessite. *Geochim Cosmochim Acta* 73, 4142-4150.
- Landing, W.M., Bruland, K.W., **1987**. The Contrasting Biogeochemistry of Iron and Manganese in the Pacific-Ocean. *Geochim Cosmochim Acta* 51, 29-43.
- Lee, S.W., Lee, C.W., Yoon, S.B., Kim, M.S., Jeong, J.H., Nam, K.W., Roh, K.C., Kim, K.B., **2016**. Superior electrochemical properties of manganese dioxide/reduced graphene oxide nanocomposites as anode materials for high-performance lithium ion batteries. *J Power Sources* 312, 207-215.
- Liu, F., Zeng, M., Li, Y.Z., Yang, Y., Mao, M.Y., Zhao, X.J., **2016**. UV-Vis-Infrared Light Driven Thermocatalytic Activity of Octahedral Layered Birnessite Nanoflowers Enhanced by a Novel Photoactivation. *Adv Funct Mater* 26, 4518-4526.
- Lu, K., Hu, Z.Y., Xiang, Z.H., Ma, J.Z., Song, B., Zhang, J.T., Ma, H.Y., **2016**. Cation Intercalation in Manganese Oxide Nanosheets: Effects on Lithium and Sodium Storage. *Angew Chem Int Edit* 55, 10448-10452.
- Lucht, K.P., Mendoza-Cortes, J.L., **2015**. Birnessite: A Layered Manganese Oxide To Capture Sunlight for Water-Splitting Catalysis. *J Phys Chem C* 119, 22838-22846.
- Ma, B., Li, C.S., Song, Y.L., Zheng, J.J., **2016**. Effect of manganese content on hot deformation behaviour of Fe-(20/27)Mn-4Al-0.3C non-magnetic steels. *Mater Sci Tech-Lond* 32, 890-897.
- Madison, A.S., Tebo, B.M., Mucci, A., Sundby, B., Luther, G.W., 3rd, **2013**. Abundant porewater Mn(III) is a major component of the sedimentary redox system. *Science* 341, 875-878.
- Maitra, U., Naidu, B.S., Govindaraj, A., Rao, C.N.R., **2013**. Importance of trivalency and the e(g)(1) configuration in the photocatalytic oxidation of water by Mn and Co oxides. *Proc Natl Acad Sci U S A* 110, 11704-11707.
- Maltoni, S., Silvestri, A., Marcante, A., Molin, G., **2016**. The transition from Roman to Late Antique glass: new insights from the Domus of Tito Macro in Aquileia (Italy). *J Archaeol Sci* 73, 1-16.
- Morgan, J.J., **2000**. Manganese in natural waters and earth's crust: its availability to organisms. *Met Ions Biol Syst* 37, 1-34.
- Morgan, J.J., **2005**. Kinetics of reaction between O₂ and Mn(II) species in aqueous solutions. *Geochim Cosmochim Acta* 69, 35-48.
- Nurnberger, U., **1978**. Studies for Interpretation of Fatigue Behavior of as-Rolled Carbon-Silicon-Manganese Deformed Concrete Reinforcing Steels. *Stahl Eisen* 98, 657-661.
- Oldham, V.E., Mucci, A., Tebo, B.M., Luther III, G.W., **2016**. Soluble Mn(III)-L complexes are abundant in oxygenated waters and stabilized by humic ligands. *Geochim Cosmochim Acta*.
- Peng, H.H., Chen, J., Jiang, D.Y., Li, M., Feng, L., Losic, D., Dong, F., Zhang, Y.X., **2016**. Synergistic effect of manganese dioxide and diatomite for fast decolorization and high removal capacity of methyl orange. *J Colloid Interf Sci* 484, 1-9.

CHAPTER 1

- Periyasamy, S., Subramanian, P., Levi, E., Aurbach, D., Gedanken, A., Schechter, A., **2016**. Exceptionally Active and Stable Spinel Nickel Manganese Oxide Electrocatalysts for Urea Oxidation Reaction. *Acs Appl Mater Inter* 8, 12176-12185.
- Post, J., **1999**. Manganese oxide minerals: Crystal structures and economic and environmental significance. *Proceedings of the National Academy of Sciences* 96, 3447-3454.
- Remsing, R.C., McKendry, I.G., Strongin, D.R., Klein, M.L., Zdilla, M.J., **2015**. Frustrated Solvation Structures Can Enhance Electron Transfer Rates. *J Phys Chem Lett* 6, 4804-4808.
- Robinson, D.M., Go, Y.B., Mui, M., Gardner, G., Zhang, Z., Mastrogiovanni, D., Garfunkel, E., Li, J., Greenblatt, M., Dismukes, G.C., **2013**. Photochemical Water Oxidation by Crystalline Polymorphs of Manganese Oxides: Structural Requirements for Catalysis. *J Am Chem Soc* 135, 3494-3501.
- Rong, F., Zhao, J., Chen, Z., Xu, Y.X., Zhao, Y.P., Yang, Q.H., Li, C., **2016**. Highly active water oxidation on nanostructured biomimetic calcium manganese oxide catalysts. *J Mater Chem A* 4, 6585-6594.
- Ruetschi, P., **1984**. Cation-Vacancy Model for MnO_2 . *J Electrochem Soc* 131, 2737-2744.
- Sakai, N., Ebina, Y., Takada, K., Sasaki, T., **2005**. Photocurrent generation from semiconducting manganese oxide nanosheets in response to visible light. *J Phys Chem B* 109, 9651-9655.
- Sherman, D.M., **2005**. Electronic structures of iron(III) and manganese(IV) (hydr)oxide minerals: Thermodynamics of photochemical reductive dissolution in aquatic environments. *Geochim Cosmochim Acta* 69, 3249-3255.
- Shumlas, S.L., Singireddy, S., Thenuwara, A.C., Attanayake, N.H., Reeder, R.J., Strongin, D.R., **2016**. Oxidation of arsenite to arsenate on birnessite in the presence of light. *Geochem T* 17.
- Siffert, C., Sulzberger, B., **1991**. Light-Induced Dissolution of Hematite in the Presence of Oxalate - a Case-Study. *Langmuir* 7, 1627-1634.
- Spiro, T.G., Bargar, J.R., Sposito, G., Tebo, B.M., **2010**. Bacteriogenic Manganese Oxides. *Accounts Chem Res* 43, 2-9.
- Sposito, G., **2008**. The chemistry of soils, 2nd ed. *Oxford University Press*, Oxford.
- Statham, P.J., Yeats, P.A., Landing, W.M., **1998**. Manganese in the eastern Atlantic Ocean: processes influencing deep and surface water distributions. *Mar Chem* 61, 55-68.
- Stone, A.T., **1983**. The reduction and dissolution of Mn(III) and Mn(IV) oxides by organics, W.M. Keck Laboratory of Environmental Engineering Science - Division of Engineering and Applied Science. *California Institute of Technology*, Pasadena, California, p. 323.
- Stumm, W., Morgan, J.J., **1996**. Aquatic chemistry: chemical equilibria and rates in natural waters. *Wiley*.
- Sulzberger, B., Laubscher, H., **1995**. Reactivity of various types of iron (III)(hydr) oxides towards light-induced dissolution. *Mar Chem* 50, 103-115.
- Sulzberger, B., Laubscher, H., **2009**. Photochemical Reductive Dissolution of Lepidocrocite. American Chemical Society, Washington, DC, pp. 279-290.
- Sunda, W.G., Huntsman, S.A., **1990**. Diel Cycles in Microbial Manganese Oxidation and Manganese Redox Speciation in Coastal Waters of the Bahama-Islands. *Limnol Oceanogr* 35, 325-338.

- Sunda, W.G., Huntsman, S.A., **1994**. Photoreduction of Manganese Oxides in Seawater. *Mar Chem* 46, 133-152.
- Sunda, W.G., Huntsman, S.A., Harvey, G.R., **1983**. Photo-Reduction of Manganese Oxides in Seawater and Its Geochemical and Biological Implications. *Nature* 301, 234-236.
- Takashima, T., Hashimoto, K., Nakamura, R., **2012**. Mechanisms of pH-Dependent Activity for Water Oxidation to Molecular Oxygen by MnO₂ Electrocatalyst. *J Am Chem Soc* 134, 1519-1527.
- Tebo, B.M., Bargar, J.R., Clement, B.G., Dick, G.J., Murray, K.J., Parker, D., Verity, R., Webb, S.M., **2004**. Biogenic manganese oxides: Properties and mechanisms of formation. *Annual Review of Earth and Planetary Sciences* 32, 287-328.
- Tebo, B.M., Clement, B.G., Dick, G.J., **2007**. Biotransformations of Manganese. *Manual of Environmental Microbiology*, 3rd Ed, 1223-1238.
- Villalobos, M., Toner, B., Bargar, J., Sposito, G., **2003**. Characterization of the manganese oxide produced by *Pseudomonas putida* strain MnB1. *Geochim Cosmochim Acta* 67, 2649-2662.
- Voelker, B.M., Morel, F.M.M., Sulzberger, B., **1997**. Iron redox cycling in surface waters: Effects of humic substances and light. *Environ Sci Technol* 31, 1004-1011.
- Waite, T.D., **1990**. Photo-Redox Processes at the Mineral-Water Interface, *Mineral-Water Interface Geochemistry*, pp. 559-603.
- Waite, T.D., Wrigley, I.C., Szymczak, R., **1988**. Photoassisted Dissolution of a Colloidal Manganese Oxide in the Presence of Fulvic-Acid. *Environ Sci Technol* 22, 778-785.
- Webb, S.M., Tebo, B.M., Bargar, J.R., **2005**. Structural influences of sodium and calcium ions on the biogenic manganese oxides produced by the marine *Bacillus* sp., strain SG-1. *Geomicrobiol J* 22, 181-193.
- Wiechen, M., Berends, H.M., Kurz, P., **2012a**. Water oxidation catalysed by manganese compounds: from complexes to 'biomimetic rocks'. *Dalton Transactions* 41, 21-31.
- Wiechen, M., Zaharieva, I., Dau, H., Kurz, P., **2012b**. Layered manganese oxides for water-oxidation: alkaline earth cations influence catalytic activity in a photosystem II-like fashion. *Chem Sci* 3, 2330-2339.
- Wilson, D.E., **1980**. Surface and Complexation Effects on the Rate of Mn(II) Oxidation in Natural-Waters. *Geochim Cosmochim Acta* 44, 1311-1317.
- Young, K.J., Gao, Y., Brudvig, G.W., **2011**. Photocatalytic Water Oxidation Using Manganese Compounds Immobilized in Nafion Polymer Membranes. *Aust J Chem* 64, 1221-1228.
- Zhou, F.L., Izgorodin, A., Hocking, R.K., Armel, V., Spiccia, L., MacFarlane, D.R., **2013**. Improvement of Catalytic Water Oxidation on MnO_x Films by Heat Treatment. *ChemSusChem* 6, 643-651.

Chapter 2. Experimental approach

The purpose of this chapter is to describe the photoreactor setup used in this thesis, as well as to provide an overview of the key analytical and spectroscopic techniques used in this dissertation. Furthermore, since the approach followed in this study applies techniques from the materials science community to answer an environmental geochemistry research question, a brief review of the techniques is necessary to provide the reader with a context for the work described in the following chapters. The design, characterization and use of the photoreactor setup, the analytical techniques to determine the photoreduction of Mn in this setup (Mn(III) quantification and average Mn oxidation number titration), and the techniques used to observe the photoexcitation mechanism on the electron-transfer timescale (femto- to microseconds) will be described.

2.1. Photoreactor design

Background. The primary requirement for the experiments in this dissertation is the design and development of a photoreactor with set requirements. In particular, the light source in the photoreactor must be able to initiate the investigated reactions and be easily characterizable, and we must be able to run the experiments in it for multiple days. We opted to custom-design a photoreactor instead of using a commercially available photoreactor such as a solar simulator. The drawbacks of a sunlight simulator include the broad wavelength employed that is more difficult to characterize precisely and the difficulty to optimize the irradiation geometry to specific requirements. In our custom setup, the choice of a single wavelength for the irradiation rendered the characterization of the photon flux much more precise through chemical actinometry than would have been the case with a solar simulator. Furthermore, the design of our photoreactor allowed us to optimize the irradiation efficiency to birnessite suspensions: the use of particle suspensions that tend to settle required an effective mixing that was achieved by a flow-through configuration.

Design and construction of the photoreactor. The designed flow through photoreactor, of which the designs and photographs are shown in **ANNEX 1**, was composed of 2 main components: the irradiation module and the flow-through module. The design was based on a

CHAPTER 2

prototype built by Dr. Benjamin Gilbert (Lawrence Berkeley National Laboratory, CA, USA), which had proven to work for the photoreduction of birnessite in preliminary experiments. The irradiation module was composed of 3x high power light emitting diodes (1W LEDs from ProLight Opto Technology Corporation) tuned at 400 nm that were mounted with thermally conductive paste onto a cooling support (An Enzotech[®] WMST-81 MOSFET – metal-oxide semiconductor field-effect transistor - liquid cooler designed for ASUS PC motherboards). This LED and mosfet cooling assembly was mounted on a custom built support in order to be positioned onto a breadboard. The cooling support was connected to an aquarium pump with rubber tubing, which was submerged in a container with tap water, in order to cool the LEDs, which emit heat on the opposite side from where they emit light. Cooling of the LEDs serves to optimize their efficiency and lifetime, as well as to avoid overheating the setup. The LEDs were equipped with focusing lenses (60° focusing radius) from the same brand (ProLight) to optimize the photon flux to the flow through module. The three LEDs were connected in series at around 1 cm from each other to a 700 mA DC output, 220 V AC input power source, which was plugged directly into a power outlet. During the experimental run, the aquarium pump ran continuously to keep the temperature of the irradiation assembly at room temperature (20° C).

The flow-through module was designed to allow the mineral suspension to flow in a closed circuit by means of a peristaltic pump and Teflon[®] tubing into a quartz flow through cuvette (Hellma Analytics), except for the portions connected to the peristaltic pump, which were in Tygon[®]. This cuvette was connected on the top and on the bottom to the tubing, and positioned into an aluminum casing support that kept it in vertical position and aligned with the LED array. The casing support also both shielded the photoreactor from external light and avoided dispersion of the LED light. The choice of aluminum with respect to other non-reflective materials allowed internal reflection of the light, increasing the photon flux to the cuvette. Furthermore, this setup allowed us to position three photoreactors close to one another on a breadboard in order to run 3 experiments simultaneously.

The final assembly, as shown in **Figure 5, ANNEX 1**, was placed in a « dark room » that was screened by ambient light through the use of thick dark-blue curtains. During operation, a red light was used to allow subsampling of the reactors while minimizing any light exposure to the system. The calculation of the quantum yield of the photoreduction reaction,

which defines the number of molecules photochemically reacted divided by the number of photons absorbed, could be calculated exclusively by using the photon flux to the photoreactor as quantified with chemical actinometry. A solar simulator, on the other hand, requires the photon flux to be measured either with a series of different chemical actinometers, each sensitive to different wavelengths, or with solar irradiance meters, which is a solid device that measures irradiance on a surface.

Characterization of the photon flux. The photon flux of the irradiation module to the flow-through module was measured by chemical actinometry. Chemical actinometry uses the photochemical properties of a chemical compound with a well-known quantum yield to back-calculate the moles of photons absorbed in the system. The advantage of this technique is that it accounts for the geometry of the setup since the actinometer is a solution that flows through the system identically to the mineral suspensions. One of the most commonly used actinometers in the 220-550 nm spectrum is potassium ferrioxalate. The use of a chemical actinometer in this system was possible because the LEDs were tuned to a single irradiation wavelength. The disadvantage of the chemical actinometry is that not necessarily all wavelengths are taken into account, which may lead to errors in the measurement of the photon flux. However, this disadvantage is counterbalanced by the error introduced using a solar irradiance meter, which does not take into account the geometry of the setup, which is often difficult to estimate with precision in a complex setup. The photon flux to the flow-through module was evaluated by potassium ferrioxalate ($\text{Fe}(\text{C}_2\text{O}_4)_3^{3-}$) actinometry (Parker, 1953; Hatchard and Parker, 1956) as modified by Montalti et al. (2006). This technique involves the irradiation of a photochemically sensitive molecule for which the quantum yield is well known at the wavelength at which it is employed. Because the photon flux is defined as the moles of photons absorbed in unit time, and the quantum yield of the actinometer is well known at every wavelength, this technique only requires a measurement of irradiation time and moles of converted actinometer. By using potassium ferrioxalate, the photoreduction of Fe(III) to Fe(II) is obtained through irradiation, and the quantification of Fe(II) obtained spectrophotometrically after complexation of the irradiated actinometer with a 1,10 phenanthroline solution. Briefly, 20 mL of 0.012 M potassium ferrioxalate ($\text{K}_3[\text{Fe}(\text{C}_2\text{O}_4)_3]$) were circulated through the photoreactor. Samples (0.4 mL) collected after 10, 25, 50, 75 and 100 seconds were added to BrandTech[®] plastic UV-cuvettes previously filled with 0.8 mL

CHAPTER 2

0.1% buffered 1.10-phenanthroline solution and 1.4 mL of ultrapure water, shaken and left in the dark for 30 minutes. The extinction coefficient of the Fe(II)-phenanthroline complex was measured at 510 nm in a dark room ($\epsilon_{510} = 11100 \text{ L mol}^{-1} \text{ cm}^{-1}$). The photon flux was then calculated according to:

$$\varphi = \frac{Nh\nu}{t} = \frac{\text{moles of Fe(II)-phenanthroline}}{\Phi_{400 \text{ nm}} \times t \times F}$$

where $\Phi_{400 \text{ nm}}$ is the quantum yield of the ferrioxalate at 400 nm (equal to 1.14 (Montalti et al., 2006)), t is the irradiation time and F is the fraction of light absorbed by the ferrioxalate solution, which in this case was equal to unity (Montalti et al., 2006).

Use. Once assembled in a 3x array on the breadboard (**Figure 5 – ANNEX 1**), a photoreaction experiment was carried out by preparing a 500 mL stock suspension of a given concentration of Mn oxide (typically between 250 and 500 μM on a Mn molar basis), which was then divided into two 250 mL sub-aliquots in glass bottles covered with aluminium foil. One of these suspensions was kept in the dark and one was irradiated by inserting the tubing of the photoreactors into holes in the bottle caps. Both bottles were put on a magnetic stir plate (6x positions for 3x dark and light samples, one pair per photoreactor) to stir the bottle contents. The suspension to be irradiated was circulated through the photoreactor for a set amount of time (typically 4 to 5 days) using a peristaltic pump at 80 rpm with 1.6 mm inner diameter Tygon tubing (65 ml/min) connected to the Teflon tubing of the remaining setup. All these operations were carried out under diffuse red light. Once the experiment was completed, cleaning of the flow through setup was achieved by flowing ultrapure water through the system in one way and in the other. Typically, an initial aliquot of 1 L water was flown to remove any particles trapped in the tubing and cuvette, followed by two aliquots of 4 L in one direction and in the other, respectively. Visual inspection of the cuvettes under irradiation was achieved to evaluate whether any particles remained attached to the cuvette walls. In the rare cases where the first aliquot of water was insufficient to remove the particles (particles sticking to the tubing and cuvette), an aliquot of a 3% HNO_3 and 2 mM oxalic acid solution was flown through the system until no particles were visible, followed by an additional rinse with 1 L water and the 4 L rinse in one direction and the other, respectively. Rinse the cuvettes with water prior to the acid solution turned out to be critical since a precipitate formed in the cuvettes upon acid

rinsing of the system with containing residual suspensions that had contained both pyrophosphate and calcium. Failure to identify this contamination led to several months of unusable data collection, in particular when we were trying to evaluate the effect of suspension concentration on the photoreduction efficiency of the mineral. Furthermore, if the circuit was dried after the final rinse with water, precipitation occurred. Therefore, once the rinse was complete, the inlet and outlet tubing were connected to each other before detaching the peristaltic pump, to maintain the system full with clean MQ water while not in use. The Tygon® tubing that was connected to the pump was replaced every 3-4 weeks because of wear and tear prevented homogeneous flow beyond this time.

2.2. Identification and quantification of photoreduced Mn

Mn(III) quantification by extraction with sodium pyrophosphate. The photoreduction of $\delta\text{-MnO}_2$ may lead to either a 1 or 2 electron reaction to yield Mn(III) or Mn(II). Divalent manganese can be determined easily because it is stable as a soluble ion in the solution phase. However, this is not true for Mn(III), which remains sorbed onto the surface. Therefore, an analytical method was required to determine precisely the amount of Mn(III) that formed upon photoreduction. A common lab-based method that is known to complex Mn(III) in birnessite without being redox-active itself is sodium pyrophosphate (Wang and Stone, 2003). This complexing agent has been used extensively to quantify Mn(III) formed upon oxidation of Mn(II) by potassium permanganate (Lingane and Karplus, 1946), to evaluate whether Mn(II) oxidation by microorganisms leads to an intermediate Mn(III) species (Stone, 1983; Kostka et al., 1995; Webb et al., 2005), as well as to characterize the amount of Mn(III) present in various Mn oxide phases (Klewicki and Morgan, 1995; Klewicki and Morgan, 1999) or accumulated during organic-promoted reduction of Mn oxides (Wang and Stone, 2003). The protocol for Mn(III) quantification with sodium pyrophosphate involves the equilibration of the mineral in excess PP for a given amount of time, 48 hours (Klewicki and Morgan, 1998), and then to measure the absorbance of the filtrate by UV-Vis spectrophotometry at 2 wavelengths ($\epsilon_{254\text{ nm}} = 6562\text{ M}^{-1}\text{ cm}^{-1}$ and $\epsilon_{484\text{ nm}} = 100\text{ M}^{-1}\text{ cm}^{-1}$ – **Table 1**), depending on the concentration of Mn(III) (Klewicki and Morgan, 1998). We found that the minimum PP : Mn ratio for Mn(III) extraction with this technique was 25 :1. We validated the PP extraction method by

determining the extinction coefficient for the Mn(III)-PP complex using a set of Mn(III)-acetate standards (**Figure 1**) and comparing it with published values (**Table 1**).

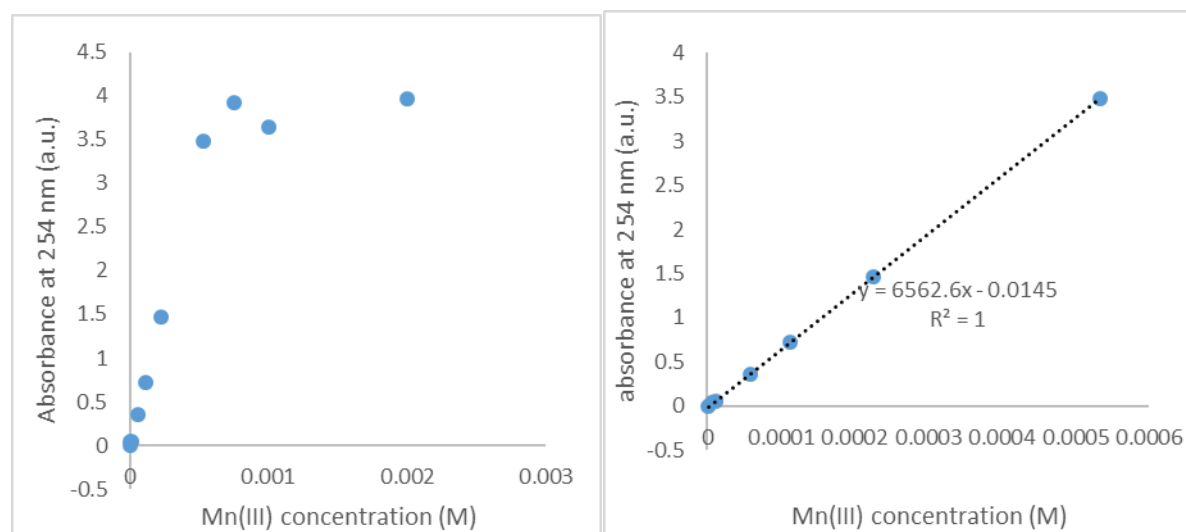


Figure 1 *right*) Calibration curve for the Mn(III)-acetate-pyrophosphate standards used for the determination of the extinction coefficient of Mn(III)-pyrophosphate at 254 nm by UV-Vis spectrometry; *left*) absorbance of all of the standards at 254 nm; *right*) calibration curve selecting only standards below 500 μ M, which followed the beer-lambert law, thus fell into the linear range allowing us to assign an extinction coefficient for Mn(III)-pyrophosphate.

Table 1: Comparison of the obtained extinction coefficient with literature values

Mn(III) conc range	ligand to mn ratio	medium	wavelength	epsilon	reference
mM	4:1	MN3 medium	480	100 /M*cm	Kostka et al. (1995)
uM	4:1	MN3 medium	290	1600 /M*cm	Kostka et al. (1995)
mM	10:1	Deionized water	484	96 /M*cm	Klewicki and Morgan (1995)
uM	20:1 to 4:1	seawater	480	65 /M	Webb et al. (2005)
uM	20:1 to 4:1	seawater	258	6750 /M	Webb et al. (2005)
0-500 uM	25:1	Deionized water	254	6562/M*cm	This work
0.5 - 1 mM	25:1	Deionized water	484	99.9 /M*cm	This work

Average Mn oxidation number (AMON) determination by potentiometric titration. The determination of the AMON of the mineral before irradiation was carried out by titration of the Mn oxidation number. Although different titration protocols are described in the literature for Mn : the iodometric, oxalometric and potentiometric titrations (Gaillot, 2002; Villalobos et al., 2003), the advantages of the potentiometric titration over the oxalometric and iodometric titrations is a more precise determination of the AMON, as described by (Gaillot, 2002; Gaillot

et al., 2003; Grangeon et al., 2008). In particular, it has the critical advantage of not requiring an independent measurement of the total Mn concentration by a separate technique. The detailed description of the protocol is described in the materials and methods of **Chapter 3**. Briefly, this titration protocol involves the titration of excess Fe(II) remaining after reductive dissolution of the oxides in a Fe(II) solution with KMnO_4 and back titration of dissolved Mn(II) to Mn(III) with KMnO_4 in a 3 step titration procedure. We decided to apply this method after validating it on known oxides. This was achieved by measuring the AMON of birnessite end-members for which the oxidation number was known from published studies (Gaillot et al., 2003; Feng et al., 2004; Duckworth and Sposito, 2007). This value was then compared with the amount of extracted Mn(III) with sodium pyrophosphate on the same minerals, which provided two independent measurements of Mn(III) content (**Table 2**). Once validated, the AMON determination of irradiated samples and samples kept in the dark was measured and compared to the amount of extracted Mn(III), to evaluate whether all Mn that was not Mn(IV) was Mn(III) or a combination of Mn(III) and Mn(II).

Table 2: Mn extractions results. The results are in accordance with calculations from AMON (potentiometric titration): $\delta\text{-MnO}_2\text{-}_0$ (AMON 3.84): 81% Mn(IV) + 19% Mn(III) or 90.5% Mn(IV) + 9.5% Mn(II), $\delta\text{-MnO}_2\text{-}_1$ (AMON TcBi (AMON 3.84): 84% Mn(IV) + 16% Mn(III), KBi (AMON 3.90): 91% Mn(IV) + 9% (Mn(III).

	ICP-OES measurements: Mn sol/Mn tot				AMON \pm standard deviation on triplicate measurements
	Na ₂ P ₂ O ₇ at pH 6.5				
	150 mM	100 mM	75 mM	50 mM	
$\delta\text{-MnO}_2\text{-}_0$	0.21	0.19	0.17	0.18	3.82 \pm 0.01
$\delta\text{-MnO}_2\text{-}_1$	0.02	0.01	0.01	0.01	4.06 \pm 0.02
$\delta\text{-MnO}_2\text{-}_3$	0.01	0.01	0.01	0.01	4.11 \pm 0.01
$\delta\text{-MnO}_2\text{-}_4$	0.02	0.02	0.01	0.01	4.11 \pm 0.01
TcBi	0.16	0.15	0.15	0.08	3.84 \pm 0.05
Kbi	0.10	0.11	0.10	0.07	3.90 \pm 0.01

2.3. Photoexcitation mechanism

Photoreduction largely depends on the photoexcitation mechanism which occurs on very fast timescales as most electron transfer processes. In a system where multiple components are present, it is necessary to identify the timescales for the photon absorption and electron transfer processes in order to identify the photoreduction mechanism. In the context of this dissertation, it was important to identify the timescales for i) photoexcitation of the

electron into the conduction band, ii) electron or hole scavenging by surface species, and iii) electron-hole recombination. The comparison of these timescales allowed us to discriminate the different steps of the photoreduction process. In particular, if the timescales for electron excitation and scavenging were shorter than the timescales of electron-hole recombination, this could confirm that photoexcitation governs the photoreduction process, otherwise the observed process is likely related to a chemical process (Balzani et al., 2014). Also, the electron-hole recombination timescales are important because they describe the lifetime of photoexcited electrons and holes, and therefore provide the timescale during which photoexcited electrons can participate in the photoreduction process. These timescales, on the order of femto- to nanoseconds, require the use of ultrafast time-resolved spectroscopic techniques, such as ultrafast pump-probe optical spectroscopy and time resolved X-ray absorption spectroscopy.

2.3.1. Ultrafast (transient absorption) pump-probe optical spectroscopy

Overview of the technique. Ultrafast pump-probe optical spectroscopy is a technique that combines « traditional » optical spectroscopy, such as UV-Vis, infrared or Raman spectroscopy, with an ultrafast laser to provide information with up to femtosecond (10^{-15} s) time resolution. These techniques measure real time motion in diatomic molecules as well as elementary chemical reactions in gases, liquids, solids and biological molecules (Bressler and Chergui, 2004). Furthermore, they have been used to probe photoexcitation dynamics in photosensitive materials, such as electron-hole pair generation and their relaxation, as well as electron transfer from surface sorbed species.

The term pump-probe itself defines how the technique works : a « pump » signal, often a laser pulse, excites the material, whereas the « probe » signal provides a measure of the material after a given time delay from the pump. The time resolution (Δt) depends largely on the characteristics of the laser, as well as on the configuration of the acquisition setup. In particular, the ultrafast lasers used are pulsed lasers, whereby the pulse duration and the separation between pulses determines the time resolution of the measurement (Shah, 1999). A typical optical pump-probe setup has two main components: the optical source, which is often a laser or a combination of two lasers, and the acquisition setup, which is often a spectrophotometer. A schematic representation of a pump-probe setup is given in **Figure 3**.

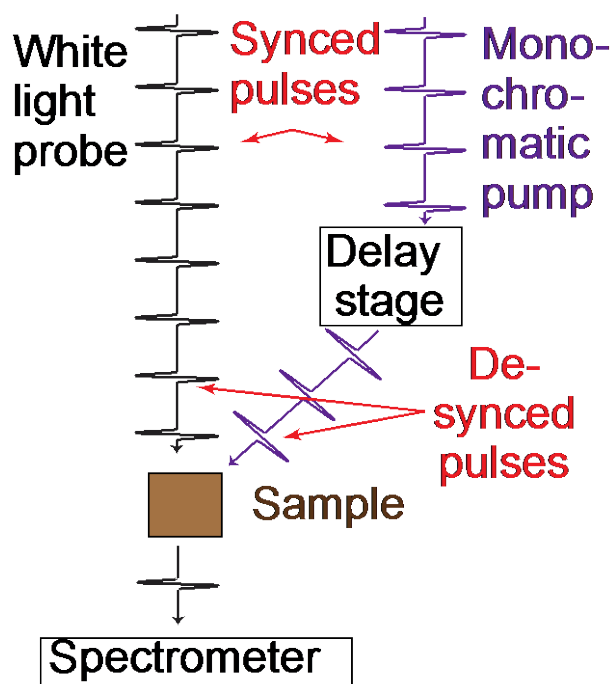


Figure 3. schematic representation of a degenerate ultrafast optical pump-probe setup.

The optical source is usually an ultrafast laser, for which the pulse width, shape, wavelength, energy and repetition rate are well known, and define the time resolution and application range of the instrument (Shah, 1999). A review of ultrafast lasers can be obtained in Svelto et al. (1996). Depending on the setup, one can distinguish two kinds of pump-probe spectroscopy based on the optical source : degenerate and non-degenerate (Shah, 1999). In the first case, the pump and the probe pulse trains come from the same laser source, but are split into two beams of which one is delayed optically with respect to the other before being focused on the sample. The optical delay is often achieved by a mechanical stage, which increases the pathlength of the beam to de-synchronize the originally synchronized pump and probe pulse trains. The probe pulse can then be either converted into a white light or to another frequency with appropriate optical devices, such as crystals or optical parametric amplifiers. The de-synchronization of these pulses allows the user to observe with the probe the optical properties of the material with a time resolution that depends on the extent of de-synchronization of the laser pulses. The amount of delay that can be achieved essentially depends on the pulse width, generally minimized as much as possible in the design of the laser, and the pulse repetition rate (Svelto et al., 1996; Shah, 1999). In non-degenerate pump probe spectroscopy, either two

CHAPTER 2

synchronized lasers or a laser and a separate white light source are used (Shah, 1999). The advantage of the second technique is that the time resolution becomes independent of the laser repetition rate, and thus can be extended to timescales of seconds. In this work, we used both degenerate and non-degenerate pump lasers, tuned at 400 nm.

The acquisition module is typically a spectrophotometer adapted to the wavelength characteristics of the probe signal, which defines the wavelength spectrum that will be acquired. Various acquisition techniques have been developed in combination with ultrafast lasers in pump-probe spectroscopy, amongst which transmission, reflectance and Raman spectroscopies (Shah, 1999). In this work, UV-Vis transmission spectroscopy was employed as the acquisition technique. In such a setup, data is collected continuously on either a diode array or a CCD camera (Shah, 1999), and the data acquisition software converts the optical delay into a time delay by electronics in the case of a degenerate setup and non-degenerate setup, respectively.

Two signals can be identified in a pump-probe spectrometer: the ground state spectrum, which is the absorption spectrum of the material before the pump signal excites it, and the excited state spectrum, which is the absorbance of the material at a given delay after the pump pulse has excited it. Because of the small differences in absorption between excited and ground state signals, the spectrometer software usually collects the data as a differential transmission, or transient absorption (TA), which is given by $\Delta A/A_0 = (A - A_0)/A_0$, where A is the absorbance at time t , and A_0 is the ground state absorbance (Shah, 1999).

Data collection and analysis. Ultrafast transient absorption pump-probe spectroscopy data, as collected in this work, is given as a 2D matrix where each column represents a wavelength and each row represents a time delay, whereas the values in the matrix represent the differential absorbance. This matrix can be loaded into any data processing software, and converted into a 2D intensity plot, from which either « wavelength slices » or « time slices » can be extracted: the transient absorption data can be plotted as a function of probed wavelength, to obtain a transient absorption spectrum at a given delay time, or as a function of delay time at a given wavelength to investigate particular features as a function of time. In general, two main features can be observed in any transient absorption spectrum of a photosensitive material: a positive and a negative signal, which indicate the appearance and

disappearance, respectively, of optical features compared to the ground state absorbance. The positive signal is called the excited or enhanced state absorption (ESA), whereas the negative signal is called the ground state bleach. In the case of semiconducting nanoparticles, these two features, describe the population of photoexcited electrons and photoexcitable electrons in the valence band, respectively. Changes in the ESA over time describes the evolution of the photoexcited electrons in the conduction band, whereas changes in the ground state bleach describe the recombination of the photoexcited electrons and holes in the valence band.

2.3.2. Time resolved X-ray absorption spectroscopy (TRXAS)

One of the main difficulties that arise in all optical pump-probe studies on complex systems is the interpretation of the spectroscopic data in terms of molecular structure. Therefore, there have been expansions of this technique to obtain molecular-scale information that is element specific. One such expansion is time resolved X-ray absorption spectroscopy. This technique is similar to ultrafast pump probe spectroscopy in that it uses a laser pump, but instead of using an UV-Vis probe, the probe is an X-ray source, generally from a synchrotron. In particular, synchrotron based X-ray sources provide X-ray energy tunability and brilliance. The use of a synchrotron-based X-ray probe, by exciting core electrons in the material, has the advantage of providing information on valence changes of given elements in the system, as well as providing information of structural changes in the material within the local bonding environment of the absorber atom. The time resolution of TRXAS is typically limited by the pulse width of the X-ray pulses (~30-100 ps) (Bressler and Chergui, 2004). A detailed review of the X-ray absorption spectroscopy technique is given elsewhere (Kelly et al., 2008; Calvin, 2013). The requirement of a synchrotron source largely complicates the experimental setup compared to all optical pump-probe spectroscopy. In particular, the frequency and pulse duration of the X-ray source is fixed by the synchrotron specifics and cannot generally be altered for the ultrafast spectroscopy studies. In a typical setup, specific electrons that are isolated from the other electrons in the electron bunch are identified and selected by the beamline (with various techniques – see Bressler and Chergui (2004)), which greatly reduces the X-ray photon flux to the sample compared to a traditional XAS beamline. Therefore, each datapoint at a particular energy or a particular delay time collected in a TR-XAS experiment typically requires 1-10 s of accumulation time (Bressler and Chergui, 2004). The low number

CHAPTER 2

of incident photons also requires optimization of signal to noise ratio without introducing confounding beam damage issues. The sample must be therefore optimized to achieve the optimum S/N ratio with the least amount of X-ray photons absorbed. Conversely, the laser pulse must be able to excite enough sample to give a detectable change. Finally, the detector used must have a sufficiently fast response to avoid saturation during acquisition. Examples of such detectors are streak cameras and avalanche photodiodes (Bressler and Chergui, 2004). The setup used in this study is described in detail in **Chapter 4**.

The TRXAS technique has been successfully applied to study systems that range from the dissociation of the CO ligand in carboxymyoglobin in biological systems (Mills, 1984), to photoinduced electron transfer between metallo-organic molecules such as Fe(III)-porphyrin to a Zn-porphyrin in coordination chemistry on the microsecond timescale (Thiel et al., 1993; Chen et al., 1999). In material science, investigations have been pushed to the nanosecond domain with semiconductor-to-metal phase transition investigations (Johnson et al., 2003) or photodissociation of nickel tetraphenylporphyrin (Chen et al., 2001). The current challenge is expanding the technique to the picosecond or subfemtosecond timescale, with experiments carried out essentially in material science investigations such as photoinduced electronic changes in semiconductors. In particular, the work of Adams et al. (2002) coupled optical and X-ray absorption pump probe spectroscopy to investigate electron and hole dynamics in the semiconductor gallium arsenide (GaAs). In particular, the use of X-ray absorption spectroscopy assigned the photoexcitation process to discrete levels instead of band states, which could not be obtained by all optical pump-probe spectroscopy. Other studies investigated metal-to-ligand charge transfer reactions in $[\text{Ru}^{\text{II}}(\text{bpy})_3]^{2+}$ (Saes et al., 2004) or $[\text{Cu}^{\text{I}}(\text{dmp})_2]^{2+}$ (Chen et al., 2003). In particular, the use of TRXAS allowed the authors to investigate photoexcitation-dependent valence changes in the metals by observing the time dependent XANES and EXAFS on the metal K-edge. Of greater relevance to this dissertation, Katz et al. (2012) used TRXAS to investigate the electron mobility in dye-sensitized iron oxyhydroxide nanoparticles. In this case, TRXAS was used to expand the observations obtained by all optical pump-probe spectroscopy to investigate changes in short-range structural topology of the minerals upon electron transfer. The results allowed the authors to identify electron hopping across the mineral bulk through a localized lower valence metal site (polaron). This short review shows that the novelty of the field and the wide space still

available for development. Nevertheless, the technique is promising to obtain detailed structural information on processes occurring on ultrafast timescales in materials, which is of primary importance to understand the photochemical mechanisms involving semi-conducting mineral nanoparticles.

2.4. References

- Adams, B.W., DeCamp, M.F., Dufresne, E.M., Reis, D.A., **2002**. Picosecond laser-pump, x-ray probe spectroscopy of GaAs. *Rev Sci Instrum* 73, 4150-4156.
- Balzani, V., Ceroni, P., J., A., **2014**. *Photochemistry and Photophysics: Concepts, Research, Applications*, Weinheim, Germany.
- Bressler, C., Chergui, M., **2004**. Ultrafast X-ray absorption spectroscopy. *Chem Rev* 104, 1781-1812.
- Calvin, S., **2013**. XAFS for everyone. *CRC Press - Taylor and Francis Group*.
- Chen, L.X., Jager, W.J.H., Jennings, G., Gosztola, D.J., Munkholm, A., Hessler, J.P., **2001**. Capturing a photoexcited molecular structure through time-domain X-ray absorption fine structure. *Science* 292, 262-264.
- Chen, L.X., Lee, P.L., Gosztola, D., Svec, W.A., Montano, P.A., Wasielewski, M.R., **1999**. Time-resolved X-ray absorption determination of structural changes following photoinduced electron transfer within bis-porphyrin heme protein models. *J Phys Chem B* 103, 3270-3274.
- Chen, L.X., Shaw, G.B., Novozhilova, I., Liu, T., Jennings, G., Attenkofer, K., Meyer, G.J., Coppens, P., **2003**. MLCT state structure and dynamics of a copper(I) diimine complex characterized by pump-probe X-ray and laser spectroscopies and DFT calculations. *J Am Chem Soc* 125, 7022-7034.
- Duckworth, O.W., Sposito, G., **2007**. Siderophore-promoted dissolution of synthetic and biogenic layer-type Mn oxides. *Chem Geol* 242, 497-508.
- Feng, X.H., Zu, Y.Q., Tan, W.F., Liu, F., **2004**. Preparative parameter effects on synthesis of birnessite by O-2 oxidation. *Pedosphere* 14, 63-70.
- Gaillot, A.C., **2002**. Caractérisation structurale de la birnessite: Influence du protocole de synthèse.
- Gaillot, A.C., Flot, D., Drits, V.A., Manceau, A., Burghammer, M., Lanson, B., **2003**. Structure of Synthetic K-rich Birnessite Obtained by High-Temperature Decomposition of KMnO₄. I. Two-Layer Polytype from 800 °C Experiment. *Chem Mater* 15, 4666-4678.
- Grangeon, S., Lanson, B., Lanson, M., Manceau, A., **2008**. Crystal structure of Ni-sorbed synthetic vernadite: a powder X-ray diffraction study. *Mineral Mag* 72, 1279-1291.
- Hatchard, C.G., Parker, C.A., **1956**. A New Sensitive Chemical Actinometer. II. Potassium Ferrioxalate as a Standard Chemical Actinometer. *P R Soc A* 235, 518-536.
- Johnson, S.L., Heimann, P.A., Lindenberg, A.M., Jeschke, H.O., Garcia, M.E., Chang, Z., Lee, R.W., Rehr, J.J., Falcone, R.W., **2003**. Properties of Liquid Silicon Observed by Time-Resolved X-Ray Absorption Spectroscopy. *Phys Rev Let* 91, 157403.
- Katz, J.E., Zhang, X.Y., Attenkofer, K., Chapman, K.W., Frandsen, C., Zarzycki, P., Rosso, K.M., Falcone, R.W., Waychunas, G.A., Gilbert, B., **2012**. Electron Small Polarons and Their Mobility in Iron (Oxyhydr)oxide Nanoparticles. *Science* 337, 1200-1203.

CHAPTER 2

- Kelly, S.D., Hesterberg, D., Ravel, B., **2008**. Analysis of soils and minerals using X-ray absorption spectroscopy, *Methods of soil analysis. Part 5. Mineralogical methods*, pp. 387-464.
- Klewicki, J., Morgan, J., **1999**. Dissolution of β -MnOOH particles by ligands: pyrophosphate, ethylenediaminetetraacetate, and citrate. *Geochim Cosmochim Acta* 63, 3017-3024.
- Klewicki, J.K., Morgan, J.J., **1995**. Dissolution of Mn(III) Oxides in the Presence of Stabilizing Ligands. *Abstr Pap Am Chem S* 209, 117-ENVR.
- Klewicki, J.K., Morgan, J.J., **1998**. Kinetic behavior of Mn(III) complexes of pyrophosphate, EDTA, and citrate. *Environ Sci Technol* 32, 2916-2922.
- Kostka, J.E., Luther, G.W., Nealson, K.H., **1995**. Chemical and Biological Reduction of Mn(III)-Pyrophosphate Complexes - Potential Importance of Dissolved Mn(III) as an Environmental Oxidant. *Geochim Cosmochim Acta* 59, 885-894.
- Lingane, J.J., Karplus, R., **1946**. New Method for Determination of Manganese. *Industrial and Engineering Chemistry-Analytical Edition* 18, 191-194.
- Mills, D.M., **1984**. Time-Resolved X-Ray-Diffraction and Spectroscopy. *Acta Crystallogr A* 40, C393-C393.
- Montalti, M., Credi, A., Prodi, L., Gandolfi, M.T., **2006**. Handbook of photochemistry. *CRC press*.
- Parker, C.A., **1953**. A New Sensitive Chemical Actinometer .1. Some Trials with Potassium Ferrioxalate. *P R Soc A* 220, 104-116.
- Saes, M., Bressler, C., van Mourik, F., Gawelda, W., Kaiser, M., Chergui, M., Bressler, C., Grolimund, D., Abela, R., Glover, T.E., Heimann, P.A., Schoenlein, R.W., Johnson, S.L., Lindenberg, A.M., Falcone, R.W., **2004**. A setup for ultrafast time-resolved x-ray absorption spectroscopy. *Rev Sci Instrum* 75, 24-30.
- Shah, J., **1999**. Ultrafast spectroscopy of semiconductors and semiconductor nanostructures, 2nd enl. ed. *Springer Verlag*, Berlin ; New York.
- Stone, A.T., **1983**. The reduction and dissolution of Mn(III) and Mn(IV) oxides by organics, W.M. Keck Laboratory of Environmental Engineering Science - Division of Engineering and Applied Science. *California Institute of Technology*, Pasadena, California, p. 323.
- Svelto, O., De Silvestri, S., Denardo, G., **1996**. Ultrafast processes in spectroscopy. *Plenum Press*, New York.
- Thiel, D.J., Livins, P., Stern, E.A., Lewis, A., **1993**. Microsecond-Resolved Xafs of the Triplet Excited-State of Pt₂(P₂O₅H₂)₄(4-). *Nature* 362, 40-43.
- Villalobos, M., Toner, B., Bargar, J., Sposito, G., **2003**. Characterization of the manganese oxide produced by Pseudomonas putida strain MnB1. *Geochim Cosmochim Acta* 67, 2649-2662.
- Wang, Y., Stone, A.T., **2003**. Soluble Mn(III) complexes arising from the reaction of pyrophosphate and phosphonate-containing chelating agents with manganese(III,IV) (HYDR)oxides. *Abstr Pap Am Chem S* 226, U471-U471.
- Webb, S.M., Dick, G.J., Bargar, J.R., Tebo, B.M., **2005**. Evidence for the presence of Mn(III) intermediates in the bacterial oxidation of Mn(II). *Proc Natl Acad Sci U S A* 102, 5558-5563.

Chapter 3. Controlled synthesis of δ -MnO₂: an in-depth characterization of the synthesis products

This chapter was initially submitted and rejected by the Journal of Colloid Interface Science, and will be resubmitted to American Mineralogist with the title “Solution pH as a driver of specific surface area and coherent scattering domain size of δ -MnO₂ nanoparticles”, Marafatto FF, Peña J.

3.1. Abstract

Layer-type Mn oxides (birnessite) are characterized by high redox reactivity, nanoscale dimensions and the presence of point defects in the form of layer vacancies. These properties, together with their common occurrence in the environment, make these minerals key players in the biogeochemical cycle of carbon and many trace metals. Delta MnO₂, which is synthesized by reacting Mn(II) and Mn(VII) in the presence of NaOH, is considered an analog of natural birnessites and has been used widely in reactivity studies. Here, we investigate the effect of varying the synthesis pH and reagent addition speed, on the physico-chemical properties of the mineral. We produced δ -MnO₂ batches with specific surface areas (SSA) ranging from 119 to 259 m² g⁻¹ and crystallite sizes ranging from about 3 to 7 nm. Our results show not only that pH is the key driver of SSA and nanoparticle aggregation, but that SSA can be tuned by varying the pH of washed post-synthesis materials. Crystallite size, on the other hand, is inversely correlated with SSA and changes only upon acidification of post-synthesis samples, which suggests that proton-promoted reduction of Mn(IV) leads to changes in crystal structure or size.

Keywords

δ -MnO₂, mineral synthesis, birnessite, vernadite, nanoparticles, specific surface area, BET

3.2. Introduction

Birnessite minerals (layer-type Mn oxides) are among the most widespread oxides in the environment (Post, 1999). They often occur in association with other phases (i.e. with Fe

CHAPTER 3

oxides in desert varnishes, soils, sediments and ocean nodules), or are found embedded in a biofilm matrix (Stumm and Morgan, 1996; Post, 1999; Villalobos et al., 2003; Tebo et al., 2004). These minerals have either monoclinic or hexagonal sheet symmetry, depending on the Mn(III) content of the Mn octahedral layers (Burns, 1976). Birnessite minerals found in soils and sediments tend to have hexagonal sheet symmetry and be nanocrystalline (Tebo et al., 2004), with particles composed of randomly stacked sheets of edge-sharing MnO_6 octahedra held together by interlayer alkaline cations and water (Post, 1999; Villalobos et al., 2003). Birnessites are known to have Mn(III) substitution for Mn(IV), point defects in the form of Mn(IV) vacancies and high specific surface area deriving from their small particle size. The combination of these properties render these minerals exceptionally reactive towards the sorption of trace metals (Ruetschi, 1984; Marcus et al., 2004; Peacock and Sherman, 2007; Simanova et al., 2015). Furthermore, the high redox potential of the Mn(IV)/Mn(II) and Mn(III)/Mn(II) couples makes these minerals among the strongest oxidants present in nature (Sherman, 1984; Morgan, 2000; Sposito, 2008).

Given their broad importance in environmental processes, the sorption and oxidative properties of birnessite have been investigated in numerous laboratory studies (Tebo et al., 2004 and references therein ; Wang et al., 2012; Remucal and Ginder-Vogel, 2014 and references therein). For example, the sorption of toxicant metals such as Pb, Zn, Cd, Ni (Zasoski and Burau, 1988; Villalobos et al., 2005; Peacock and Sherman, 2007; Grangeon et al., 2012; Simanova et al., 2013) as well as the sorption and oxidation of As, Co, Cr (Manceau et al., 1997; Nico and Zasoski, 2000; Lafferty et al., 2010; Simanova and Peña, 2015) by birnessite minerals has been extensively studied. Multiple studies have also investigated the degradation of organic compounds, including pollutants such as phenols and anilines (Remucal and Ginder-Vogel, 2014 and references therein) and low molecular weight aliphatic organic acids (Wang and Stone, 2006a, b). Furthermore, birnessite minerals have been studied to investigate their role in the photochemical oxidation of water, both to understand the photoreduction mechanism (Marafatto et al., 2015) and their use as potential water oxidation catalysts (Hocking et al., 2011; Wiechen et al., 2012). Most mechanistic laboratory studies employ $\delta\text{-MnO}_2$ as an analog of natural birnessite with hexagonal sheet symmetry and nanoscale dimensions (Post, 1999; Villalobos et al., 2005; Wang et al., 2012; Simanova et al., 2015). This mineral is characterized by exclusively Mn(IV) octahedral nanosheets held

together by Na^+ ions and water molecules, which balance the excess negative charge of the sheets.

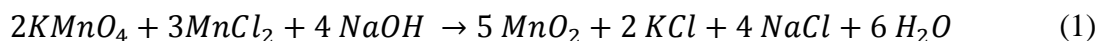
The most commonly cited synthesis pathway for $\delta\text{-MnO}_2$ involves the oxidation of Mn(II) by Mn(VII) in the presence of NaOH (Villalobos et al., 2003). The mineral nanoparticles obtained through this procedure are less than 10 nm across the crystallographic ab plane and consist of 2 to 3 turbostratically stacked sheets (Murray, 1974; Villalobos et al., 2003). However, this preparation can lead to minerals with variations in both SSA, varying between 120 and 315 m^2/g (Buser and Graf, 1955; Murray, 1974; Godfredsen and Stone, 1994; Villalobos et al., 2003; Duckworth and Sposito, 2007; Lafferty et al., 2010), and Mn(III) content, with average Mn oxidation numbers (AMON) reported between 3.69 (Grangeon et al., 2008) and 4.01 (Villalobos et al., 2003). Furthermore, reactivity varies strongly with these physicochemical properties. For example, both the adsorption of transition metals on $\delta\text{-MnO}_2$ (Villalobos et al., 2003; Simanova et al., 2015) and the oxidation of organic compounds by birnessite (Remucal and Ginder-Vogel, 2014) have been shown to depend on SSA and AMON of the mineral. While differences in Mn(III) content in the products stem from the Mn(VII):Mn(II) ratio employed in the synthesis (Villalobos et al., 2003), to date, the synthesis parameters that control the SSA of the products have not been investigated systematically.

The objective of this study was to evaluate the effect of two synthesis parameters, reagent addition rate and NaOH amount, on the physicochemical properties of $\delta\text{-MnO}_2$. Both of these variables can influence the kinetics of nucleation (Thanh et al., 2014). In addition, the amount of NaOH was also the main difference in the two most cited synthesis protocols (Murray, 1974; Villalobos et al., 2003). We synthesized six batches of $\delta\text{-MnO}_2$ by varying the speed of MnCl_2 addition and the amount of NaOH (directly related to synthesis pH), while keeping constant all other parameters as described in Villalobos et al. (2003). We then characterized the minerals by measuring their chemical composition (alkali to Mn ratio, Mn(III) content and AMON), specific surface area (SSA) as measured by BET theory N_2 adsorption, water content, and crystal structure. Finally, we evaluated the reversibility of the physical-chemical properties of the as-synthesized minerals by equilibrating different suspensions to pH values that were several units above or below the synthesis pH value.

3.3. Materials and methods

3.3.1. Background

The most common synthesis of δ -MnO₂ requires mixing stoichiometric amounts of MnCl₂ and KMnO₄ in the presence of NaOH under vigorous stirring according to the following reaction:



where NaOH is used to neutralize the acid formed during the reaction and to enhance the kinetics of Mn(II) oxidation. The two most cited protocols use either 4 (Murray, 1974) or 5 moles (Villalobos et al., 2003) of NaOH. Under condition of excess NaOH, Villalobos et al. (Villalobos et al., 2003; Villalobos et al., 2006) obtained a mineral with the following chemical formula



with Na and H₂O assigned to interlayer positions. Their mineral had a BET-SSA of 120 m²/g, a coherent scattering domain (CSD) size of 5 nm along the crystallographic *ab* plane and 2-3 MnO₂ layers stacked turbostratically along the crystallographic *c* axis. Below, we summarize the protocol followed by Villalobos et al. (2003):

- Solutions of 1280 ml of 0.2 M KMnO₄, 1280 ml of 0.3 M MnCl₂ and 1440 ml of 0.5 M NaOH were prepared separately in volumetric flasks to yield a 2:3:5 mole ratio of Mn(VII):Mn(II):NaOH.
- The KMnO₄ solution was added to the NaOH solution at a rate of 256 ml/min (5 min total time) under vigorous stirring.
- The MnCl₂ solution was added to the KMnO₄ + NaOH mixture at a rate of 36 ml/min (35 min total time) under vigorous stirring.
- The suspension was allowed to settle for 4 hours. The supernatant was syphoned to reduce the washing volume.
- The suspension obtained in Step 4 was centrifuged at 27500 relative centrifugal force (RCF) for 20 minutes at 25° C in 250 ml polypropylene co-polymer (PPCO) bottles. The supernatant was discarded after centrifugation.

- The mineral paste was resuspended in 1 M NaCl, washed by shaking for 1 hour and centrifuged (27500 RCF, 20 min, 25°C). The supernatant was discarded. This washing procedure was repeated four more times, with washing times that ranged from 1 hour to overnight. This step exchanges K^+ for Na^+ as the interlayer counter ion.
- The mineral paste was washed a total of 10 times as described in Step 5, but using MQ water instead of NaCl. The washing times ranged from 1 hour to overnight. This step removes all Na from the supernatant.
- The final product was divided into 2 aliquots: one was kept in suspension and equilibrated at pH 8 and the other was freeze-dried.

3.3.2. Mineral synthesis

All solutions, unless specified otherwise, were prepared using A.C.S.-grade reagents and fresh MQ water ($18 \Omega \cdot \text{cm}$). Six batches of $\delta\text{-MnO}_2$ were prepared with three modifications of the protocol established by Villalobos et al. (2003) (**Figure S1, Table 1**). First, we downscaled the reagent volumes (Step 1) to obtain a final suspension volume of 940 mL. We used 300 ml of 0.2 M KMnO_4 , 300 ml of 0.3 M MnCl_2 and 340 ml of NaOH. Potassium MnO_4^- was purchased as a standardized 0.2 M solution (Sigma-Aldrich). The MnCl_2 solutions were prepared using $\text{MnCl}_2 \cdot 4\text{H}_2\text{O}$ ($\geq 99\%$, ReagentPlus[®]) and nitrogen-purged MQ water; prior to use, the Mn(II) concentration was measured by ICP-OES spectrometry. The accurate determination of Mn(II) concentration is necessary to avoid the accumulation of Mn(III) in the products if excess Mn(II) is used, as we could observe in preliminary syntheses. Second, the concentration of NaOH was varied between 0.4 M and 0.6 M. Third, the addition speed of MnCl_2 to the KMnO_4 and NaOH mixture (Step 3) was varied between 18 ml/min and 72 ml/min. The different $\delta\text{-MnO}_2$ batches are identified by a letter-number scheme where the letter indicates the molarity of the NaOH solution used (A = 0.4 M, B = 0.5 M, C = 0.6 M) and the number indicates the MnCl_2 addition speed (1 = 18 ml/min, 2 = 36 ml/min and 3 = 72 ml/min). Finally, we repeated the A3 synthesis to verify the reproducibility of the protocol and refer to this sample as A3_b.

Table 1: Synthesis parameters

Sample name	MnCl ₂ addition [mL/min]	NaOH [M]
δ-MnO ₂ _A1	18	0.4
δ-MnO ₂ _A2	36	0.4
δ-MnO ₂ _A3	72	0.4
δ-MnO ₂ _A3b	72	0.4
δ-MnO ₂ _B2	36	0.5
δ-MnO ₂ _B3	72	0.5
δ-MnO ₂ _C2	36	0.6

All syntheses were carried out in a wide neck 1 L Erlenmeyer flask (15 cm bottom diameter) and reagent addition rate was controlled by a Cole-Parmer Masterflex peristaltic pump and Tygon[®] tubing (**Figure S1**). The flask contents were mixed vigorously using an overhead paddle stirrer (IKA RW 16 basic) set at 500 rpm and equipped with a BOLA PTFE-coated 4-blade stirrer shaft (5.5 cm propeller head diameter and 2 cm propeller blade height). Once the addition of reagents was completed, the suspension was left to settle for 30 min instead of 4 hours (Step 4) and 100-200 ml of clear supernatant were syphoned. The remaining suspension (800-900 ml) was transferred to 250 ml PPCO centrifuge bottles for washing as described in Steps 5 – 7. After each washing cycle, the pH of the supernatant was measured with Merck Millipore pH paper. The electrical conductivity (Mettler EL30 conductivity meter) of the supernatant was also measured after each MQ washing cycle (Step 7). No further washing steps were conducted once the conductivity of the supernatant fell below 30 μS/cm to avoid losing significant amounts of the product. Typically, five washing cycles were sufficient to meet this criterion.

After synthesis, half of the suspension was freeze dried and stored at -20 °C, whereas the remaining half was stored in suspension at room temperature in the dark without further pH equilibration. In a separate set of experiments, an aliquot of sample C2 (high NaOH) was equilibrated to pH 4 and an aliquot of sample A2 (low NaOH) was equilibrated to pH 11 for 7 days to test whether solution pH could modify the physicochemical properties measured for the “as-synthesized” minerals. Suspension pH was maintained constant using a Metrohm 718 stat titrino with either 50 mM NaOH or 50 mM HCl. The C2 and A2 samples equilibrated at pH 4 and pH 11 are identified as C2_H and A2_OH, respectively.

3.3.3. Chemical analyses

The chemical composition of δ -MnO₂ was characterized with respect to the alkali metal content, Mn(III) content, average Mn oxidation number and water content. The Na,K:Mn ratio was measured by inductively coupled plasma optical emission spectrometry (ICP-OES, Perkin Elmer Optima 8300) from samples digested in a 3% HNO₃ and 0.05 M H₂C₂O₄ solution. The average Mn oxidation number (AMON) was determined by a three-step potentiometric titration that yields a concentration-independent measure of AMON (Grangeon et al., 2008) with a Metrohm 888 Titrando automatic titrator equipped with a Pt potentiometric electrode. Briefly, 15 mg of δ -MnO₂ were dissolved in a 0.01 M Mohr's salt [(NH₄)₂Fe(SO₄)₂•6H₂O] solution and residual Fe(II) was titrated with 0.01 M KMnO₄. A parallel Mohr's salt solution, to which no mineral was added but whose mass was matched gravimetrically on an analytical balance (\pm 0.001 g precision), was also titrated with 0.01 M KMnO₄. The difference in the volume of KMnO₄ used in these two titrations thus provided the amount of Fe(II) required to reductively dissolve the mineral. The amount of Mn(II) generated by reductive dissolution of the mineral was back titrated with 0.02 M KMnO₄ to Mn(III), which was trapped by complexation with excess sodium pyrophosphate (Na₄P₂O₇, abbreviated hereafter as PP) (Kostka et al., 1995; Klewicki and Morgan, 1998; Webb et al., 2005). The sensitivity of this method was assessed by AMON determinations of MnCl₂, Mn(III)-acetate powder and pyrolusite (\square -MnO₂, 99.99 % trace metals basis). The measured values were accurate within 0.05 AMON units of the theoretical oxidation numbers, which is equivalent to a 5% uncertainty in the Mn(III) and Mn(IV) content for a mineral containing exclusively Mn(III) and Mn(IV). A reproducibility of 0.02 - 0.04 AMON units was determined from the standard deviation of triplicate measurements on the synthesis products (**Table 2**).

A second measure of average Mn oxidation number was obtained by determining the amount of Mn(III) extractable by pyrophosphate (Kostka et al., 1995; Klewicki and Morgan, 1999; Wang and Stone, 2003). Briefly, 5 mg of dry sample were equilibrated in excess PP with a 20:1 PP:Mn ratio (50 ml of 20 mM PP at pH 6.5) for 48 hours in polypropylene centrifuge tubes in the dark. Pyrophosphate is a redox-inert chelator (Wang and Stone, 2008), thus no Mn(III) should be generated by reduction of Mn(IV) during the extraction. The absorbance of a filtered aliquot was measured at 254 nm ($\epsilon = 6562 \text{ M cm}^{-1} \text{ L}^{-1}$) in a 1 cm path length quartz

cuvette using a 20 mM PP solution as a blank. To obtain the mole fraction of Mn(III), the Mn(III) concentration measured spectrophotometrically was divided by the total Mn concentration in the suspension, as measured by ICP-OES analysis of an acid-digested suspension aliquot. All measurements were conducted in triplicate. Finally, this method was validated through AMON measurements of two well-defined Mn oxide phases under the assumption that each mineral consisted exclusively of Mn(III) and Mn(IV). For triclinic birnessite [$\text{Na}_{0.25}\text{Mn(III)}_{0.16}\text{Mn(IV)}_{0.84}\text{O}_2 \cdot 0.66 \text{H}_2\text{O}$ (Feng and Lingrel, 1994)], we found 15.3 ± 0.5 % PP-extractable Mn(III) and an AMON value of 3.84 ± 0.05 , which corresponds to 11 – 21 % Mn(III). For K-birnessite [$\text{K}_{0.265}\text{Mn(III)}_{0.10}(\text{Mn(IV)})_{0.825}\text{Vac.}_{0.175}\text{O}_2 \cdot 0.68 \text{H}_2\text{O}$ (Gaillot et al., 2003)], we found 10.3 ± 0.5 % extractable Mn(III) and an AMON value of 3.90 ± 0.01 , which corresponds to 9 – 11 % Mn(III). These independent measurements of Mn(III) are in excellent agreement. However, the uncertainty on Mn(III) content as extracted by PP is generally lower than that determined by the potentiometric titration method.

To determine the amount of water strongly sorbed at the mineral surface, we performed thermogravimetric analyses (Mettler Toledo TGA/SDTA 851e) by heating approximately 30 mg of sample in alumina crucibles between 30 °C and 480 °C at a rate of 10°C/min. The water content was determined by subtracting the TGA curve of an empty crucible from the TGA curve of the sample, and normalizing this mass loss value by the initial sample mass. The structural water content was obtained by measuring the weight loss percentage between 80° C and 250° C (Villalobos et al., 2006).

3.3.4. Structural characterization of the synthesis products

The δ -MnO₂ products were characterized in terms of specific surface area, mineral phase and intermediate-range structure (< 2 nm) using freeze-dried samples, whereas short-range structure (< 6 Å) was characterized on samples filtered onto 0.45 µm nitrocellulose membranes from mineral suspensions. Specific surface area was determined by a 5-point BET theory N₂ adsorption isotherm at 77 K (Micromeritics Gemini 2375). The measurement uncertainty was defined by the instrument error (5 %).

Synchrotron-XRD (SR-XRD) patterns were acquired at the Swiss-Norwegian beamline of the European Synchrotron Radiation Facility (BM01B - ESRF) from powders packed into

Kapton[®] polyimide capillaries mounted on a goniometric stage, which was spun at 50-100 rpm during data acquisition. Diffraction patterns were acquired with the SPEC software (Certified Scientific Software ©) on a 2D CCD plate using a 0.54 Å radiation wavelength. Data reduction was carried out with FIT-2D (Hammersley, 1997) using a LaB₆ standard for calibration. The 2D XRD patterns were extracted from the background-subtracted azimuthal images using custom routines written in the Python programming language [PyFAI (Kieffer and Karkoulis, 2013)]. The SR-XRD patterns were background subtracted by subtracting the diffraction pattern of an empty polyimide capillary from the diffraction pattern of the sample. These data were used to estimate particle size according to the Scherrer formula (Patterson, 1939), which provides a volume-averaged dimension along the direction perpendicular to the diffracting plane (Patterson, 1939; Warren, 1990):

$$L = K\lambda/B\cos\Theta \quad (3)$$

where L is the cube root of a spherical particle (nm), K is the Scherrer constant, B is the broadening of the reflection (in rad) and λ (nm) and Θ (rad) are the radiation wavelength and the scattering angle, respectively. We estimated particle size by approximating B as the FWHM of the diffraction peaks, as determined by fitting Gaussian functions to the diffracting peaks and K values of 0.726 to 1.027 (Langford and Wilson, 1978).

X-ray absorption spectra were collected at the Swiss light source (SLS) in Villigen, Switzerland, at beamline SuperXAS-X10DA, with a beam current of 400 mA. Manganese K-edge spectra were acquired at room temperature in transmission mode using a quick-scanning Si(111) double crystal monochromator oscillating around the Mn K-edge (6.4 – 6.9 KeV) at a frequency of 1 Hz. The X-ray energy was calibrated with a Mn metal foil by setting the first inflection point in the first derivative of the X-ray absorption near edge structure (XANES) spectrum to 6539 eV. The samples were mounted on acrylic sample holders, sealed with polyimide tape. The spectra were inspected to verify that no beam-induced damage occurred and then averaged with the JAQ software (M., 2015). All data reduction was performed in ATHENA (Ravel and Newville, 2005) to obtain XANES and EXAFS (extended X-ray absorption fine structure) spectra, a GUI built on the IFEFFIT engine (Newville, 2001). Averaged spectra were background subtracted and normalized by fitting the pre-edge region

with a linear function and the post-edge region with a quadratic function, and setting $E_0 = 6554$ eV, $R_{bkg} = 1.0$ Å, no clamps, k-weight = 3, normalization order 3.

3.4. Results

3.4.1. Physical-chemical characterization

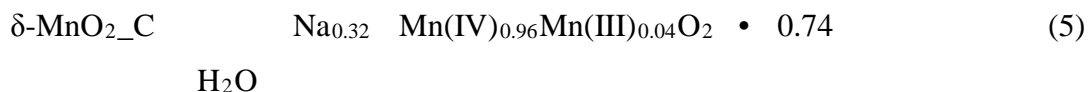
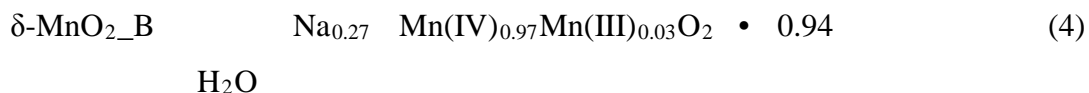
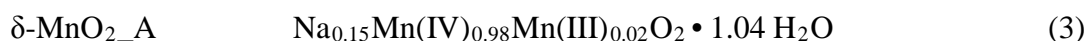
Table 2 summarizes the chemical characteristics of the different δ -MnO₂ samples. At the end of Step 4 in the synthesis protocol, the supernatant pH was close to 4, 8 and 12 for the A, B, and C mineral series, respectively. At the end of the MQ washing steps (Step 7), the supernatant pH increased to 6 for the “A” minerals, whereas the pH decreased to 8 and 11 for the B and C minerals, respectively. The electrical conductivity decreased by one order of magnitude at each MQ washing step, from ~ 10 mS/cm to < 10 μ S/cm after 5 washing steps, except in the high pH synthesis (C2). In this batch, the conductivity of the supernatant did not decrease below 433 μ S/cm after the third washing step and the supernatant contained colloiddally-stable particles.

Table 2: Physico-chemical properties of synthesis products.

Sample name	Na/Mn [%]	EC ¹ [μ S/cm]	pH ¹	Mn(III)-PP ¹ \pm SD [%]	AMON ¹ \pm SD	SSA ¹ \pm σ [m ² /g]	CSD (<i>ab</i> plane) [nm]
δ -MnO ₂ _A1	16.1	4	6	2.57 \pm 0.92	4.03 \pm 0.03	196 \pm 10	4.30 – 6.08
δ -MnO ₂ _A2	16.6	8	6	1.99 \pm 0.29	4.02 \pm 0.02	190 \pm 10	4.30 – 6.08
δ -MnO ₂ _A3	16.0	4	6	2.07 \pm 0.38	4.03 \pm 0.01	259 \pm 13	4.22 – 5.97
δ -MnO ₂ _A3b	16.7	4	6	1.77 \pm 0.03	4.06 \pm 0.04	257 \pm 13	4.08 – 5.77
δ -MnO ₂ _B2	30.2	10	8	2.07 \pm 0.52	4.03 \pm 0.01	163 \pm 8	3.59 – 5.08
δ -MnO ₂ _B3	28.9	10	8	2.14 \pm 0.79	4.02 \pm 0.01	167 \pm 8	3.49 – 4.93
δ -MnO ₂ _C2	35.1	433	11	4.05 \pm 0.26	4.00 \pm 0.02	119 \pm 6	2.83 – 4.00
δ - MnO ₂ _C2_H	-	-	11	2.88 \pm 0.35	3.99 \pm 0.01	117 \pm 6	5.01 – 7.09
δ -MnO ₂ _C2_H	-	-	4	5.66 \pm 1.58	3.92 \pm 0.01	213 \pm 11	4.72 – 6.67

¹The electrical conductivity (EC) and pH were measured in the supernatant at the end of the synthesis. The precision of the pH measurement was ± 1 . ²Standard deviations (SD) were calculated from triplicate measurements; σ indicates instrument error.

After freeze drying and grinding in an agate mortar, all minerals were of comparable color, between dark brown and black. Chemical analysis showed that the Na: Mn ratio increased from 16% to 35% as the synthesis pH increased from 4 to 12, whereas the K: Mn ratio was less than 0.1% in all samples. The AMON measurements gave values between 4.00 ± 0.02 at high pH and 4.06 ± 0.04 at low pH. These AMON values, which are accurate to 0.05 AMON units, are consistent with the calculated AMON based on PP extractions. However, we measured about 2 % PP-extractable Mn(III) in all samples, except for batch C2, which showed $4.3\% \pm 0.7\%$ Mn(III) (**Table 2**). Because PP is a non-redox active chelating agent (41), any aqueous Mn(III) must derive from the mineral as Mn(III). However, for sample C2, which had a pH of 11, it is not possible to rule out the production of additional Mn(III) as the pH was lowered from 11 to 6.5 (Manceau et al., 2013). Finally, the structural water content as determined from TGA curves (**Figure S2**) was comparable between samples: decreasing from 17 % to 12 % as the synthesis pH increased from 4 to 12. Based on these measurements, we assigned a chemical formula to each synthesis product:



3.4.2. Structural characterization

Among the structural properties, we found that the SSA measured by BET theory N₂ adsorption was proportional to the amount of NaOH employed for the synthesis, as shown in **Figure 1A**. The SSA also correlates with the MnCl₂ addition rate, although only in the low pH samples (A1, A2 and A3, **Figure 1B**). Finally, aging of suspensions of the washed minerals did not have a significant effect on the BET-SSA, as indicated by a smaller than 3 % change in SSA measurements of a $\delta\text{-MnO}_2$ batch (Marafatto et al., 2015) stored as a suspension for about 11 months. The long-term stability of the particles suggests mineral storage in suspension, rather than as freeze-dried powders, may be preferable to avoid particle aggregation or changes in aggregate morphology that may not be reversible after re-suspension (58).

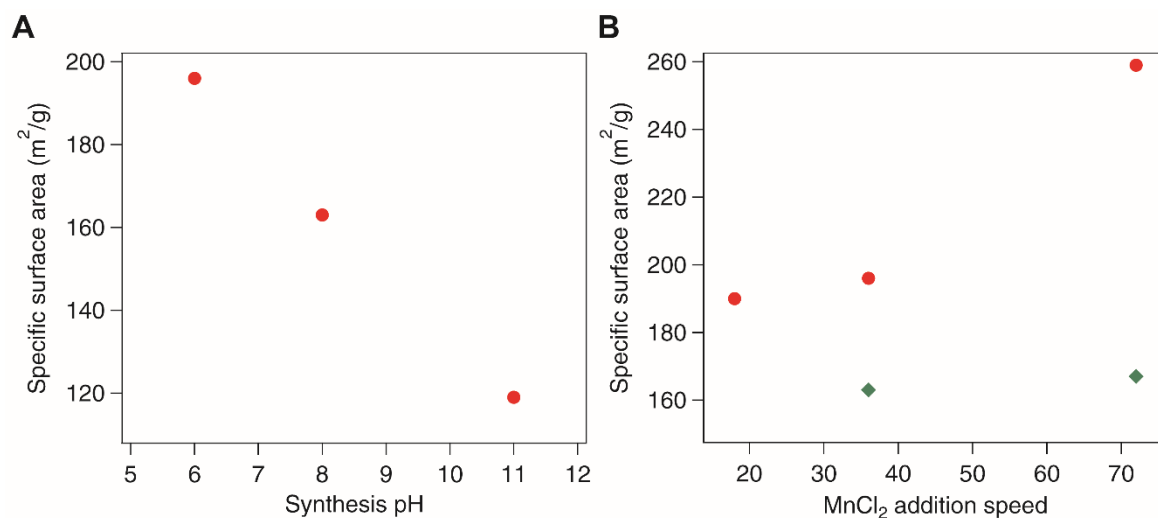


Figure 1A) Specific surface area as a function of pH (equivalent to NaOH concentrations of 0.4 M, 0.5 M and 0.6 M, respectively) for minerals synthesized with MnCl₂ addition rate of 36 ml/min; **B)** Specific surface area as a function of MnCl₂ addition rate for minerals synthesized with 0.4 M NaOH (red circles) and 0.5 M NaOH (green diamonds).

In **Figure 2** the powder SR-XRD patterns for the different δ -MnO₂ samples show the characteristic broad reflections of the $20l$, $11l$ planes at $\sim 12^\circ 2\Theta$ and $02l$, $31l$ planes at $\sim 25^\circ 2\Theta$ (Villalobos et al., 2003). The ratio between these d-spacings is close to $\sqrt{3}$, which indicates hexagonal symmetry. However, there are differences between samples that are worth noting. For example, the $02l$, $31l$ reflection at $12^\circ 2\Theta$ shows greater asymmetry at higher 2Θ angles in the high pH samples compared to the lower pH samples. This broadening is related to the coherent scattering domain (CSD) size in the ab plane, as well as to the position of interlayer species (Na, H₂O and Mn(III), if present) (Villalobos et al., 2006). The “bumps” visible in the 2Θ region between the $20l, 11l$ and the $02l, 31l$ reflection are sensitive to the position of interlayer species with respect to the octahedral layer. The broadening of the $20l, 11l$ peak, on the other hand, is strictly related to the CSD size: a broader peak indicates a smaller CSD (Villalobos et al., 2006). The greater CSD size along the ab plane of the samples synthesized at low pH relative to those synthesized at high pH is apparent in **Figure 3**, where we compare a subset of the diffraction patterns. Finally, through application of the Scherer equation, we estimated CSD sizes along the ab plane that ranged from 5.19 ± 0.89 to 3.42 ± 0.59 nm (**Table 2**). The formation of smaller crystallites at high pH values is consistent with the base-catalyzed oxidation (and nucleation) of Mn.

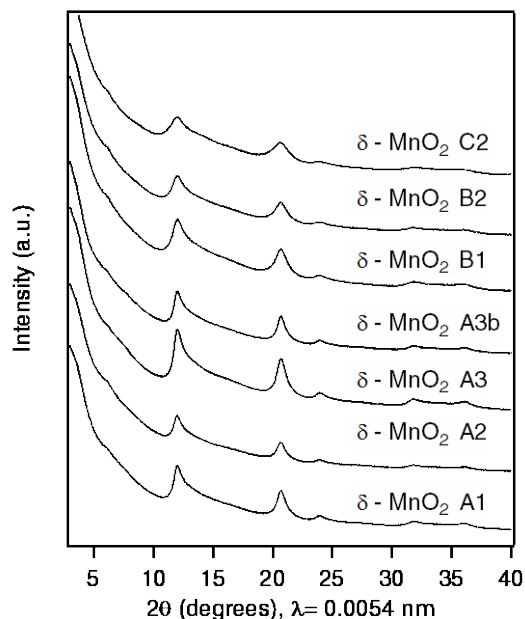


Figure 2: SR-XRD patterns for the synthesized minerals. The diagnostic broad diffraction peaks at 13° and 21° 2θ , equivalent to d spacings of 0.35-0.36 and 0.24 nm respectively, are visible, and represent the reflections from the 211, 111 and 311, 111 crystallographic planes, respectively.

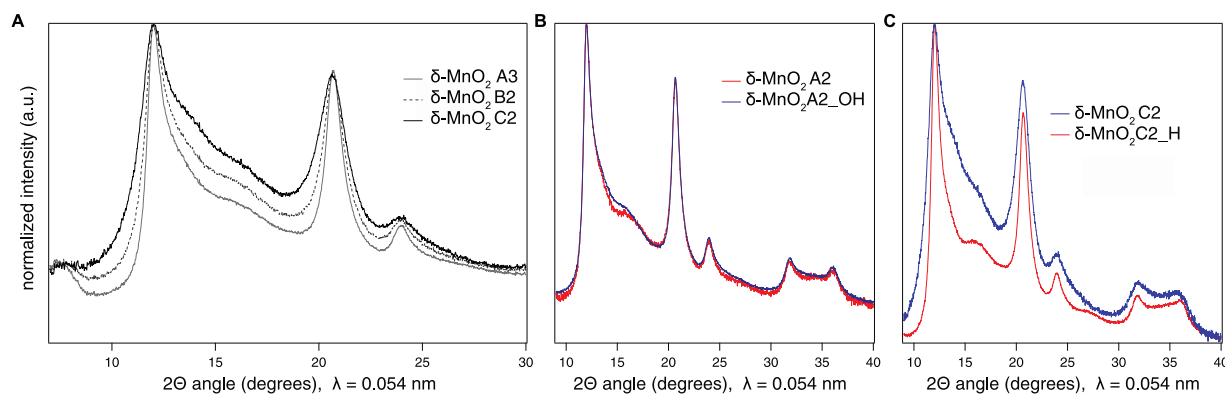


Figure 3: SR-XRD patterns showing the 211, 111 and 311, 111 reflections in a subset of samples show different degrees of peak broadening. Data was background subtracted by subtracting the diffraction pattern of the empty kapton capillary between 5° and 40° 2θ , then each diffraction pattern was normalized to the maximum intensity of the reflection at 12° 2θ . A) SR-XRD data for the three synthesis batches chosen as endmembers based on BET-SSA (δ - MnO_2 A3, B2 C2). 2θ ; B) SR-XRD of δ - MnO_2 A2 and δ - MnO_2 A2 after equilibrating at pH 10 for 1 week; C) SR-XRD of δ - MnO_2 C2 and δ - MnO_2 C2 after equilibrating to pH 4 for 1 week.

The XANES and EXAFS Mn K-edge spectra collected from all samples are shown in **Figures 5** and **6**, respectively. Consistent with wet chemical data, the XANES and first derivative of the XANES (**Figures 5**) show that Mn(IV) is the prevalent oxidation state in all samples. The white line position at 0.5 absorption units is 6551.9 eV, which is consistent with the energy reported previously for a mineral composed dominantly of Mn(IV) (Bargar et al.,

2005). The EXAFS spectra from the different samples (**Figure 6**) are also in good agreement with the published EXAFS spectrum of δ -MnO₂ (Marcus et al., 2004). In particular, the “staircase” feature between 4 and 6 Å⁻¹ indicates a mineral of the phyllosilicate family, whereas the absence of symmetric oscillations peaking at 8.1 and 9.2 Å⁻¹ in the “indicator” region between 7.8 and 9.6 Å⁻¹ indicates the absence of interlayer Mn(III) and low to no Mn(III) in the octahedral layer (Manceau et al., 2004). This data is consistent with the XANES spectra and PP extraction results, which show Mn(III) at levels below the 5-10% detection limit of XAS (Bargar et al., 2000).

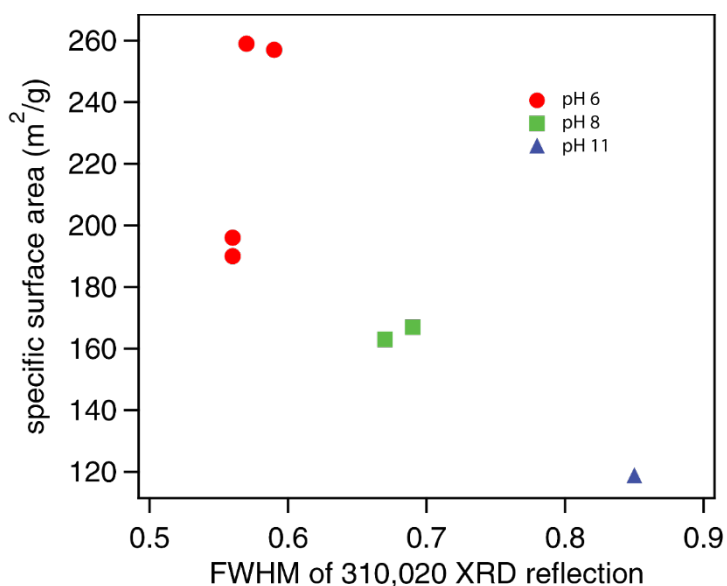


Figure 4: Comparison of the specific surface area and the FWHM of the 310,020 reflection in the XRD diffraction patterns shown in Figure 3, which is inversely proportional to the coherent scattering domain size along the crystallographic *ab* plane.

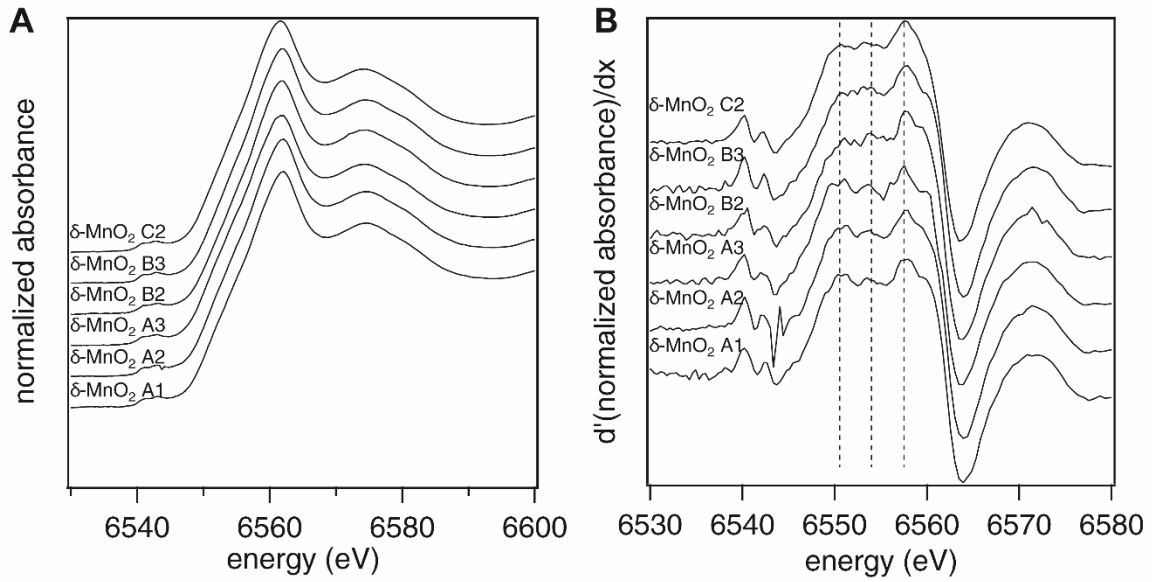


Figure 5 **A)** Normalized XANES spectra for the various minerals, all showing the same white-line position; **B)** First derivative of the XANES spectra shown in A, with indication of the features that are sensitive to changes in AMON.

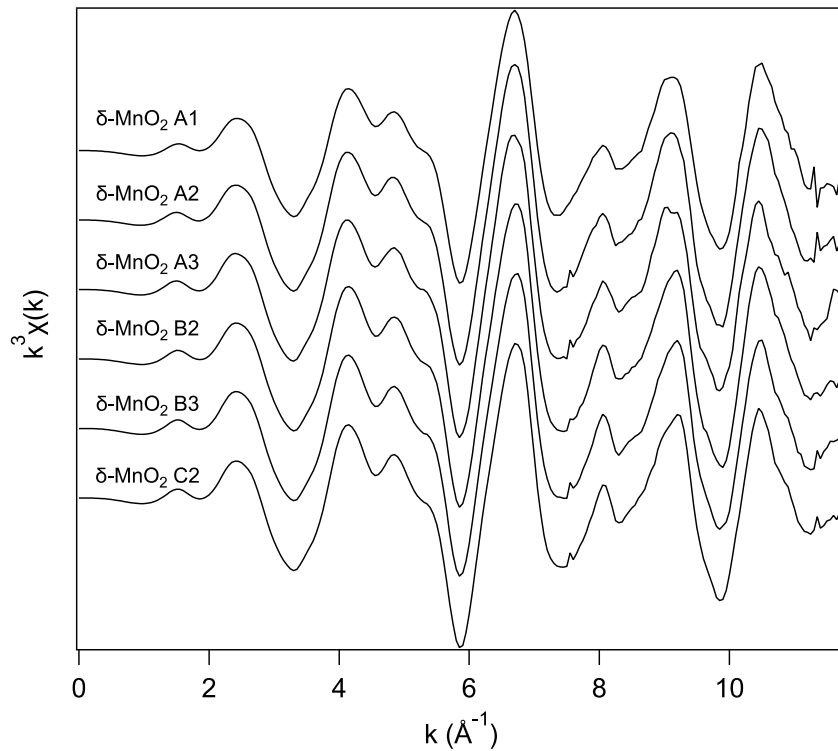


Figure 6. EXAFS spectra collected from all mineral samples. The “staircase” and “indicator” regions show the typical features of a phyllosilicate phase with little to no Mn(III).

3.5. Discussion

Mn(IV) content. Our potentiometric titration and PP extraction measurements show that all δ -MnO₂ preparations consisted dominantly of Mn(IV) (**Table 2**). These results indicate that neither MnCl₂ addition speed nor NaOH concentration influence the oxidation state of Mn in the mineral. Instead, the Mn valence in the products is governed by the Mn(VII)/Mn(II) ratio, such that lowering the Mn(VII)/Mn(II) ratio from 0.67 to 0.52 leads to a decrease in AMON value from 4.02 to 3.70 – 3.80 (Villalobos et al., 2003; Duckworth and Sposito, 2007). In a separate synthesis where we applied a stoichiometric ratio of 0.52 Mn(VII) to Mn(II), we obtained a comparable Mn(III) content: 20.3% \pm 1.4% Mn(III) and an AMON of 3.80 \pm 0.01. This was also observed in the preliminary synthesis batch where excess Mn(II) was added (approximately 0.45 Mn(VII):Mn(II) ratio instead of 0.67). In this synthesis, the products were found to contain 30% Mn(III).

Na:Mn ratio. The δ -MnO₂ batches we synthesized varied with respect to Na:Mn content. The minerals that were synthesized at higher pH had a greater Na:Mn ratio than those synthesized at low pH, which was also observed by Manceau et al. (2013). This result can be rationalized chemically and geometrically. Because δ -MnO₂ has a negative surface charge over most of the pH scale (PZC \sim 2-3 (Sposito, 2008)), the excess in surface charge will be balanced by cations. In addition, as the solution pH increases and proton activity decreases, Na⁺ can compete more effectively for negatively charged surface sites. The Na:Mn content can also be related to particle size and surface site density. We built nearly circular monolayer MnO₂ model particles using the XRD-derived estimates of CSD size and a vacancy content equal to 0.06 mol vacancy mol⁻¹ Mn (Villalobos et al., 2006) using Crystalmaker[®]. For each particle, we calculated the amount of Na⁺ needed to balance the negative charge arising from all undersaturated oxygen atoms under the assumption that each vacancy site requires 4 Na⁺ ions (+4 charge deficit) and lateral edge sites accommodate 1 or 2 Na⁺ ions depending on whether the oxygen atom is doubly or singly coordinated to Mn, respectively. We found that as the CSD of the minerals decreased from 5 nm to 3 nm, the Na: Mn ratio increased from 0.85 to 1.31. The 35 % increase in the Na: Mn ratio is consistent with our measurements, which showed a 48 % increase in the Na: Mn ratio with decreasing CSD size along the crystallographic *ab* plane and increasing synthesis pH.

Crystallite size. The CSD sizes along the *ab* plane that we estimated from the broadening of the *20l,11l* reflection in the X-ray diffraction patterns showed that crystallite size decreased moderately 5.19 ± 0.89 to 3.42 ± 0.59 nm as the synthesis pH was increased. The acidification or basification of the washed mineral samples, however, influenced the CSD size differently. The SR-XRD pattern for sample C2_H showed less broadening in the main diffraction peaks relative to sample C2 (**Figure 3**), indicating an increase in crystallite size along the *ab* plane from about 3.4 to 6.0 nm. The basified sample (A2_OH), on the other hand, showed no structural change with respect to the parent mineral and did not exhibit any change in the Mn(III) content. The small to moderate increase in C2_H upon acidification relative to C2 supports the hypothesis that proton-promoted reduction of Mn(IV) with the electron deriving from water or Cl⁻ ions (Grätzel et al., 1985; Marafatto et al., 2015) and/or crystallite growth may occur upon acidification.

Specific surface area. The specific surface area of the different mineral preparations ranged from 119 to 259 m² g⁻¹ (**Figure 1A**). BET theory N₂ adsorption, which measures the amount of gas that can be physisorbed on the mineral surface per unit mass, can yield an indirect measurement of particle size (Sing et al., 1985). However, BET-SSA measurements generally cannot distinguish an aggregate from a single crystallite when the size of the crystallite is on the order of a few nanometers (Sing et al., 1985). In fact, a plot of the FWHM of the *310,020* reflection in the XRD patterns, which is proportional to the CSD size of the *ab* plane (**Table 2**), against the SSA shows an inverse correlation between the XRD-sensitive CSD size and SSA. Thus, we suggest that the BET-SSA values reflect the specific surface area of aggregated crystallites.

Two studies on Fe oxide nanoparticles have shown that BET-SSA can underestimate particle size when there is nanoparticle aggregation (Gilbert et al., 2009). The authors found that increasing solution pH from 5 to 10 and ionic strength from 0.01 to 1 M led to 30 % and 10 % decreases in BET-SSA, respectively. In our samples, we also found that solution pH strongly influenced the BET-SSA. However, we observed a 40 % increase in BET-SSA as pH increased from 6 to 11. The opposite trends observed for ferrihydrite and δ -MnO₂ may be explained by differences in surface charge and/or particle shape, which likely affects particle aggregation dynamics (Gilbert et al., 2009). In our samples, we expect that aggregation due to

ionic strength would cause a small to negligible impact on the BET-SSA since the ionic strength varied by 0.1 M across the different syntheses. An additional factor that may influence the measured BET-SSA is the length of time during which the freshly precipitated particles settle in the mother liquor before the washing (ionic strength 0.5 M; Step 4 in synthesis protocol). In fact, the B2 synthesis replicated the procedure of Villalobos et al. (2), but used a 30 minutes settling time instead of a 4 hour settling time and yielded BET-SSA of 163 ± 8 m²/g and 120 ± 2 m²/g, respectively. Thus, we suggest that the settling time after reagent mixing may have a moderate effect on the SSA since particle growth or aggregation processes may occur during that time.

The acidification or basification of the mineral samples showed large differences in BET-SSA relative to the parent mineral. In particular, the SSA of C2_H increased to values comparable to the low pH samples, from 119 ± 6 to 213 ± 4 m²/g, whereas A2_OH decreased in SSA from 190 ± 10 m²/g to 117 ± 2 m²/g. These observations indicate that the BET-SSA of the minerals is a dynamic property that can be modified after synthesis, and support our conclusion that BET provides a measure of the surface area of aggregates rather than structural properties such as CSD size. Furthermore, the increase in Na content at the particle edges as the suspension pH increases may promote aggregation between crystallites and lower the accessibility of aqueous species to these surface sites.

3.6. Conclusions

This work tested the effect of varying synthesis parameters on the composition and structure of δ -MnO₂ nanoparticles. All minerals showed hexagonal sheet symmetry in the *ab* plane and the lack of ordered stacking along the *c*-axis direction. About 98 % Mn(IV) in all but one synthesis was observed by measurements of Mn valence, whereas the “outlier” batch only 96 % Mn(IV). Our results showed that the BET-SSA can be tuned by varying the NaOH concentration and, to a lesser extent, by the speed of MnCl₂ addition during the synthesis. We also found that changes in suspension pH post-synthesis are sufficient to modify the BET-SSA. We obtained the highest BET-SSA for minerals synthesized at pH 4 ($259 \text{ m}^2 \text{ g}^{-1}$) or by acidification of the mineral post-synthesis from pH 11 ($119 \text{ m}^2 \text{ g}^{-1}$) to pH 4 ($213 \text{ m}^2 \text{ g}^{-1}$). However, the coherent scattering domain size along the *ab* plane decreased and Na content increased with increasing suspension pH. Thus, we suggest that the increase of Na at

nanoparticle edges leads to nanoparticle aggregation and, thus, lower BET-SSA. The reversibility of BET-SSA in acidified or basified samples further confirms that suspension pH and Na content drive aggregation. The findings of this study are significant to the geochemistry and environmental science communities since BET-SSA has been shown to correlate with the reactivity of birnessite minerals with respect to the sorption of toxic metals and metalloids (Villalobos et al., 2005; Lafferty et al., 2010; Simanova et al., 2015) and organic contaminant degradation (Remucal and Ginder-Vogel, 2014, and references therein). In various other studies, mineral reactivity (e.g., sorption, desorption, dissolution, etc.) has been also been related to particle size and particle aggregation (Nico and Zamoski, 2000; Gilbert et al., 2009; Liu et al., 2009; Kuhn et al., 2014). Therefore, we strongly recommend that future studies report the synthesis and mineral characterization protocols accurately and account for the reversible effect of solution pH on the BET-SSA. Finally, studies to decouple the effects of nanoparticle aggregation, which may lower reactivity of edge surface sites, and increasing solution pH, which enhances the adsorption of cations but diminishes the adsorption of oxyanions, may shed light on the conditions that favor reactivity of the edge surface sites (Simanova et al., 2015; Villalobos, 2015; van Genuchten and Pena, 2016).

3.7. Acknowledgements

This research was funded by the Swiss National Science Foundation (Grant # 200021_143742). We thank Imelda Doussou Etui and Dr. Anna Simanova for their contributions to the synthesis and characterization of the minerals as well as for useful discussions. We are grateful to Michela Brunelli and Emerich Hermann at the Swiss-Norwegian beamline (BM01B) of the European Synchrotron Radiation Facility (Grenoble, France) for their assistance with X-ray scattering measurements and Maarten Nachtegaal at the SuperXAS beamline (X10DA) of the Swiss Light Source (Villigen, Switzerland) for his assistance with XAS data collection.

3.8. References

CrystalMaker®: a crystal and molecular structures program for Mac and Windows, 2.7.7 ed. *CrystalMaker Software Ltd*, Oxford, England.

- Bargar, J.R., Tebo, B.M., Bergmann, U., Webb, S.M., Glatzel, P., Chiu, V.Q., Villalobos, M., **2005**. Biotic and abiotic products of Mn(II) oxidation by spores of the marine *Bacillus* sp. strain SG-1. *Am Mineral* 90, 143-154.
- Bargar, J.R., Tebo, B.M., Villinski, J.E., **2000**. In situ characterization of Mn(II) oxidation by spores of the marine *Bacillus* sp strain SG-1. *Geochim Cosmochim Acta* 64, 2775-2778.
- Burns, R.G., **1976**. Uptake of Cobalt into Ferromanganese Nodules, Soils, and Synthetic Manganese(IV) Oxides. *Geochim Cosmochim Acta* 40, 95-102.
- Buser, W., Graf, P., **1955**. Differenzierung Von Mangan(II)-Manganit Und Delta-MnO₂ Durch Oberflächenmessung Nach Brunauer-Emmet-Teller. *Helv Chim Acta* 38, 830-834.
- Duckworth, O.W., Sposito, G., **2007**. Siderophore-promoted dissolution of synthetic and biogenic layer-type Mn oxides. *Chem Geol* 242, 497-508.
- Feng, J.N., Lingrel, J.B., **1994**. Analysis of Amino-Acid-Residues in the H5-H6 Transmembrane and Extracellular Domains of Na,K-ATPase Alpha-Subunit Identifies Threonine-797 as a Determinant of Ouabain Sensitivity. *Biochemistry* 33, 4218-4224.
- Gaillot, A.C., Flot, D., Drits, V.A., Manceau, A., Burghammer, M., Lanson, B., **2003**. Structure of Synthetic K-rich Birnessite Obtained by High-Temperature Decomposition of KMnO₄. I. Two-Layer Polytype from 800 °C Experiment. *Chem Mater* 15, 4666-4678.
- Gilbert, B., Ono, R.K., Ching, K.A., Kim, C.S., **2009**. The effects of nanoparticle aggregation processes on aggregate structure and metal uptake. *J Colloid Interf Sci* 339, 285-295.
- Godtfredsen, K.L., Stone, A.T., **1994**. Solubilization of Manganese Dioxide-Bound Copper by Naturally-Occurring Organic-Compounds. *Environ Sci Technol* 28, 1450-1458.
- Grangeon, S., Lanson, B., Lanson, M., Manceau, A., **2008**. Crystal structure of Ni-sorbed synthetic vernadite: a powder X-ray diffraction study. *Mineral Mag* 72, 1279-1291.
- Grangeon, S., Manceau, A., Guilhermet, J., Gaillot, A.C., Lanson, M., Lanson, B., **2012**. Zn sorption modifies dynamically the layer and interlayer structure of vernadite. *Geochim Cosmochim Acta* 85, 302-313.
- Grätzel, M., Kiwi, J., Morrison, C.L., Davidson, R.S., Tseung, A.C., **1985**. Visible-light-induced photodissolution of α -Fe₂O₃ powder in the presence of chloride anions. *J Chem Soc Farad T* 1 81, 1883-1890.
- Hammersley, A.P., **1997**. FIT2D: An Introduction and Overview, ESRF Internal Report
- Hocking, R.K., Brimblecombe, R., Chang, L.Y., Singh, A., Cheah, M.H., Glover, C., Casey, W.H., Spiccia, L., **2011**. Water-oxidation catalysis by manganese in a geochemical-like cycle. *Nat Chem* 3, 461-466.
- Kieffer, J., Karkoulis, D., **2013**. PyFAI, a versatile library for azimuthal regrouping. *J Phys Conf Ser* 425.
- Klewicki, J., Morgan, J., **1999**. Dissolution of β -MnOOH particles by ligands: pyrophosphate, ethylenediaminetetraacetate, and citrate. *Geochim Cosmochim Acta* 63, 3017-3024.
- Klewicki, J.K., Morgan, J.J., **1998**. Kinetic behavior of Mn(III) complexes of pyrophosphate, EDTA, and citrate. *Environ Sci Technol* 32, 2916-2922.
- Kostka, J.E., Luther, G.W., Nealson, K.H., **1995**. Chemical and Biological Reduction of Mn(III)-Pyrophosphate Complexes - Potential Importance of Dissolved Mn(II) as an Environmental Oxidant. *Geochim Cosmochim Acta* 59, 885-894.
- Kuhn, K.M., DuBois, J.L., Maurice, P.A., **2014**. Aerobic Microbial Fe Acquisition from Ferrihydrite Nanoparticles: Effects of Crystalline Order, Siderophores, and Alginate. *Environ Sci Technol* 48, 8664-8670.

- Lafferty, B.J., Ginder-Vogel, M., Sparks, D.L., **2010**. Arsenite Oxidation by a Poorly Crystalline Manganese-Oxide 1. Stirred-Flow Experiments. *Environ Sci Technol* 44, 8460-8466.
- Langford, J.I., Wilson, A.J.C., **1978**. Scherrer after 60 Years - Survey and Some New Results in Determination of Crystallite Size. *J Appl Crystallogr* 11, 102-113.
- Liu, J., Aruguete, D.M., Murayama, M., Hochella, M.F., **2009**. Influence of Size and Aggregation on the Reactivity of an Environmentally and Industrially Relevant Manomaterial (PbS). *Environ Sci Technol* 43, 8178-8183.
- M., O., **2015**. JAQ Analyzes QEXAFS, 3.3.46 ed. *Bergische Universität Wuppertal*.
- Manceau, A., Drits, V.A., Silvester, E., Bartoli, C., Lanson, B., **1997**. Structural mechanism of Co²⁺ oxidation by the phylломanganate buserite. *Am Mineral* 82, 1150-1175.
- Manceau, A., Marcus, M.A., Grangeon, S., Lanson, M., Lanson, B., Gaillot, A.C., Skanthakumar, S., Soderholm, L., **2013**. Short-range and long-range order of phylломanganate nanoparticles determined using high-energy X-ray scattering. *J Appl Crystallogr* 46, 193-209.
- Manceau, A., Marcus, M.A., Tamura, N., Proux, O., Geoffroy, N., Lanson, B., **2004**. Natural speciation of Zn at the micrometer scale in a clayey soil using X-ray fluorescence, absorption, and diffraction. *Geochim Cosmochim Acta* 68, 2467-2483.
- Marafatto, F.F., Strader, M.L., Gonzalez-Holguera, J., Schwartzberg, A., Gilbert, B., Pena, J., **2015**. Rate and mechanism of the photoreduction of birnessite (MnO₂) nanosheets. *Proc Natl Acad Sci U S A* 112, 4600-4605.
- Marcus, M.A., Manceau, A., Kersten, M., **2004**. Mn, Fe, Zn and As speciation in a fast-growing ferromanganese marine nodule. *Geochim Cosmochim Acta* 68, 3125-3136.
- Morgan, J.J., **2000**. Manganese in natural waters and earth's crust: its availability to organisms. *Met Ions Biol Syst* 37, 1-34.
- Murray, J.W., **1974**. The surface chemistry of hydrous manganese dioxide. *J Colloid Interf Sci* 46, 357-371.
- Newville, M., **2001**. IFEFFIT: interactive XAFS analysis and FEFF fitting. *J Synchrotron Radiat* 8, 322-324.
- Nico, P.S., Zasoski, R.J., **2000**. Importance of Mn(III) availability on the rate of Cr(III) oxidation on delta-MnO₂. *Environ Sci Technol* 34, 3363-3367.
- Patterson, A.L., **1939**. The Scherrer formula for X-ray particle size determination. *Physical review* 56, 978.
- Peacock, C.L., Sherman, D.M., **2007**. Sorption of Ni by birnessite: Equilibrium controls on Ni in seawater. *Chem Geol* 238, 94-106.
- Post, J., **1999**. Manganese oxide minerals: Crystal structures and economic and environmental significance. *Proceedings of the National Academy of Sciences* 96, 3447-3454.
- Ravel, B., Newville, M., **2005**. ATHENA, ARTEMIS, HEPHAESTUS: data analysis for X-ray absorption spectroscopy using IFEFFIT. *J Synchrotron Radiat* 12, 537-541.
- Remucal, C.K., Ginder-Vogel, M., **2014**. A critical review of the reactivity of manganese oxides with organic contaminants. *Environ Sci-Proc Imp*.
- Ruetschi, P., **1984**. Cation-Vacancy Model for MnO₂. *J Electrochem Soc* 131, 2737-2744.
- Sherman, D.M., **1984**. The electronic structures of manganese oxide minerals. *Am Mineral* 69, 788-799.
- Simanova, A.A., Bone, S.E., Bargar, J., Sposito, G., Peña, J., **2013**. Ni sorption at the particle edges of synthetic and biogenic birnessite. *Mineral Mag* 79, 2214.

- Simanova, A.A., Kwon, K.D., Bone, S.E., Bargar, J.R., Refson, K., Sposito, G., Pena, J., **2015**. Probing the sorption reactivity of the edge surfaces in birnessite nanoparticles using nickel(II). *Geochim Cosmochim Acta* 164, 191-204.
- Simanova, A.A., Peña, J., **2015**. Time-Resolved Investigation of Cobalt Oxidation by Mn(III)-Rich δ -MnO₂ Using Quick X-ray Absorption Spectroscopy. *Environ Sci Technol* 49, 10867-10876.
- Sing, K.S.W., Everett, D.H., Haul, R.A.W., Moscou, L., Pierotti, R.A., Rouquerol, J., Siemieniewska, T., **1985**. Reporting Physisorption Data for Gas Solid Systems with Special Reference to the Determination of Surface-Area and Porosity (Recommendations 1984). *Pure Appl Chem* 57, 603-619.
- Sposito, G., **2008**. The chemistry of soils, 2nd ed. *Oxford University Press*, Oxford.
- Stumm, W., Morgan, J.J., **1996**. Aquatic chemistry: chemical equilibria and rates in natural waters. *Wiley*.
- Tebo, B.M., Bargar, J.R., Clement, B.G., Dick, G.J., Murray, K.J., Parker, D., Verity, R., Webb, S.M., **2004**. Biogenic manganese oxides: Properties and mechanisms of formation. *Annual Review of Earth and Planetary Sciences* 32, 287-328.
- Thanh, N.T.K., Maclean, N., Mahiddine, S., **2014**. Mechanisms of Nucleation and Growth of Nanoparticles in Solution. *Chem Rev* 114, 7610-7630.
- van Genuchten, C.M., Pena, J., **2016**. Sorption selectivity of birnessite particle edges: a d-PDF analysis of Cd(ii) and Pb(ii) sorption by [small delta]-MnO₂ and ferrihydrite. *Environ Sci-Proc Imp*.
- Villalobos, M., **2015**. The Role of Surface Edge Sites in Metal(loid) Sorption to Poorly-Crystalline Birnessites. *Acs Sym Ser* 1197, 65-87.
- Villalobos, M., Bargar, J., Sposito, G., **2005**. Mechanisms of Pb(II) Sorption on a Biogenic Manganese Oxide. *Environ Sci Technol* 39, 569-576.
- Villalobos, M., Lanson, B., Manceau, A., Toner, B., Sposito, G., **2006**. Structural model for the biogenic Mn oxide produced by *Pseudomonas putida*. *Am Mineral* 91, 489-502.
- Villalobos, M., Toner, B., Bargar, J., Sposito, G., **2003**. Characterization of the manganese oxide produced by *Pseudomonas putida* strain MnB1. *Geochim Cosmochim Acta* 67, 2649-2662.
- Wang, Y., Feng, X.H., Villalobos, M., Tan, W.F., Liu, F., **2012**. Sorption behavior of heavy metals on birnessite: Relationship with its Mn average oxidation state and implications for types of sorption sites. *Chem Geol* 292, 25-34.
- Wang, Y., Stone, A.T., **2003**. Soluble Mn(III) complexes arising from the reaction of pyrophosphate and phosphonate-containing chelating agents with manganese(III,IV) (HYDR)oxides. *Abstr Pap Am Chem S* 226, U471-U471.
- Wang, Y., Stone, A.T., **2006a**. The citric acid-Mn(III,IV)O(2)(birnessite) reaction. Electron transfer, complex formation, and autocatalytic feedback. *Geochim Cosmochim Acta* 70, 4463-4476.
- Wang, Y., Stone, A.T., **2006b**. Reaction of Mn(III,IV) (hydr)oxides with oxalic acid, glyoxylic acid, phosphonoformic acid, and structurally-related organic compounds. *Geochim Cosmochim Acta* 70, 4477-4490.
- Wang, Y., Stone, A.T., **2008**. Phosphonate- and Carboxylate-Based Chelating Agents that Solubilize (Hydr)oxide-Bound MnIII. *Environ Sci Technol* 42, 4397-4403.
- Warren, B.E., **1990**. X-ray diffraction, Dover ed. *Dover Publications*, New York.

- Webb, S.M., Dick, G.J., Bargar, J.R., Tebo, B.M., **2005**. Evidence for the presence of Mn(III) intermediates in the bacterial oxidation of Mn(II). *Proc Natl Acad Sci U S A* 102, 5558-5563.
- Wiechen, M., Zaharieva, I., Dau, H., Kurz, P., **2012**. Layered manganese oxides for water-oxidation: alkaline earth cations influence catalytic activity in a photosystem II-like fashion. *Chem Sci* 3, 2330-2339.
- Zasoski, R.J., Burau, R.G., **1988**. Sorption and Sorptive Interaction of Cadmium and Zinc on Hydrated Manganese Oxide. *Soil Sci Soc Am J* 52, 81-87.

Chapter 4. The mechanism and rate of δ -MnO₂

photoreduction in a simplified system

This chapter was submitted and published in Proceedings of the American Society of Sciences (PNAS), Vol. 112 issue 15, with the title “Rate and mechanism of the photoreduction of birnessite (MnO₂) nanosheets”, Marafatto FF, Strader ML, Gonzalez-Holguera J, Schwartzberg A, Gilbert B, Peña J (doi: 10.1073/pnas.1421018112), and is presented in this dissertation with slight modifications. The originally published article is presented in Annex 6.

4.1. Abstract

The photo-reductive dissolution of Mn(IV) oxide minerals in sunlit aquatic environments couples the Mn cycle to the oxidation of organic matter and fate of trace elements associated with Mn oxides, but the intrinsic rate and mechanism of mineral dissolution in the absence of organic electron donors is unknown. We investigated the photoreduction of δ -MnO₂ nanosheets at pH 6.5 with Na or Ca as the interlayer cation under 400 nm light irradiation and quantified the yield and timescales of Mn(III) production. Our study of transient intermediate states using time-resolved optical and X-ray absorption spectroscopy showed key roles for chemically distinct Mn(III) species. The reaction pathway involves: 1) formation of Jahn-Teller distorted Mn(III) sites in the octahedral sheet within 0.6 ps of photoexcitation; 2) Mn(III) migration into the interlayer within 600 ps; and 3) increased nanosheet stacking. We propose that irreversible Mn reduction is coupled to hole scavenging by surface water molecules or hydroxyl groups, with associated radical formation. This work demonstrates the importance of direct MnO₂ photoreduction in environmental processes and provides a framework to test new hypotheses regarding the role of organic molecules and metal species in photochemical reactions with Mn oxide phases. The timescales for the production and evolution of Mn(III) species and a catalytic role for interlayer Ca²⁺ identified here from spectroscopic measurements can also guide the design of efficient Mn-based catalysts for water oxidation.

4.2. Significance Statement

The photoreductive dissolution of Mn oxides governs the biogeochemical cycle of Mn and the fate of organic and inorganic species associated with Mn oxides in the euphotic zones of marine and freshwater systems. Mn oxide minerals also have garnered interest as water oxidation catalysts inspired by the Mn_4CaO_4 cluster of photosystem II. However, the mechanism of water oxidation by MnO_2 and the rate limiting steps for this reaction are unknown. In this study, we couple flow-through experiments and ultrafast pump-probe optical and X-ray absorption spectroscopy to develop a photoreduction model that includes the mechanism and timescales for the initial electron transfer steps in the oxidation of water by MnO_2 .

4.3. Introduction

Manganese is a key element in environmental processes, catalytic materials, and biological systems due to its rich redox chemistry and ability to form species with a high oxidizing potential. Photochemical processes can enhance significantly the cycling of Mn between the +4, +3 and +2 valence states (Sunda and Huntsman, 1990; Armstrong, 2008; Hocking et al., 2011). Photoreduction of Mn(IV) is the first step in the reductive dissolution of birnessite minerals in the euphotic zone of marine and lacustrine environments (Sunda and Huntsman, 1994; Morgan, 2000; Spiro et al., 2010). This process couples the biogeochemical cycle of Mn to the redox cycling of carbon and trace metals associated with Mn oxide phases. In addition, the greater role of Mn(IV) photoreduction relative to microbial Mn(II) oxidation leads to the predominance of dissolved over particulate Mn in the photic zone of natural waters (Sunda and Huntsman, 1990). Thermodynamic calculations predict that direct photoexcitation of Mn oxides in water by visible light will lead to net metal reduction over a wide range of environmentally-relevant pH values (Sherman, 2005). However, experimental evidence of direct photoexcitation of MnO_2 and subsequent photoreduction of Mn(IV) in the absence of organic electron donors is currently lacking. Experimental studies on the photochemical cycling of Mn have incorporated natural organic ligands that can enhance metal reduction via multiple pathways (Waite et al., 1988; Sunda and Huntsman, 1994; Kim et al., 2012). These studies have identified aqueous Mn(II) as a reaction end product but have not investigated the fate of Mn(III) in the dissolution process, even though Mn(III) is a necessary intermediate in

the reduction of Mn(IV) to Mn(II) (Luther III, 2005) and an important component of environmental systems (Madison et al., 2013).

The photochemistry of Mn also enables solar-energy harvesting (Sakai et al., 2005) and water-oxidation catalysis in synthetic and biological systems (Armstrong, 2008; Kolling et al., 2012; Johnson et al., 2013). Mn-based cluster compounds (Hsu et al., 2012; Wiechen et al., 2012) and disordered birnessite nanoparticles (Hocking et al., 2011) can exhibit analogous reactivity to the water-oxidizing center of photosystem II. Metal reduction is a key step in water oxidation using Mn oxide catalysts (Hocking et al., 2011; Wiechen et al., 2012; Birkner et al., 2013; Robinson et al., 2013) with evidence that Mn(III) plays an important role in O₂ generation (Takashima et al., 2012). However, no information on the intrinsic kinetics or efficiency of Mn(IV) reduction has been reported to date. Furthermore, the structural and chemical constraints on the mechanism of Mn photoreduction are not known for any Mn phase (Birkner et al., 2013; Robinson et al., 2013), although a recent study of MnO₂-based water oxidation showed that the substitution of Na with Ca in the interlayer of MnO₂ greatly enhances reactivity (Wiechen et al., 2012). The mineralogy literature suggests that the interlayer cations which balance the excess charge in the MnO₂ sheet may influence its photoreactivity because the interlayer cations in birnessite are known to bind water molecules to the neighboring MnO₂ octahedral sheets via hydrogen bonding, with the strength of the interactions dependent on the cation valence (Drits et al., 1998; Johnson and Post, 2006; Cygan et al., 2012). However, the specific role of Ca in the photoreduction process is unknown (Wiechen et al., 2012).

The current work combines laboratory-based experiments and ultrafast pump-probe spectroscopy to investigate the photoreduction of δ -MnO₂, a fully oxidized synthetic analog of natural birnessites, which is comprised of randomly stacked MnO₂ nanosheets that extend only a few nanometers in the *ab* plane. The first objective was to measure the photoreduction efficiency of δ -MnO₂ in flow-through experiments by 400-nm illumination of aqueous suspensions of δ -MnO₂, with Na (Na-MnO₂) or Ca (Ca-MnO₂) as the interlayer cation. The second objective was to elucidate the mechanism of photoreduction by following the coupled changes in Mn valence and coordination that follow photon absorption over picosecond to microsecond timescales using time-resolved optical (Gilbert et al., 2013) and X-ray (Katz et

al., 2012) absorption spectroscopy. Pyrophosphate was used in the flow-through experiments to quantitate Mn(III) but was not added during spectroscopic experiments because the time-scale for Mn(III) production could be determined directly from the transient X-ray absorption data.

4.4. Materials and methods

ACS-grade Chemicals were purchased from Sigma-Aldrich or Merck; Nafion was purchased from Fuel Cell Earth LLC (Clearwater, FL, USA). All solutions were prepared with ultrapure water ($18 \text{ M}\Omega \cdot \text{cm}$). The $\delta\text{-MnO}_2$ phase used in flow-through photodissolution experiments and pump-probe experiments was synthesized according to Villalobos et al. (2003), and was comparable to the mineral B2 described in **Chapter 3**. Synthesis and characterization of the mineral phase are described in the **SI text (ANNEX 4)**. All experiments were carried out at ambient temperature, on suspensions under aerated conditions or purged with $\text{N}_{2(\text{g})}$ or $\text{He}_{2(\text{g})}$.

Efficiency of MnO_2 photoreduction. Flow-through experiments were carried out to verify whether $\delta\text{-MnO}_2$ photoreduction by band gap excitation generated reduced Mn ions irreversibly and to measure the rates and efficiency of the process. A preliminary plan to sensitize the oxides with Safranin T, an organic dye used for biological staining, in order to investigate the ligand to metal charge transfer kinetics similarly as described Gilbert et al. (2013) failed. This was due to rapid degradation of the dye without irradiation upon sorption to the oxide in preliminary studies. We prepared oxide suspensions containing $500 \mu\text{M}$ Mn and 25 mM sodium pyrophosphate (PP) to trap Mn(III) with a final pH of 6.5 (no pH-adjustment was required). The Ca- MnO_2 suspensions were prepared by equilibrating the oxide with $\text{CaCl}_{2(\text{aq})}$ in a 3:1 molar ratio. All suspensions were equilibrated in the dark for 3 days prior to irradiation. The suspensions were then divided into 2 aliquots: one was used as a dark control and the second was recirculated through a flow-through quartz cuvette. Irradiation for 72 hours was provided by an array of three 1-W light emitting diodes (LEDs) at 400 nm (3.1 eV), close to the maximum UV-vis absorbance of a Na- MnO_2 suspension in water (**Figure S5a**). The photoreactor was screened from ambient light.

Every 24 hours a sample aliquot was collected for ICP-OES measurement of $[\text{Mn}_{\text{TOT}}]$ after digestion with 0.05 M $\text{H}_2\text{C}_2\text{O}_4$ and 3% HNO_3 and another was filtered through a 0.2 μm polyethersulfone syringe filter for ICP-OES measurement of $[\text{Mn}_{(\text{aq})}]$ and $[\text{Mn(III)-PP}]$ quantification by UV-vis spectrophotometry ($\epsilon_{254 \text{ nm}} = 6562 \text{ L mol}^{-1} \text{ cm}^{-1}$) with 1 cm path length quartz cuvettes using a 25 mM PP solution as a blank. Measurements of $[\text{Mn}_{(\text{aq})}]$ and $[\text{Mn(III)-PP}]$ were within 10 %, with concentrations ranging from 10 to 50 μM . Experiments were conducted in duplicate; suspension pH was 6.5 ± 0.2 before and after irradiation.

Complementary experiments were carried out to confirm that PP did not influence Mn photoreduction. Experiments were conducted as described above but in the absence of PP and with Na-MnO₂ supplemented with 10 mM NaCl. After 0, 24, 48 and 72 hours of irradiation, 10 mL sample aliquots were collected, mixed with 2 mL of a 100 mM PP stock solution (pH 6.5) and placed on an end-to-end shaker for 24 hours in the dark. Measurements of $[\text{Mn}_{\text{TOT}}]$, $[\text{Mn}_{(\text{aq})}]$ and $[\text{Mn(III)-PP}_{(\text{aq})}]$ were made as described above; suspension pH was 6.5 ± 0.2 before and after irradiation.

The rate of Mn(III) production was determined from linear regression of Mn(III)-PP against time, after correction for any Mn(III) released in dark control experiments. We then calculated the apparent quantum yield for Mn(III) generation, which is defined as the amount of photoproduced Mn(III) per photon absorbed by the MnO₂ suspension (**ANNEX 1**). To calculate the number of photons absorbed, we measured the photon flux to the photoreactor by chemical actinometry using potassium ferrioxalate and then scaled the photon flux to the ratio of the absorbance of MnO₂ to ferrioxalate (**Chapter 2**).

Optical transient absorption spectroscopy. Optical transient absorption (TA) spectroscopy can be used to follow excited-state valence electron dynamics in semiconducting metal oxides (Gilbert et al., 2013). Optical TA experiments were carried out on a HELIOS femtosecond transient absorption spectrometer and on an EOS sub-nanosecond transient absorption spectrometer from Ultrafast systems installed at the Molecular Foundry, Lawrence Berkeley National Laboratory, Berkeley, USA. The laser source for both instruments was a Coherent Libra Amplified Femtosecond Laser System operating at 1 kHz with 45 fs pulse duration. The laser output was split, one arm passing through a Coherent OPerA optical parametric amplifier (OPA) to produce pump pulses at 400 nm, the other arm delivered to the

transient absorption system where a white-light probe pulse was generated in a sapphire plate or by a fiber white light source (Leukos-STM) for the HELIOS and EOS spectrometers, respectively. The intensity of the pump beam was measured to be $800 \text{ nJ pulse}^{-1}$. Time delay was provided by a mechanical delay stage on the HELIOS setup and by instrument electronics on the EOS setup. Spectra were collected between 335 and 900 nm.

Samples of Ca-MnO_2 and Na-MnO_2 were either kept in their original aqueous suspension or resuspended in an aqueous solution of 1.5% Nafion in 3% isopropanol. The Nafion polymer reduced particle aggregation and there is no evidence that it influences the photochemical behavior of birnessite-based photocatalysts (Hocking et al., 2011; Young et al., 2011). Furthermore, the comparison of TA data of Na-MnO_2 in water *vs* in an aqueous Nafion solution showed no detectable differences on pico- to nanosecond timescales (**Figure S9**). The 3% isopropanol was evaporated in air from the Nafion solution for 12 h before starting the measurements to ensure complete isopropanol evaporation. Additional Na-MnO_2 samples were re-suspended in 0.1 M terephthalic acid (TPA), a hydroxyl radical trap (Barreto et al., 1995), and measured on the EOS setup. The samples were measured in 1 mm path length quartz cuvettes and stirred with a magnetic stir bar or recirculated in a flow-through cuvette. The optimum MnO_2 concentration for TA measurements ranged from 3 to 6 mM on a Mn molar basis, corresponding to an optical density (OD) at 400 nm between 0.8 and 1.6 absorption units on 0.5 mm path length quartz cuvettes. Spectra were collected from -10 ps to 8 ns (relative to laser pulse) on the HELIOS system and from 1 ns to 50 μs on the EOS system. Custom user routines developed in the Igor Pro software (WaveMetrics Inc., Lake Oswego, OR, USA) were used to process the data, including correction of the time dependent frequency modulation of the laser (laser chirp) on the signal to within ~ 0.15 ps and to extract transient kinetic data at 354 nm and 550 nm from 2D plots of spectra versus time. Igor Pro was also used to fit first-order exponential decay kinetics to the extracted data. The decay kinetics for all samples were adequately reproduced by fitting two exponential time constants (**SI text – ANNEX 4**).

Light-initiated time-resolved X-ray absorption spectroscopy. LITR-XAS excites core electrons and yields information on the oxidation state and local bonding environment of the probed atoms following light excitation (Katz et al., 2012). LITR-XAS experiments were carried out at Beamline 6.0.1 at the Advanced Light Source (ALS, Berkeley, USA). At this

beamline, the X-ray beam pulses are isolated with an X-ray chopper and combined with the output of a femtosecond Ti:Sapphire laser system with a power output of 800 mW measured at the sample position. The X-ray energy was scanned across the Mn K-edge (6530 eV to 6595 eV). Ground state and transient X-ray absorption spectra were collected in fluorescence mode with an avalanche photodiode (APD) fitted with Soller slits and a Cr filter. The 400 nm laser pulse was obtained by converting the 800 nm output from the 4 kHz Ti:Sapphire laser system with an optical parametric amplifier (OPA). The laser pulse was synchronized to a single electron bunch by locking the 62.5 MHz repetition rate of the laser system oscillator to the 499.64 MHz of the synchrotron's radiofrequency cavity to an accuracy of less than 20 ps. The full width at half maximum (FWHM) of the laser and X-ray pulses were 0.1 ps and 70 ps, respectively. Finally, the time zero delay between X-ray and laser pulses was determined using an iron(II) tris(2,2'-bipyridine) solution, which exhibits distinct changes in absorption at the Fe K-edge upon laser excitation.

The laser and X-ray beams intersected the sample in a closed He_{2(g)} purged chamber. Samples were recirculated from a bottle on a stir plate through a nozzle forming a 600- μ m diameter liquid jet. The size of the X-ray beam on the sample was 60 by 60 μ m. To begin an experiment, 250 mL suspensions of approximately 10 mM Ca- and Na-MnO₂ were prepared. Before data acquisition, the chamber and sample were purged with He_{2(g)}. Each experimental condition was repeated in duplicate on suspensions recirculated for up to 4 hours to obtain transient and kinetic data. For transient X-ray absorption experiments, spectra were collected at a fixed time delay and the monochromator was scanned from 40 eV below to 70 eV above the Mn K-edge (6539 eV). The transient spectra were 3-point smoothed for plotting. Kinetic data were acquired by setting the monochromator at a fixed energy position and varying the time delay between laser and X-ray pulses. In both acquisition modes, data were collected before and after laser irradiation at the chosen time delay in order to extract ground state and excited state spectra. Following each LITR-XAS experiment, the samples were retained for analysis by X-ray diffraction. To assess the possibility of X-ray radiation damage, a conservative Mn:photon ratio was calculated. We estimated that 10¹⁴ X-ray photons are delivered to the sample over the 4 hour timespan of the experiment, compared to approximately 10²¹ Mn atoms in the sample (**SI text**). The Mn:photon ratio was thus estimated to be 10⁶:1, strongly suggesting that X-ray beam damage is negligible.

4.5. Results

Efficiency of MnO₂ photoreduction. Flow-through experiments were carried out to evaluate the irreversibility of MnO₂ photoreduction, to identify the reduced Mn species and to quantify the efficiency of the process. The irradiation of 500 μM δ-MnO₂ suspensions at pH 6.5 ± 0.2 in 1 cm path length flow-through cuvettes showed irreversible Mn(III) generation upon 400 nm irradiation under a photon flux of 0.77 μE s⁻¹, which is comparable to that of sunlight between 400 and 600 nm (calculations in SI text). We measured the steady formation of Mn(III) at a rate of 2.20 ± 0.27 μmol Mn(III) day⁻¹ (95% confidence interval) in Ca-MnO₂ suspensions and 1.50 ± 0.19 μmol Mn(III) day⁻¹ in Na-MnO₂ suspensions containing pyrophosphate (PP) as a Mn(III) trapping agent (**Figure S1**). These rates were corrected for any release of Mn(III) in dark controls (0.2 – 0.9 μmol Mn(III) day⁻¹). The non-zero dark release is attributed to the extraction of residual Mn(III) not detectable by the method used to determine average Mn oxidation number (AMON). Apparent quantum yields of 8.2 ± 0.1 × 10⁻⁴ and 3.1 ± 0.3 × 10⁻⁴ (95% confidence interval) were calculated for Ca-MnO₂ and Na-MnO₂, respectively. Similar rates measured in suspensions where PP was added after irradiation (**Figure S1**) indicate that PP does not influence photoreduction. Further evidence that PP and Mn(III)-PP do not influence Mn photoreduction comes from their UV-vis spectra, which show no absorption at 400 nm (Wang and Stone, 2008).

Optical transient absorption spectroscopy. **Figures 1 and 2** present optical transient absorption (TA) spectra and kinetics, respectively, for Ca-MnO₂ acquired at subpicosecond to microsecond timescales. Equivalent data for Na-MnO₂ are presented in **Figures S2 – S3**. All samples were re-suspended in 1.5% Nafion to reduce particle aggregation. Following photoexcitation at 400 nm, the TA spectra acquired at a few picoseconds exhibited a broad excited-state absorption (ESA) feature with maximum intensity at 538 nm (Ca-MnO₂; **Figure 1**) or 570 nm (Na-MnO₂; **Figure S2a**). The TA spectra also showed a ground-state bleach extending from the laser wavelength to the lowest wavelength measurable (~335 nm); the bleach reflects the decrease in the population of valence band electrons that remain in the ground state. After correcting for the laser chirp, the comparison of the TA kinetics at 345 and 550 nm showed a rise in ESA intensity that was delayed relative to the prompt bleach signal. The maximum ESA intensity occurred at ~0.3 ps for Ca-MnO₂ (**Figure 2a**) and ~0.6 ps for

Na-MnO₂ (**Figure S3a**). The ESA and bleach signals decayed with similar dynamics up to ~10 ps (**Figure 2b**). The ESA then decayed completely within 1 ns but the bleach signal remained detectable on the microsecond timescale. The decay kinetics of the bleach differed for Ca- vs Na-MnO₂ (**Figure 1c**), although both samples exhibited short (sub- μ s, τ_1) and long (10 – 30 μ s, τ_2) decay timescales (**Table 1**).

Table 1: Time constants obtained from fitting the EOS data with exponential decay functions (*cf.* **Fig. S7**). A time offset of 0.047 μ s was used for all data.

	τ_1 [μ s] \pm st.dev	τ_2 [μ s] \pm st.dev	χ^2
Na-MnO₂			
water	0.36 ± 0.03	15.31 ± 0.96	11.03
TPA	0.36 ± 0.04	14.38 ± 1.32	18.68
Nafion	0.24 ± 0.02	10.14 ± 0.63	12.68
Ca-MnO₂			
Nafion	0.81 ± 0.06	27.35 ± 1.75	6.53

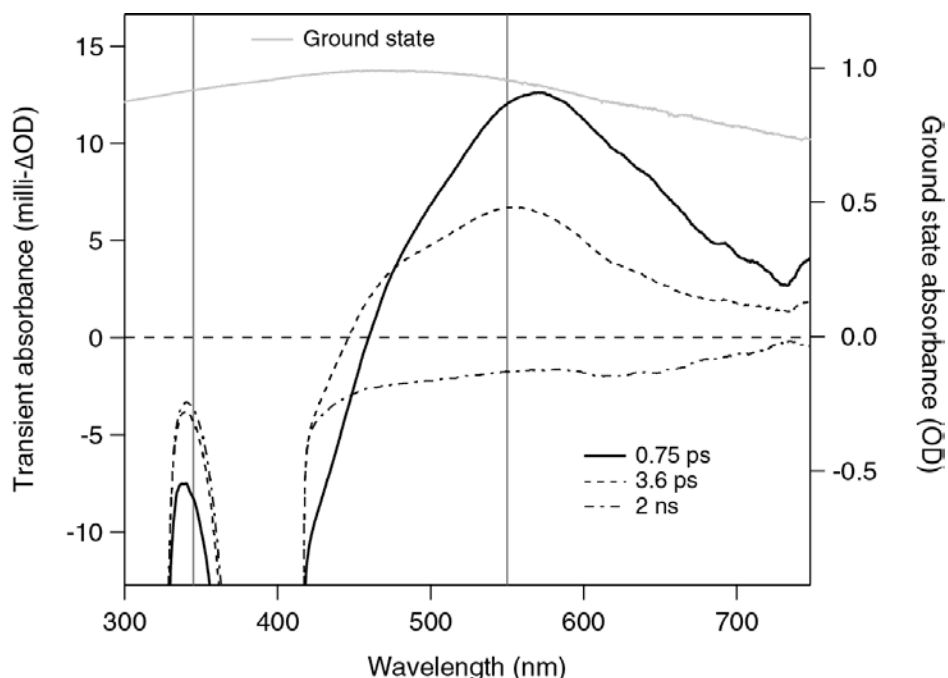


Figure 1. Optical transient absorption (TA) spectra acquired from Ca-MnO₂ in an aqueous suspension containing Nafion at 0.75 ps, 3.6 ps and 2 ns after photoexcitation at 400 nm. The TA spectra (milli- Δ OD units; left axis) are compared to the ground-state UV-vis absorption spectra (OD units; right axis). Vertical lines at 550 nm (the maximum intensity of the excited state absorption) and at 345 nm (ground-state bleach) indicate wavelengths chosen for kinetics analysis. The data from 390 – 410 nm are affected by scattering of the excitation beam. Equivalent TA data for Na-MnO₂ are given in **Figure S2a**.

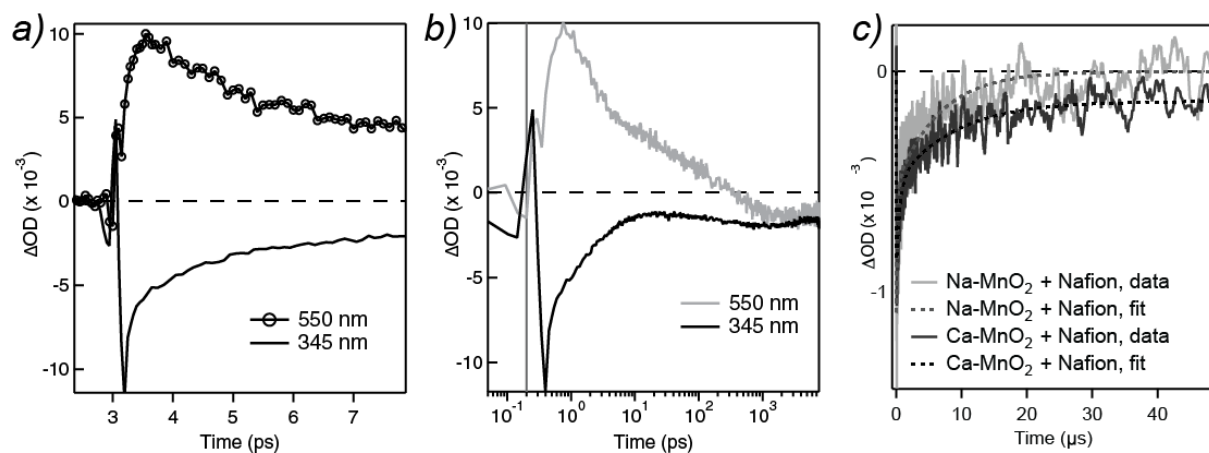


Figure 2. Summary of optical transient absorption kinetics acquired from Ca-MnO₂ in an aqueous suspension containing Nafion. (a) Transient kinetic traces show a slight delay in the onset of the excited-state absorption (ESA) at 550 nm relative to the bleach at 345 nm. (b) Decay kinetics of the ESA and bleach up to 8 ns. The time-zero was shifted by 0.2 ps to enable plotting on a logarithmic scale. Equivalent data for Na-MnO₂ are given in **Figures S3 a** and **b**. (c) Comparison between the decay kinetics of the bleach at 580 nm for Ca-MnO₂ and Na-MnO₂ in Nafion, fitted with two-component exponential decay functions.

Direct comparison of the fitted first-order decay constants for Ca-MnO₂ and Na-MnO₂ in Nafion-stabilized suspensions reveals that the recombination rates are 3-4 fold slower in the

presence of interlayer Ca. In particular, the τ_2 values indicate that the bleach returns to baseline within 50 μs for Na-MnO₂ (5 half-lives elapsed, 0.02% of initial signal remains), whereas for Ca-MnO₂ the bleach does not return to the baseline within the resolution of the experiment (2 half-lives elapsed, 8% of initial signal remains). Slightly slower decays were observed for samples prepared without Nafion, possibly indicating an effect of aggregation upon recombination rates. Slower decay could occur if recombination involved diffusion of soluble species, but this effect is impossible to explain confidently and is smaller than the influence of the interlayer cation (**SI text**). The addition of the anionic hydroxyl radical scavenger, terephthalic acid (TPA), had no detectable effect on the decay kinetics for Na-MnO₂.

Light initiated time-resolved X-ray absorption spectroscopy. Selected ground-state Mn K-edge spectra collected during a single four-hour LITR-XAS experiment with Ca-MnO₂ are displayed in **Figure 3**. The increase in the absorption intensity at 6550 eV (**Figure 3 inset**) shows a shift of the Mn K-edge to lower energies, which is consistent with a decrease in the average oxidation state of Mn (Villalobos et al., 2003). Thus, 400-nm laser excitation causes the accumulation of reduced Mn. A difference X-ray absorption (ΔXA) spectrum, obtained by subtracting the initial ground state spectrum from the three-hour ground state spectrum, is included in **Figure 3** to emphasize the irreversible change in Mn valence and bonding environment after three hours of irradiation.

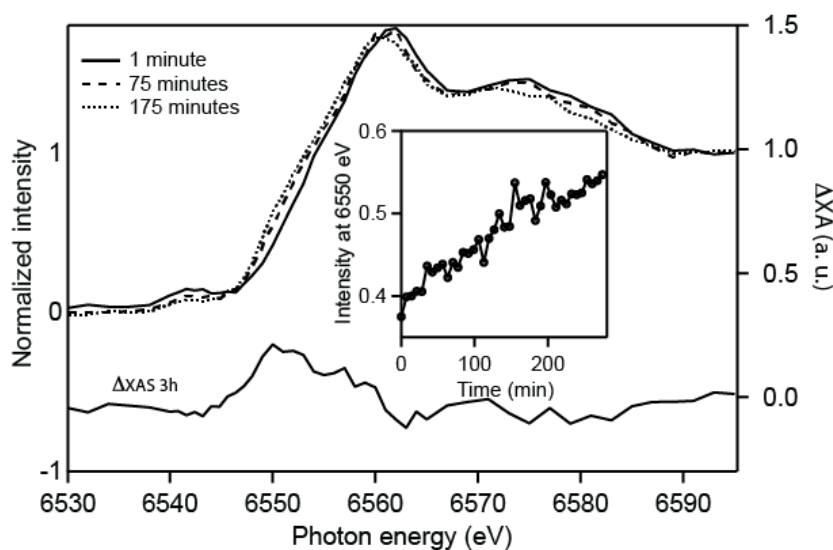


Figure 3. Ground-state Mn K-edge X-ray absorption (XA) spectra show the steady reduction of Mn in a ~ 10 mM Ca-MnO₂ suspension at pH 6.5 during a *ca.* 4-hour laser-pump/X-ray probe study. Spectra are shown for 1 minute (solid line), 19 minutes (dashed line) and 175 minutes (dotted line) after the onset of the experiment (left vertical axis). The difference (Δ XA) spectrum obtained by subtracting the spectrum at 175 minutes from the spectrum at 1 minute (right vertical axis) is included beneath the XA spectra. Inset shows the XA intensity at 6550 eV as a function of time, which indicates an increase in reduced Mn.

Transient Δ XA spectra were obtained by subtracting the ground state spectrum from the excited state spectra at delay times of up to 10 ns (**Figure 4a**). The first oscillation between 6540 and 6570 eV in the transient Δ XA spectrum at a 50 ps delay indicates a shift in the absorption edge position to lower energies that is consistent with the formation of reduced Mn (*cf.* **Figure 3**). The feature is approximately constant from 50 ps (the temporal resolution of the experiment) to 10 ns (the latest timepoint studied). As shown in **Figure 4b**, transient kinetic data at 6550 eV confirmed the prompt formation and negligible decay of the signal for reduced Mn. Within 600 ps, we observed modulations at energies above 6570 eV, the fine-structure portion of the transient Δ XA spectrum, which reflect changes in the coordination environment of Mn. Finally, the close agreement between the transient Δ XA data at 10 ns and the Δ XA data associated with permanent photoreduction at 3 hours indicates that at least a fraction of the reduced Mn species observed at 10 ns persists indefinitely.

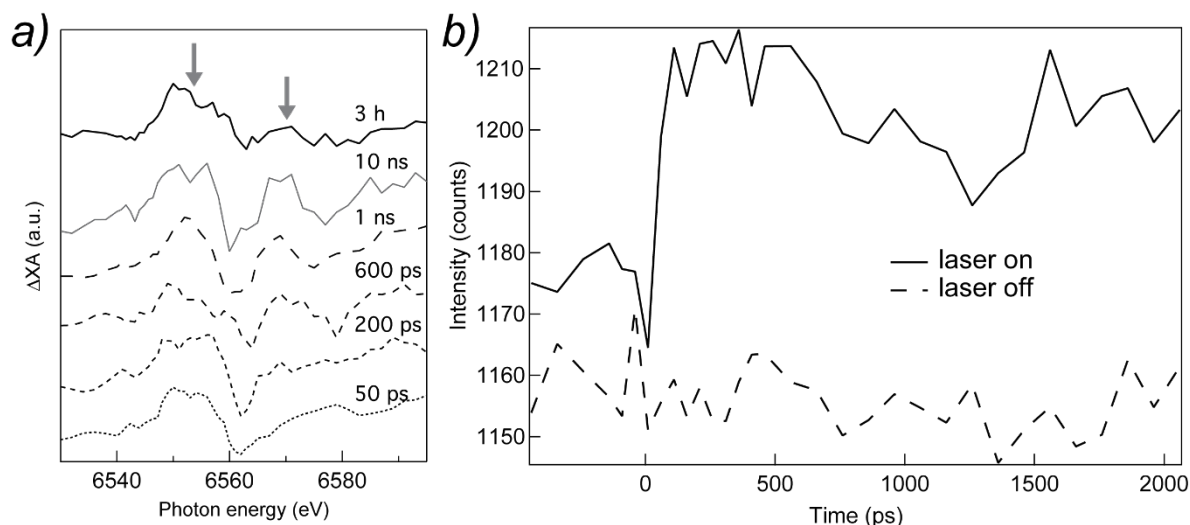


Figure 4. (a) ΔXA spectra at various delay times reveal a prompt change in the Mn oxidation state (feature at 6550 eV – first arrow) and evolution in fine structure within 1 ns (feature at 6570 eV – second arrow). The ground state ΔXA spectrum, obtained by subtracting the ground spectrum at 175 minutes from the ground spectrum at 1 minute (cf. **Figure 3**), is shown for comparison with the transient ΔXA spectra. (b) Kinetic traces of the X-ray absorption intensity at 6552 eV with (solid line) and without (dashed line) the laser pump confirm a prompt change in Mn valence and no decay within 2 ns.

The long-term effect of Mn(III) accumulation on the irradiated Mn oxide was assessed by characterization of the mineral structure. Powder X-ray diffraction (XRD) patterns acquired from samples prior to laser irradiation show broad $hk0$ peaks at 2.4 Å and 1.4 Å and no stacking peak at 7.2 Å (in d-spacing). This pattern is characteristic of δ -MnO₂ nanosheets with hexagonal sheet symmetry and fewer than three randomly stacked sheets (Villalobos et al., 2003). Following laser irradiation, the XRD patterns showed additional 001 and 002 Bragg reflections (**Figure S4**) that are consistent with increased ordered stacking of the MnO₂ sheets (Villalobos et al., 2003).

4.6. Discussion

Efficiency of Mn(IV) oxide photoreduction. Our flow-through experiments show that the irreversible photoreduction of δ -MnO₂ to form Mn(III) occurs readily under environmentally relevant conditions in the absence of any electron donor other than water. In addition, our measurements indicate no production of Mn(II). The apparent quantum yield of the process at pH 6.5 is up to two orders of magnitude larger than the quantum yield measured for γ -Fe₂O₃(s) at pH 3.0, $\sim 10^{-5}$ (Litter and Blesa, 1992), and comparable to the value measured for γ -FeOOH(s) at pH 3.0, $\sim 10^{-3}$ (Borer et al., 2009). Furthermore, Fe photoreduction in water

has only been observed at pH values below 5. These results emphasize the importance of photoreduction in the redox cycling of Mn oxides relative to Fe oxides and support the thermodynamic calculations presented by Sherman (2005), which indicate that photoreduction may occur at higher pH values for Mn oxides than for Fe oxides.

Environmental Mn cycling is frequently coupled to the oxidation of dissolved organic matter (DOM). Manganese oxide photodissolution in the presence of 10 to 40 mg/L DOM has been reported to have a five to ten-times greater efficiency (Waite et al., 1988) than measured here for MnO₂ photoreduction without organics. Dissolved organic matter can increase the accumulation of reduced Mn by acting as the chromophore that either initiates electron transfer to the mineral (Waite et al., 1988) or photolyzes to generate reactive oxygen species (Sunda and Huntsman, 1994); by acting as an electron donor to the photoexcited mineral; or by providing ligands that can complex intermediate Mn³⁺ as Mn(III)_(aq) species (Madison et al., 2013). Due to the optical properties of DOM, the first mechanism is only important under UV-light, which is a minor component of the sun's irradiance spectrum on the Earth's surface and has a lower penetration depth (up to ~25m) in natural waters than visible wavelengths (~100m) (Smith and Baker, 1981). The complexation of reduced manganese by DOM is likely to occur independently from the photoreduction mechanism. Thus, our results indicate that Mn photoreduction in which water serves as electron donor must be a significant contributor to any overall environmental rate.

Manganese redox dynamics. We used the time-resolved optical and X-ray data to construct a model for the photoexcitation and evolution of Mn(III) states in δ -MnO₂ as visualized in **Figure 5**.

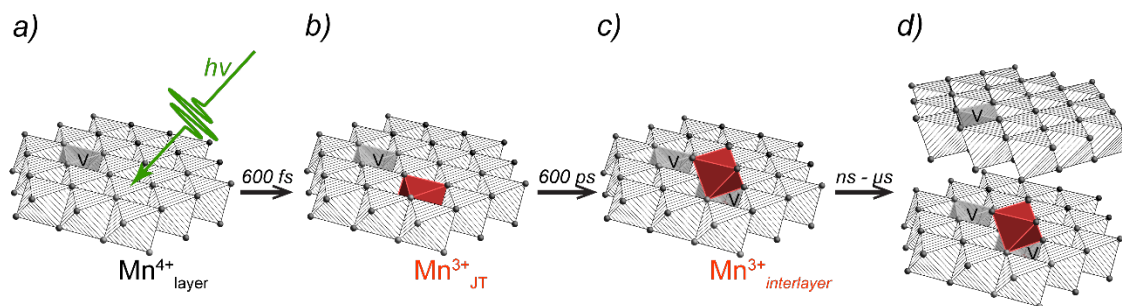


Figure 5. Proposed model for the evolution of metal redox chemistry during δ -MnO₂ photoreduction. (a) Absorption of a photon ($h\nu$) by a single Mn(IV) oxide nanosheet that includes metal vacancy sites (V); (b) Formation within 600 fs of a Jahn-Teller distorted Mn(III) state within the nanosheet (dark red octahedron); (c) Migration within 1 ns of Mn(III) from the nanosheet to an adsorption site above a new vacancy; (d) Increased nanosheet stacking due to increased compensation of sheet negative charge by interlayer Mn(III). Water molecules are omitted for clarity.

A transient Jahn-Teller distorted Mn(III) intermediate forms in the nanosheet. We interpret the transient optical ESA that appears within 0.3 – 0.6 ps, and that has a lifetime less than 1 ns, as a transient intermediate Mn(III) state that is formed by a ligand-to-metal charge-transfer excitation that excites an oxygen-centered valence electron into the metal $3d$ state (Sherman, 2005). This interpretation requires justification because transient electronic excitations observed in TA spectroscopy of metal oxides could be associated with either electrons (*e.g.*, the transitions of electrons promoted to the conduction band) or holes (*i.e.*, new excitations within the valence band). For example, band-gap excitation of hematite (α -Fe₂O₃) generates a prompt optical ESA centered at 580 nm attributed to hole excitations based on UV-vis spectra of a thin-film hematite electrode under oxidizing *vs* reducing conditions (Barroso et al., 2013). In the present case, however, the delayed onset of the ESA is consistent with electronic relaxation into a polaronic state, as observed for photoexcitation of manganites (Wu et al., 2009). Polaron formation would be expected for the creation of a Mn(III) state, for which Jahn-Teller (JT) distortion of the octahedron can lower the ground state energy by adopting high spin d^4 electron configuration and splitting the e_g and t_{2g} orbitals (Burns, 1993). In this depiction, the ESA is caused by low-energy excitations of the extra electron localized in the JT state. Additionally, UV-vis spectra from well characterized MnO_x phases show that Mn(III) located in the MnO₂ sheets confers absorption features in the visible range between 400 and 600 nm (**Figure S5**).

The line shape of the ESA reported here closely matches a feature in the UV-vis spectrum reported for a birnessite anode poised at sufficiently positive potentials to oxidize water (Takashima et al., 2012). Takashima et al. (2012) assigned the optical feature between 400 – 600 nm to adsorbed Mn(III) based on pyrophosphate extractions. However, any Mn(III) extracted by pyrophosphate after the electrochemical oxidation of water reflects only the final Mn(III) state. Our kinetic measurements demonstrate that the visible ESA is due to a transient state.

A long-lived interlayer Mn(III) adsorbate between the nanosheets. We propose that the loss of the optical ESA signal (*i.e.*, the JT state) is caused by two processes occurring on different timescales. Within the first 10 ps, the ESA decay and that of the bleach were closely coupled, indicating electron-hole recombination. Further decay of the ESA signal, however, was not matched by further loss of the bleach. The LITR-XAS also showed that within ~600 ps there was a change in the Mn bonding environment but no loss of the reduced Mn state. We explain these trends by the displacement of Mn(III) from the nanosheet layer into the hydrated interlayer region, with the formation of a vacancy site beneath (**Figure 5c**). Prior studies have established that Mn(III) cations can reside stably within the interlayer of birnessite nanosheets to reduce the sheet steric strain (Gaillot et al., 2003; Manceau et al., 2013). The JT distortion at the Mn(III) site could drive its migration into the interlayer, where it can act as an adsorbed cation that enhances the stacking of the negatively-charged sheets (**Figure 5d**). In addition, JT distorted Mn(III) sites have been reported as key species for water oxidation (Robinson et al., 2013). The migration of JT distorted Mn(III) from the MnO₂ sheet into the interlayer and change in Mn(III) bonding environment may decrease the overall reactivity of the material for multi-electron water oxidation. Thus, our finding has implications regarding the mechanistic constraints on Mn oxide photocatalysis. The formation of new vacancy sites likely also alters the optical absorption properties of the modified nanosheet (Kwon et al., 2009). Our model, however, requires that the putative interlayer Mn(III) ion lack an optical absorption signature in the 335 – 800 nm range. This could not be verified through published studies of the UV-vis absorption spectra of Mn³⁺ because this species is unstable in aqueous solution (Wang and Stone, 2008; Madison et al., 2013).

Hole dynamics: recombination vs. water oxidation chemistry. Photoexcitation of δ -MnO₂ and the generation of Mn(III) must be accompanied by the formation of valence band holes. Hole states in transition metal oxides are typically localized at oxygen sites but holes that form close to surface sites may participate in reactions with water, including steps in the four-electron oxygen evolution reaction (OER) (Tang et al., 2008) or with aqueous ions such as Cl⁻ (Grätzel et al., 1985).

The bleach signal in the TA data shows complete return to the ground state after 50 μ s or longer, indicating that most of the hole states are able to recombine with the photoexcited electrons in Mn(III) even after migration of the metal ion into the interlayer. Although we proved that net photoreduction occurs, the apparent quantum yield is too low for the irreversible fraction to be detectable above the statistical noise in the TA data. Recombination may involve exclusively solid-phase species, or the formation of chemical intermediates. Borer et al. (2009) used a hydroxyl radical scavenger to demonstrate the generation of hydroxyl radicals (OH[•]) through hole reaction with surface hydroxyls on γ -FeOOH, but in that case only an anionic scavenger was able to react with the net positively charged surface of iron oxyhydroxides. In the present case, we were unable to identify a cationic hydroxyl scavenger that was stable against dark reaction with Mn(IV), and the anionic TPA may have been unable to interact with the net negatively charged δ -MnO₂ surface. Nevertheless, surface bound hydroxyl groups on birnessite have been identified in a synthetic Mn(III)-bearing microcrystalline birnessite phase from the interpretation of thermogravimetric data (Gaillot et al., 2003). Reactions between OH[•] species could yield H₂O₂ or other ROS that could oxidize Mn(III) back to Mn(IV) and thus reduce the net quantum yield of direct photoreduction by band gap excitations. Our efforts are currently dedicated to identifying these radical species, which can also enhance microbial Mn oxidation (Hansel et al., 2012) and induce cellular oxidative stress.

Influence of interlayer cation on MnO₂ photoreduction. We observed that the interlayer cations, which balance the negative layer charge, influence the optical properties and photochemistry of layer-type MnO₂, as observed previously in water-oxidation studies (Wiechen et al., 2012). The slower microsecond timescale kinetics for Ca- vs Na-MnO₂ and greater apparent quantum yield, which cannot be explained by aggregation (**SI text – ANNEX**

4), suggest a catalytic role for this ion that reduces the rate at which interlayer Mn(III) species and photoexcited hole states can recombine. Because Ca^{2+} has a greater hydration enthalpy (Cygan et al., 2012) and longer water-exchange constants than Na^+ (10^8 s^{-1} vs 10^9 s^{-1}) (Stumm and Morgan, 1996), its catalytic role may reduce the mobility of water and other species in the interlayer. However, Ca also caused red-shifts in both ground-state and transient UV-vis spectra (**Figures S3b** and **S6a**), indicating that this ion has significant chemical interactions with the Mn oxide nanosheets. Further work will be required to fully determine the role of Ca, but the model proposed here provides a basis for future studies.

4.7. Environmental implications

This work provides new insight into the mechanism, rates and chemical controls on the photoreduction of fully-oxidized Mn oxide phases that are the initial products of biological manganese oxidation (Spiro et al., 2010) and that may have been precursors to biological water-oxidation catalysts (Johnson et al., 2013). The evidence we provide for $\delta\text{-MnO}_2$ photoreduction in the absence of organic electron donors establishes this pathway as an important component of the Mn cycle. That this reaction occurs at 400 nm indicates that it is important at all depths of the water column to which visible light penetrates, including depths where dissolved organic matter is not photoactive. The broad absorbance of MnO_2 suggests that photoreduction can occur across a wide spectrum of solar irradiation, although further experiments will be required to establish the wavelength dependence. Photoreduction creates Mn(III) states that are stabilized by adsorption at interlayer sites and increase nanosheet stacking. Our results also suggest that Mn(IV) photoreduction in sunlit environments may cause initial biogenic Mn(IV) oxides to transform to a phase with varying amounts of Mn(III) (Spiro et al., 2010). We cannot generalize our conclusions to the many other phases of birnessites that can be found in nature, but we anticipate that photochemical transformations of these phases will retain similar mechanistic aspects, although the net rates may be influenced by Mn(III) content.

4.8. Acknowledgements

We thank Drs. M. Hertlein and T. E. Glover for assistance with the X-ray measurements, and Drs. K. Sand and T. Adatte for the acquisition of high energy X-ray

scattering data and XRD patterns, respectively, and three anonymous reviewers for their valuable comments. F.F.M. and J.P. acknowledge support from the Swiss National Science Foundation (proposal No. 200021_143742) and a grant from the Sandoz Family Foundation. B.G. was supported by the Director, Office of Science, Office of Basic Energy Sciences, of the U.S. Department of Energy (BES-DOE) under Contract No. DE-AC02-05CH11231. Research at the Molecular Foundry and the Advanced Light Source was supported by BES-DOE under Contract No. DE-AC02-05CH11231. PDF data were acquired at the Advanced Photon Source, operated for BES-DOE by Argonne National Laboratory under Contract No. DE-AC02-06CH11357.

4.9. References

- Armstrong, F.A., **2008**. Why did Nature choose manganese to make oxygen? *Philos Trans R Soc Lond B Biol Sci* 363, 1263-1270; discussion 1270.
- Barreto, J.C., Smith, G.S., Strobel, N.H., McQuillin, P.A., Miller, T.A., **1995**. Terephthalic acid: a dosimeter for the detection of hydroxyl radicals in vitro. *Life Sci* 56, PL89-96.
- Barroso, M., Pendlebury, S.R., Cowan, A.J., Durrant, J.R., **2013**. Charge carrier trapping, recombination and transfer in hematite (α -Fe₂O₃) water splitting photoanodes. *Chem Sci* 4, 2724-2734.
- Birkner, N., Nayeri, S., Pashaei, B., Najafpour, M.M., Casey, W.H., Navrotsky, A., **2013**. Energetic basis of catalytic activity of layered nanophase calcium manganese oxides for water oxidation. *Proc Natl Acad Sci U S A* 110, 8801-8806.
- Borer, P., Sulzberger, B., Hug, S.J., Kraemer, S.M., Kretzschmar, R., **2009**. Photoreductive dissolution of iron(III) (hydr)oxides in the absence and presence of organic ligands: experimental studies and kinetic modeling. *Environ Sci Technol* 43, 1864-1870.
- Burns, R.G., **1993**. Mineralogical applications of crystal field theory, Second ed. *Cambridge University Press*, Cambridge.
- Cygan, R.T., Post, J.E., Heaney, P.J., Kubicki, J.D., **2012**. Molecular models of birnessite and related hydrated layered minerals. *Am Mineral* 97, 1505-1514.
- Drits, V.A., Lanson, B., Gorshkov, A.I., Manceau, A., **1998**. Substructure and superstructure of four-layer Ca-exchanged birnessite. *Am Mineral* 83, 97-118.
- Gaillot, A.C., Flot, D., Drits, V.A., Manceau, A., Burghammer, M., Lanson, B., **2003**. Structure of Synthetic K-rich Birnessite Obtained by High-Temperature Decomposition of KMnO₄. I. Two-Layer Polytype from 800 °C Experiment. *Chem Mater* 15, 4666-4678.
- Gilbert, B., Katz, J.E., Huse, N., Zhang, X., Frandsen, C., Falcone, R.W., Waychunas, G.A., **2013**. Ultrafast electron and energy transfer in dye-sensitized iron oxide and oxyhydroxide nanoparticles. *Phys Chem Chem Phys* 15, 17303-17313.
- Grätzel, M., Kiwi, J., Morrison, C.L., Davidson, R.S., Tseung, A.C., **1985**. Visible-light-induced photodissolution of α -Fe₂O₃ powder in the presence of chloride anions. *J Chem Soc Farad T* 1 81, 1883-1890.

CHAPTER 4

- Hansel, C.M., Zeiner, C.A., Santelli, C.M., Webb, S.M., **2012**. Mn(II) oxidation by an ascomycete fungus is linked to superoxide production during asexual reproduction. *Proc Natl Acad Sci U S A* 109, 12621-12625.
- Hocking, R.K., Brimblecombe, R., Chang, L.Y., Singh, A., Cheah, M.H., Glover, C., Casey, W.H., Spiccia, L., **2011**. Water-oxidation catalysis by manganese in a geochemical-like cycle. *Nat Chem* 3, 461-466.
- Hsu, Y.K., Chen, Y.C., Lin, Y.G., Chen, L.C., Chen, K.H., **2012**. Birnessite-type manganese oxides nanosheets with hole acceptor assisted photoelectrochemical activity in response to visible light. *J Mater Chem* 22, 2733-2739.
- Johnson, E.A., Post, J.E., **2006**. Water in the interlayer region of birnessite: Importance in cation exchange and structural stability. *Am Mineral* 91, 609-618.
- Johnson, J.E., Webb, S.M., Thomas, K., Ono, S., Kirschvink, J.L., Fischer, W.W., **2013**. Manganese-oxidizing photosynthesis before the rise of cyanobacteria. *Proc Natl Acad Sci U S A* 110, 11238-11243.
- Katz, J.E., Zhang, X.Y., Attenkofer, K., Chapman, K.W., Frandsen, C., Zarzycki, P., Rosso, K.M., Falcone, R.W., Waychunas, G.A., Gilbert, B., **2012**. Electron Small Polarons and Their Mobility in Iron (Oxyhydr)oxide Nanoparticles. *Science* 337, 1200-1203.
- Kim, K., Yoon, H.I., Choi, W., **2012**. Enhanced dissolution of manganese oxide in ice compared to aqueous phase under illuminated and dark conditions. *Environ Sci Technol* 46, 13160-13166.
- Kolling, D.R., Cox, N., Ananyev, G.M., Pace, R.J., Dismukes, G.C., **2012**. What Are the Oxidation States of Manganese Required To Catalyze Photosynthetic Water Oxidation? *Biophys J* 103, 313-322.
- Kwon, K.D., Refson, K., Sposito, G., **2009**. On the role of Mn(IV) vacancies in the photoreductive dissolution of hexagonal birnessite. *Geochim Cosmochim Acta* 73, 4142-4150.
- Litter, M.I., Blesa, M.A., **1992**. Photodissolution of Iron-Oxides .4. A Comparative-Study on the Photodissolution of Hematite, Magnetite, and Maghemite in Edta Media. *Can J Chem* 70, 2502-2510.
- Luther III, G.W., **2005**. Manganese(II) oxidation and Mn(IV) reduction in the environment - Two one-electron transfer steps versus a single two-electron step. *Geomicrobiol J* 22, 195-203.
- Madison, A.S., Tebo, B.M., Mucci, A., Sundby, B., Luther, G.W., 3rd, **2013**. Abundant porewater Mn(III) is a major component of the sedimentary redox system. *Science* 341, 875-878.
- Manceau, A., Marcus, M.A., Grangeon, S., Lanson, M., Lanson, B., Gaillot, A.C., Skanthakumar, S., Soderholm, L., **2013**. Short-range and long-range order of phyllo-manganate nanoparticles determined using high-energy X-ray scattering. *J Appl Crystallogr* 46, 193-209.
- Morgan, J.J., **2000**. Manganese in natural waters and earth's crust: its availability to organisms. *Met Ions Biol Syst* 37, 1-34.
- Robinson, D.M., Go, Y.B., Mui, M., Gardner, G., Zhang, Z., Mastrogiovanni, D., Garfunkel, E., Li, J., Greenblatt, M., Dismukes, G.C., **2013**. Photochemical Water Oxidation by Crystalline Polymorphs of Manganese Oxides: Structural Requirements for Catalysis. *J Am Chem Soc* 135, 3494-3501.

- Sakai, N., Ebina, Y., Takada, K., Sasaki, T., **2005**. Photocurrent generation from semiconducting manganese oxide nanosheets in response to visible light. *J Phys Chem B* 109, 9651-9655.
- Sherman, D.M., **2005**. Electronic structures of iron(III) and manganese(IV) (hydr)oxide minerals: Thermodynamics of photochemical reductive dissolution in aquatic environments. *Geochim Cosmochim Acta* 69, 3249-3255.
- Smith, R.C., Baker, K.S., **1981**. Optical-Properties of the Clearest Natural-Waters (200-800 Nm). *Appl Optics* 20, 177-184.
- Spiro, T.G., Bargar, J.R., Sposito, G., Tebo, B.M., **2010**. Bacteriogenic Manganese Oxides. *Accounts Chem Res* 43, 2-9.
- Stumm, W., Morgan, J.J., **1996**. Aquatic chemistry: chemical equilibria and rates in natural waters. *Wiley*.
- Sunda, W.G., Huntsman, S.A., **1990**. Diel Cycles in Microbial Manganese Oxidation and Manganese Redox Speciation in Coastal Waters of the Bahama-Islands. *Limnol Oceanogr* 35, 325-338.
- Sunda, W.G., Huntsman, S.A., **1994**. Photoreduction of Manganese Oxides in Seawater. *Mar Chem* 46, 133-152.
- Takashima, T., Hashimoto, K., Nakamura, R., **2012**. Mechanisms of pH-Dependent Activity for Water Oxidation to Molecular Oxygen by MnO₂ Electrocatalyst. *J Am Chem Soc* 134, 1519-1527.
- Tang, J., Durrant, J.R., Klug, D.R., **2008**. Mechanism of photocatalytic water splitting in TiO₂. Reaction of water with photoholes, importance of charge carrier dynamics, and evidence for four-hole chemistry. *J Am Chem Soc* 130, 13885-13891.
- Villalobos, M., Toner, B., Bargar, J., Sposito, G., **2003**. Characterization of the manganese oxide produced by *Pseudomonas putida* strain MnB1. *Geochim Cosmochim Acta* 67, 2649-2662.
- Waite, T.D., Wrigley, I.C., Szymczak, R., **1988**. Photoassisted Dissolution of a Colloidal Manganese Oxide in the Presence of Fulvic-Acid. *Environ Sci Technol* 22, 778-785.
- Wang, Y., Stone, A.T., **2008**. Phosphonate- and Carboxylate-Based Chelating Agents that Solubilize (Hydr)oxide-Bound Mn(III). *Environ Sci Technol* 42, 4397-4403.
- Wiechen, M., Zaharieva, I., Dau, H., Kurz, P., **2012**. Layered manganese oxides for water-oxidation: alkaline earth cations influence catalytic activity in a photosystem II-like fashion. *Chem Sci* 3, 2330-2339.
- Wu, K.H., Hsu, T.Y., Shih, H.C., Chen, Y.J., Luo, C.W., Uen, T.M., Lin, J.Y., Juang, J.Y., Kobayashi, T., **2009**. Ultrafast optical probes of polaron dynamics in La_{0.7}Ca_{0.3}MnO₃ thin films. *J Appl Phys* 105.
- Young, K.J., Gao, Y., Brudvig, G.W., **2011**. Photocatalytic Water Oxidation Using Manganese Compounds Immobilized in Nafion Polymer Membranes. *Aust J Chem* 64, 1221-1228.

Chapter 5. The pH-dependent photoreduction of δ -MnO₂: increased surface protonation leads to greater rates of irreversible Mn(III) photogeneration

This chapter will be submitted to Environmental Science and Technology with slight modifications as “Photoreduction of δ -MnO₂: low pH enhances the rates of structural stabilization of photogenerated Mn(III)”, Marafatto FF, Schwartzberg A, Gilbert B, Peña J.

5.1. Abstract

The high reactivity of layer Mn oxides (birnessites) towards organic and inorganic sorption and oxidation is intrinsically linked to the stability of these oxides against reductive processes. One such process is photoreduction, which has been predicted in theory and observed in natural settings yielding dissolved Mn(II) in a light-initiated two electron transfer process from surface sorbed species. However, the photoreduction mechanism has only been confirmed recently by experiments. In particular, the irradiation of birnessite in the absence of organic electron donors yields Mn(III), which remains on the mineral surface. The experiments were carried out at pH 6.5, but the natural surface environments in which birnessites are found are governed by pH conditions that range from acidic to alkaline. To predict the stability of birnessite against photoreduction in such environments, it is therefore important to evaluate the effect of pH on the rate and mechanism of birnessite photoreduction. In this study, we evaluated the pH-dependence of the rates and mechanism of birnessite photoreduction with macroscopic flow-through photoreactor experiments and ultrafast optical pump-probe spectroscopy, respectively. Our results show that lower pH leads to greater photoreduction rates, but these rates are not reflected in a different photoreduction mechanism. We suggest that protonation of the mineral surface decreases the Mn-O bond strength, the breaking of which is a necessary step to stabilize photoreduced Mn(III) in the mineral interlayer.

5.2. Introduction

Birnessite minerals (layer type Mn(IV,III) oxides) are highly reactive, influencing the fate of many organic and inorganic species in a wide range of environments (Post, 1999; Tebo et al., 2004). These minerals are also susceptible to photoreductive dissolution, whereby light initiates the reduction of Mn(III,IV) to Mn(II) and the release of the latter to solution (Waite, 1990). However, photoreductive processes may also lead to the reduction of Mn(IV) to Mn(III) on the mineral surface, without dissolution (Marafatto et al., 2015). Dissolved Mn(II) may then be oxidized by microorganisms, generating birnessite minerals. In such a scenario, a complete oxidation-reduction cycle may occur on the timescale of hours to days (Sunda and Huntsman, 1990). Because of the reactivity of birnessites, these oxidation/reduction processes may affect the biogeochemical cycle of other chemical species, either in solution or associated with the mineral. Although multiple investigations have been carried out to determine the microbial oxidation mechanism on the molecular scale (Tebo et al., 2004; Hansel et al., 2012), only few studies have investigated the photoreduction process. Furthermore, the existing studies on the photoreduction of Mn oxides involved complex systems that were composed of multiple light-sensitive components such as microorganisms and organic compounds, which precluded decoupling direct Mn photoreduction from other photochemical or microbiological processes (Sunda and Huntsman, 1994).

The photoreduction mechanism of birnessite was elucidated only recently by investigating the effect of irradiation on aqueous mineral suspensions in the presence of only water and background electrolytes. The results showed that irradiation of mineral suspensions leads to the accumulation of Mn(III) on the mineral surface, without release of Mn(II) to solution (Marafatto et al., 2015). The main finding of the study evidenced a role for the crystallographic location of photogenerated Mn(III) (i.e. in the interlayer vs in the nanosheet) in determining the irreversible photoreduction rate, in line with recent studies that have demonstrated the importance of Mn(III) in driving many environmental and engineered processes (Luther III, 2005; Webb et al., 2005; Madison et al., 2013; Robinson et al., 2013; Simanova and Peña, 2015). Furthermore, through the use of time-resolved pump-probe spectroscopy we identified the kinetics for electronic transitions following photoexcitation of the mineral. The use of a simplified system allowed us to develop a model for the

photoreduction mechanism by constraining the interpretation of the results to the few components that were present: water, δ -MnO₂ and either NaCl or CaCl₂ electrolyte. However, the experiments were conducted at a single solution pH value of 6.5.

Solution pH is the master variable that drives the aqueous and redox speciation of inorganic species in many sunlit aquatic environments. Additionally, the fate of dissolved species in such environments is often related to the ubiquitous presence of Fe and Mn oxides (Hochella et al., 2008). These environments are also characterized by a broad range of pH conditions, from the strongly acidic conditions of acid mine drainage (pH < 3), to moderately alkaline conditions of ocean waters (pH ~ 8.3). Since Fe and Mn oxides are known to be semiconductors, that is light is able to promote electronic transitions that can lead to changes in the mineral (Sherman, 2005), the effect of sunlight on the stability of these oxides has the potential to affect the mobility of many inorganic species associated with them in these environments. Thermodynamic predictions indicate that photoreduction should increase with decreasing pH for both Fe and Mn oxides (Sherman, 2005). These predictions have been confirmed by experimental studies for Fe oxides (Borer et al., 2009a). The authors showed a decrease in the rates of lepidocrocite (FeOOH) photoreduction from $\sim 4 \times 10^{-10} \text{ M s}^{-1}$ at pH 2 to negligible at pH values above 4 in a solar simulator. The decrease in rate with increasing pH was interpreted as an increase in the Fe(II) reoxidation rate by dissolved oxygen or reactive oxygen species. However, the redox speciation of Mn is different than that of Fe: while Fe is stable in two oxidation states, Fe(II) and Fe(III), Mn occurs as Mn(II), Mn(III) and Mn(IV). Additionally, the stability of aqueous Fe(II) against oxidation by oxygen is constrained to very low pH, whereas Mn(II) can be stable as an aqueous species in the presence of oxygen for several years at pH values of seawater (~8.3) without the catalytic effect of microorganisms (Morgan, 2000). Although these differences may lead to a difference in the pH dependence of Mn oxide photoreduction, there have not been experimental studies investigating this to date.

The aim of this study was to expand the current model for the photoreduction of birnessite to include the effect of solution pH. To achieve this goal, δ -MnO₂ suspensions with average Mn oxidation number (AMON) of 4.03 ± 0.01 and specific surface area (SSA) of $163 \pm 8 \text{ m}^2/\text{g}$ at pH 4.0, 6.5 and 8.0 were irradiated with 400 nm light. Rates of Mn(III) formation were measured on hour to day timescales in flow-through photoreactors. The photoexcitation

mechanism, on the other hand, was investigated on femtosecond to microsecond timescales by measuring the kinetics of electron/hole pair generation and decay with transient absorption all-optical pump-probe spectroscopy. Our results show that irreversible formation of Mn(III) in the dark as well as following mineral irradiation with water or Cl⁻ as the electron donor depends on pH. These results suggest that Mn(III) stabilization as a surface species, which inhibits electron/hole recombination, is likely favored by the protonation of surface sites, which may also be responsible for proton promoted dissolution in the dark.

5.3. Materials and methods

ACS reagent-grade chemicals were purchased from Sigma-Aldrich or Merck. All solutions and suspensions were prepared with ultrapure water (18 M Ω). The MnO₂ phase used in batch photodissolution experiments and pump-probe experiments was δ -MnO₂. This synthetic mineral was prepared and characterized following previous methods (Villalobos et al., 2003). Briefly, the minerals were characterized by a SSA of 163 ± 8 m²/g, an AMON of 4.03 ± 0.01 , a crystallite size of ~ 4 nm and a chemical formula of Na_{0.27}Mn(IV)_{0.97}Mn(III)_{0.03}•0.94H₂O. A brief description of the synthesis and characterization of the products is reported in the supporting information. All experiments were carried out at ambient temperature and either open to the atmosphere or under a N_{2(g)} purge to exclude O₂ and CO₂.

Flow-through photoreactor experiments. Batch experiments were carried out at different pH values to measure the rates and efficiency of the photoreduction process. We prepared suspensions of 22 - 25 mg L⁻¹ δ -MnO₂, corresponding to a concentration of 218 - 254 μ M Mn, at pH 4.0, 6.5 and 8.0 by diluting concentrated aqueous mineral suspensions with MQ water (**Table S1**). Suspensions contained 12.5 mM sodium pyrophosphate (PP), added from stock solutions previously equilibrated at pH 4.0, 6.5 or 8.0 through dropwise addition of 4 M HCl, to trap Mn(III) in the Mn(III)-PP complex ($\log k_{\text{apparent pH 8.0}} = 31.35$) (Parker et al., 2004). We confirmed that PP was able to efficiently trap Mn(III) at pH 4.0, 6.5 and 8.0 by preparing Mn(III)-PP solutions with Mn(III)-Acetate in PP, filtering them through 0.2 μ m polyethersulphone (PES) filters, and comparing the UV-Vis quantified Mn(III)-PP with the total Mn concentration measured by ICP-OES spectrometry. At all pH values tested the UV-Vis-determined Mn(III) was equivalent to the ICP-OES quantified total Mn within

experimental and instrumental error (5%), as shown previously for pH 6.5 (Marafatto et al., 2015). In the photoreduction experiments, excess PP in the suspension also acted as a pH buffer. All mineral + PP suspensions were equilibrated in the dark over the weekend prior to irradiation. The suspensions were then divided into 2 aliquots: one bottle was mixed with a magnetic stirrer as a dark control and the second was recirculated through a 1-cm flow-through quartz cuvette in a flow-through system with a peristaltic pump. Irradiation was provided by a photoreactor composed of an array of three 1W light emitting diodes (LEDs) at 400 nm (3.1 eV). Independent experiments were run simultaneously using an array of 3 photoreactors that were assembled onto a breadboard support and screened from each other to avoid interferences. The photon flux to each photoreactor was evaluated with ferrioxalate actinometry, as described previously (**Chapter 4**). This value was different for each photoreactor due to small differences in the individual LED outputs, power supply output and irradiation geometry (**Chapter 2**). The photoreactor setup was then screened from ambient light with a black curtain. All sample collection and other manipulations necessary during the irradiation period were conducted under diffuse red light.

Samples were irradiated for a total of 96 hours, with dark control experiments performed in parallel under exactly the same conditions as the irradiated samples. Reactors were sampled approximately every 6 hours for the first 48 hours and every 8 hours for the last 48 hours. The total manganese concentration in suspension $[\text{Mn}]_{\text{tot}}$ was measured in duplicate at each timepoint by inductively coupled plasma optical emission spectrometry (ICP-OES) after digestion of an aliquot with 0.01 M $\text{H}_2\text{C}_2\text{O}_4$ and 3% HNO_3 . The $[\text{Mn(III)-PP}]$ was quantified by filtering an additional aliquot through a 0.2 μm PES syringe filter, discarding the first ml, and measuring the absorbance of the filtrate by UV-Vis spectrophotometry ($\epsilon_{254\text{ nm}} = 6562\text{ L mol}^{-1}\text{ cm}^{-1}$) with 1 cm path length quartz cuvettes, using a 12.5 mM PP solution as a blank. Experiments were conducted in triplicate.

To evaluate whether the trends in photoreduction rate as a function of pH were affected by the presence of PP, we performed complementary experiments without PP addition on $\text{N}_{2(\text{g})}$ -purged suspensions of MnO_2 . Nitrogen purge was necessary to reduce the effect of atmospheric CO_2 on the pH adjustment. We have previously shown that N_2 purge does not alter the photoreduction rates compared to aerated conditions (Marafatto et al., 2015). In these

experiments, mineral suspensions were prepared in 10 mM NaCl electrolytes with pH maintained at pH 4.0 and 8.0 through the use of a Metrohm STAT titrator 906 automatic titrator. Data at pH 6.5 is available from a previous study (Marafatto et al., 2015). One mL of a 100 mM PP stock solution (equilibrated at pH 4.0 or 8.0) was added to a 7 mL aliquot of mineral suspension collected at set timepoints (up to 3 samples per day) within the 96 hours of the irradiation experiment, and placed on an end-to-end shaker for 48 hours in the dark. Measurements of $[Mn]_{tot}$ and $[Mn(III)-PP]$ were carried out as described above after the 48-hour equilibration. The main observable difference in these experiments was extensive aggregation in the minerals, which was not present in experiments where PP was added before irradiation, since PP also helped keep particles in suspension.

The rate of Mn(III) production was determined from linear regression of extracted Mn(III)-PP against time, after correcting for any Mn(III) released in dark control experiments. To account for the different photon flux in each photoreactor a scaling factor was applied: The photon flux of each reactor was divided by the photon flux of the reactor with highest irradiance, and the Mn(III) rates were then normalized by this scaling factor for comparison. We then calculated the quantum yield for Mn(III) generation, which is defined as the amount of photogenerated Mn(III) per photon absorbed by the δ -MnO₂ suspension. To calculate the number of photons absorbed, we first measured the photon flux to the photoreactor by chemical actinometry using potassium ferrioxalate (Parker, 1953; Hatchard and Parker, 1956; Montalti et al., 2006) and then scaled the photon flux to the ratio of the absorbance of δ -MnO₂ at the different pH values to that of ferrioxalate, according to the following equation (Marafatto et al., 2015):

$$\Phi = \frac{f_{Mn(III),t} \times \text{moles of Mn}}{\varphi * t \times \frac{A_{400 \text{ nm}, MnO_2}}{A_{400 \text{ nm}, ferrioxalate}}} \quad (1)$$

where $f_{Mn(III), t}$, the fraction of photoreduced Mn after time, t , is multiplied by the total number of moles of Mn in the system; φ is the photon flux measured for the photoreactor (units of $\mu\text{E/s}$) (Marafatto et al., 2015); and $A_{400 \text{ nm}, MnO_2}$ and $A_{400 \text{ nm}, ferrioxalate}$ are the absorbances (in OD units) of δ -MnO₂ at pH 4.0, 6.5 or 8.0 and ferrioxalate at 400 nm measured in 1 cm path length quartz cuvettes with water as a blank.

Optical transient absorption spectroscopy. Optical transient absorption (TA) spectroscopy is sensitive to excited-state valence electron dynamics and can be used to follow the dynamics of electronic states in semiconducting metal oxides (Cherepy et al., 1998; Zhang, 2000; Gilbert et al., 2013). Optical TA experiments were carried out on a HELIOS femtosecond transient absorption spectrometer and on an EOS sub-nanosecond transient absorption spectrometer from Ultrafast Systems at the Molecular Foundry (Lawrence National Laboratory, Berkeley, CA USA). The laser source for both instruments was a Coherent Libra amplified femtosecond laser operating at 1 kHz with 45 fs pulse duration. The laser output was split into two arms. The first arm passed through a Coherent OPerA optical parametric amplifier (OPA) to produce tunable pump pulses. A white-light probe pulse was generated in the transient absorption system either by sapphire plate via the second arm of the laser output or by a fiber white light source (Leukos-STM) for the HELIOS and EOS spectrometers, respectively. The pump pulse used in our measurements was tuned at 400 nm. The intensity of the pump beam was measured to be 800 nJ pulse⁻¹. Time delay was provided by a mechanical delay stage on the HELIOS setup and by instrument electronics on the EOS setup. Spectra were collected between 330 and 800 nm.

Aqueous oxide suspensions were resuspended in aqueous PP solutions pre-equilibrated at pH 4.0, 6.5 or 8.0 in order to give a 20:1 PP:Mn ratio. As per a previous study (Marafatto et al., 2015), the sample concentration for the TA measurement was tuned to obtain an optical density (OD) between 0.8 and 1.6 absorption units on 0.5 mm path length cuvettes, corresponding to an oxide concentration between 3 and 6 mM. The purpose of resuspending in PP was to assure consistency with the photoreduction experiment conditions and avoid severe aggregation of the particles, especially at low pH. 10 to 15 ml of sample were recirculated in 1-mm pathlength flow-through cuvettes, and spectra were collected from -10 ps to 8 ns (relative to the laser pulse) on the HELIOS system and from 1 ns to 200 μ s on the EOS system. Data was collected on the EOS system only for the pH 8.0 and pH 4.0 samples, because differences between these samples were within the noise of the data, therefore we judged that the pH 6.5 data would not have shown differences. Custom user routines developed in the IGOR Pro software (WaveMetrics Inc., Lake Oswego, OR, USA) were used to process the data, including correction of the time dependent frequency modulation of the laser (laser chirp) on the signal to within \sim 150 fs. Custom routines were also used to extract transient

kinetic data at 354, 450 and 580 nm from 2D plots of spectra versus time, after shifting the data by +1 ps to allow the kinetic data to be plotted on a logarithmic scale. IGOR Pro was also used to fit first-order exponential decay kinetics to the extracted data. The decay kinetics for all samples were adequately reproduced by fitting two exponential time constants.

5.4. Results

Flow-through photoreactor experiments. The irradiation of δ -MnO₂ suspensions at pH 4.0, 6.5 and 8.0 in the presence of PP resulted in the accumulation of Mn(III) over time (**Figure 1A**). The suspensions at lower pH resulted in greater Mn(III) production than those at higher pH (~6% at pH 4.0, ~4.5% at pH 6.5, ~1.5% at pH 8.0, of the total Mn present, respectively), indicating that solution pH affects the rate of irreversible Mn(III) generation. The amount of Mn(III) generated in the dark was also higher at pH 4.0 (~3% Mn total) than at pH 6.5 and pH 8.0 (~2% and 0.7% Mn total, respectively - **Figure S1**). The Mn(III) amount was regressed against time (4 days) without forcing the intercept through zero to obtain a photoreduction rate. Linear regression with a non-zero intercept gave a better fit than forcing linear regression with a zero intercept. A plot of the residuals showed that these were homoscedastic only for a non-zero intercept (**Figures S3**). The photoreduction rates thus obtained were $9.17 \pm 0.43 \times 10^{-11} \text{ M s}^{-1} + 2.9 \times 10^{-7} \text{ M}$ for pH 4.0, $6.67 \pm 0.23 \times 10^{-11} \text{ M s}^{-1}$ for pH 6.5, and $2.42 \pm 0.25 \times 10^{-11} \text{ M s}^{-1}$ for pH 8.0 (errors calculated as the 95% confidence interval on the slope). Only the pH 4.0 data had a significant intercept, leading us to include it in the rate, whereas for the pH 6.5 and 8.0 data the intercept values were within the confidence interval calculated on the rate. The photoreduction quantum yield, which represents the efficiency of the photoreduction process, was calculated to be $1.90 \pm 0.09 \times 10^{-4}$ (pH 4.0), $1.44 \pm 0.4 \times 10^{-4}$ (pH 6.5) and $7.46 \pm 3.5 \times 10^{-5}$ for the pH 8.0 samples (errors calculated as 95% confidence interval on replicates).

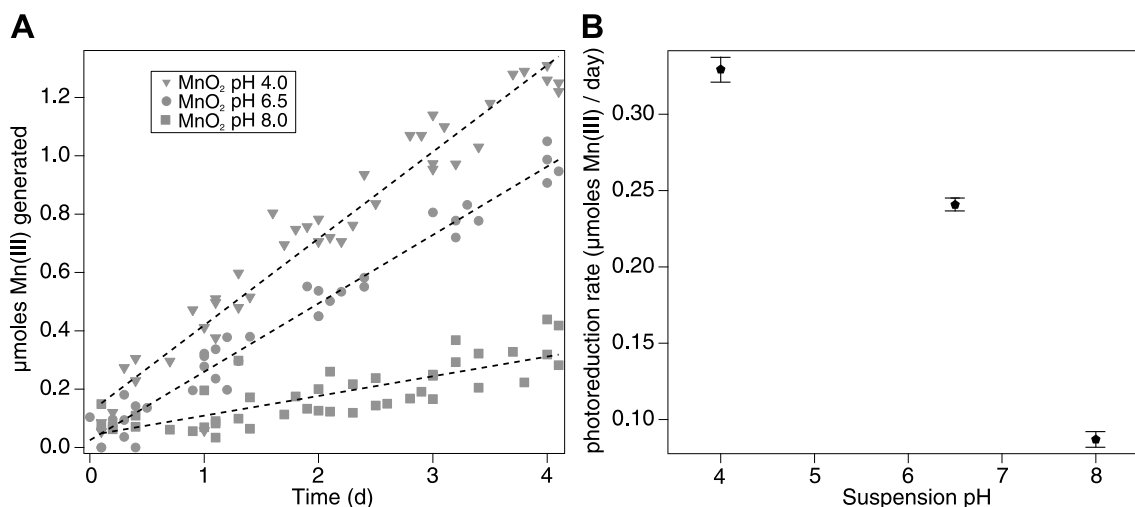


Figure 1A) Time course plot showing the photoreduction of δ -MnO₂ suspensions in the presence of PP as a function of pH. Dashed lines indicate the linear interpolations plotted to calculate the rates reported in the main text; **B)** Photoreduction rates, obtained from the slope of the linear regressions in **Figure 1A**, plotted against suspension pH. Error bars are plotted as the 95% confidence interval.

The results of the pH stat experiments with 10 mM NaCl background electrolyte and the absence of PP are shown in **Figure S2**. The results confirmed the trends observed in the experiments where PP was added before irradiation, although the amounts of photogenerated Mn(III) were different. In particular, the measured photoreduction rates were 2-3 times greater than those obtained in the PP experiments: $3.17 \pm 0.49 \times 10^{-10} \text{ M s}^{-1}$ and $4.92 \pm 4.78 \times 10^{-11} \text{ M s}^{-1}$ for pH 4.0 and pH 8.0, respectively (errors calculated as 95% confidence interval on the slope). The quantum yield calculated for the reaction in this case was $1.08 \pm 0.2 \times 10^{-3}$ for pH 4.0 and $2.5 \pm 1.2 \times 10^{-4}$ for pH 8.0 (errors calculated as 95% confidence interval on replicates). Fits were carried out on the data only up to 53 hours (2.2 days). The measurements made beyond 2 days were visibly affected by extensive aggregation, which led to large scatter in the data.

Optical transient absorption spectroscopy. The optical transient absorption spectra of δ -MnO₂ suspensions in excess PP are shown in **Figure 2**. The transient absorption spectra extracted at a delay of 5 ps in **Figure 2A** show the two main features: i) below 430 nm the signal is characterized by the ground state bleach, where the negative ΔOD represents the population of electron/hole pairs generated upon photoexcitation, ii) above 430 nm, the signal is dominated by a positive ΔOD peaking at 580 nm, the excited state absorption (ESA), that represents the evolution of photoexcited electrons in the conduction band of the mineral. In

particular, we previously assigned the ESA in δ -MnO₂ to the localization of the photoexcited electrons into transient Mn(III) states (Marafatto et al., 2015). The optical transient absorption spectra and kinetics of the ground state bleach and ESA extracted at 345 nm and 580 nm, respectively, did not differ substantially from one another as a function of pH (**Figures 2A, 2C and 2D**). However, a slight red-shift in the shoulder at 450 nm of the ESA at 5 ps could be seen as a function of pH (**Figure 2A and 2B**). The ESA values extracted at 450 nm for the 3 experimental pH conditions, shown in **Figure 2B**, confirm that the decay kinetics are identical in all three samples once the signal has reached its maximum intensity. However, the rise to the maximum intensity of the ESA was slower for the higher pH samples than the lower pH samples, as shown in **Figure 2B** between 10⁰ and 10¹ ps.

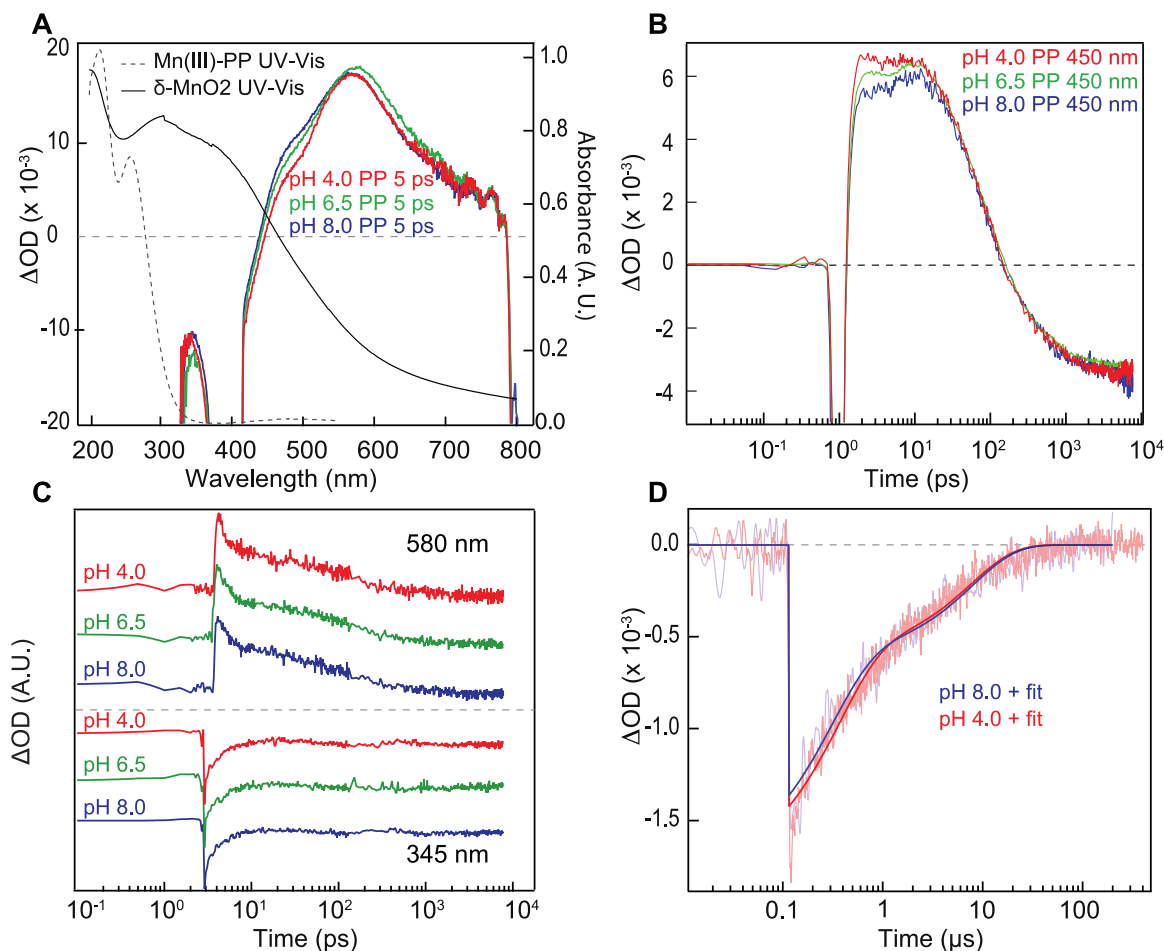


Figure 2A) Comparison between the ground state UV-Vis absorption spectrum of δ -MnO₂, Mn(III)-PP and the transient absorption spectrum extracted at a 5 ps delay for δ -MnO₂ at pH 4.0, 6.5 and 8.0 in the presence of PP above 430 nm the signal is dominated by the enhanced state absorption (ESA), below 430 it is dominated by the ground state bleach, except for the laser scatter at 400 nm \pm 20 nm; **B)** Transient absorption kinetics for the excited state absorption extracted at 450 nm for the 3 experimental pH values studied; **C)** Transient absorption kinetics for the excited state absorption extracted at 580 nm (upper curves) and the ground state bleach extracted at 345 nm (lower curves) for the samples at different pH; **D)** Transient absorption kinetics collected on the EOS setup, showing the ground state bleach extracted at 580 nm up to 200 μ s delay time.

To evaluate whether there could be a trend between ESA and ground state bleach as a function of pH, the maximum intensity of the ESA was normalized to the maximum intensity of the ground state bleach for each sample. This operation allowed us to visually identify the differences between samples. To check whether this trend was conserved across the TA spectra, this operation was carried out on three different wavelengths for both the ESA and ground state bleach, chosen to be equally representative of these portions of the signal: < 430 nm for the ground state bleach excluding the laser scatter region; > 440 nm for the ESA. The

results shown in **Figure 3** indicate that the values do not show a decrease with increasing pH, which is in contrast with the photoreduction rate measurements.

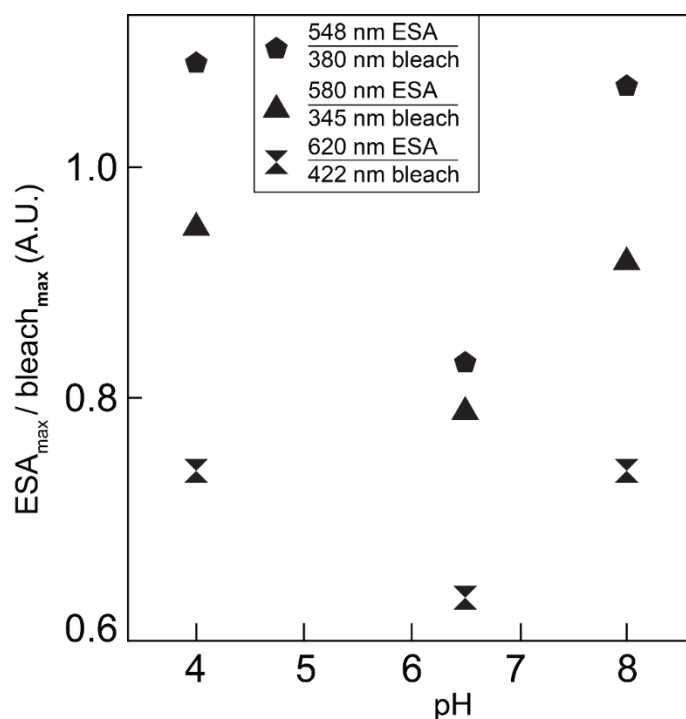
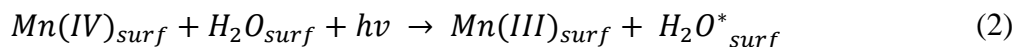


Figure 3. Comparison between the maximum intensity of the enhanced state absorption, normalized by the maximum intensity of the ground state bleach, extracted at 3 different wavelengths, as a function of pH, showing no apparent trend with pH.

5.5. Discussion

The results of this study show that the photoreduction of δ -MnO₂ increases with decreasing pH. However, this difference is not reflected substantially in the photoexcitation dynamics probed by ultrafast pump probe optical spectroscopy. In addition, the amount of Mn(III) trapped in the dark, which also varied as a function of pH, indicates that changes in solution pH are sufficient to modify the redox state of the mineral without photoexcitation. The comparison between the δ -MnO₂ photoreduction rates (**Figure 1**) and the photoexcitation dynamics (**Figure 2**) as a function of pH therefore suggests that the pH-dependence of macroscopic photoreduction rates are likely controlled by a chemical step that is independent from the photoexcitation of the mineral.

Under the assumption that the overall chemical reaction can be represented only by H₂O and Mn atoms on the surface of the mineral, Mn(III) photogeneration can be described by the following expression:



Where Mn(IV)_{surf} is a Mn atom in the nanosheet, H₂O_{surf} is an adsorbed water molecule, *hν* is the photon, Mn(III)_{surf} is the photoreduced Mn atom after migration to the interlayer, and H₂O*_{surf} is the hypothesized oxidized species. Solution pH can affect this reaction either by modifying the oxidizable species (H₂O) or the reducible species (Mn). Based on the Eh-pH stability diagram for H₂O, water is oxidized more favorably at high pH. However, our results suggest a greater formation of the oxidized species coupled to Mn photoreduction at lower pH than at higher pH. Therefore, the rates of photoreduction are likely dominated by the effect of pH on the surface of δ-MnO₂, which will be discussed in the following paragraphs.

pH effect on the mineral surface. δ-MnO₂ is characterized by a low point of zero charge (PZC) of around 1-3 (Gray et al., 1978; Tan et al., 2008). However, recent studies on ion and oxyanion sorption have suggested that edge sites of δ-MnO₂ may be protonated at higher pH values than the known PZC (Villalobos, 2015; van Genuchten and Pena, 2016). In particular, singly-coordinated edge sites may be protonated at pH values as high as 6 (Villalobos, 2015). This conclusion was based on bond strength calculations, which showed a degree of surface oxygen saturation for δ-MnO₂ lying between that of β-MnO₂ and ferrihydrite, characterized by a PZC of ~6 and 7-8, respectively. The main differences in our experiments between pH 4.0, 6.5 and 8.0 is the amount of H⁺ available from the surrounding solution to sorb onto the edge sites. Because of the increased availability of H⁺ with lower pH, the protonation of the edge sites is expected to increase. The Na⁺ content could also have changed as a function of pH (**Chapter 3**), but it was not possible to evaluate given that Na⁺ was in excess in all experimental conditions. The protonation of surface Mn-O leads to an increase in their hydration, which contributes to reduce the bond strength between these groups and the solid lattice. This effect is what leads to proton promoted dissolution on the oxide surface (Stone, 1983). The formation of Mn(III) in the dark as a function of pH supports this observation, since lower pH led to four times more Mn(III) formation than higher pH. The release of Mn(III) in

the dark also suggests that there may be a thermodynamic drive to the accumulation of Mn(III) in the mineral, for which protonation alone is sufficient to drive Mn reduction and light simply accelerates the process. The increase in protonation of edge sites may also bridge Cl⁻ ions to the mineral surface, known hole scavengers (Grätzel et al., 1985) that were present in the pH STAT experiments. This could explain the enhanced photoreduction rates observed in the pH STAT experiments compared to the PP experiments. Finally, quick X-ray absorption spectroscopy experiments on the effect of pH on the structure of triclinic birnessite (data not shown) have shown that the reduction of pH below 5 results in the rapid migration of Mn(III) from the layer to the interlayer. Therefore, low pH may also favor the presence of Mn(III) as an adsorbate in the interlayer vs the nanosheet.

Effect of pH on the photon absorption by δ -MnO₂. The absorption of a photon by δ -MnO₂ results in the formation of an electron/hole pair, where the photoexcited electron is localized around the Mn atom, and the related hole is localized around the oxygen atom (Gerische.H, 1966; Sherman, 2005). This process can be seen as the breaking of a Mn-O bond (Maruska and Ghosh, 1978) and the formation of a transient Mn(III) species which we attribute to the ESA feature in **Figure 2A**. Therefore, a weakening of the Mn-O bond prior to photon absorption may enhance the probability that photon absorption will result in the formation of a transient Mn(III) species. We previously suggested that the delay in the rise of the ESA to its maximum intensity, lasting approximately 600 fs, could be assigned to the timescale required for the formation of the transient Mn(III) species (Marafatto et al., 2015). **Figure 2B**, which shows the kinetics of the ESA feature (~transient Mn(III) formation) extracted at 450 nm, suggests that the timescale for its formation is faster at low pH (more surface protonation) than at high pH (less surface protonation).

Electron transfer from sorbed water molecules and structural rearrangement. In order to complete the photoreduction process, the transient Mn(III) species must find a structural configuration that hinders electron-hole recombination. This final reaction step requires hole scavenging by a surface-sorbed species. We previously identified the stabilization of transient Mn(III) through its migration from the nanosheet to the interlayer region (Marafatto et al., 2015). Since the quantum yield for the photoreduction is on the order of $10^{-4} - 10^{-5}$, most of the photogenerated electron/hole pairs recombine without the rearrangement of Mn(III) in a

stable structural site. Despite the low quantum yield, the migration of transient Mn(III) species to the interlayer is favoured in the presence of protonated surface sites because Mn(III) is less strongly bound to the lattice than in the presence of deprotonated surface sites. Additionally, a Mn(IV) to Mn(III) reduction results in a decrease in the charge to radius ratio (ionic potential – IP), which increases the exchange rate with coordination ligands (for example, water molecules (Stumm and Morgan, 1996)) and therefore decreases the Mn-O bond strength that keeps it bound to the layer. Furthermore, since the Mn(III) octahedron is characterized by Jahn-Teller distortion that is absent in Mn(IV) (Burns, 1993), the steric strain in the nanosheet is increased with the formation of Mn(III) in an almost fully Mn(IV) sheet. The accumulation of Mn(III) in the interlayer or adsorbed at the edge sites would create no additional steric strain. The interlayer site that can be occupied by Mn(III) is either above/below an octahedral vacancy in a triple corner sharing configuration or above/below an edge site in a double corner or edge sharing configuration. From a geometric perspective, the most likely site for the stabilization of Mn(III) is the double corner sharing configuration, above or below an edge site (**SI text**).

Formation and evolution of oxidized species. The formation of an oxidized species, which is a necessary by-product of the irreversible reduction of Mn(IV), has not been observed experimentally. We suggest that coordinated water molecules are most likely the electron donor in the process, given that no other electron-donating species are present in the main system we studied (PP system). Chloride might contribute to the photoreduction of Mn(IV), since it has been shown to enhance the rate of Fe oxide photoreduction (Grätzel et al., 1985), but Cl⁻ is only present in the pH-STAT experiments, therefore cannot explain the results in the PP-only system. Although we expect that adsorbed water (H₂O or OH⁻) is the dominant oxidized species, the full oxidation of water to form molecular oxygen is not likely, since this reaction would require the scavenging of 4 holes by two water molecules. This reaction is unlikely given the low quantum yield of the photoreduction process. Instead, we suggest that Mn(IV) photoreduction is coupled to the formation of a radical species, most likely OH[•]. Although this hypothesis remains to be verified, it is supported by our results and is the most likely pathway, given the simple chemical composition of the studied system. Furthermore, OH[•] radicals were identified as the oxidized species in the photoreduction of lepidocrocite in water (Borer et al., 2009b). In future studies, the presence of OH[•] may be confirmed by radical trapping experiments with probe compounds that do not react with the birnessite mineral. In fact, our

attempts to trap the likely end product deriving from combination of two hydroxyl radicals, H_2O_2 , failed because the probe compounds reacted with $\delta\text{-MnO}_2$. One such compound could be benzyl trimethyl ammonium (BTMA), which is known to react strongly with hydroxyl radicals ($k_{\text{OH}} = 4 \times 10^9 \text{ M}^{-1} \text{ s}^{-1}$) (Buxton et al., 1988).

The steps in the photoreduction process analyzed in the previous paragraphs can be summarized by the following chemical expressions:

1. $2 \text{Mn(IV)}_{\text{layer}}\text{O}\equiv\text{H}_2\text{O} + h\nu \leftrightarrow 2 \text{Mn(III)}_{\text{layer}}\text{O}^*\equiv\text{H}_2\text{O}$ (photon absorption by $\delta\text{-MnO}_2$)
2. $2 \text{Mn(III)}_{\text{layer}}\text{O}^*\equiv\text{H}_2\text{O} \leftrightarrow 2 \text{Mn(III)}_{\text{layer}}\text{-O}\equiv\text{H}_2\text{O}^*$ (e^- transfer from sorbed H_2O)
3. $2 \text{Mn(III)}_{\text{layer}}\text{-O}\equiv\text{H}_2\text{O}^* \rightarrow 2 \text{Mn(III)}_{\text{interlayer}}\text{-OH}^* + 2 \text{H}^+$ (formation of OH^* species)

Where the oxidized species are hypothetical, since they have not yet been measured experimentally, and protonation has been excluded for simplicity. A graphical representation of the protonation effect on the surface during photoreduction is given in **Figure 4**.

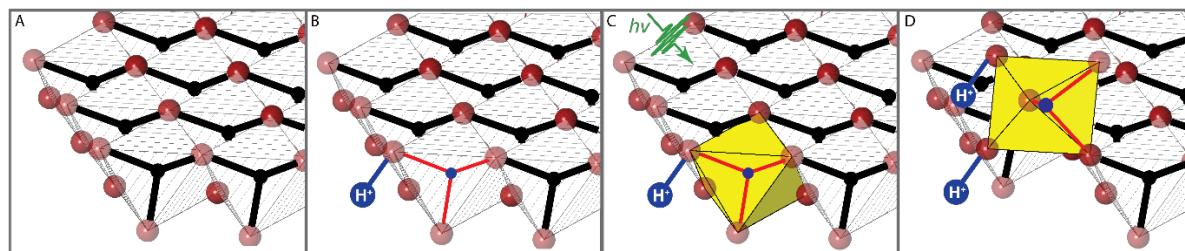


Figure 4. Simplified graphical representation of the steps leading from protonation to Mn(III) stabilization in an out-of-plane site. The thickness of the lines representing the Mn-O bonds is intended to represent the bond strength. A) mineral before pH equilibration; B) protonation of the surface (for simplicity, only one site is shown protonated); C) irradiation of the mineral and resulting formation of a transient Mn(III) species in the layer; D) as a consequence of the reduction in the Mn-O bond strength from protonation, the Mn(III) octahedron can partially detach from the surface to find a stable Mn(III) position, as an adsorbed interlayer Mn(III) species.

5.6. Environmental implications

The results of this study allow us to expand the existing model for birnessite photoreduction by band gap excitation to include the effect of solution pH. Solution pH is a master variable in environmental systems that affects multiple processes, from mineral formation to aqueous speciation and ion sorption (Stumm and Morgan, 1996). The considerably higher rate of $\delta\text{-MnO}_2$ photoreduction compared to that of Fe oxides and in the

absence of organic electron donors confirm the importance of Mn photoreduction in a broader range of environmental systems than Fe oxides (Sherman, 2005). Furthermore, the Fe oxide studies showed an important role for Fe reoxidation on the oxide surface, which we assume to not occur once Mn(III) is stabilized out of the *001* plane. Moreover, our results indicate a pathway for Mn(III) accumulation in the mineral, which has been related to the reduced sorptive capacity of birnessite minerals (Simanova et al., 2015). The sorption of inorganic species on birnessites has been intensely researched in environmental contexts that ranged from low pH-governed acid mine drainage (Kimball et al., 1995; Fuller and Harvey, 2000) to ocean waters (pH 8.1) (Peacock and Sherman, 2007), but have rarely been observed as a function of light. Therefore, our results contribute to the understanding of the behaviour of birnessites in such contexts, which are often affected by diel variations in sunlight.

5.7. Acknowledgements

This research was funded by the Swiss National Science Foundation (Grant # 200021_143742). B. Gilbert was supported by the Director, Office of Science, Office of Basic Energy Sciences, of the US Department of Energy (BES-DOE) Contract DE-AC02-05CH11231. Research at the Molecular Foundry was supported by BES-DOE Contract DE-AC02-05CH11231. We thank Laetitia Monbaron for the logistical help for the Laboratory studies in Lausanne, Switzerland.

5.8. References

- Borer, P., Kraemer, S.M., Sulzberger, B., Hug, S.J., Kretzschmar, R., **2009a**. Photodissolution of lepidocrocite (γ -FeOOH) in the presence of desferrioxamine B and aerobactin. *Geochim Cosmochim Acta* 73, 4673-4687.
- Borer, P., Sulzberger, B., Hug, S.J., Kraemer, S.M., Kretzschmar, R., **2009b**. Photoreductive dissolution of iron(III) (hydr)oxides in the absence and presence of organic ligands: experimental studies and kinetic modeling. *Environ Sci Technol* 43, 1864-1870.
- Burns, R.G., **1993**. Mineralogical applications of crystal field theory, Second ed. *Cambridge University Press*, Cambridge.
- Buxton, G.V., Greenstock, C.L., Helman, W.P., Ross, A.B., **1988**. Critical-Review of Rate Constants for Reactions of Hydrated Electrons, Hydrogen-Atoms and Hydroxyl Radicals ($\cdot\text{OH}/\cdot\text{O}$ -) in Aqueous-Solution. *J Phys Chem Ref Data* 17, 513-886.
- Cherepy, N.J., Liston, D.B., Lovejoy, J.A., Deng, H.M., Zhang, J.Z., **1998**. Ultrafast studies of photoexcited electron dynamics in gamma- and alpha-Fe₂O₃ semiconductor nanoparticles. *J Phys Chem B* 102, 770-776.

- Fuller, C.C., Harvey, J.W., **2000**. Reactive uptake of trace metals in the hyporheic zone of a mining-contaminated stream, Pinal Creek, Arizona. *Environ Sci Technol* 34, 1150-1155.
- Gerische, H., **1966**. Electrochemical Behavior of Semiconductors under Illumination. *J Electrochem Soc* 113, C75-&.
- Gilbert, B., Katz, J.E., Huse, N., Zhang, X., Frandsen, C., Falcone, R.W., Waychunas, G.A., **2013**. Ultrafast electron and energy transfer in dye-sensitized iron oxide and oxyhydroxide nanoparticles. *Phys Chem Chem Phys* 15, 17303-17313.
- Grätzel, M., Kiwi, J., Morrison, C.L., Davidson, R.S., Tseung, A.C., **1985**. Visible-light-induced photodissolution of α -Fe₂O₃ powder in the presence of chloride anions. *J Chem Soc Farad T* 1 81, 1883-1890.
- Gray, M.J., Malati, M.A., Rophael, M.W., **1978**. Point of Zero Charge of Manganese Dioxides. *J Electroanal Chem* 89, 135-140.
- Hansel, C.M., Zeiner, C.A., Santelli, C.M., Webb, S.M., **2012**. Mn(II) oxidation by an ascomycete fungus is linked to superoxide production during asexual reproduction. *Proc Natl Acad Sci U S A* 109, 12621-12625.
- Hatchard, C.G., Parker, C.A., **1956**. A New Sensitive Chemical Actinometer. II. Potassium Ferrioxalate as a Standard Chemical Actinometer. *P R Soc A* 235, 518-536.
- Hochella, M.F., Lower, S.K., Maurice, P.A., Penn, R.L., Sahai, N., Sparks, D.L., Twining, B.S., **2008**. Nanominerals, mineral nanoparticles, and Earth systems. *Geochim Cosmochim Acta* 72, A382-A382.
- Kimball, B.A., Callender, E., Axtmann, E.V., **1995**. Effects of Colloids on Metal Transport in a River Receiving Acid-Mine Drainage, Upper Arkansas River, Colorado, USA. *Appl Geochem* 10, 285-306.
- Luther III, G.W., **2005**. Manganese(II) oxidation and Mn(IV) reduction in the environment - Two one-electron transfer steps versus a single two-electron step. *Geomicrobiol J* 22, 195-203.
- Madison, A.S., Tebo, B.M., Mucci, A., Sundby, B., Luther, G.W., 3rd, **2013**. Abundant porewater Mn(III) is a major component of the sedimentary redox system. *Science* 341, 875-878.
- Marafatto, F.F., Strader, M.L., Gonzalez-Holguera, J., Schwartzberg, A., Gilbert, B., Pena, J., **2015**. Rate and mechanism of the photoreduction of birnessite (MnO₂) nanosheets. *Proc Natl Acad Sci U S A* 112, 4600-4605.
- Maruska, H.P., Ghosh, A.K., **1978**. Photocatalytic Decomposition of Water at Semiconductor Electrodes. *Sol Energy* 20, 443-458.
- Montalti, M., Credi, A., Prodi, L., Gandolfi, M.T., **2006**. Handbook of photochemistry. *CRC press*.
- Morgan, J.J., **2000**. Manganese in natural waters and earth's crust: its availability to organisms. *Met Ions Biol Syst* 37, 1-34.
- Parker, C.A., **1953**. A New Sensitive Chemical Actinometer .1. Some Trials with Potassium Ferrioxalate. *P R Soc A* 220, 104-116.
- Parker, D.L., Sposito, G., Tebo, B.M., **2004**. Manganese(III) binding to a pyoverdine siderophore produced by a manganese(II)-oxidizing bacterium. *Geochim Cosmochim Acta* 68, 4809-4820.
- Peacock, C.L., Sherman, D.M., **2007**. Sorption of Ni by birnessite: Equilibrium controls on Ni in seawater. *Chem Geol* 238, 94-106.

- Post, J., **1999**. Manganese oxide minerals: Crystal structures and economic and environmental significance. *Proceedings of the National Academy of Sciences* 96, 3447-3454.
- Robinson, D.M., Go, Y.B., Mui, M., Gardner, G., Zhang, Z., Mastrogiovanni, D., Garfunkel, E., Li, J., Greenblatt, M., Dismukes, G.C., **2013**. Photochemical Water Oxidation by Crystalline Polymorphs of Manganese Oxides: Structural Requirements for Catalysis. *J Am Chem Soc* 135, 3494-3501.
- Sherman, D.M., **2005**. Electronic structures of iron(III) and manganese(IV) (hydr)oxide minerals: Thermodynamics of photochemical reductive dissolution in aquatic environments. *Geochim Cosmochim Acta* 69, 3249-3255.
- Simanova, A.A., Kwon, K.D., Bone, S.E., Bargar, J.R., Refson, K., Sposito, G., Pena, J., **2015**. Probing the sorption reactivity of the edge surfaces in birnessite nanoparticles using nickel(II). *Geochim Cosmochim Acta* 164, 191-204.
- Simanova, A.A., Peña, J., **2015**. Time-Resolved Investigation of Cobalt Oxidation by Mn(III)-Rich δ -MnO₂ Using Quick X-ray Absorption Spectroscopy. *Environ Sci Technol* 49, 10867-10876.
- Stone, A.T., **1983**. The reduction and dissolution of Mn(III) and Mn(IV) oxides by organics, W.M. Keck Laboratory of Environmental Engineering Science - Division of Engineering and Applied Science. *California Institute of Technology*, Pasadena, California, p. 323.
- Stumm, W., Morgan, J.J., **1996**. *Aquatic chemistry: chemical equilibria and rates in natural waters*. Wiley.
- Sunda, W.G., Huntsman, S.A., **1990**. Diel Cycles in Microbial Manganese Oxidation and Manganese Redox Speciation in Coastal Waters of the Bahama-Islands. *Limnol Oceanogr* 35, 325-338.
- Sunda, W.G., Huntsman, S.A., **1994**. Photoreduction of Manganese Oxides in Seawater. *Mar Chem* 46, 133-152.
- Tan, W.F., Lu, S.J., Liu, F., Feng, X.H., He, J.Z., Koopall, L.K., **2008**. Determination of the point-of-zero, charge of manganese oxides with different methods including an improved salt titration method. *Soil Sci* 173, 277-286.
- Tebo, B.M., Bargar, J.R., Clement, B.G., Dick, G.J., Murray, K.J., Parker, D., Verity, R., Webb, S.M., **2004**. Biogenic manganese oxides: Properties and mechanisms of formation. *Annual Review of Earth and Planetary Sciences* 32, 287-328.
- van Genuchten, C.M., Pena, J., **2016**. Sorption selectivity of birnessite particle edges: a d-PDF analysis of Cd(ii) and Pb(ii) sorption by δ -MnO₂ and ferrihydrite. *Environ Sci-Proc Imp*.
- Villalobos, M., **2015**. The Role of Surface Edge Sites in Metal(loid) Sorption to Poorly-Crystalline Birnessites. *ACS Symp Ser* 1197, 65-87.
- Villalobos, M., Toner, B., Bargar, J., Sposito, G., **2003**. Characterization of the manganese oxide produced by *Pseudomonas putida* strain MnB1. *Geochim Cosmochim Acta* 67, 2649-2662.
- Waite, T.D., **1990**. Photo-Redox Processes at the Mineral-Water Interface, *Mineral-Water Interface Geochemistry*, pp. 559-603.
- Webb, S.M., Dick, G.J., Bargar, J.R., Tebo, B.M., **2005**. Evidence for the presence of Mn(III) intermediates in the bacterial oxidation of Mn(II). *Proc Natl Acad Sci U S A* 102, 5558-5563.

CHAPTER 5

Zhang, J.Z., **2000**. Interfacial charge carrier dynamics of colloidal semiconductor nanoparticles. *J Phys Chem B* 104, 7239-7253.

Chapter 6. Photoreactivity of Ni-doped MnO₂ : pH dependent metal release reflects stabilization of photogenerated Mn(III) in the mineral structure

This chapter was written as a manuscript to be submitted for publication to Chemical Geology with the title « Irradiation of Ni-laden birnessite results in differential metal release as a function of pH », authored by Marafatto FF, Peña J.

6.1. Abstract

Layer manganese oxides (birnessite) are characterized by nanoscale dimensions and a high density of sorption sites, which make them effective sorbents of numerous trace metals. In sunlit aquatic environments, photoreduction of Mn oxides can potentially affect the mobility of associated trace metals due to the dissolution of the mineral to yield Mn(II), or accumulation Mn(III) on the mineral surface. However, the fate of trace metals adsorbed to birnessites under irradiation has only been studied in systems where mineral dissolution occurred, and not when irradiation led to accumulation of Mn(III) on the mineral. By irradiating suspensions of Ni-sorbed δ -MnO₂ at pH 4 and 8 and following the speciation of Ni and Mn in both the aqueous phase by wet chemical methods and in the solid phase by EXAFS spectroscopy, we show that 16% Mn(III) photogeneration leads to 50% Ni release at pH 4, with a redistribution of the remaining Ni from vacancy sites to edge sites. At pH 8, no Ni release occurs upon 5% Mn(III) photogeneration and only slight modifications in the Ni local coordination environment are observed. These results are relevant to surface aquatic environments that range from contaminated mining impacted sites to freshwater and saltwater bodies, where the distribution of Ni between the solid and aqueous phase can make the difference between having micronutrient or toxic effects to many life forms.

6.2. Introduction

Layer type Mn oxides (birnessite), are among the most widespread metal oxides on the Earth's surface (Post, 1999). These minerals are characterized by a high specific surface area

CHAPTER 6

and density of sorption sites both on particle edges and on octahedral vacancy sites (Sposito, 2008). Birnessite is also the strongest solid phase oxidant present in nature (Morgan, 2000; Remucal and Ginder-Vogel, 2014). A direct consequence of this reactivity is that the fate of many organic and inorganic species is coupled to the biogeochemical cycle of birnessite. Furthermore, these minerals can undergo precipitation and dissolution reactions on daily timescales in sunlit environments (Sunda and Huntsman, 1990; Haack and Warren, 2003). For example, the main formation pathway is through the enzymatic oxidation of aqueous Mn(II) to form MnO₂(s) with first rate constants of up to 10 hr⁻¹ (Morgan, 2005). Over similar timescales, the (photo)reductive dissolution of MnO₂ has been shown to yield aqueous Mn(II) in the presence of organic compounds (Sunda et al., 1983; Tebo et al., 2004). Sunlight irradiation of natural organic matter is also known to stimulate reactive oxygen species production in (Garg et al., 2011) which may lead to oxidative processes in both microorganisms and inorganic compounds (Tebo et al., 2005; Hansel et al., 2012), inhibiting microbial oxidation of Mn(II) (Sunda and Huntsman, 1994).

Birnessite is also known to influence trace metal speciation in diverse environments. For example, birnessites are the main solid phase sequestering Co, Ni, Zn and As from ocean waters in ocean nodules (Marcus et al., 2004; Peacock and Sherman, 2007), and multiple toxic trace metals in mining impacted streams (Fuller and Harvey, 2000; Haack and Warren, 2003; Fuller and Bargar, 2014). The release of trace metals in such environments may be influenced by the photoreduction of Mn oxides, but this process has not been scarcely studied. Kim et al. observed in the presence of humic acid, up to 1% release of pre-sorbed Cu(II) coupled to ~0.5 % Mn(II) was release from birnessite after 10 hours of simulated sunlight irradiation (Kim et al., 2014). Another study showed that the extent of As(III) oxidation to As(V) coupled to Mn(IV) and/or Mn(III) reduction and release of Mn(II) to solution was 25 % greater on the surface of birnessite after 8 hours of irradiation in a solar simulator compared to similar suspensions kept in the dark, (Shumlas et al., 2016). These studies showed that irradiation can influence contaminant behavior through partial desorption of the sorbed metal and enhanced metal reduction. Additionally, these studies also showed a release of Mn(II) in the dark. Manganese release was attributed to the nature of the Mn(III,IV)/As(III) redox couples investigated in the first study (Shumlas et al., 2016) and to the presence of organic compounds in the second study (Kim et al., 2014), where the oxidation of As(III) and organic compounds

by Mn was thermodynamically favourable. We have previously showed that irradiation of MnO₂ in the absence of electron donors other than water results in accumulation of Mn(III) in the interlayer region of the nanosheets without release of aqueous Mn(II) (Marafatto et al., 2015). However, the effect of sunlight on trace metal mobility in a system that undergoes photoreduction but without mineral dissolution is unknown.

The structure of birnessite, and in particular the amount and crystallographic location of Mn(III), is known to strongly affect their sorptive properties (Wang et al., 2012; Simanova et al., 2015; Simanova and Peña, 2015). For example, up to 30% Mn(III) accumulation on the mineral ($\text{mol Mn(III) mol}^{-1} \text{Mn}_{\text{tot}}$) leads to Ni sorption primarily on particle edges with respect to vacancy sites, in contrast to Mn(III)-free δ -MnO₂ (Simanova et al., 2015). The overall sorption capacity for Ni is also diminished in Mn(III)-rich δ -MnO₂ (Simanova et al., 2015). Similarly, Mn(II) sorption on the mineral at pH 4 renders Ni and Zn unable to sorb on vacancy sites (Hinkle et al., 2015) and leads to Zn release at pH 6.5 (Lefkowitz and Elzinga, 2015). In contrast, there is little to no effect above pH 7 on Zn sorption (Hinkle et al., 2015; Lefkowitz and Elzinga, 2015). Although Hinkle et al. (2015) focused on Mn(II) sorption without quantification of Mn(III) production in an anoxic system, it is very likely that Mn(II) underwent comproportionation with Mn(IV) to yield Mn(III), in particular at pH 7, since this process is well documented over a broad range of pH (Lanson et al., 2000; Elzinga, 2011; Lefkowitz et al., 2013). In another study, through refinement of powder X-ray diffraction data, Grangeon et al. (2008) showed that Mn(III) outcompetes Ni for the mineral surface at pH 4, but is unable to do so at pH 8. All these studies showed that the presence or accumulation of Mn(III) in a trace-metal laden birnessite affected the mobility of the surface-sorbed metals. Therefore, we expect similar effects during photoreduction of birnessite. Specifically, we expect that the enhanced photogeneration of Mn(III) at low pH (**Chapter 5**) will lead to competition between Ni and Mn(III) for the sorption sites in the mineral. On the other hand, at high pH this effect will be reduced both by the lower amount of Mn(III) formed and the lower affinity of the surface for Mn(III) compared to Ni.

This objective of this work is to investigate the effect of visible light irradiation both on the uptake and release of Ni from birnessite minerals as a function of pH and on the rates of Ni-laden birnessite photoreduction. Nickel was chosen because it does not undergo

CHAPTER 6

reduction or oxidation, and its sorption mechanism in the dark is well established (Manceau et al., 2007; Peacock and Sherman, 2007; Grangeon et al., 2008; Pena et al., 2010). To investigate the effect of irradiation on Ni mobility from birnessite, dilute synthetic mineral suspensions were prepared with a Ni surface loading of 5 % (mol Ni mol⁻¹ Mn) at pH 4 and pH 8 and irradiated in a flow through system under 400 nm LED irradiation for 96 hours under constant pH control. The amount of solid-phase Mn(III) produced through photoreduction as well as changes in the Ni surface loading were monitored for the duration of the experiment by wet chemical methods. X-ray absorption spectra (XAS) at the Mn and Ni K-edge were collected at the end of the experiment to investigate the local coordination environment of Ni on dark and irradiated samples. Our results show that mineral irradiation leads to 50 % desorption of Ni and modifies the coordination environment of the remaining, surface-bound Ni at pH 4, whereas no release and only slight changes in the local coordination environment are observed at pH 8. These results have strong implications in predicting the fate of Ni in multiple environmental settings where light may play a role in determining the speciation of Ni associated with birnessite minerals (Fuller and Harvey, 2000; Haack and Warren, 2003; Peacock and Sherman, 2007; Atkins et al., 2014).

6.3. Materials and methods

All chemicals were reagent grade and purchased from Sigma-Aldrich unless specified otherwise. All solutions were prepared with fresh ultrapure Milli-Q water (18 Ω • cm). The δ-MnO₂ phase used in sorption and irradiation experiments was synthesized and characterized previously (Mineral B2 from **Chapter 3**). Briefly, the synthetic mineral had an average Mn oxidation number (AMON) of 4.03 ± 0.01, a dry specific surface area (SSA), as measured by Brunauer Emmet Teller (BET) theory N_{2(g)} absorption, of 163 ± 8 m²/g, and a Na:Mn molar ratio of 0.3. The mineral phase was from the same suspension as the one used in **Chapter 5**, and comparable to the one used in **Chapter 4**.

Ni sorption. Five hundred mL suspensions containing 250 μM δ-MnO₂ (on a Mn molar basis) were prepared in 10 mM NaCl electrolyte in aluminum foil covered glass bottles and set to equilibrate on a magnetic stir plate in the dark. The pH was set to 4 or 8 on a Metrohm 906 STAT titrando automatic titrator using 50 mM HCl or NaOH titer solutions, respectively. After 4-5 hours of pH equilibration (the target pH was reached after 1 hour), aliquots of a stock NiCl₂

(8.3 mM) solution were added to the suspensions to achieve a 5% Ni loading on a Mn molar basis and to have no extra Ni in solution. The suspensions were then left to equilibrate for 2 days in the dark, keeping the pH constant. A speciation calculation with the MINEQL+ software (Schecher and McAvoy, 1992) showed that the suspensions were undersaturated with respect to homogenous precipitation of $\text{Ni}(\text{OH})_2$ at the Ni concentrations used in the sorption experiments (data not shown).

Irradiation of mineral suspensions. After the 2-day equilibration in the dark, each suspension was divided into two 250 mL aliquots in aluminum foil covered glass bottles. One suspension was recirculated in a flow-through photoreactor described previously (**Chapter 2, Annex 1**). Briefly, the photoreactor comprised a flow through quartz cuvette in a peristaltic pump driven system. Irradiation was provided by an array of 3x 1 W light emitting diodes (LEDs) tuned at 400 nm. The second aliquot was left in the dark, under the same conditions as the irradiated sample. The pH of the irradiated suspension was maintained constant by using a pH stat during the entire duration of the experiment, whereas the pH was monitored regularly on the dark aliquot (Metrohm 912 pH meter). These experiments were not conducted in excess PP since the presence of PP would have led to the formation of a Ni-PP complex that could interact with the 400 nm irradiation wavelength (**SI Text**). An equal amount of the acid or base added by the titrator to the irradiated sample was added manually to the dark control twice per day. Both suspensions were bubbled with humidified $\text{N}_{2(\text{g})}$ to minimize the effect of atmospheric $\text{CO}_{2(\text{g})}$ on the pH of the suspension. We previously showed that there are no changes in the rate and mechanism of MnO_2 photoreduction in oxygenated versus N_2 -purged conditions (Marafatto et al., 2015). The duration of each irradiation experiment was 96 hours, and experiments were conducted in triplicates under the same conditions.

Prior to starting the irradiation experiment, a 1 mL sample aliquot was taken from both suspensions and digested in 2 mL of 0.01 M $\text{H}_2\text{C}_2\text{O}_4$ and 3% HNO_3 and diluted with 9 mL of MQ water for $[\text{Mn}_{\text{TOT}}]$ and $[\text{Ni}_{\text{TOT}}]$ determination by inductively coupled plasma optical emission spectrometry (ICP-OES - Perkin Elmer Optima 8300). A 5 mL aliquot was filtered through a 0.2 μm polyethersulfone (PES) filter and measured by ICP-OES for $[\text{Mn}_{\text{AQ}}]$ and $[\text{Ni}_{\text{AQ}}]$ after acidification with 0.1 mL of 65% HNO_3 . Seven mL aliquots of each sample were collected into 15 mL PP centrifuge tubes, to which 0.75 mL of a 120 mM sodium

CHAPTER 6

pyrophosphate (PP) solution at pH 4 or 8 were added. The tubes were then covered in aluminum foil and equilibrated in the dark for 48 hours to extract Mn(III). Once equilibrated, 1 mL aliquots were collected and prepared for ICP-OES determination of $[\text{Mn}_{\text{TOT}}]$ as described previously, while the remaining suspensions were filtered through 0.2 μm PES filters and the aqueous [Mn(III)-PP] complexes were quantitated by UV-Vis spectrophotometry ($\epsilon_{254 \text{ nm}} = 6562 \text{ L mol}^{-1} \text{ cm}^{-1}$) with 1 cm path length quartz cuvettes using a 12.5 mM PP solution as a blank. We previously showed that all Mn_{AQ} measured is found as Mn(III)-PP (Marafatto et al., 2015). Sample aliquots were collected 3 times per day for aqueous Mn and Ni determination, two times per day for Mn(III)-PP quantification, and at the beginning and the end of the experiment for total Mn and Ni determination.

The amount of Ni sorbed on the mineral in the dark and in the light was evaluated by calculating the surface excess (q) expressed in $\text{mol Ni mol}^{-1} \text{ Mn}$, which is obtained by normalizing the moles of Ni adsorbed on the mineral minus the moles of Ni in solution to the moles of Mn total minus the moles of Mn in solution. These units are more useful than the conventional units of mol Ni kg^{-1} sorbent, since they facilitate the interpretation of the results in terms of vacancy site occupancy (Pena et al., 2010). The concentration of Mn in solution was below the detection limit of the instrument (0.5 μM Mn), therefore the value of q was obtained as $[(\text{Ni}_{\text{TOT}} - \text{Ni}_{\text{AQ}}) / \text{Mn}_{\text{TOT}}]$.

The rate of Mn(III) production for Ni-laden $\delta\text{-MnO}_2$ was determined by linear interpolation of the moles of Mn(III) generated after irradiation (after subtracting any Mn(III) generated in the dark) versus irradiation time and the slope represented the Mn(III) photoreduction rates, similarly as described in **Chapter 5**. The quantum yield for the photoreduction process, defined as the amount of Mn(III) formed per photon absorbed, was also calculated as described previously (**Chapter 5**). The results from Ni-laden $\delta\text{-MnO}_2$ were compared to the Mn(III) production rate in the absence of Ni to evaluate the effect of Ni on the photoreduction of $\delta\text{-MnO}_2$.

X-ray absorption spectroscopy. Separate samples were prepared for EXAFS spectroscopy following the same procedure as for the photoreduction experiments. These suspensions contained a total Mn concentration of 500 μM , compared to the photoreduction experiments that had a total concentration of 250 μM . Representative aliquots of the irradiated

sample and the dark control for the pH 8 and pH 4 experiments were collected after 96 hours of irradiation onto 0.45 μm nitrocellulose filters for XAS experiments. We calculated the amount of necessary sample to filter to give an absorption edge step of 1 at the Mn K edge with the sample mounted at 45° with respect to the incident beam (Kelly et al., 2008).

Nickel and Mn K-edge X-ray absorption (XA) spectra for the pH 4 samples were collected at beamline 23 of the European Synchrotron Radiation Facility (ESRF) using a Si 111 double crystal monochromator. The monochromator energy was calibrated using either a Mn or Ni metal foil and setting the first inflection point in the first derivative of the spectrum to 6539 or 8333 eV, respectively. Samples were mounted at 45° with respect to the incident beam on plastic sample holders, inserted in a liquid He cryostat equipped with a heating unit that increased the temperature on the sample to 80 K (to approximate the data acquisition conditions used at SSRL). Manganese K-edge spectra were collected in transmission mode up to k of 14 \AA^{-1} whereas Ni K-edge spectra were collected in fluorescence mode on a 13 element Ge detector. For data acquisition the vertical slit size was 1 mm and the horizontal slit size was varied between 4 mm and 6 mm. Three to 6 replicate scans were collected per sample per absorption edge.

The X-ray absorption spectra for the pH 8 samples were collected on the Mn K-edge and the Ni K-edge at beamline 4-1 of the Stanford Synchrotron Radiation Lightsource (Menlo Park, USA), using a Si 220, $\phi = 90^\circ$ double crystal monochromator. The incident beam was detuned to 70% at 10 keV to minimize higher-order harmonics. Vertical sample slit size was 1 mm, whereas the horizontal slit size was varied between 6 and 8 mm. The monochromator energy was calibrated with a Mn and Ni metal foil. Samples were mounted on aluminium sample holders, placed at a 45° angle with respect to the incident beam in a LN_2 cryostat (77 K). Mn K-edge spectra were collected up to k of 14 \AA^{-1} in transmission mode, whereas Ni K-edge spectra were collected up to k of 12 \AA^{-1} in fluorescence mode on a passivated implanted planar silicon (PIPS) detector equipped with soller slits to filter elastic scatter and a Co(III) foil as a filter for fluorescent photons of lower energy. Three to 4 replicate scans were collected per sample and edge.

Data reduction and analysis of the X-ray absorption near edge structure (XANES) and the extended X-ray absorption fine structure (EXAFS) spectra was carried out with Sixpack

(Webb, 2005a), a graphical user interface (GUI) built on the IFEFFIT engine (Newville, 2001). Replicate scans were aligned to a common energy scale using the metal foils to average both the fluorescence and transmission spectra. Background subtraction of the averaged spectra was achieved by fitting the pre-edge region with a Gaussian function and the post-edge region with a quadratic function, R_{bkg} was set to 1 Å, no clamps, the k-weight was set to 3, and the E_0 set at 6554 for the Mn K-edge data and 8347 for the Ni K-edge data. The k-weighted EXAFS were then Fourier-transformed with a Kaiser-Bessel transformation window in the 2-11 Å⁻¹ range for the Ni data, and the 2-14 Å⁻¹ range for the Mn data. The Mn data was analyzed qualitatively to confirm changes in the valence and local coordination environment of Mn before and after irradiation.

Shell by shell fitting of Ni EXAFS. Shell-by-shell fitting of the Ni K-edge EXAFS was carried out by fitting the experimental data with the EXAFS equation (Kelly et al., 2008) using the FEFF EXAFS fitting module of SIXPACK (Webb, 2005a). The aim of this fitting procedure was to determine the structural parameters that describe the local coordination environment of Ni on δ-MnO₂. Specifically, the Ni-Mn interatomic distances can be used to distinguish between corner-sharing and edge-sharing complexes, whereas the fitted coordination number can be used to estimate the fraction of Ni adsorbed on edge sites versus vacancy sites. The EXAFS spectra were fit using Ni-O and Ni-Mn scattering paths built with the FEFF v6L code using the atomic coordinates from density functional theory (DFT) geometry-optimized models of Ni adsorbed onto MnO₂ in a triple corner sharing (TCS) complex at a vacancy site or incorporated (INC) into the nanosheet, respectively (Pena et al., 2010; Simanova et al., 2015).

All EXAFS spectra were fit with a simplified 2-shell model in the 1- 4.1 Å $R + \Delta R$ range, which included only single scattering paths, and an extended model that included single and multiple scattering paths up to 6.1 Å $R + \Delta R$. All spectra were fit in R-space over a k-range of 2.5 – 10 Å⁻¹ and 3 – 11.9 Å⁻¹, $dk = 1$ and $dk = 3$ for the pH 4 and pH 8 data, respectively. A dK value of 1 was chosen over $dK = 3$ for the pH 4 data because it fitted the data with better precision as could be observed visually (**Figure S2**). We observed that the differences in the FT window in the $dk = 1$ and $dk = 3$ case did not sensibly cut out important data in one case or the other, but only glitches which should not affect the FT-EXAFS

considerably (Calvin, 2013) (**Figure S3**). An amplitude reduction factor (S_0^2) of 0.96 was applied based on previous studies (Pena et al., 2010). After evaluating the uncertainties on fitted parameters and visual inspection of the fit of the magnitude and imaginary part of the data, the goodness of fit was evaluated by the R-factor (a value equal or below 0.02 was deemed reasonable (Calvin, 2013)) and the reduced χ^2 as outputted by the fitting program. The model of choice as well as the constraints on the fitted interatomic distances (R), coordination numbers (CN) and Debye-Waller factors (σ^2) were selected based on chemical reasoning on the wet chemical results (q value, Mn(III) content). The R-value on all fits (≤ 0.02) indicated a satisfactory goodness of fit (Calvin, 2013).

6.4. Results

Mn photoreduction rates. The photoreduction rates for Ni-laden δ -MnO₂ at pH 4 and 8 are shown in **Figure 1** and compared with the photoreduction rates of δ -MnO₂ at pH 4 and 8 (**Chapter 5**). The data are affected by a large amount of scatter, which is attributed to particle aggregation during irradiation because of the 10 mM NaCl present as the background electrolyte. Visually observable aggregation of the mineral nanoparticles as a function of pH (**Chapters 3 and 5**) led to poor sampling, especially for the Mn_{tot} sample measured by ICP-OES, which led to scatter in the data. The aggregation was found to increase with time both in the dark and in the irradiated sample. Also, the effect of aggregation was greater in the Ni-laden δ -MnO₂ than in the δ -MnO₂ without Ni (**Chapter 5**), and greater in the pH 4 samples than in the pH 8 samples. Notwithstanding the scatter in the measurements, we calculated the photoreduction rates from linear regression of the data. The amount of Mn(III) formed was $0.88 \pm 0.46 \mu\text{mol Mn(III) day}^{-1}$ for the pH 4 series, and $0.18 \pm 0.08 \mu\text{mol Mn(III) day}^{-1}$ for the pH 8 series. The rates of photoreduction for δ -MnO₂ without Ni, for comparison, were $0.97 \pm 0.52 \mu\text{mol Mn(III) day}^{-1}$ and $0.19 \pm 0.12 \mu\text{mol Mn(III) day}^{-1}$ for the pH 4 and pH 8 data, respectively (uncertainties reported as 95 % confidence interval). The amount of Mn(II) released was below the detection limit (0.5 μM) of the ICP-OES. The quantum yield for the photoreduction process was quantified as $1.69 \pm 0.37 \times 10^{-3}$ for the pH 4 series and $3.11 \pm 0.67 \times 10^{-4}$ for the pH 8 series. The quantum yield for the photoreduction of δ -MnO₂ without Ni, on the other hand, was $1.08 \pm 0.2 \times 10^{-3}$ and $2.5 \pm 1.2 \times 10^{-4}$ for the pH 4 and pH 8 series, respectively (errors determined as standard deviation on replicates). A total of 5 % mol Mn(III)

$\text{mol}^{-1} \text{Mn}_{\text{tot}}$ was present in the mineral after 96 hours of irradiation at pH 8, compared to 16 % $\text{mol Mn(III) mol}^{-1} \text{Mn}_{\text{tot}}$ at pH 4 for the samples prepared for XAS experiments (**Table 1**), which was comparable to the amount generated in the photoreduction rate triplicate experiments.

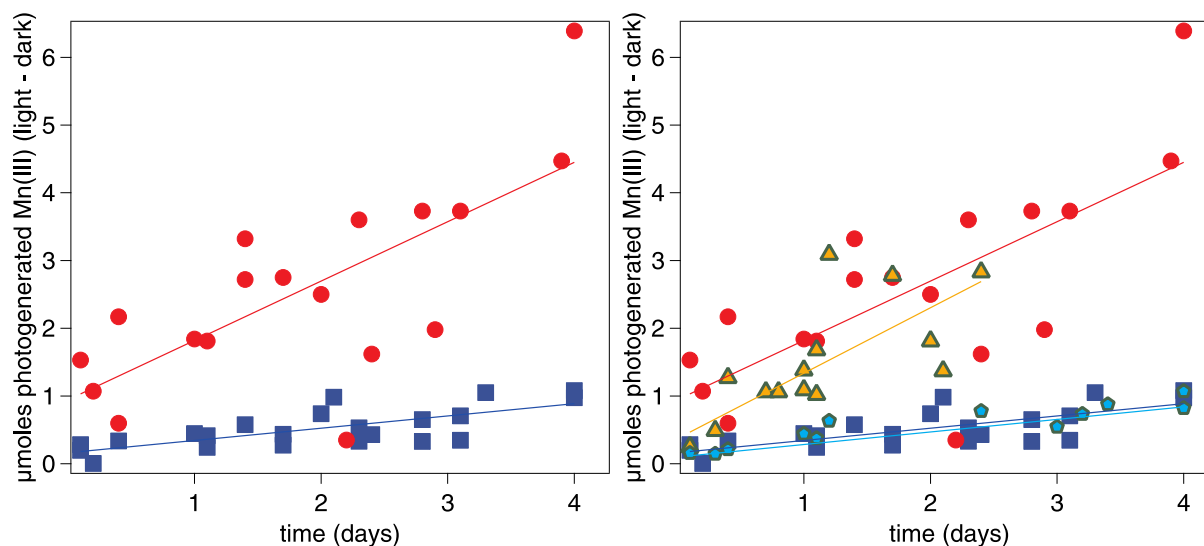


Figure 1. a - *left*) Manganese photoreduction rates in Ni-laden $\delta\text{-MnO}_2$ as a function of pH (pH 4 red circles, pH 8 blue squares); b - *right*) Manganese photoreduction rates for Ni-laden $\delta\text{-MnO}_2$ as a function of pH (symbols as in left figure) compared with the photoreduction trends of $\delta\text{-MnO}_2$ without Ni (pH 4 yellow triangles, pH 8 cyan pentagons). Although the data is strongly scattered, the rates are comparable.

Table 1: summary of the wet chemical data for the samples for which XAS data was collected.

Sample ID	pH _{aq}	qNi (mol Ni mol ⁻¹ Mn)	qMn(III) (mol Mn(III) mol ⁻¹ Mn)
Ni laden $\delta\text{-MnO}_2$ pH 4 dark	4.0	0.04	0.05
Ni-laden $\delta\text{-MnO}_2$ pH 4 light	4.0	0.02	0.16
Ni-laden $\delta\text{-MnO}_2$ pH 8 dark	8.0	0.02	0.01
Ni-laden $\delta\text{-MnO}_2$ pH 8 light	8.0	0.02	0.02

Ni release and readsorption during irradiation. The surface excess of Ni (q) on $\delta\text{-MnO}_2$ as a function of time is shown in **Figure 2a** for the pH 4 series and in **Figure 3a** for the pH 8 series. About 6% surface loading was achieved both at pH 4 and pH 8 at the beginning of the experiment. A gradual release of Ni was observed in the pH 4 data with irradiation, reaching ~50 % of the initially sorbed Ni after 96 hours of irradiation (~3 % Ni surface excess). The pH 8 data, on the other hand, did not show any net Ni release during irradiation. The experiments run for XAS data collection for which the initial surface excess was different (4 % vs 6% Ni in the dark), but the Ni dynamics were similar (~50% of the originally sorbed Ni was released after 96 hours of irradiation at pH 4) as shown by plotting the Ni surface excess

(q) normalized to the Ni surface excess at the beginning of the experiment (q_{ini}) (Figures 2b and 3b).

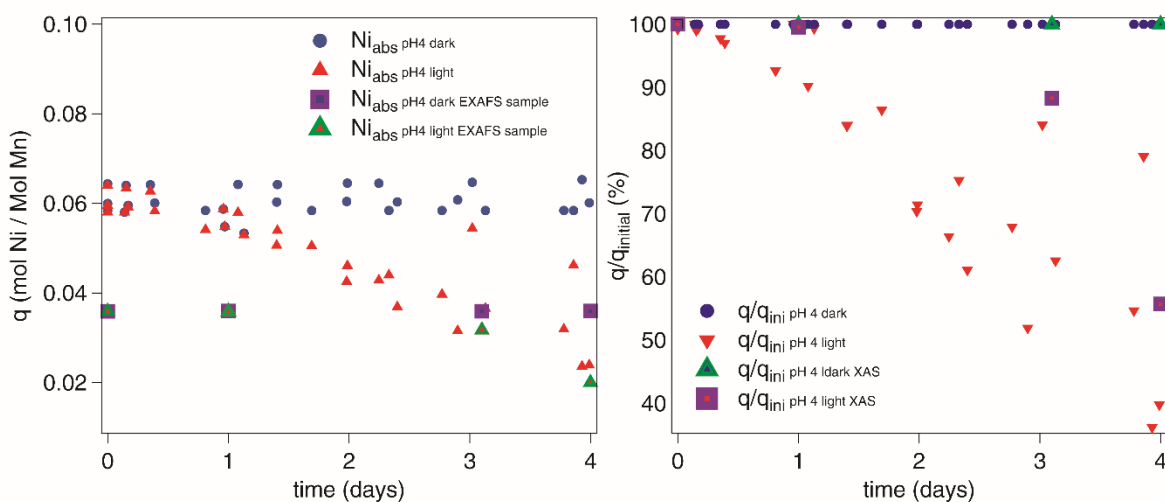


Figure 2. *a – left*) Ni surface loading as a function of irradiation time for the pH 4 experiments. Irradiation of Ni-laden δ -MnO₂ at pH 4 results in up to 50% Ni release to solution. The experiment from which the XAS sample was collected shows half the surface loading, but the same trend (up to 50% Ni release with irradiation); *b – right*) Ni surface loading normalized to the initial loading (~loading in the dark sample), to show that the Ni release in the XAS sample is comparable to the Ni release in the replicate experiments.

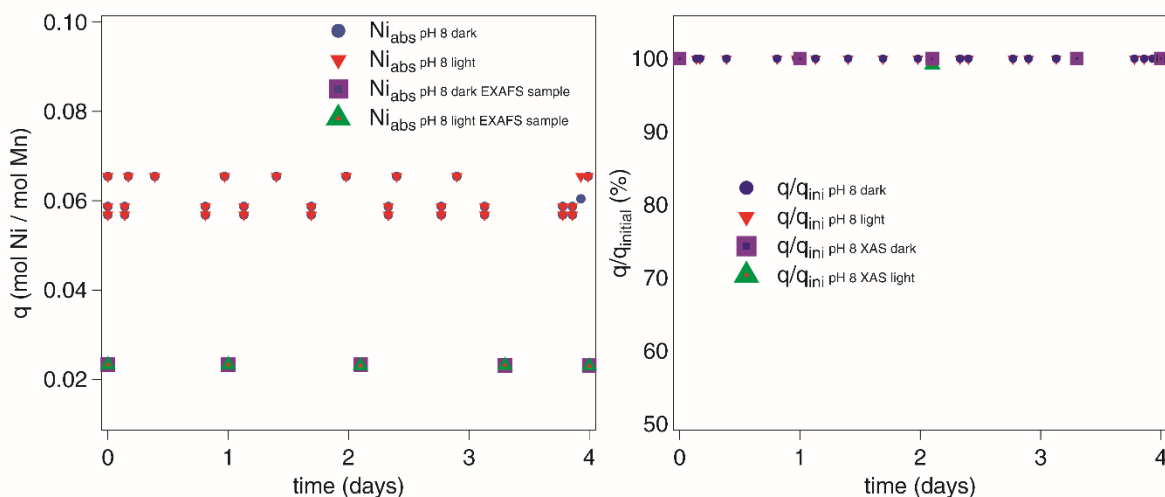


Figure 3. *a – left*) Ni surface loading as a function of irradiation time for the pH 8 experiments. Irradiation of Ni-laden δ -MnO₂ at pH 8 results in no Ni release to solution. The experiment from which the XAS sample was collected shows half the surface loading, but the same trend (no Ni release); *b – right*) Ni surface loading normalized to the initial loading (~loading in the dark sample), to show that the Ni release in the XAS sample is comparable to the Ni release in the replicate experiments.

Mn K-edge X-ray absorption spectroscopy. Mn X-ray absorption spectra for the pH 4 and pH 8 series are shown in Figures 4 and 5, respectively. The XANES spectra from the pH

4 samples shows a slight shift of the white line position to lower energies, consistent with a decrease in the AMON of the mineral, as expected from the wet chemical data ($\sim 16\%$ Mn(III) accumulation). Attempts to quantify the proportions of Mn(III) and Mn(IV) by linear combination fitting of the data using spectra for δ -MnO₂ containing only Mn(IV) and Mn₂O₃ for Mn(IV) and Mn(III), respectively, did not show appreciable differences between the dark and irradiated samples. The lack of differences was related to the low sensitivity of this technique to small changes in AMON and the high dependence on the reference spectra used (Manceau et al., 2012). The pH 8 data, on the other hand, did not show differences between dark and irradiated samples, as expected from the low amount of Mn(III) formed ($\sim 4\%$). This value is below the detection limit (5-10%) of the AMON determination by XANES (Bargar et al., 2005).

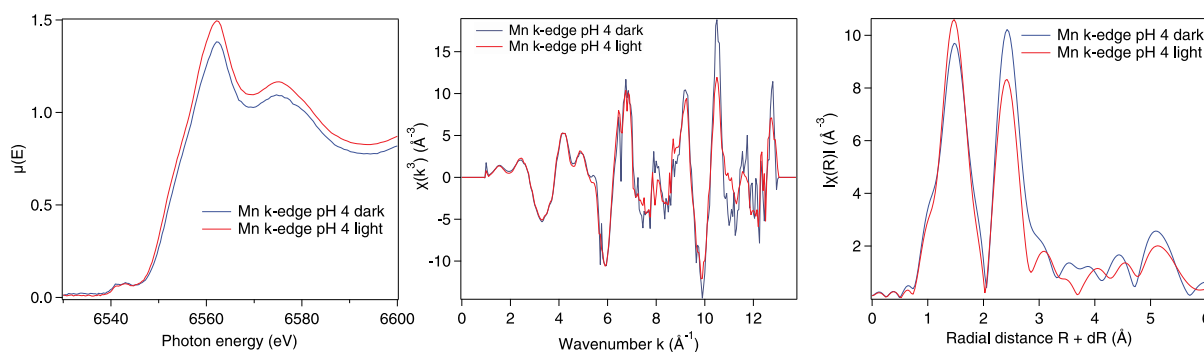


Figure 4. Manganese k-edge X-ray absorption spectra for Ni-laden δ -MnO₂ at pH 4 in the light vs in the dark. *Left*) XANES; *center*) EXAFS; *right*) Fourier transformed EXAFS.

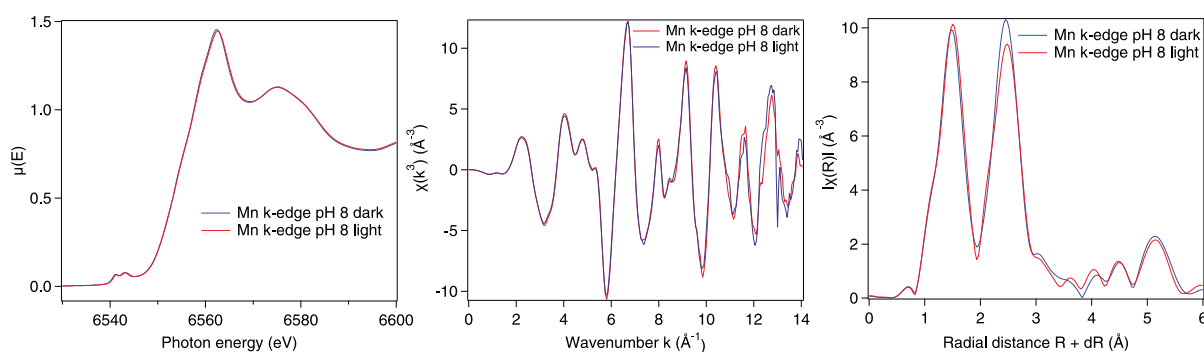


Figure 5. Manganese k-edge X-ray absorption spectra for Ni-laden δ -MnO₂ at pH 8 in the light vs in the dark. *Left*) XANES; *center*) EXAFS; *right*) Fourier transformed EXAFS.

The EXAFS spectra for both pH series show the « staircase » feature between 3 and 6 \AA^{-1} , characteristic feature of layer type Mn oxides. The spectra of both series also lack a peak

splitting in the « indicator » feature between 7.9 and 8.1 Å⁻¹, indicating low to no Mn(III) in the layers (Manceau et al., 2004). The FT-EXAFS spectra of the pH 4 series shows a reduction in the Mn-Mn peak amplitude (the second peak at ~2.3 Å R + ΔR), consistent with the presence of Mn(III) octahedrons in out-of-plane structural sites, which introduce different Mn-Mn interatomic distances. Additionally, the Jahn-Teller distortion that characterizes the Mn(III) octahedron also lowers the amplitude of this peak because of a splitting of the Mn-O distances (Webb, 2005b). In the FT-EXAFS spectra of the pH 8 series, a slight reduction in the Mn-Mn peak amplitude can be observed (**Figure 5**). This observation is consistent with the presence of some Mn(III), but considerably less than in the pH 4 data. Manganese(III) in the interlayer is also evidenced by the shoulder in the FT-EXAFS on both pH 4 and pH 8 datasets, at ~3 Å R + ΔR.

Ni K-edge XAS spectroscopy. The Ni K-edge EXAFS spectra for the pH 4 data are shown in **Figure 6a** whereas the FT-EXAFS spectra are shown in **Figure 6b**. The EXAFS spectra are strongly glitched, nevertheless there are apparent differences between the dark and light sample, which are reflected in the FT-EXAFS spectra. In particular, the EXAFS spectrum of the dark sample contains stronger amplitude oscillations than the irradiated sample at higher k-values. In particular, the oscillations between 6.5 and 8.2 Å⁻¹ are of greater amplitude, with two distinct peaks that are less discernible in the light sample. Greater amplitudes and a peak splitting are also visible, but to a lower extent, in the oscillations between 4 and 6.5 Å⁻¹. The greater amplitude in oscillations in the dark sample is consistent with a greater order in the coordination environment and a greater number of near neighbors. These differences are reflected in the FT-EXAFS spectra, which show four main features: a first sharp peak at ~1.5 Å R + ΔR, a second peak at ~3.0 Å R + ΔR, a third small peak at ~3.9 Å R + ΔR and a fourth broad peak at ~4.8 Å R + ΔR. These peaks are consistent with the interatomic distances for first and second shell Ni-O and Ni-Mn, respectively. In particular, the Ni-Mn shells reflect Ni adsorbed to vacancy sites or particle edges in a triple or double corner sharing configuration, respectively (Pena et al., 2010; Simanova et al., 2015). About 50 % reduction in the amplitude of the second peak is observed in the irradiated sample compared to the dark sample. This change in peak amplitude is consistent with an increase in disorder and/or a reduction in the number of Mn neighbors at this distance. The latter scenario would result from a change in the

proportion of Ni sorbed at vacancies (6 Mn near neighbors) versus particle edges (2-3 Mn near neighbors).

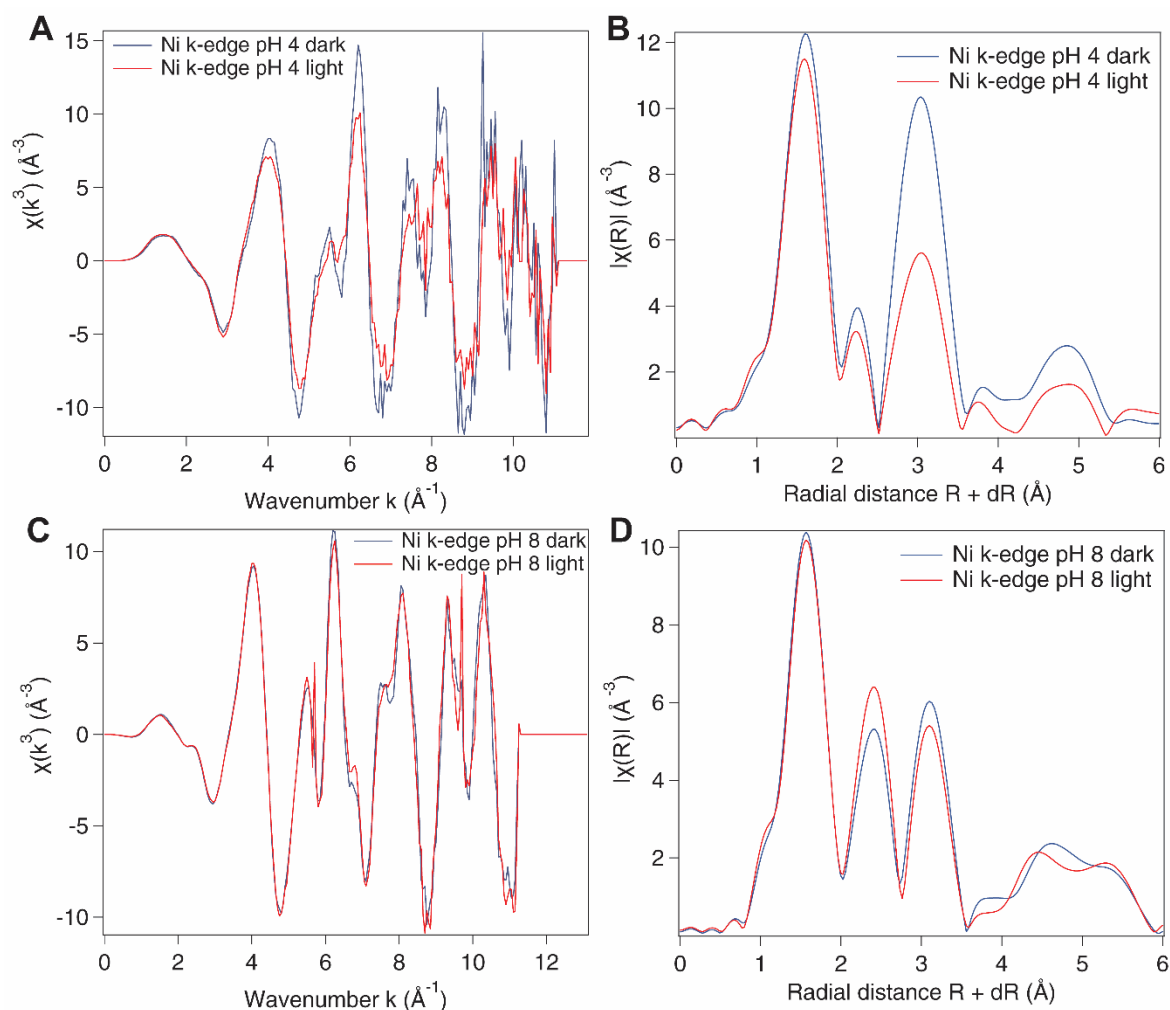


Figure 6. A) Ni K-edge EXAFS for the pH 4 light vs dark samples; B) Ni K-edge FT-EXAFS for the pH 4 light vs dark samples; C) Ni K-edge EXAFS for the pH 8 light vs dark samples; D) Ni K-edge FT-EXAFS for the pH 8 light vs dark samples.

The Ni K-edge EXAFS spectra for the pH 8 data are shown in **Figure 6c** whereas the FT-EXAFS spectra are shown in **Figure 6d**. We observed only modest differences in the EXAFS spectra of the light and dark samples compared to the pH 4 data. Among these differences, an increase in the shoulder at 7 \AA^{-1} is visible in the dark compared to the light sample. In addition, irradiation leads to the disappearance of the shoulder in the peak around 11 \AA^{-1} . In addition to the peaks observed for the pH 4 data, the FT-EXAFS spectra of the pH 8 samples show an additional peak at $\sim 2.5 \text{ \AA } R + \Delta R$, which is consistent with Ni in a double

edge sharing configuration at particle edges or incorporated into the nanosheet as predicted by the INC model (Pena et al., 2010; Simanova et al., 2015). Additionally, a broad peak composed of 3 overlapping peaks can be observed between 4 and 6 Å $R + \Delta R$. The first and third peak are consistent with distances for Ni-O and Ni-Mn on a vacancy in a triple corner sharing configuration. The second peak at ~ 4.2 Å $R + \Delta R$, on the other hand, is consistent with the second Ni-Mn shell when Ni is incorporated into the nanosheet (Pena et al., 2010; Simanova et al., 2015). The comparison between the irradiated and dark sample shows a slight reduction in the amplitude of the peak relative to Ni adsorbed as a triple corner sharing complex, and an increase in the amplitude of Ni incorporated in the nanosheet.

Shell-by-Shell fits of Ni EXAFS spectra in the $R + \Delta R < 4.1$ Å range. Fits of the Ni-O and Ni-Mn shells in the 1 - 4.1 Å range for the pH 4 and 8 data are shown in **Figure 7** and **8** and fit parameters are reported in **Tables 2** and **3**. The fits of the pH 4 data included a Ni-O path and a Ni-Mn path from the TCS model, which represent the first oxygen coordination shell of Ni (Ni-O₁) and the first Mn coordination shell of Ni when Ni is sorbed at a vacancy or edge site as a corner sharing complex (Ni-Mn_{CS}). All values for CN, R and σ^2 values were floated. The pH 8 data required an additional Ni-Mn path for Ni incorporated into the nanosheet (Ni-Mn_{INC}). Following the approach in Pena et al. (2010), the CN for the Ni-Mn peak at ~ 3 Å $R + \Delta R$ and that at ~ 2 Å $R + \Delta R$ were constrained to their theoretical values and a species abundance scaling factor (f) was used to evaluate the proportion of Ni sorbed on vacancy sites and incorporated into the nanosheet.

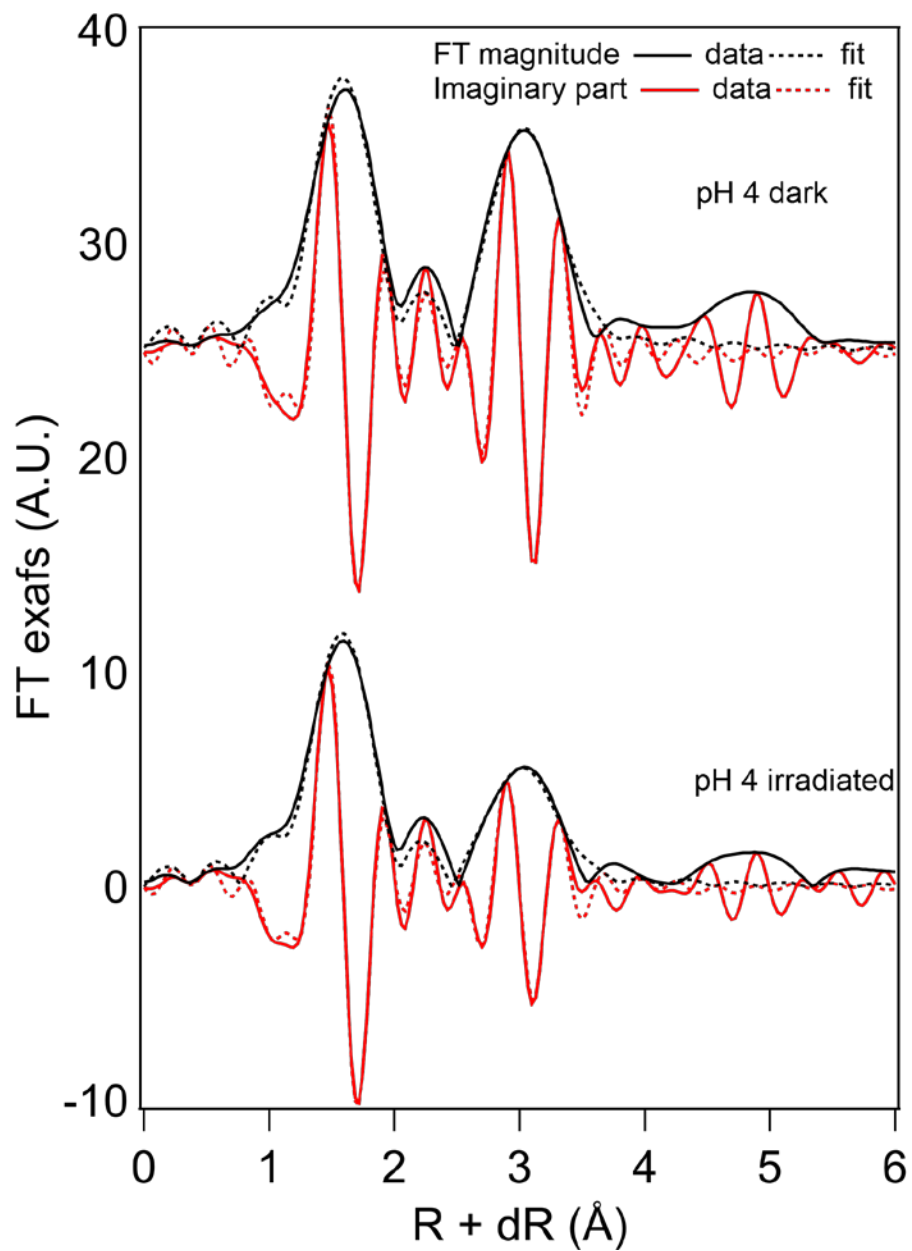


Figure 7. Ni k-edge fourier transformed EXAFS (magnitude + imaginary part) and shell by shell fits (magnitude + imaginary part) for the pH 4 samples in the dark (above) and after irradiation (below) in the simplified 2-shell fit. Fit parameters are shown in **Table 2**.

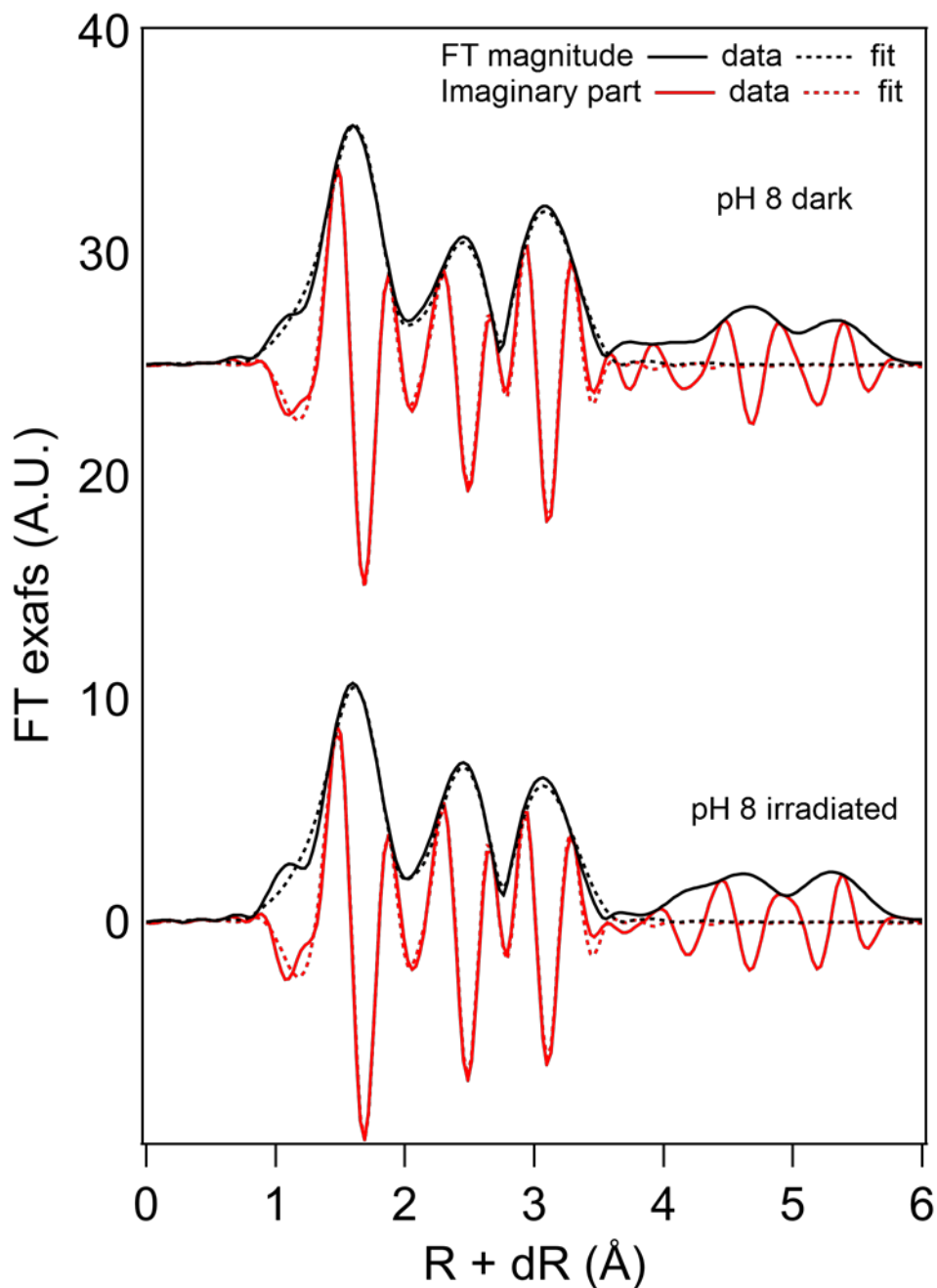


Figure 8. Ni k-edge fourier transformed EXAFS (magnitude + imaginary part) and shell by shell fits (magnitude + imaginary part) for the pH 8 samples in the dark (above) and after irradiation (below) in the simplified 2-shell fit. Fit parameters are shown in **Table 3**.

In the pH 4 data, the fit-derived distances for the Ni-O and Ni-Mn peaks of 2.05 ± 0.01 Å and 3.48 ± 0.01 Å, respectively, as well as their σ^2 values were consistent with previous studies (Pena et al., 2010; Simanova et al., 2015). The similarity in the σ^2 values obtained for the light and dark sample indicates that increased disorder resulting from Mn(III) accumulation

during irradiation cannot explain, alone, the decrease in the amplitude of the Ni-Mn_{CS} peak upon irradiation. Instead, the 50% decrease in amplitude for the Ni-Mn peak in the irradiated sample compared to the dark sample was manifest in the fitted CN values of 4.57 ± 1.58 and 8.06 ± 1.68 , respectively (**Table 2**). A CN value of 4.6 could arise from $65 \pm 40\%$ Ni adsorbed as a TCS complex on vacancy sites (CN of 6) and $35 \pm 40\%$ Ni adsorbed as a DCS complex on particle edges (CN of 2). This estimate is compromised, however, by the large uncertainties in the fitted CNs and by the high CN of the dark sample, which exceeds significantly the theoretical value of 6. In addition, the short k-range to which the data extends (k-range $2.5 - 10 \text{ \AA}^{-1}$) also contributes to the large uncertainty of the CNs. A more reliable estimate of the proportion of Ni on edge sites in the irradiated sample requires that these shortcomings in the fitted coordination number be resolved, as explored in the next sections.

Table 2: Fit scenarios for the pH 4 samples with a simplified 2-shell model (R range 1-4.1 \AA). A dK value of 0.96 was applied based on the work published by Pena et al. (2010). It can be seen that floating all parameters gives an unrealistically large CN on the Ni-Mn shell.

	Ni- laden $\delta\text{-MnO}_2$ dark	Ni-laden $\delta\text{-MnO}_2$ light
Ni-O₁		
CN	6.06 ± 0.83	6.13 ± 0.81
R (\AA)	2.06 ± 0.01	2.05 ± 0.01
σ^2 (\AA^2)	0.003 ± 0.001	0.004 ± 0.001
Ni-Mn_{TCS}		
CN	8.06 ± 1.68	4.57 ± 1.58
R (\AA)	3.49 ± 0.01	3.48 ± 0.01
σ^2 (\AA^2)	0.005 ± 0.001	0.006 ± 0.003
E0 (eV)	-1.55 ± 1.14	-1.81 ± 1.29
Red Chi2	3.88	9.07
R-factor	0.02	0.02
N vars/IDP	7/14	7/14

Table 3: Fit scenarios for the pH 8 samples with a simplified 2-shell model (R range 1-4.1 Å). A dK value of 0.96 was applied based on the work published by Pena et al. (2010).

	Ni- laden δ -MnO ₂ dark	Ni-laden δ -MnO ₂ light
Ni-O1		
CN	6.15 ± 0.74	6.04 ± 0.75
R (Å)	2.04 ± 0.01	2.04 ± 0.01
σ^2 (Å ²)	0.005 ± 0.001	0.005 ± 0.001
Ni-Mn_{INC}		
CN	6 * (1- f)	6 * (1- f)
R (Å)	2.86 ± 0.01	2.86 ± 0.01
σ^2 (Å ²)	0.004 ± 0.001	0.004 ± 0.001
Ni-Mn_{TCS}		
CN	6 * f	6 * f
R (Å)	3.48 ± 0.01	3.47 ± 0.01
σ^2 (Å ²)	σ^2 Ni-Mn _{TCS}	σ^2 Ni-Mn _{TCS}
f	0.68 ± 0.03	0.60 ± 0.03
E ₀ (eV)	-2.04 ± 1.08	-2.30 ± 1.09
Red Chi ²	36.97	3.44
R-factor	0.02	0.02
N vars/IDP	8/17	8/17

The fit derived distances for the Ni-O and Ni-Mn_{CS} shells in the pH 8 data were consistent with the pH 4 data and Pena et al. (2010) and (Manceau et al., 2007; Peacock and Sherman, 2007). The interatomic distance obtained for the Ni-Mn_{INC} shell (2.86 ± 0.01), as well as all other floated variables were also consistent with published values (Pena et al., 2010). No large differences between the dark and light sample were observed, particularly for the σ^2 values and interatomic distances fitted for the Ni-Mn paths. Assuming that no significant amount of Ni was adsorbed at the particle edges in these samples, the values obtained on the species abundance fractional parameter (f), indicate that the amount of Ni incorporated into the nanosheet increased from $60 \pm 3\%$ to $68 \pm 3\%$ with irradiation compared to Ni adsorbed on vacancies in a TCS complex.

Alternative shell-by-shell fit scenarios for pH 4 Ni EXAFS spectra in the $R + \Delta R < 4 \text{ \AA}$ range. The large uncertainties in the fitted CNs of the dark and light sample (20-40 %) and the high CN of the dark sample (8.06 ± 1.68) indicate that the simple 2-shell model does not fully explain the pH 4 data. A likely explanation for these fitting results is that absorber-scatter pairs not included in the two-shell model contribute amplitude of the Ni-Mn_{CS} peak. Based on the structural models for Ni-TCS and Ni-INC, the shells most likely to influence the amplitude of the Ni-Mn_{CS} peak are the Ni-O shell at around 3.5 Å (Ni-TCS model) and a Ni-Mn path at around 2.9 Å (Ni-INC model). Specifically, the TCS model contains a Ni-O shell between 3.44 and 3.71 Å, whereas the INC model shows Ni-Mn scattering between 2.82 and 3 Å. Based on these constraints, we tested four fit scenarios to address the shortcomings of the two-shell fits for the dark sample. We also applied these four fit scenarios to the irradiated data to evaluate whether the CN of the Ni-Mn shell was affected similarly as the CN of Ni-Mn shell of the dark sample.

In fit scenarios one and two, we assumed that the large amplitude of the Ni-Mn peak at 3 Å $R + \Delta R$ could be explained by the scattering from the second Ni-O shell. The TCS model includes 3 oxygen atoms that are each triply coordinated to Mn at around 3.44 Å and 3 atoms that are doubly-coordinated to Mn at a distance of 3.51 - 3.70 Å. Scenario 1 assumed that the EXAFS spectra were sensitive to all 6 oxygen scatterers. To test this assumption, the model included a Ni-O path (Ni-O₂) with a fixed CN of 6 and an R value of 3.54 Å, equal to the average distance between all paths in the model related to these oxygens. The Debye-Waller factor was floated to evaluate whether the value fitted was physically reasonable. In the second scenario, we assumed that only the triply-coordinated oxygens contributed to the amplitude at 3 Å $R + \Delta R$. The variation between the theoretical interatomic distances between Ni and these three atoms is small (3.446 Å, 3.449 Å and 3.454 Å) and the triple-coordination of these atoms with Mn is consistent with a greater rigidity in the structure for the dark sample, which almost only contains Mn(IV) (AMON = 4). To test this assumption, we added the Ni-O₂ shell with the CN set to 3 and the interatomic distance set to 3.45 Å. The Debye-Waller factor in this case was constrained to that of the Ni-O₁ shell. In the third and fourth scenarios, we assumed that the large CN and uncertainty on the Ni-Mn peak at 3 Å $R + \Delta R$ was due to a missing Ni-Mn shell at 2.86 Å related to Ni incorporated into the nanosheet (Ni-Mn_{INC} - CN = 6 - scenario 3) or bound to Mn(IV) as a double edge sharing complex on a particle edge (Ni-Mn_{ES} - CN = 2 -

scenario 4) (Pena et al., 2010; Simanova et al., 2015). The Debye-Waller factors of all Ni-Mn paths were constrained to those of Ni-Mn_{CS}, and the CN of the Ni-Mn_{CS} peak was floated. Additionally, the fit statistics were not considerably affected by the inclusion of these paths, as was expected since the purpose of including these paths was not to increase the goodness of fit but to give a chemical explanation to the high CN value obtained.

In the fits of the dark data (**Figure S4a, Table S1**), the inclusion of the Ni-O₂ shell with a CN of 6 (scenario 1) did not result in a considerable decrease of the CN on the Ni-Mn_{CS} path nor a decrease in the CN uncertainty with respect to the initial fit. By applying a CN of 3 and the shorter interatomic distance (scenario 2), the CN on the Ni-Mn_{CS} path decreased to 6.62 ± 1.60 . No large differences were observable in the other fitted parameters as well as in the R-factor. Scenarios 3 and 4, which included a Ni-Mn_{ES} path to model the shoulder at around $2 \text{ \AA } R + \Delta R$, returned unreasonably high fitted values on the CN of the Ni-Mn_{CS} peak. The effect was greater for scenario 4 than scenario 3, and in both cases the mismatch was visually evident. These results suggest that Ni-O₂ may be the source of the high CN fitted in the free 2-shell fit. Furthermore, Ni-O₂ is more likely responsible for this CN than Ni-Mn_{ES}.

In the fits of the irradiated data (**Figure S4b, Table S2**), scenario 1 did not change considerably the CN on the Ni-Mn_{CS} path, whereas scenario 2 lowered the CN of Ni-Mn_{CS} in the irradiated sample to 3.22 ± 1.52 . However, in both scenarios the uncertainty on the CN increased (40-50%). Compared to the dark data, the interatomic distances for the fitted Ni-Mn_{CS} peak decreased from $3.49 \pm 0.01 \text{ \AA}$ to $3.48 \pm 0.01 \text{ \AA}$, whereas the Debye-Waller factors increased slightly. Also for the Ni-O₁ shell the interatomic distance decreased from $2.06 \pm 0.01 \text{ \AA}$ to $2.05 \pm 0.01 \text{ \AA}$ while the Debye-Waller factor increased from $0.003 \pm 0.001 \text{ \AA}$ to $0.004 \pm 0.001 \text{ \AA}$. The R-factor, on the other hand, was 0.02 in both cases. However, compared to the dark data, there was a visual mismatch between data and fit when this shell was included. Similarly to the dark data, scenarios 3 and 4 gave unreasonably high values on the CN of the Ni-Mn_{CS} peak and were a visually identifiable mismatch. Therefore, the irradiated data did not benefit greatly from the additional shells as the dark data did.

The pH 4 fits in the $1 - 4 \text{ \AA } R + \Delta R$ range gave appreciable results but pointed out issues in the CN value of the dark sample, as well as large uncertainties on the fitted CN of both the dark and irradiated sample. By carrying out the alternative fit scenarios, we propose

the high CN on the dark sample to be related to the Ni-O₂ shell. The uncertainties on the CN, on the other hand, increased by adding this shell in both the dark and irradiated sample. Through supplementary fits on other data with Ni adsorbed on vacancy sites and edge sites (Simanova et al., 2015), we observed that extending the data range FT-window up to a value of 11.9 Å⁻¹ changed the uncertainty on the CN from 40 % to 30 %. However, this was not possible with our data because the data beyond 10 Å⁻¹ was not usable.

Shell-by-Shell fits of Ni EXAFS spectra in the $R + \Delta R < 6.1$ Å range. Based on the fits results in the 1 - 4 Å R + ΔR range, we extended the fits to 6.1 Å R + ΔR in order to test which features were distinguishable from the noise in the FT-EXAFS and to attempt to reduce the uncertainty in the fitted CN since improved and more constrained fits would provide a better estimate of the proportion of Ni-Mn_{CS} distributed between edge sites and vacancies. The shell-by-shell model fits chosen for the pH 4 and 8 data are shown with the data as magnitude and imaginary part of the Fourier transform in **Figures 9 and 10**, respectively. A summary of all fitting parameters and constraints for the pH 4 and pH 8 data in the full range fits is reported in **Tables 4 and 5**, respectively.

Table 4: Optimized fit parameters for the pH 4 EXAFS data. The S_0^2 value was set to 0.96 based on published data (Pena et al., 2010). The amplitude (A) for the different shells is defined by the product of the CN and a scaling parameter (f), where f refers to the fraction of Ni in TCS complexes above vacancies and $(1-f)$ refers to the fraction of Ni as a double edge sharing complex at the particle edges.

Sample ID	Ni-laden δ -MnO ₂ pH 4 dark	Ni-laden δ -MnO ₂ pH 4 light	Ni-laden δ - MnO ₂ pH 4 dark	Ni-laden δ - MnO ₂ pH 4 light
Ni-O₁				
CN	6.23 ± 0.69	6.33 ± 0.65		
R (Å)	2.05 ± 0.01	2.05 ± 0.01		
σ^2 (Å ²)	0.003 ± 0.001	0.004 ± 0.001		
Ni-O₂			Ni-O₄	
CN	3		CN	CN_{Ni-O1}
R (Å)	3.45		R (Å)	5.47 ± 0.05
σ^2 (Å ²)	σ^2_{Ni-O1}		σ^2 (Å ²)	σ^2_{Ni-O1}
Ni-Mn_{TCS1}			Ni-Mn_{TCS2}	
CN	6.94 ± 1.37	6 * f + 2 * ($1-f$)	CN	$CN_{Ni-MnTCS1}$
R (Å)	3.49 ± 0.01	3.47 ± 0.01	R (Å)	5.42 ± 0.02
σ^2 (Å ²)	0.005 ± 0.002	0.005 ± 0.002	σ^2 (Å ²)	$\sigma^2_{Ni-MnTCS1}$
Ni-O₃				
CN	6.29 ± 2.73	4.12 ± 2.45		
R (Å)	4.52 ± 0.03	4.49 ± 0.04	f	0.56 ± 0.28
σ^2 (Å ²)	σ^2_{Ni-O1}	σ^2_{Ni-O1}		
E0 (eV)	-1.34 ± 0.90	-2.11 ± 0.99		
Red Chi2	2.70	5.73		
R-factor	0.018	0.022		
N vars/IDP	11/24	11/24		

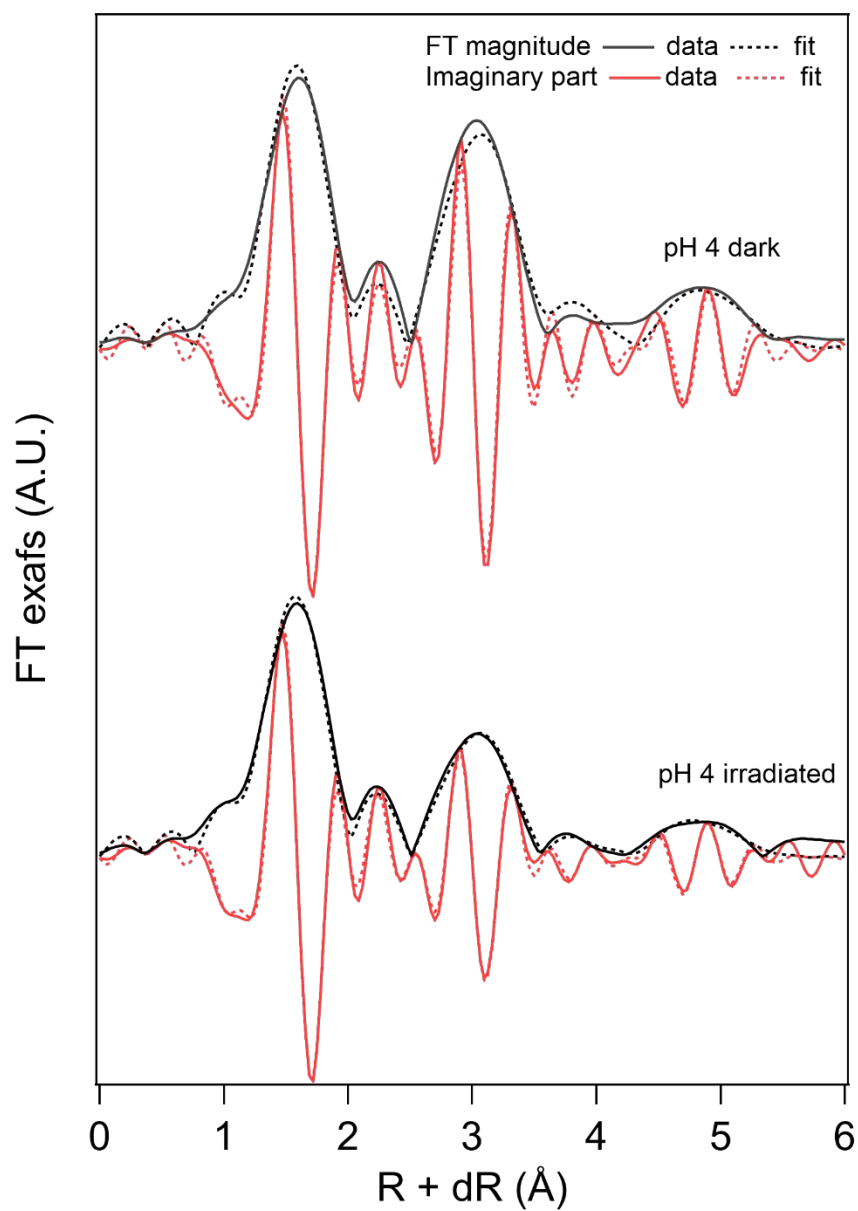


Figure 9. Ni k-edge fourier transformed EXAFS (magnitude + imaginary part) and shell by shell fits (magnitude + imaginary part) for the pH 4 samples in the dark (above) and after irradiation (below) in the full range fit (1 – 6.1 \AA). Fit parameters are shown in **Table 4**.

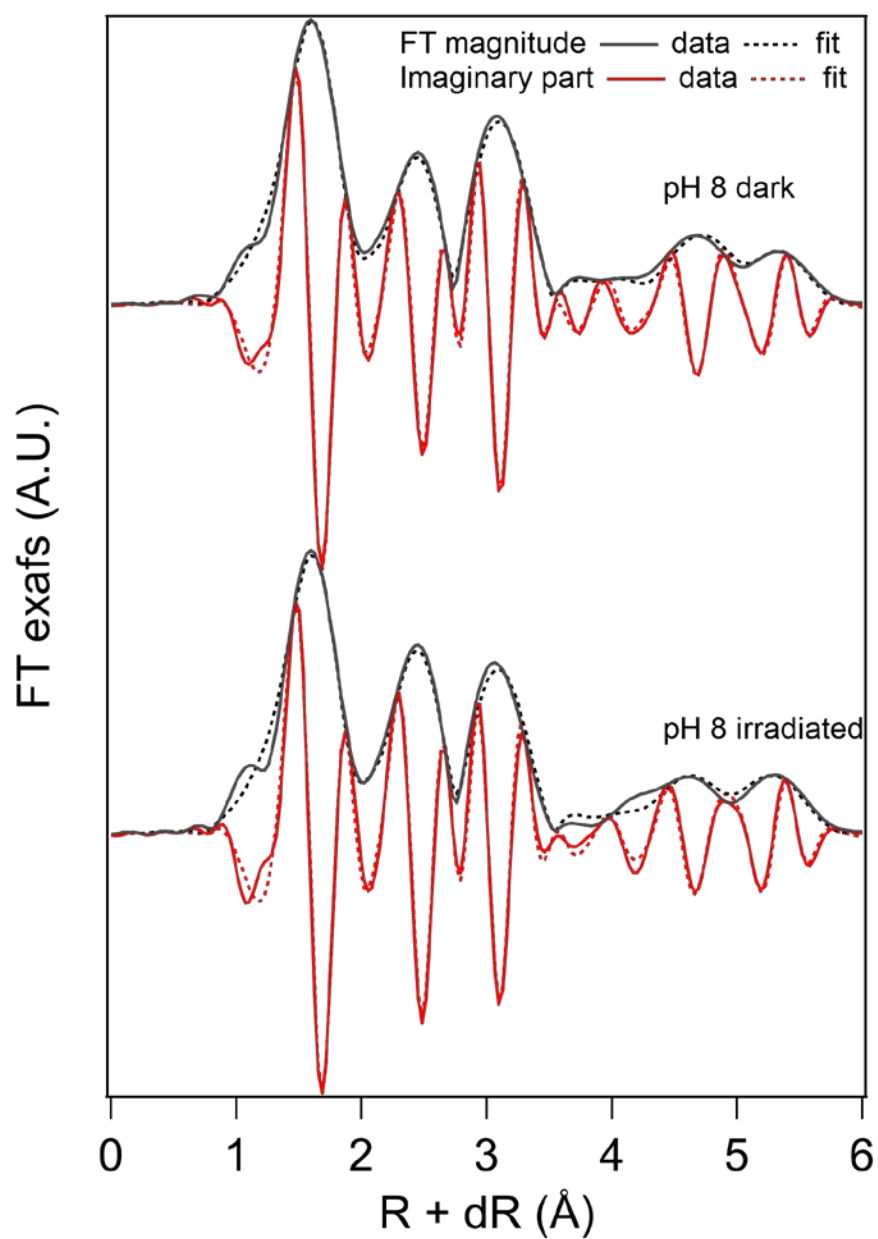


Figure 10. Ni k-edge fourier transformed EXAFS (magnitude + imaginary part) and shell by shell fits (magnitude + imaginary part) for the pH 8 samples in the dark (above) and after irradiation (below). Fit parameters are shown in **Table 5**.

CHAPTER 6

Table 5: Optimized fit parameters for the pH 8 data. The constraints for the coordination numbers and the debye waller factors (σ^2), as well as the value for S_0^2 (set to 0.96), were obtained from Pena et al. (2010). The amplitude (A) for the different shells is defined by the product of the CN and a scaling parameter (f), where f refers to the fraction of Ni in TCS complexes above vacancies and $(1-f)$ refers to the fraction of Ni incorporated into the nanosheet.

Sample ID	Ni-laden δ -MnO ₂ pH 8 dark	Ni-laden δ -MnO ₂ pH 8 light		Ni-laden δ -MnO ₂ pH 8 dark	Ni-laden δ -MnO ₂ pH 8 light
Ni-O₁					
CN	6.19 ± 0.49	6.07 ± 0.59			
R (Å)	2.03 ± 0.003	2.03 ± 0.005			
σ^2 (Å ²)	0.005 ± 0.001	0.005 ± 0.001			
Ni-Mn_{INC1}			Ni-Mn_{TCS2}		
A	6 x (1- f)	6 x (1- f)	A	6 x f	6 x f
R (Å)	2.86 ± 0.01	2.86 ± 0.01	R (Å)	5.37 ± 0.02	5.36 ± 0.03
σ^2 (Å ²)	0.004 ± 0.0002	0.004 ± 0.0003	σ^2 (Å ²)	$\sigma^2_{Ni-MnINC2}$	$\sigma^2_{Ni-MnINC2}$
Ni-Mn_{TCS1}			Ni-Mn_{MSP}		
A	6 x f	6 x f	CN	6	6
R (Å)	3.47 ± 0.01	3.47 ± 0.01	R (Å)	5.67 ± 0.01	5.66 ± 0.02
σ^2 (Å ²)	$\sigma^2_{Ni-MnINC}$	$\sigma^2_{Ni-MnINC}$	σ^2 (Å ²)	$\sigma^2_{Ni-MnINC2}$	$\sigma^2_{Ni-MnINC2}$
Ni-O₂					
A	(9 x f) + ((1 - f) x 12)	(9 x f) + ((1 - f) x 12)			
R (Å)	4.44 ± 0.02	4.45 ± 0.03			
σ^2 (Å ²)	0.009 ± 0.003	0.01 ± 0.005			
Ni-Mn_{INC2}					
A	6 x (1- f)	6 x (1- f)	f	0.68 ± 0.02	0.60 ± 0.02
R (Å)	5.00 ± 0.02	4.98 ± 0.03			
σ^2 (Å ²)	0.004 ± 0.001	0.006 ± 0.002			
E0 (eV)	-2.32 ± 0.65	-2.47 ± 0.79			
Red Chi2	2.12	2.10			
R-factor	0.010	0.014			

In the pH 4 fits, only single scattering paths were included, since multiple scattering paths did not improve the fit and increased the uncertainties in the fitted parameters. The dark data included the Ni-O₂ shell with the constraints from scenario 2 (**Table S1**), as well as all additional Ni-O and Ni-Mn single scattering paths from the Ni-TCS model up to 6.1 Å $R + \Delta R$. Debye-Waller factors and CN values were floated for Ni-O₁ and the first Ni-Mn_{Cs} path, and constrained to these values for similar scattering pairs at further distance. Interatomic distances were floated for all paths. The CN value for Ni-O₃ was floated because constraining it to 9, the number of O scatterers in the model at this distance (4.5 Å) as described in Pena et al. (2010), led to a visual mismatch in the fit compared to the data. The irradiated data did not

include the Ni-O₂ shell, since the visual mismatch between data and fit increased and the uncertainty on the fitted CN did not decrease appreciably. The absence of the Ni-O₂ shell may also be justified by the lower amount of Ni bound to vacancies, so a lower sensitivity of the EXAFS to the oxygen scatterers relative to this shell, as well as the increased disorder in the structure introduced by Mn(III) stabilizing in the interlayer (See **Chapters 3 and 5**). The fits for this sample included a species abundance parameter that was applied to quantify the proportion of Ni adsorbed as a TCS complex on vacancy sites (CN=6) and that adsorbed as a DCS complex on edge sites (CN=2), which are both at the same interatomic distance of 3.47 Å. All other paths and constraints were the same as in the dark sample. The goodness of fit on both samples was deemed reasonable by an R-value of 0.02.

The fitted Debye-Waller factors for the Ni-O and Ni-Mn paths and the interatomic distances for the paths in the dark sample were consistent with Pena et al. (2010). Some differences were observed between the interatomic distances of the dark and irradiated sample. In particular, the interatomic distances in the irradiated sample were shorter than in the dark sample, with differences of 0.02 Å increasing up to 0.03 Å with increasing interatomic distance. This decrease is consistent with the accumulation of Mn(III) in the mineral (increased disorder and decrease in Ni-O and Ni-Mn distances). The fitted CN value for the Ni-O₃ was also lower in the irradiated sample than in the dark sample, with a large uncertainty. This is consistent with a more rigid and ordered structure, since the mineral is composed almost exclusively of Mn(IV), which would result in a more homogeneous range of distances of these scatterers from Ni. This extended model returned a 10% decrease in the uncertainty of the CN of the Ni-Mn_{DCS} shell, as quantified on the *f* parameter (28 % uncertainty) compared to the 2-shell fits (40-50 %).

The fits of the pH 8 data included all single scattering paths from the TCS as well as from the INC models. An additional collinear multiple scattering path was included to model the feature at $\sim 5.5 \text{ \AA } R + \Delta R$, which was poorly fitted by using only single scattering paths (**Figure S5**). The path was chosen by exclusion, by first adding all collinear multiple scattering paths and removing the ones that did not give satisfying results. Only one collinear multiple scattering path remained, and results from the interaction between the photoelectron and Mn atoms situated along one direction of the mineral *ab* plane. In analogy with the simplified 2-

shell fits, the constraints on the data were obtained from Pena et al. (2010). The CN for the multiple scattering path was constrained to 6, which is the number of equivalent scattering paths calculated by the DFT optimized model, whereas the interatomic distance was floated and the Debye-Waller factor was set to that of the second Ni-Mn_{CS} path. The Ni-Mn shells were constrained to each other by means of the fractional parameter (Pena et al., 2010). The fractional parameter was also used to constrain the CN value on the Ni-O₃ shell as described in the cited study. All resulting fits returned R values of ≤ 0.02) and physically reasonable fit parameters (Calvin, 2013).

All fitted values were consistent with those published in Pena et al. (2010). The differences between the interatomic distances for the Ni-Mn paths did not differ substantially between dark and irradiated samples, similarly to the simplified 2-shell fit. The error estimated on the fractional parameter decreased from 3% to 2% in the extended range model compared to the 2-shell model, which is consistent with greater constraints to the fit given by the inclusion of the second Ni-Mn shell. One difference between the dark and irradiated sample was the Debye-Waller of the Ni-Mn_{CS2} path, which increased from 0.004 ± 0.001 to 0.006 ± 0.002 with irradiation. This difference is consistent with the presence of some Mn(III) in the interlayer, which increases the disorder in distances between Ni and Mn atoms.

6.5. Discussion

Comparison of δ -MnO₂ photoreduction with Ni and without Ni. The Mn(IV) photoreduction rates in the presence of up to 6% Ni sorbed onto the surface showed differences that were within the measurement uncertainty compared to those of δ -MnO₂ in the absence of Ni (**Chapter 5**). Some authors have suggested that up to 8% Ni sorbed onto birnessite may catalyze water oxidation (Du et al., 2015; Thenuwara et al., 2016), therefore potentially increasing the photoreduction rate. However, the 4 electron transfer reaction between MnO₂ and water described in the photocatalysis studies was pushed to completion yielding molecular oxygen in a photoelectrochemical cycle, where the oxide is « regenerated » by electro-oxidation. In their study, Du et al. (2015) showed a two-fold increase in the catalytic activity of a NiO-MnO₂ nanocomposite compared to MnO₂. In another study, the presence of Ni in the interlayer was shown to stabilize the oxide in subsequent oxidation/reduction cycles compared to undoped birnessite, and the authors suggest the catalytic activity to be enhanced by the

electro-oxidation of Ni^{2+} to Ni^{3+} (Thenuwara et al., 2016). Conversely, we have proposed that the rate limiting step in our system is the Mn(III) migration to the interlayer and/or the scavenging of the proposed reactive radicals from the mineral surface without generation of oxygen (**Chapter 5**). The absence of the electrochemical oxidation of Ni could therefore explain why a greater photocatalytic activity is not reflected in greater photoreduction rates.

Ni release and Mn(III) accumulation at low pH in irradiated suspensions. The 50% change in surface loading of Ni with irradiation, together with the results from the shell-by-shell fits for the pH 4 samples show that the release of Ni with irradiation is accompanied by a change in the coordination environment of the adsorbed Ni. In particular, the decrease in the amplitude of the Ni-Mn_{CS} peak from a fitted value of around 6.94 ± 1.37 to a fitted value of 4.24 ± 1.12 is consistent with a significant proportion of Ni desorbing from a TCS complex on a vacancy (6 near Mn neighbors) to readsorb on corner sharing sites on the particle edge where the number of Mn neighbors would decrease to 2. The EXAFS fits suggest that the remaining 2% Ni is distributed between corner sharing complexes on the edges and on the vacancies in a proportion of $44 \pm 28\%$ and $56 \pm 28\%$, respectively. Our results suggest that this displacement and re-distribution is related to the accumulation of Mn(III). From the EXAFS fitting results, the 4% Ni surface excess in the dark sample is initially situated on vacancy sites, and there is a low amount of Mn(III) present. It is unlikely that Ni was initially present on edge sites because : *i*) at pH 4, Ni has only been observed to sorb as a TCS complex above vacancies when they are available (Peacock and Sherman, 2007; Grangeon et al., 2008; Pena et al., 2010); *ii*) even a small amount of Ni sorbed on edge sites would affect the CN value considerably because the surface loading is very low (2%), giving a fitted value lower than 6 (Simanova et al., 2015). In the irradiated sample, photoreduction leads to a gradual increase of Mn(III) in the mineral. The photogenerated Mn(III) is then stabilized in the interlayer on vacancy sites, which are partially occupied by Ni (**Chapter 4** and **Chapter 5**). The Ni bound to vacancies is displaced as a consequence of Mn(III) accumulation, which is consistent with the observations of Grangeon et al. (2008). In that study, the authors observed that Ni displaced Na and H⁺ but not Mn(III) at pH 3-4, suggesting that the vacancy sites have a greater affinity for Mn(III) than Ni at low pH.

The desorption and re-adsorption of Ni to the edge sites of the particles shed light not only on how trace metal mobility changes upon birnessite irradiation, but also provide evidence that photogenerated Mn(III) must be stabilized in interlayer sites, capping vacancy sites. The vacancy content of δ -MnO₂ has been indirectly estimated in different ways, amongst which the electrostatic charge balance by Na atoms (4 Na atoms per vacancy) (Villalobos et al., 2006) or by EXAFS studies on Ni sorption (Simanova et al., 2015), and it has been shown to range between 6% and 11%. This vacancy content is also pH dependent (more vacancies at lower pH) (Simanova et al., 2015). We can assume a vacancy content for our mineral on the high end of 11%, given the low pH of our experiments. Since the Ni loading is much lower than the vacancy content of the mineral, and this Ni is displaced upon Mn(III) generation, the formation of Mn(III) must strongly diminish the vacancy content. We have previously suggested that photogenerated Mn(III) may be produced either on edge sites, since these sites are the most protonated and thus are less strongly bound to the mineral (**Chapter 5**), or in the bulk mineral but not adjacent to existing vacancies, because photoreduction would produce two adjacent vacancies, which would introduce a very large and localized charge deficit. Therefore, any generation of Mn(III) in the bulk could increase the vacancy content, but these newly formed vacancies would be unavailable to Ni. The generation of Mn(III) on edge sites and its migration to the interlayer, as suggested in **Chapter 5**, may provide a more consistent explanation for the desorption and re-distribution of Ni observed in our experiments. If we assume an initial vacancy content on the high end of 11% and 1% Ni still on vacancies after irradiation, then as much as 10% Mn(III) generated near edge sites would be required to migrate to interlayer sites to cap empty vacancies and displace Ni_{TCS} complexes. The remaining 6% Mn(III) may be generated in the bulk, increasing the total vacancy content of the mineral to 17%. Future studies would be required to confirm the site of Mn(III) formation and its potential to migrate within the mineral.

High pH only leads to changes in Ni coordination environment. Although the amount of Ni sorbed on δ -MnO₂ at pH 8 after 96 hours of irradiation remained unchanged compared to the sample kept in the dark, a small but distinguishable change in the coordination environment of Ni could be observed from the EXAFS data. The fit procedure showed an $8 \pm 2\%$ decrease in TCS complexes on vacancy sites upon irradiation in favor of the INC configuration. The absence of Ni desorption is consistent with the observations of Grangeon

et al. (2008), who reported that Ni can partially displace Mn(III) at high pH. Additionally, Lefkowitz and Elzinga (2015) observed that Zn(II) sorption was enhanced at pH 7.5. Therefore, any Mn(III) formed would not cause Ni release because the Mn(III) amount formed is below the amount of still available vacancies. The slight change in coordination environment observed could be explained by the increase in stress and strain of the crystallite during the formation of transient Mn(III) species and their stabilization in the interlayer. This change could lead to more degrees of freedom for the mineral to accommodate Ni(II), a larger octahedron than Mn(IV), in the nanosheet.

6.6. Environmental implications

The results of this study shed light on the mobility of Ni associated with birnessite under irradiation without mineral dissolution, and has implications in the prediction of trace metal mobility in both contaminated and natural environments affected by sunlight. Irradiation has been shown to enhance the oxidation of As on the surface of MnO₂ (Shumlas et al., 2016), as well as induce Cu release in the presence of humic acids (Kim et al., 2014). However, these studies involved mineral dissolution, whereas we show that changes in surface-bound trace metals can occur even without mineral dissolution. The results of the pH 4 series are particularly relevant to environments such as acid-mine drainage impacted streams (Haack and Warren, 2003) or acid saline lakes where Mn(II) oxidation is enhanced (Tebo, 1991; Bowen and Benison, 2009). In such environments, sunlight irradiation may affect both metal sorption and release from birnessite minerals on diel timescales : not only does the presence of Mn(III) in the mineral reduce its capacity for trace metal sorption (Wang et al., 2012; Simanova et al., 2015), we show here that the accumulation of Mn(III) by photoreduction may lead to desorption of previously-sorbed metals. Furthermore, the local changes in solution pH due to microbial respiration (decrease in pH) and photosynthesis (pH increase) in the immediate proximity of the cells (Haack and Warren, 2003), make these results relevant to a wider range of environmental settings which may include freshwater bodies (e.g. lakes, rivers, ponds) and marine settings.

The results from the pH 8 experiments complement the knowledge on the sorption of Ni in seawater by including the effect of sunlight. Most of the previous experiments have studied the mechanism of Ni sorption on δ -MnO₂ at pH values of seawater in the dark

CHAPTER 6

(Manceau et al., 2007; Peacock and Sherman, 2007; Pena et al., 2010; Atkins et al., 2014; Simanova et al., 2015). However, the sorption of Ni combined with the biogenic formation and sunlight-mediated transformation of birnessite in such environments may be different than previously predicted from dark-only experiments (Balistrieri et al., 1994; Francis and Tebo, 1999; Pena et al., 2010), especially because irradiation of ocean waters ranges from daily to monthly cycles from equatorial regions to polar regions, respectively. The results presented here show that sunlight promotes incorporation of Ni compared to surface complexation as a TCS on top of vacancy sites, similarly to the effect of increased reaction time and increased pH in the dark (Peacock and Sherman, 2007).

6.7. Acknowledgements

This research was funded by the Swiss National Science Foundation (Grant # 200021_143742). We are grateful to Vera Cuartero Yague at BM 23 of the European Synchrotron Radiation Facility and Ryan Davis at BL 4-1 of the Stanford Synchrotron Radiation Lightsource for their support with X-ray absorption measurements. We thank Prof. Kideok D. Kwon, of Kangwon National University, South Korea, for providing the DFT models used for the shell-by-shell fits of EXAFS data.

6.8. References

- Atkins, A.L., Shaw, S., Peacock, C.L., **2014**. Nucleation and growth of todorokite from birnessite: Implications for trace-metal cycling in marine sediments. *Geochim Cosmochim Acta* 144, 109-125.
- Balistrieri, L.S., Murray, J.W., Paul, B., **1994**. The Geochemical Cycling of Trace-Elements in a Biogenic Meromictic Lake. *Geochim Cosmochim Acta* 58, 3993-4008.
- Bargar, J.R., Tebo, B.M., Bergmann, U., Webb, S.M., Glatzel, P., Chiu, V.Q., Villalobos, M., **2005**. Biotic and abiotic products of Mn(II) oxidation by spores of the marine *Bacillus* sp. strain SG-1. *Am Mineral* 90, 143-154.
- Bowen, B.B., Benison, K.C., **2009**. Geochemical characteristics of naturally acid and alkaline saline lakes in southern Western Australia. *Appl Geochem* 24, 268-284.
- Calvin, S., **2013**. XAFS for everyone. *CRC Press - Taylor and Francis Group*.
- Du, X., Ding, Y., Xiang, X., **2015**. Enhanced Photocatalytic Water Oxidation Efficiency with NiO@MnO₂ Catalysts Based on Abundant Metals. *Energy Environ Focus* 4, 307-315.
- Elzinga, E.J., **2011**. Reductive transformation of birnessite by aqueous Mn(II). *Environ Sci Technol* 45, 6366-6372.
- Francis, C., Tebo, B., **1999**. Marine *Bacillus* spores as catalysts for oxidative precipitation and sorption of metals. *Journal of molecular microbiology and*

- Fuller, C.C., Bargar, J.R., **2014**. Processes of Zinc Attenuation by Biogenic Manganese Oxides Forming in the Hyporheic Zone of Pinal Creek, Arizona. *Environ Sci Technol* 48, 2165-2172.
- Fuller, C.C., Harvey, J.W., **2000**. Reactive uptake of trace metals in the hyporheic zone of a mining-contaminated stream, Pinal Creek, Arizona. *Environ Sci Technol* 34, 1150-1155.
- Garg, S., Rose, A.L., Waite, T.D., **2011**. Photochemical production of superoxide and hydrogen peroxide from natural organic matter. *Geochim Cosmochim Acta* 75, 4310-4320.
- Grangeon, S., Lanson, B., Lanson, M., Manceau, A., **2008**. Crystal structure of Ni-sorbed synthetic vernadite: a powder X-ray diffraction study. *Mineral Mag* 72, 1279-1291.
- Haack, E., Warren, L.A., **2003**. Biofilm hydrous manganese oxyhydroxides and metal dynamics in acid rock drainage. *Environ Sci Technol* 37, 4138-4147.
- Hansel, C.M., Zeiner, C.A., Santelli, C.M., Webb, S.M., **2012**. Mn(II) oxidation by an ascomycete fungus is linked to superoxide production during asexual reproduction. *Proc Natl Acad Sci U S A* 109, 12621-12625.
- Hinkle, M.A.G., Becker, K.G., Catalano, J.G., **2015**. Impact of Mn(II)-manganese oxide reactions on trace element fate, *Ion Interactions at the Mineral-Water Interface During Biogeochemical Iron and Manganese Cycling*, p. 174.
- Kelly, S.D., Hesterberg, D., Ravel, B., **2008**. Analysis of soils and minerals using X-ray absorption spectroscopy, *Methods of soil analysis. Part 5. Mineralogical methods*, pp. 387-464.
- Kim, E.J., Kim, J., Choi, S.C., Chang, Y.S., **2014**. Sorption behavior of heavy metals on poorly crystalline manganese oxides: roles of water conditions and light. *Environ Sci-Proc Imp* 16, 1519-1525.
- Lanson, B., Drits, V.A., Silvester, E., Manceau, A., **2000**. Structure of H-exchanged hexagonal birnessite and its mechanism of formation from Na-rich monoclinic busserite at low pH. *Am Mineral* 85, 826-838.
- Lefkowitz, J.P., Elzinga, E.J., **2015**. Impacts of Aqueous Mn(II) on the Sorption of Zn(II) by Hexagonal Birnessite. *Environ Sci Technol* 49, 4886-4893.
- Lefkowitz, J.P., Rouff, A.A., Elzinga, E.J., **2013**. Influence of pH on the reductive transformation of birnessite by aqueous Mn(II). *Environ Sci Technol* 47, 10364-10371.
- Manceau, A., Lanson, M., Geoffroy, N., **2007**. Natural speciation of Ni, Zn, Ba, and As in ferromanganese coatings on quartz using X-ray fluorescence, absorption, and diffraction. *Geochim Cosmochim Acta* 71, 95-128.
- Manceau, A., Marcus, M.A., Grangeon, S., **2012**. Determination of Mn valence states in mixed-valent manganates by XANES spectroscopy. *Am Mineral* 97, 816-827.
- Manceau, A., Marcus, M.A., Tamura, N., Proux, O., Geoffroy, N., Lanson, B., **2004**. Natural speciation of Zn at the micrometer scale in a clayey soil using X-ray fluorescence, absorption, and diffraction. *Geochim Cosmochim Acta* 68, 2467-2483.
- Marafatto, F.F., Strader, M.L., Gonzalez-Holguera, J., Schwartzberg, A., Gilbert, B., Pena, J., **2015**. Rate and mechanism of the photoreduction of birnessite (MnO₂) nanosheets. *Proc Natl Acad Sci U S A* 112, 4600-4605.
- Marcus, M.A., Manceau, A., Kersten, M., **2004**. Mn, Fe, Zn and As speciation in a fast-growing ferromanganese marine nodule. *Geochim Cosmochim Acta* 68, 3125-3136.

- Morgan, J.J., **2000**. Manganese in natural waters and earth's crust: its availability to organisms. *Met Ions Biol Syst* 37, 1-34.
- Morgan, J.J., **2005**. Kinetics of reaction between O-2 and Mn(II) species in aqueous solutions. *Geochim Cosmochim Acta* 69, 35-48.
- Newville, M., **2001**. IFEFFIT: interactive XAFS analysis and FEFF fitting. *J Synchrotron Radiat* 8, 322-324.
- Peacock, C.L., Sherman, D.M., **2007**. Sorption of Ni by birnessite: Equilibrium controls on Ni in seawater. *Chem Geol* 238, 94-106.
- Pena, J., Kwon, K.D., Refson, K., Bargar, J.R., Sposito, G., **2010**. Mechanisms of nickel sorption by a bacteriogenic birnessite. *Geochim Cosmochim Acta* 74, 3076-3089.
- Post, J., **1999**. Manganese oxide minerals: Crystal structures and economic and environmental significance. *Proceedings of the National Academy of Sciences* 96, 3447-3454.
- Remucal, C.K., Ginder-Vogel, M., **2014**. A critical review of the reactivity of manganese oxides with organic contaminants. *Environ Sci-Proc Imp*.
- Schecher, W.D., McAvoy, D.C., **1992**. MINEQL+: a software environment for chemical equilibrium modeling. *Comput Environ Urban* 16, 65-76.
- Shumlas, S.L., Singireddy, S., Thenuwara, A.C., Attanayake, N.H., Reeder, R.J., Strongin, D.R., **2016**. Oxidation of arsenite to arsenate on birnessite in the presence of light. *Geochem T* 17.
- Simanova, A.A., Kwon, K.D., Bone, S.E., Bargar, J.R., Refson, K., Sposito, G., Pena, J., **2015**. Probing the sorption reactivity of the edge surfaces in birnessite nanoparticles using nickel(II). *Geochim Cosmochim Acta* 164, 191-204.
- Simanova, A.A., Peña, J., **2015**. Time-Resolved Investigation of Cobalt Oxidation by Mn(III)-Rich δ -MnO₂ Using Quick X-ray Absorption Spectroscopy. *Environ Sci Technol* 49, 10867-10876.
- Sposito, G., **2008**. The chemistry of soils, 2nd ed. *Oxford University Press*, Oxford.
- Sunda, W.G., Huntsman, S.A., **1990**. Diel Cycles in Microbial Manganese Oxidation and Manganese Redox Speciation in Coastal Waters of the Bahama-Islands. *Limnol Oceanogr* 35, 325-338.
- Sunda, W.G., Huntsman, S.A., **1994**. Photoreduction of Manganese Oxides in Seawater. *Mar Chem* 46, 133-152.
- Sunda, W.G., Huntsman, S.A., Harvey, G.R., **1983**. Photo-Reduction of Manganese Oxides in Seawater and Its Geochemical and Biological Implications. *Nature* 301, 234-236.
- Tebo, B.M., **1991**. Manganese(Ii) Oxidation in the Suboxic Zone of the Black-Sea. *Deep-Sea Res* 38, S883-S905.
- Tebo, B.M., Bargar, J.R., Clement, B.G., Dick, G.J., Murray, K.J., Parker, D., Verity, R., Webb, S.M., **2004**. Biogenic manganese oxides: Properties and mechanisms of formation. *Annual Review of Earth and Planetary Sciences* 32, 287-328.
- Tebo, B.M., Johnson, H.A., McCarthy, J.K., Templeton, A.S., **2005**. Geomicrobiology of manganese(II) oxidation. *Trends in Microbiology* 13, 421-428.
- Thenuwara, A.C., Cerkez, E.B., Shumlas, S.L., Attanayake, N.H., McKendry, I.G., Frazer, L., Borguet, E., Kang, Q., Remsing, R.C., Klein, M.L., Zdilla, M.J., Strongin, D.R., **2016**. Nickel Confined in the Interlayer Region of Birnessite: an Active Electrocatalyst for Water Oxidation. *Angew Chem Int Edit* 55, 10381-10385.
- Villalobos, M., Lanson, B., Manceau, A., Toner, B., Sposito, G., **2006**. Structural model for the biogenic Mn oxide produced by *Pseudomonas putida*. *Am Mineral* 91, 489-502.

- Wang, Y., Feng, X.H., Villalobos, M., Tan, W.F., Liu, F., **2012**. Sorption behavior of heavy metals on birnessite: Relationship with its Mn average oxidation state and implications for types of sorption sites. *Chem Geol* 292, 25-34.
- Webb, S.M., **2005a**. SIXpack: a graphical user interface for XAS analysis using IFEFFIT. *Phys Scripta* T115, 1011-1014.
- Webb, S.M., **2005b**. Structural characterization of biogenic Mn oxides produced in seawater by the marine bacillus sp. strain SG-1. *Am Mineral* 90, 1342-1357.

Chapter 7. Conclusions

Birnessite is one of nature's strongest oxidants, and its reactivity towards the sorption and/or oxidation of many organic and inorganic compounds depends on its structural and chemical stability. The reduction of Mn in these oxides may diminish their overall reactivity, either through reductive dissolution and release of Mn(II) or by accumulation of Mn(III) on the mineral surface. Manganese reduction may also lead to a release of associated metals or inhibit the degradation of organic compounds. One process by which Mn reduction occurs is photoreduction, a process that can diminish the reactivity of birnessite. However, photoreduction of birnessites has only been investigated in systems where photoactive, electron-rich organic compounds were also present. The objective of this dissertation work was to study the photoreduction of birnessite in a simplified system where the hypothesis that MnO₂ could be intrinsically photoreduced could be easily tested. To this end, the first molecular scale knowledge on the rate and mechanism of δ -MnO₂ photoreduction in simple electrolyte solutions was obtained by bridging the fields of environmental and material science. We combined the experimental techniques applied to study Fe oxide photochemistry within environmental systems with those developed for Mn oxide photocatalysis. Ultrafast techniques, more commonly used for catalysis studies, alongside X-ray absorption spectroscopy allowed us to explore the photoreduction mechanism of birnessite on the molecular scale and couple it to photoreduction rates obtained with techniques more familiar to the environmental science community.

Summary. After introducing the importance of photochemical processes in Mn oxides in **Chapter 1**, and the analytical techniques and experimental approach adopted for this dissertation work in **Chapter 2**, the birnessite that was the most adapted to the experiments because of its physicochemical properties, δ -MnO₂, was chosen, synthesized and characterized in depth in **Chapter 3** with respect to its physicochemical properties. This mineral is characterized primarily by small particle size and an average Mn oxidation number close to 4, indicating that it is constituted almost exclusively of Mn(IV) atoms in the nanosheet. To propose a time-resolved photoreduction mechanism for each reaction step from photoexcitation to irreversible photoreduction, we studied a simplified system in which δ -

MnO₂ was present in an aqueous suspension containing only sodium, calcium, chloride or pyrophosphate. In **Chapter 4** the proposed mechanism of Mn photoreduction is described. First, the photoexcitation of the mineral results in the formation of transient Mn(III) species in the nanosheet, coupled with a one-electron transfer from adsorbed water molecules. Subsequently, a small fraction of these transient Mn(III) species become irreversibly stabilized in the interlayer, as demonstrated by the low quantum yield of this process ($\sim 10^{-4}$). These results suggest that electron transfer from water molecules to Mn oxides leads to the formation of a radical species, the fate and existence of which requires further analysis. Nevertheless, a hydroxyl radical (OH[•]) is the most likely intermediary species given the simplicity of the studied system. A hydroxyl radical species is also consistent with the interpretation of similar Fe photochemistry studies (Borer et al., 2009). In **Chapter 5**, the photoreduction rates measured at hour to day resolution were shown to be pH dependent. Our results suggest that increased protonation of mineral edges at low pH enhances the stabilization of Mn(III) as an adsorbed species in the interlayer by weakening the Mn-O bonds that bind the Mn octahedron to the nanosheet. Furthermore, these results suggest that Mn(III) formation may not occur exclusively in the bulk mineral, but also on particle edges. In **Chapter 6** we confirmed that photogenerated Mn(III) migrates to vacancy sites in the mineral, as suggested by extended X-ray absorption fine structure (EXAFS) spectroscopic analysis of irradiated Ni-laden birnessite. The displacement of Ni from vacancies to edge sites upon photoreduction is consistent with photogenerated Mn(III) occupying vacancy sites. At high pH, the decreased formation of Mn(III) does not result outcompete Ni for the vacancy sites. Nevertheless, the small changes in Ni coordination on the surface of δ -MnO₂ do not rule out Mn(III) migration to the interlayer since both Ni and Mn(III) can be accommodated on vacancy sites in the interlayer at the low Mn(III) content and low Ni surface loading of these experiments.

Implications. The photoreduction model obtained in **Chapter 4** provides empirical evidence to support the thermodynamic and computational studies of the feasibility of birnessite photoreduction through band gap photoexcitation by a ligand to metal charge transfer process. The previously hypothesized two-electron transfer process that leads to photoreductive dissolution does not occur in the absence of strong electron donors (e.g., organic compounds) (Sunda et al., 1983; Sunda and Huntsman, 1990, 1994). Contrary to thermodynamic predictions (Sherman, 2005), a one-electron transfer process leads to Mn(III)

accumulation on the mineral surface without mineral dissolution. These results also indicate that one pathway for the accumulation of Mn(III) in birnessite minerals, even though the initial microbial oxidation product is a fully oxidized MnO_2 , could be through photoreduction (Spiro et al., 2010). The expansion of the model to include the effect of pH (**Chapter 5**) has strong implications for multiple natural aquatic environments, where the reactivity of Mn oxides may be modulated in the presence of sunlight by the accumulation of Mn(III) in the mineral. The sorption capacity of birnessite minerals is proportional to the Mn(III) content (Simanova et al., 2015) and the average Mn oxidation state (AMON) of the mineral (Remucal and Ginder-Vogel, 2014), where higher Mn(III) content and a lower AMON result in a decrease in mineral reactivity. The experiments designed to quantify the effect of pH on the photoreduction of birnessite showed a greater accumulation of Mn(III) with lower pH. These results have implications on the reactivity of birnessites in multiple environmental settings, such as the low pH conditions of acid mine drainage, where the natural attenuation of toxic metals often relies on pre-existing Mn oxides. Low pH conditions can also be found at the microscale in environments that are generally governed by circumneutral to alkaline pH, such as ocean and lake waters, due to the localized effect of microbial activity, respiration and photosynthesis (Haack and Warren, 2003). The effect of pH on Mn-O bond strength can also have effects on the water oxidation capacity of birnessite in a photoelectrochemical cell, since it has been recently suggested that weakened Mn-O bonds provide active sites for water oxidation catalysis (Geng et al., 2016). Furthermore, irradiation of birnessite and the consequent accumulation of Mn(III) can strongly affect the mobility of Ni in acid conditions, as we showed in **Chapter 6**, therefore inhibiting the natural attenuation potential of birnessites in acidic environments also for other aqueous trace metals that are sequestered by birnessite similarly to Ni (e.g. Zn, Cu). At higher pH, the increase in incorporation of Ni in birnessite with irradiation suggests that sunlight may be partly responsible for the incorporation of Ni and similar trace metals on birnessite in ocean waters, which are characterized by pH values of ~ 8.3 . The reactivity of birnessite in sunlit environments will be overall decreased by the accumulation of Mn(III) on the mineral, although this effect may be reduced by biological oxidation and diel to monthly fluctuations in irradiation.

7.1. Directions of future research

The research in this dissertation provides the first experimental evidence for the molecular scale photoreduction mechanism of birnessites, identifying the effect of light in addition to the control of pH, a key environmental parameter, on the mineral photoreduction rates. The mechanism for Mn photoreduction within the context of environmental systems raised three specific questions that can be addressed in future studies:

- What is the role of interlayer cations in the photoreduction rates?
- What is the location and amount of Mn(III) formed upon photoreduction?
- What is the oxidized species coupled to Mn photoreduction?

Additionally, the effect of aggregation on the specific surface area of the minerals observed during the synthesis of δ -MnO₂ requires further investigations, also to solve the issues of aggregation observed during the pH-dependent photoreduction experiments. Finally, the simplified model of photoreduction will gain more environmental relevance once it is expanded to include the effect of organic compounds and multichromatic irradiation, simulating the effect of sunlight. In the following sections, we highlight our findings and discuss strategies to address these future research opportunities.

The relationship between Na, pH and surface area of δ -MnO₂. The surface area of birnessite has been related by multiple authors to the reactivity of Mn oxides towards sorption of organic and inorganic compounds (Villalobos et al., 2005; Remucal and Ginder-Vogel, 2014). However, there have not been studies investigating how the surface area of the minerals is affected by the synthesis conditions. In **Chapter 3**, we investigate the effect of synthesis conditions on the surface area of the minerals, and observe that a reduction in synthesis pH leads to δ -MnO₂ minerals with greater specific surface area, as measured by BET theory nitrogen adsorption, which is coupled to a lower Na : Mn ratio. Conversely, the crystallite size is greater with lower pH. These results suggest that the specific surface area is related to the aggregation state of the crystallites, which may be related to the Na content on the mineral surface. Sodium is known to adsorb on the surface of δ -MnO₂ to balance the negative charge arising from particle edges and octahedral vacancies. At low pH, protonation may explain the reduced Na : Mn ratio, whereas more alkaline conditions increase this ratio as only Na is

present to balance the negative charge. At high pH, Na could also sorb on edge sites, promoting particle aggregation.

The correlation between Na content and birnessite synthesis pH, as well as the distribution of Na between basal surfaces and edge sites on the mineral warrant additional studies from XRD modelling, which would allow us to better constrain the structural model for the synthesized particles. Furthermore, the dry BET surface area does not reflect the specific surface area of nanoparticles in aqueous suspensions (Gilbert et al., 2009). A general issue is understanding how to best describe the reactive surface area of a material and what property provides the most reasonable measure between BET theory N_2 absorption and other techniques. Particle aggregation also likely affects the photoreactivity of the minerals in the absence of electrolytes such as sodium pyrophosphate that we showed reduce aggregation (**Chapters 5 and 6**). Therefore, understanding the dependence of photoreduction on the “wet” specific surface area of the minerals could account for some of the differences observed as a function of pH in the absence and presence of pyrophosphate. One option to measure the surface area of δ - MnO_2 in solution, once the structural model is better constrained, would be through dynamic light scattering to investigate the hydrodynamic radius of particle aggregates as well as their distribution in suspension. Additionally, small angle X-ray scattering experiments could help investigate the fractal dimensions of the aggregates, but require a well constrained starting model (Gilbert et al., 2009). The results of such experiments would have implications on how the “wet” surface area of the minerals affects the sorptive properties of the minerals.

The design of efficient engineered systems for the depollution of contaminated waters relies on the characterization of such properties in “wet” conditions. The evaluation of photoreduction rates as a function of fractal dimensions of the particles and “wet” surface area could also allow us to better constrain the photoreduction model in the identification of the most active sites for photon absorption and/or Mn(III) photogeneration, as discussed in the following subsections.

Identifying the oxidized species in the photoreduction of δ - MnO_2 . In **Chapter 4**, we explore the photoreduction mechanism of δ - MnO_2 with water as the most likely electron donor when only NaCl, sodium pyrophosphate and $CaCl_2$ are present as electrolytes. Although the

results from ultrafast spectroscopy allow us to observe the individual steps and timescales of the photoreduction mechanism from photoexcitation to Mn(III) accumulation in the interlayer, we only have the capacity to experimentally follow the reduced Mn species. The species that oxidizes upon Mn reduction still has to be confirmed. Based on the simplicity of the system and on photocatalysis studies of water oxidation conducted within material science (Hocking et al., 2011; Wiechen et al., 2012b), we hypothesize that water sorbed on the mineral surface is the species which undergoes partial oxidation. The presence of small amounts of Cl⁻ may also play a role, however this species is only present in the experiments without sodium pyrophosphate, as further described in **Chapter 5**. Based on studies on Fe oxide photoreduction (Borer et al., 2009), we hypothesize that this partial oxidation involves the formation of a hydroxyl radical species, which may or may not evolve into H₂O₂.

To test these hypotheses, experiments should be carried out in the presence of chemical compounds that react with hydroxyl radical species with elevated reaction rate constants. One such species has been identified in benzyl trimethyl ammonium, since it is a positively charged species that may sorb onto the mineral surface subsequently quenching the reactive radical species formed upon photoreduction. An experimental setup where the photoreactor is coupled to a flow-through UV-Vis cuvette for periodical collection of UV-Vis spectra in a spectrophotometer, all while purging the system from oxygen with N_{2(g)}, has proven to be logistically feasible in preliminary tests. The main analytical challenge remains to avoid direct interactions between the probe compound and the mineral, which is known to react with many organic molecules (Remucal and Ginder-Vogel, 2014).

The results from such a study, in which the reactivity of the mineral with the probe compound could be determined and subtracted by corresponding dark experiments, would allow us to confirm the photoreduction model and assign chemical expressions for the overall reaction. Furthermore, the rate-limiting step in the process has been assigned to the reaction of the adsorbed water molecules with the photoexcited mineral. Therefore, confirming the existence of radical species coupled to Mn photoreduction could provide insight for the material science community, for which the photoreduction/photocorrosion of the mineral is an unwanted effect. Within the environmental science community, identifying the formation of reactive radicals upon Mn photoreduction could have implications on the rates of

photoreduction, since the presence of radical scavengers in natural environments could potentially enhance the photoreduction rates by enhancing the formation of stable Mn(III). The scavenging of reactive radicals could also explain the greater photoreduction rates in natural environments without necessarily invoking a 2-electron transfer from organic compounds.

Investigating the role of Ca in the photoreduction of δ -MnO₂. The results from **Chapter 4** show that Ca plays a role in the photoreduction process, enhancing the rates of δ -MnO₂ photoreduction. However, the role of this cation in the photoreduction process is still unknown, and in our studies the presence of Cl⁻, a known hole scavenger (Grätzel et al., 1985), could not be excluded because of the use of CaCl₂. Calcium has been shown to affect Mn photocatalysis in other studies (Wiechen et al., 2012a), is known to be an essential cation in the microbial oxidation of Mn(II) (Webb et al., 2005), and is present in high concentrations in many natural environments. Furthermore, recent observations have shown that the identity of interlayer cations can affect water frustration in the interlayer region and greater water frustration has been shown to enhance the water oxidation capacity of birnessite (Remsing et al., 2015).

Additional investigations will be required to evaluate the role of Ca in the absence of Cl⁻ ions. An experimental design where equilibration of the mineral with CaCl₂ and then rinsing the suspension of Cl⁻ in a similar fashion as described in **Chapter 3** would allow us to verify whether the observed photoreduction enhancement is related to Ca or to the Cl⁻ anions. These experiments should be carried out at the different pH values that were tested in **Chapter 5**, pH 4.0, 6.5 and 8.0, in order to compare the effect of the interlayer cation as a function of pH. The issue of aggregation that was present with the pH-STAT equilibration should be addressed beforehand. To avoid the confounding effects of aggregation in the absence of sodium pyrophosphate, a non-redox active buffer that does not complex Mn(III) (e.g., phosphate buffer) could be used, after verifying that it does not complex Ca thereby extracting it from the mineral surface.

Understanding the effect of Ca on the photoreduction of birnessite could expand the photoreduction model to many natural environments where Ca may often replace Na in the interlayer of birnessite minerals. The role of Ca also has implications in material science where this cation is required in the water oxidizing center (WOC) of photosystem II (Armstrong,

2008) and has been linked to a greater photocatalytic activity of Mn oxides in a WOC-mimicking system (Wiechen et al., 2012b).

Identifying the structural location for Mn(III) formation. Our results from **Chapter 5** suggest that the greater photoreduction rate with decreasing pH is related to protonation of the surface, which decreases the Mn-O bond strength thus enhancing Mn(III) stabilization in the interlayer. However, we could not assess whether Mn(III) originates on the edge sites or in the bulk of the mineral. This was indirectly probed in the following work (**Chapter 6**), by observing the absorption and desorption of Ni from the mineral surface as a function of irradiation and pH. Here, we suggest that Mn(III) at low pH is formed somewhere in the mineral, migrates to the interlayer and displaces Ni until all vacancies are occupied. In this study, no information was obtained on whether Mn(III) was initially formed on the edge sites or in the mineral bulk, but we confirmed that Mn(III) was stabilized on vacancy sites. Additionally, preliminary studies on triclinic birnessite, a birnessite characterized by 16 to 30% Mn(III) exclusively incorporated in the nanosheet, show that the location of Mn(III) strongly affected the photoreactivity of birnessite: In conditions of no vacancies and Mn(III) exclusively in the nanosheet, the mineral does not photoreduce and the transient absorption bleach signal is suppressed.

Future studies could identify the sites for Mn(III) formation, for example, by designing time-resolved X-ray absorption spectroscopy (TRXAS) experiments on the oxygen K-edge. In such a study, the reaction at pH 4 (greatest photoreduction rate) could be probed by observing the changes in the oxygen coordination environment as a function of irradiation. The results of such a study would help us understand whether Mn(III) is formed on edge sites, where O atoms are bound to Mn and protons, or in the mineral bulk, where O atoms are bound only to Mn atoms. The design of such an experiment is particularly challenging because of the presence of oxygen in most materials and solvents, such as water in which the mineral suspensions are found. These challenges could be overcome by dispersing the mineral in a non-aqueous solvent in an atmosphere purged from oxygen with He_{2(g)}.

Identifying the location in which Mn(III) forms is important to both expand the photoreduction model and to predict how the reactivity of the mineral will be affected when organic or inorganic compounds are sorbed onto it. In fact, these compounds can sorb

preferentially on vacancy sites or edge sites, therefore the formation of Mn(III) on edge sites or in the bulk affects the remobilization potential of these compounds differently. The location of Mn(III) could also have implications on the aggregation state of the mineral if it is formed on edge sites, similarly as Na cations at high pH in the synthesis study (**Chapter 3**).

Limit to the amount of Mn(III) that δ -MnO₂ can accommodate. By considering the structure of birnessite, there should be a limit to the amount of vacancies that can be formed before the hexagonal layer structure is completely disrupted. Therefore, there must be a physical limit to the accumulation of Mn(III) in the mineral, determined by the amount of vacancy sites and edge sites that the mineral can accommodate. Burns (1976) suggested that the maximum amount of vacancies the mineral can physically accommodate is 1/6th of the total Mn atoms present, thus 17 %. From a geometric calculation based on a 5 nm particle on the *ab* plane (~ 287 Mn octahedra), we expect there to be an additional ~47 edge sites, which would result in the limit of edges + vacancies being equal to ~33 % Mn(III). This observation is based on the assumption that the mineral will not convert to a triclinic phase, which is found with Mn(III) incorporated in the nanosheet (Drits et al., 1997). The conversion of triclinic to hexagonal birnessite can occur rapidly (within seconds to minutes) by lowering the pH from 9 to 3 (Lanson et al., 2000). However, preliminary studies show that the opposite does not occur within hour to day timescales. Therefore, we expect that over time the rate of Mn(III) formation should decrease as the physical limit is reached, since the incorporation of Mn(III) adsorbed in the interlayer is kinetically limited: we expect that any Mn(III) migrated in the interlayer cannot incorporate back into the nanosheet. Preliminary transient absorption studies on *c*-disordered H⁺ birnessite, a mineral containing ~20% Mn(III) distributed between the interlayer and the nanosheet/edges, show similar optical properties but a lower photoreactivity compared to δ -MnO₂ (**Figure 1**).

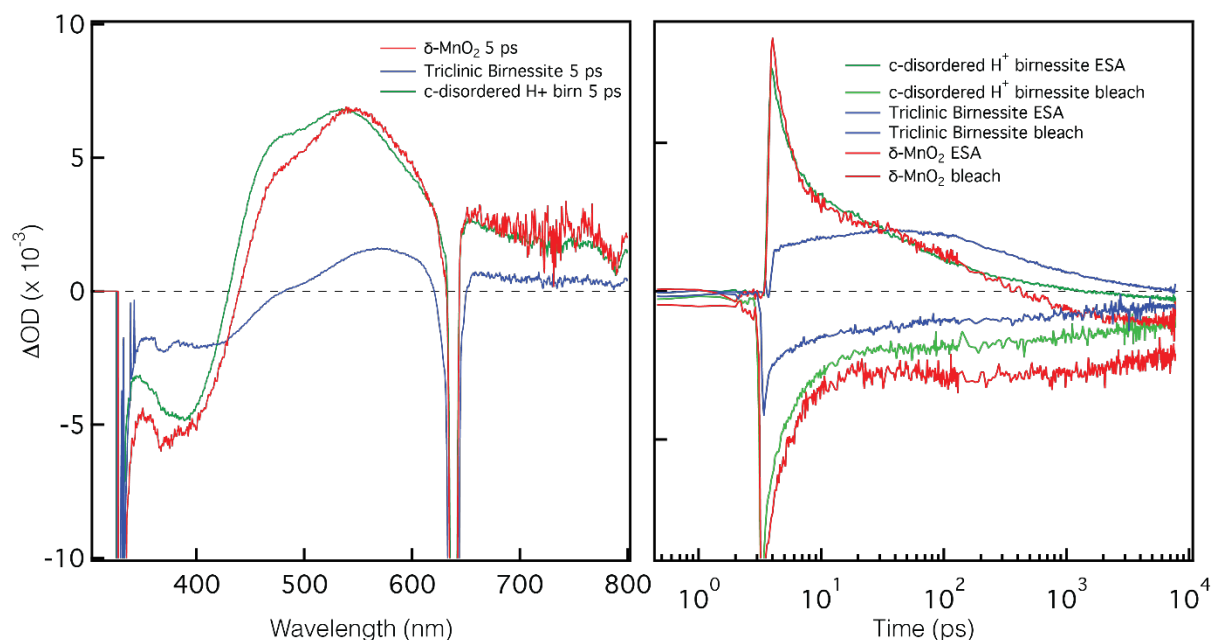


Figure 2: Ultrafast pump-probe optical spectroscopy data for 3 different minerals of the birnessite family: δ -MnO₂, c-disordered H⁺ birnessite, and Triclinic birnessite.

Experiments to probe the physical limit of Mn(III) in δ -MnO₂ can be run by irradiating suspensions for long timescales where sodium pyrophosphate is added after irradiation to evaluate whether Mn(III) formation and accumulation in the mineral versus time increases linearly or plateaus. These experiments would be carried out at pH 4 since it is the pH at which the greatest photoreduction rate is achieved and where Mn(III) is not stable as an incorporated species (from the studies on triclinic birnessite pH equilibration). These experiments could also be carried out on Ni laden minerals and combined with EXAFS spectroscopy to obtain indirect information on the surface speciation of Mn(III). We have shown that the accumulation of 13 % Mn(III) in the mineral results in 50 % Ni release, and half of the remaining Ni migrates/desorbs and readsorbs onto edge sites. These results suggest that photogenerated Mn(III) occupies vacancy sites previously occupied by Ni. Previous studies have shown that the sorption of Ni on a δ -MnO₂ phase characterized by up to 30 % Mn(III) resulted in Ni binding almost exclusively to particle edges, in contrast to exclusively sorbing to vacancy sites in a Mn(III)-free mineral (Simanova et al., 2015). We would expect that by reaching the calculated limit of 33 % Mn(III) content, all Ni would be released to solution, confirming that the mineral has reached the maximum amount of edge and vacancy sites it can physically accommodate. Furthermore, we expect the resulting mineral to not be reactive towards the

sorption of trace metals. The absence of pyrophosphate would be necessary to avoid extracting Mn(III) while it is formed. As described in the previous subsection, the issue of aggregation has to be investigated beforehand. Using a phosphate buffer would be a solution, once it is verified that it does not interact with the photoreaction and the structure of the mineral.

The confirmation that there is a physical limit to the amount of Mn(III) that can be accumulated in the mineral would allow us to better understand the stability and reactivity of birnessite minerals in natural environments. Additionally, these results would have implications on engineered systems, where the reduced reactivity of Mn(III)-rich birnessites would require the extraction of Mn(III) to restore the original reactivity. Recent studies have also shown that there is a relationship between Mn(III) and vacancy content in birnessite for electrochemical capacitor applications (Gao et al., 2017). In those studies, an increased vacancy content leads to greater electric capacitance (the ability to store electric charge), whereas the presence of Mn(III) cations in the interlayer promote polaron hopping conduction, which improves the electrical conductivity of the nanosheet. These results may explain the lower photoreactivity of Mn(III)-rich birnessite that we observed (c-disordered H⁺ birnessite). In fact, an improved conductivity may lead to faster electron-hole recombination (less intraband traps that may lead to hole scavenging), which may in turn lead to less irreversible photoreduction.

Comparing the effect of other trace metals on δ -MnO₂ photoreduction. Given the diversity of the bonding configurations and redox reactivities of different trace metals on birnessite, We propose further evaluation of the effect of irradiation on the sorbed metal mobility and mineral photoreduction in the presence of redox active metals such as Co, for which the sorption and redox mechanism on birnessite has been recently elucidated at different pH values in our group (Pena et al., 2013; Simanova and Peña, 2015). We expect that photoreduction of δ -MnO₂ will enhance the Co oxidation rates, as recently shown for As species (Shumlas et al., 2016). Finally, by investigating the sorption dynamics of a metal that binds to the mineral surface in a different coordination than Ni (such as Zn: tetrahedral as well as octahedral), we expect that the accumulation of Mn(III) can compete with Zn for vacancy sites even when the latter is tetrahedrally bound, extending the results of **Chapter 6** to elements that bind in tetrahedral coordination. These predictions are based on recent studies that show a

decrease in Zn sorption with increasing Mn(III) content in the mineral at low pH (Yin et al., 2017).

Since the coordination of the metal on the mineral surface likely modifies the band structure of the mineral as it introduces different electronic states, these additional states may affect the rates of δ -MnO₂ photoreduction. For example, the presence of these metals may act as electron or hole traps, extending the lifetime of photoexcitation and thus increasing the probability for hole scavenging by surface sorbed hole scavengers. Cobalt and Zn are frequently found associated with birnessite in ocean environments, but their sorption mechanisms have always been studied in the dark. These elements can be both nutrients and toxic, depending on their concentration in solution. Mineral oxides, amongst which birnessite, contribute to governing the mobility of these transition metals in aqueous environments by scavenging them from the solution. By investigating the effect of irradiation on the mobility of these elements, we expect to contribute to the understanding of their biogeochemical cycle in sunlit environments, which may have important effects on their toxicity for living organisms.

Investigating the effect of organic compounds in the current δ -MnO₂ photoreduction model. The further expansion of this model to more environmentally relevant systems will require the inclusion of organic compounds. Organic compounds can either act as stronger electron donors than water in a ligand to metal charge transfer mechanism, or they can themselves act as the chromophore in the photoreaction. In both cases, we expect that the strong electron donating capacity of organic compounds to birnessite minerals will result in a complete, 2-electron transfer process, yielding aqueous Mn(II) as the end product of photoreduction.

The photoreduction with the the mineral or the organic as the chromophore can both be probed in the photoreactor setup designed in this dissertation work. In particular, the first process can be probed by evaluating the photoreduction of δ -MnO₂ in the presence of simple organic molecules such as pyruvate, citrate or oxalate. The second process, on the other hand, can be probed by sorbing more complex organic compounds, such as fulvic or humic acids, onto δ -MnO₂ and irradiating with a longer wavelength which would minimize the photoreactivity of the mineral compared to the organic compound. By carrying out dark controls, any reductive dissolution of the mineral by the organic compounds in the dark may

be corrected. In preliminary experiments, we observed that the addition of 10% (mol/mol) sodium oxalate to a suspension containing δ -MnO₂ and pyrophosphate resulted in a steady accumulation of Mn(III) in the dark over a several hour period, whereas in the absence of pyrophosphate aqueous Mn(II) was formed, indicating that pyrophosphate quenches the reaction by scavenging Mn(III) once it is formed.

These experiments would allow us to expand the understanding of birnessite photoreduction to include the effect of organic compounds, which are often present in environmental settings, and address the uncertainties that still remain from the previous studies on the environmental photochemistry of manganese (Sunda et al., 1983; Sunda and Huntsman, 1990, 1994).

The effect of irradiation wavelength on the quantum yield of Mn(III) photogeneration. The experiments carried out in this study were all characterized by monochromatic irradiation close to the peak wavelength of the sunlight irradiance spectrum, which is 400 nm (**Figure 2**). The photoreduction yield was then obtained by dividing the amount of Mn(III) produced by the amount of photons absorbed, resulting in a value close to 10^{-4} . Since sunlight irradiance is characterized by a multitude of wavelengths of visible light, and δ -MnO₂ absorbs light over the whole visible spectrum (as shown by its UV-Vis absorption spectrum, **Figure S5 Annex 3**, as well as inferred by its brown/black color), we expect that the quantum yield for photoreduction might increase if the mineral is exposed to simulated sunlight, as can be achieved by irradiating the mineral suspensions in a sunlight simulator. We have collected preliminary transient absorption spectra with an irradiation (pump) at wavelengths different than 400 nm, namely at 320 nm and 700 nm, and observed that the photoexcitation and decay kinetics are identical to those at 400 nm, only of lower intensity (**Figure 3**). These results suggest that δ -MnO₂ will react to sunlight over the whole visible spectrum, where the photoreductive process will be enhanced compared to that at 400 nm, and are also corroborated by recent studies that show a photocatalytic activity of birnessite in degrading CO under irradiation of the full solar spectrum (Liu et al., 2016). The actual quantum yield may not be affected, since it is normalized by the amount of photons absorbed, but the photoreduction rates will likely be greater.

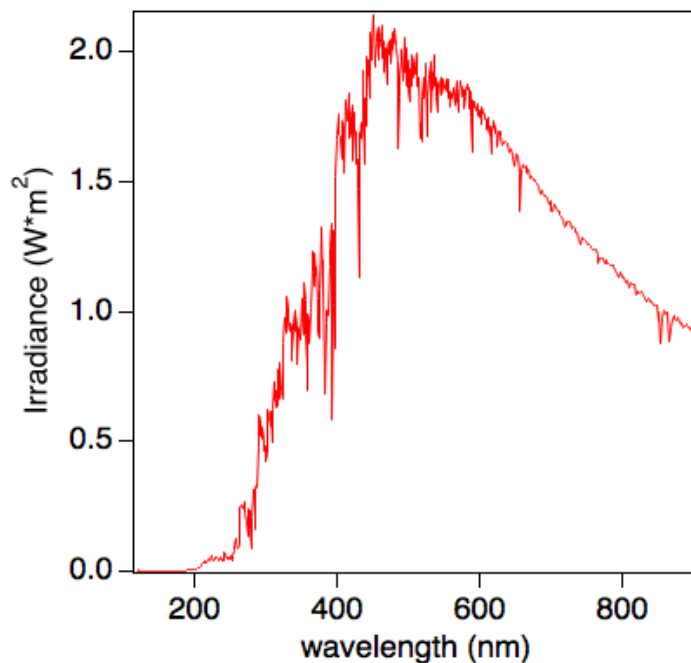


Figure 2: Reference spectrum for the solar irradiance according to the standard ASTM E490 AM0.

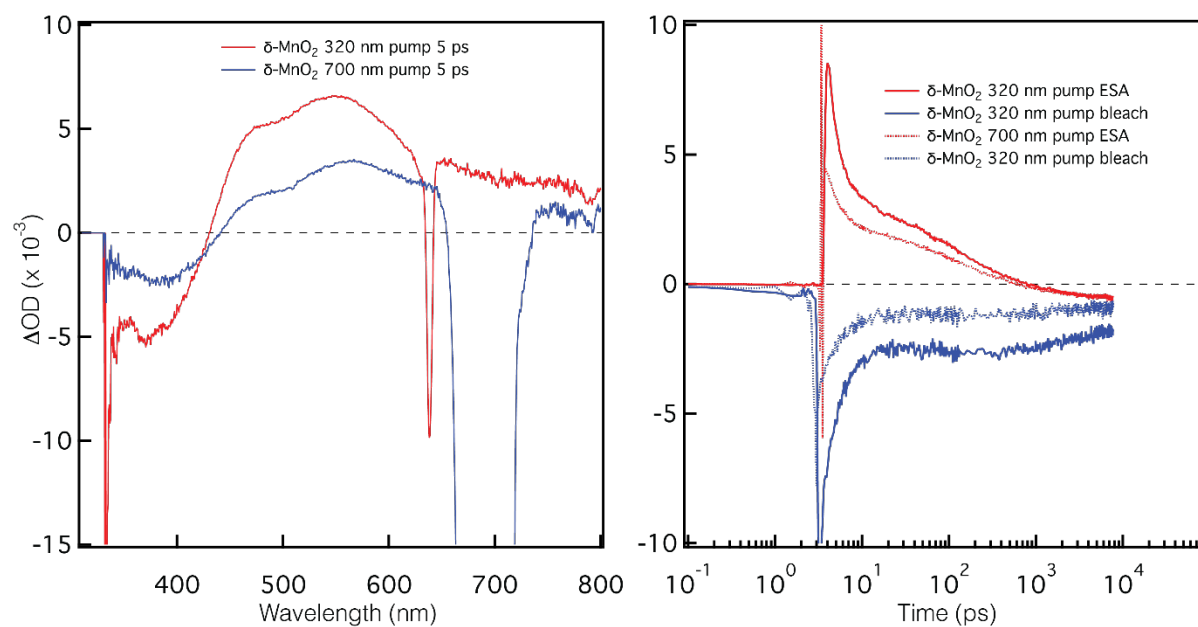


Figure 3: Ultrafast pump-probe optical spectroscopy data for δ -MnO₂ with irradiation at 2 different wavelengths, 320nm and 600 nm, showing the same photoexcitation and decay kinetics for both the enhanced state adsorption feature (ESA) as well as for the ground state bleach.

To investigate the photoreduction under a broad wavelength range, the same flow-through photoreactor setup can be installed under a commercially available sunlight simulator. The issue of photon flux quantification, as described in **Chapter 2**, must be tackled. Precise

knowledge of the photoreactor geometry must be obtained since the easiest way to characterize the photon flux in such instruments is through a spectral irradiance meter that measures the irradiance on a photosensitive surface and then reports the surface/normalized value as W/m^2 . Alternatively, the photoreactor setup can be screened from the irradiation by covering the tubing with aluminum foil, only leaving the flow through cuvette exposed to light, since its geometry is easily characterized.

7.2. References

- Armstrong, F.A., **2008**. Why did Nature choose manganese to make oxygen? *Philos Trans R Soc Lond B Biol Sci* 363, 1263-1270; discussion 1270.
- Borer, P., Sulzberger, B., Hug, S.J., Kraemer, S.M., Kretzschmar, R., **2009**. Photoreductive dissolution of iron(III) (hydr)oxides in the absence and presence of organic ligands: experimental studies and kinetic modeling. *Environ Sci Technol* 43, 1864-1870.
- Burns, R.G., **1976**. Uptake of Cobalt into Ferromanganese Nodules, Soils, and Synthetic Manganese(IV) Oxides. *Geochim Cosmochim Acta* 40, 95-102.
- Drits, V.A., Silvester, E., Gorshkov, A.I., Manceau, A., **1997**. Structure of synthetic monoclinic Na-rich birnessite and hexagonal birnessite .1. Results from X-ray diffraction and selected-area electron diffraction. *Am Mineral* 82, 946-961.
- Gao, P., Metz, P., Hey, T., Gong, Y.X., Liu, D.W., Edwards, D.D., Howe, J.Y., Huang, R., Mixture, S.T., **2017**. The critical role of point defects in improving the specific capacitance of delta-MnO₂ nanosheets. *Nat Commun* 8.
- Geng, Z.B., Wang, Y.X., Liu, J.H., Li, G.S., Li, L.P., Huang, K.K., Yuan, L., Feng, S.H., **2016**. delta-MnO₂-Mn₃O₄ Nanocomposite for Photochemical Water Oxidation: Active Structure Stabilized in the Interface. *Acs Appl Mater Inter* 8, 27825-27831.
- Gilbert, B., Ono, R.K., Ching, K.A., Kim, C.S., **2009**. The effects of nanoparticle aggregation processes on aggregate structure and metal uptake. *J Colloid Interf Sci* 339, 285-295.
- Grätzel, M., Kiwi, J., Morrison, C.L., Davidson, R.S., Tseung, A.C., **1985**. Visible-light-induced photodissolution of α -Fe₂O₃ powder in the presence of chloride anions. *J Chem Soc Farad T* 1 81, 1883-1890.
- Haack, E., Warren, L.A., **2003**. Biofilm hydrous manganese oxyhydroxides and metal dynamics in acid rock drainage. *Environ Sci Technol* 37, 4138-4147.
- Hocking, R.K., Brimblecombe, R., Chang, L.Y., Singh, A., Cheah, M.H., Glover, C., Casey, W.H., Spiccia, L., **2011**. Water-oxidation catalysis by manganese in a geochemical-like cycle. *Nat Chem* 3, 461-466.
- Lanson, B., Drits, V.A., Silvester, E., Manceau, A., **2000**. Structure of H-exchanged hexagonal birnessite and its mechanism of formation from Na-rich monoclinic buserite at low pH. *Am Mineral* 85, 826-838.
- Liu, F., Zeng, M., Li, Y.Z., Yang, Y., Mao, M.Y., Zhao, X.J., **2016**. UV-Vis-Infrared Light Driven Thermocatalytic Activity of Octahedral Layered Birnessite Nanoflowers Enhanced by a Novel Photoactivation. *Adv Funct Mater* 26, 4518-4526.
- Pena, J., Simanova, A.A., Bargar, J.R., Sposito, G., **2013**. Sorption of Cobalt and Nickel by Biogenic Birnessite. *Mineralogical Magazine* 77, 1946.

- Remsing, R.C., McKendry, I.G., Strongin, D.R., Klein, M.L., Zdilla, M.J., **2015**. Frustrated Solvation Structures Can Enhance Electron Transfer Rates. *J Phys Chem Lett* 6, 4804-4808.
- Remucal, C.K., Ginder-Vogel, M., **2014**. A critical review of the reactivity of manganese oxides with organic contaminants. *Environ Sci-Proc Imp*.
- Sherman, D.M., **2005**. Electronic structures of iron(III) and manganese(IV) (hydr)oxide minerals: Thermodynamics of photochemical reductive dissolution in aquatic environments. *Geochim Cosmochim Acta* 69, 3249-3255.
- Shumlas, S.L., Singireddy, S., Thenuwara, A.C., Attanayake, N.H., Reeder, R.J., Strongin, D.R., **2016**. Oxidation of arsenite to arsenate on birnessite in the presence of light. *Geochem T* 17.
- Simanova, A.A., Kwon, K.D., Bone, S.E., Bargar, J.R., Refson, K., Sposito, G., Pena, J., **2015**. Probing the sorption reactivity of the edge surfaces in birnessite nanoparticles using nickel(II). *Geochim Cosmochim Acta* 164, 191-204.
- Simanova, A.A., Peña, J., **2015**. Time-Resolved Investigation of Cobalt Oxidation by Mn(III)-Rich δ -MnO₂ Using Quick X-ray Absorption Spectroscopy. *Environ Sci Technol* 49, 10867-10876.
- Spiro, T.G., Bargar, J.R., Sposito, G., Tebo, B.M., **2010**. Bacteriogenic Manganese Oxides. *Accounts Chem Res* 43, 2-9.
- Sunda, W.G., Huntsman, S.A., **1990**. Diel Cycles in Microbial Manganese Oxidation and Manganese Redox Speciation in Coastal Waters of the Bahama-Islands. *Limnol Oceanogr* 35, 325-338.
- Sunda, W.G., Huntsman, S.A., **1994**. Photoreduction of Manganese Oxides in Seawater. *Mar Chem* 46, 133-152.
- Sunda, W.G., Huntsman, S.A., Harvey, G.R., **1983**. Photo-Reduction of Manganese Oxides in Seawater and Its Geochemical and Biological Implications. *Nature* 301, 234-236.
- Villalobos, M., Bargar, J., Sposito, G., **2005**. Mechanisms of Pb(II) Sorption on a Biogenic Manganese Oxide. *Environ Sci Technol* 39, 569-576.
- Webb, S.M., Tebo, B.M., Bargar, J.R., **2005**. Structural influences of sodium and calcium ions on the biogenic manganese oxides produced by the marine *Bacillus* sp., strain SG-1. *Geomicrobiol J* 22, 181-193.
- Wiechen, M., Berends, H.M., Kurz, P., **2012a**. Water oxidation catalysed by manganese compounds: from complexes to 'biomimetic rocks'. *Dalton Transactions* 41, 21-31.
- Wiechen, M., Zaharieva, I., Dau, H., Kurz, P., **2012b**. Layered manganese oxides for water-oxidation: alkaline earth cations influence catalytic activity in a photosystem II-like fashion. *Chem Sci* 3, 2330-2339.
- Yin, H., Wang, X., Qin, Z., Ginder-Vogel, M., Zhang, S., Jiang, S., Liu, F., Li, S., Zhang, J., Wang, Y., **2017**. Coordination geometry of Zn²⁺ on hexagonal turbostratic birnessites with different Mn average oxidation states and its stability under acid dissolution. *Journal of Environmental Sciences*.

ANNEXES

ANNEX 1. Photoreactor design

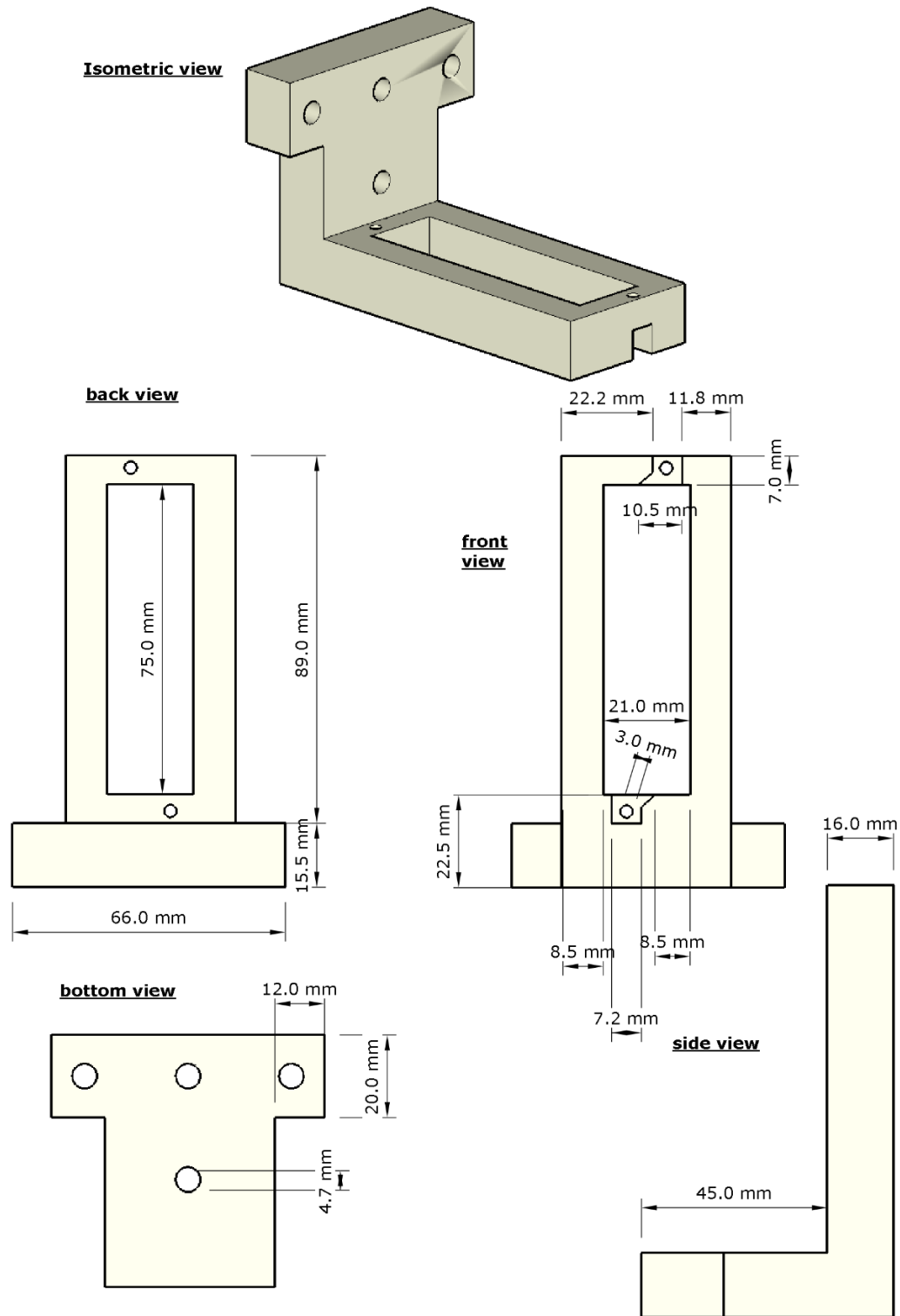


Figure 1. Technical drawing for the Irradiation module support

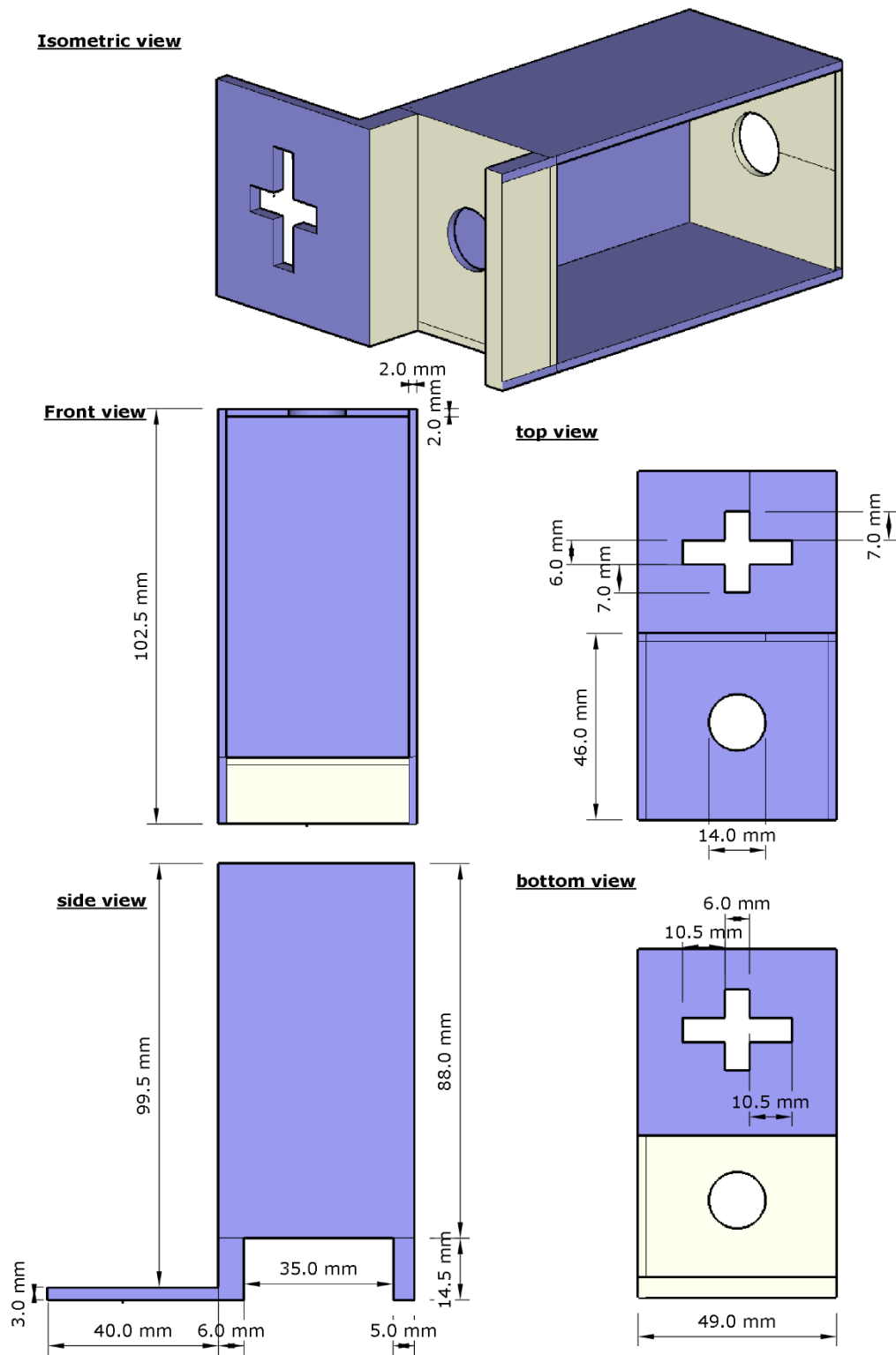


Figure 2. Technical drawing for the flow-through module.

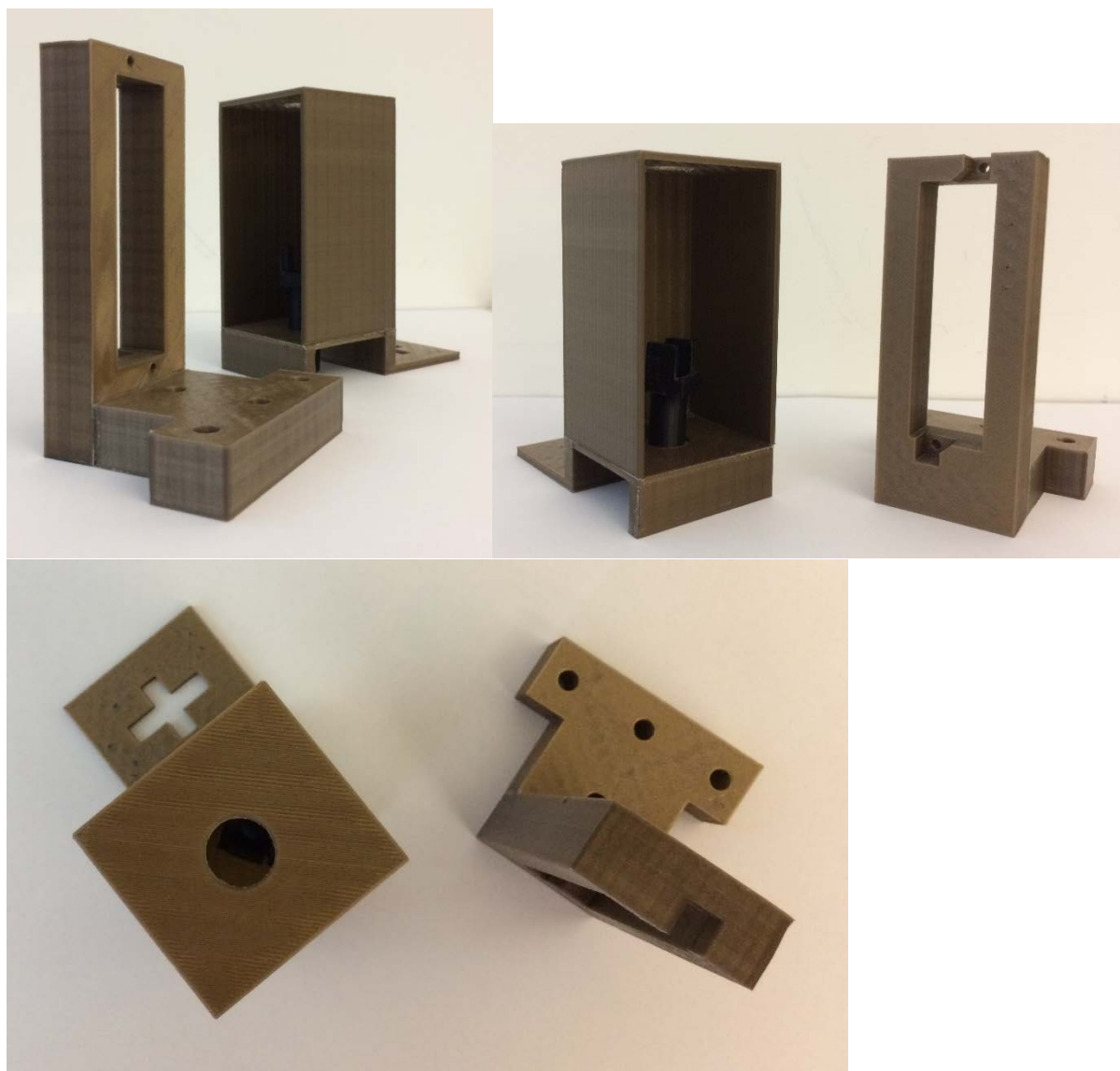


Figure 3. Photographs of the 1 :1 scale 3D printed prototype of the photoreactor setup (irradiation and flow-through modules).



Figure 4. The various components of the irradiation setup, as well as the flow through cuvette. from top left to bottom right : Pump tubing, MOSFET cooler, LEDs, focusing lenses, thermally conductive paste, flow through cuvette, LED DC power driver.

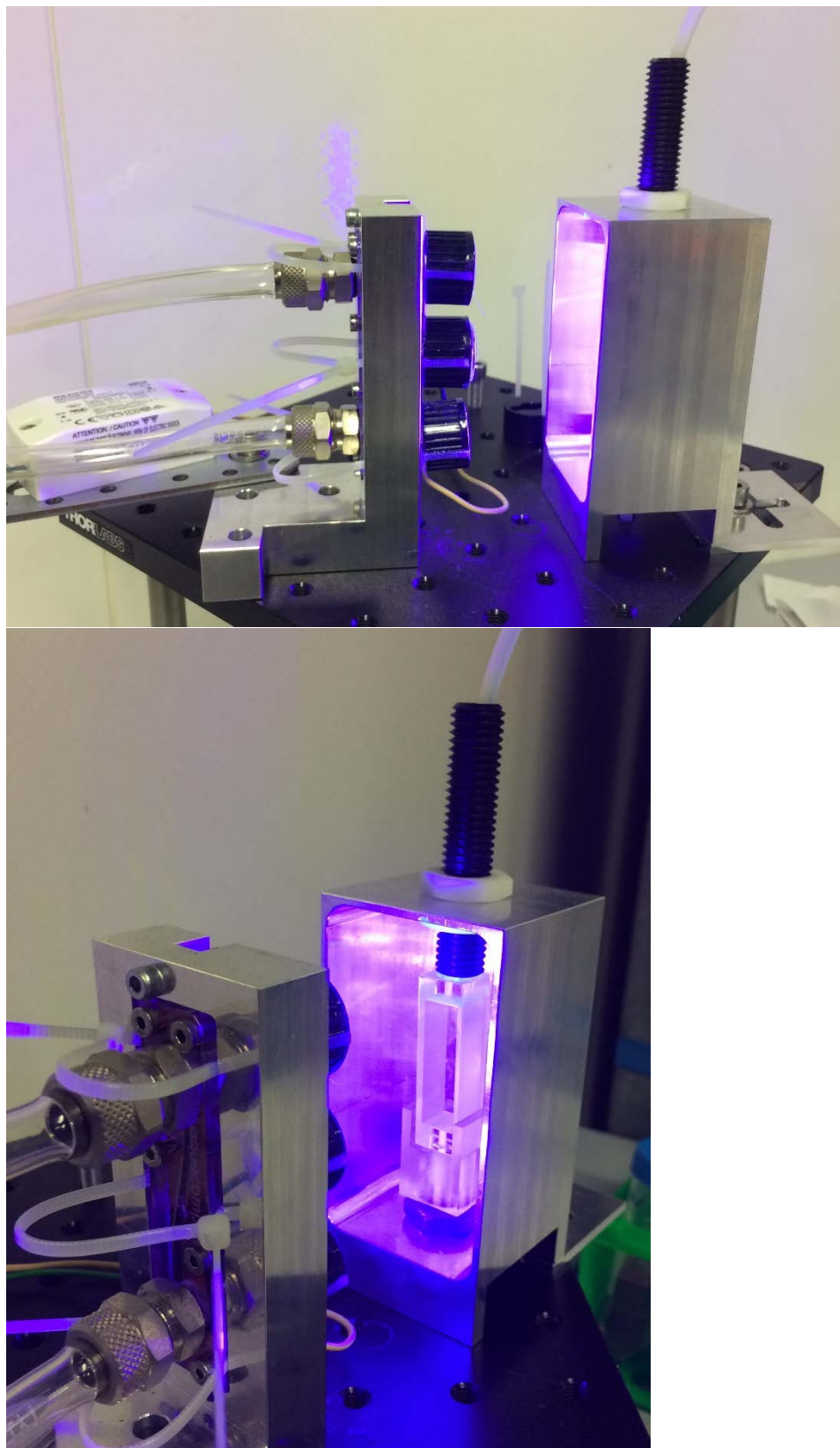


Figure 5. Photographs of the assembled photoreactor setup



Figure 6. Detail of the cuvette installation in the flow-through module



Figure 7. Photograph of the photoreactor setup assembly (3x photoreactors side by side on a breadboard support, connected to the peristaltic pump).

ANNEX 2. Supporting information for Chapter 3

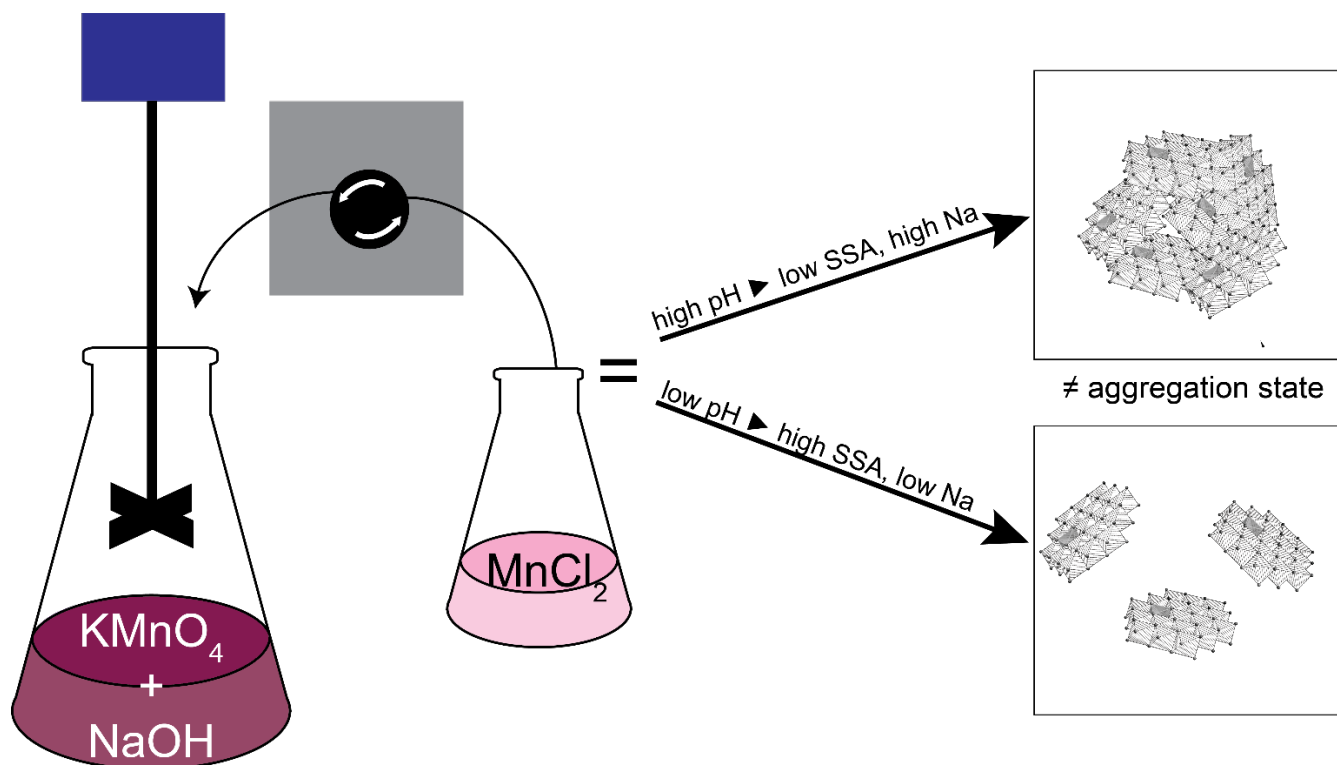


Figure 0: Graphical abstract describing the main methods and findings of this work

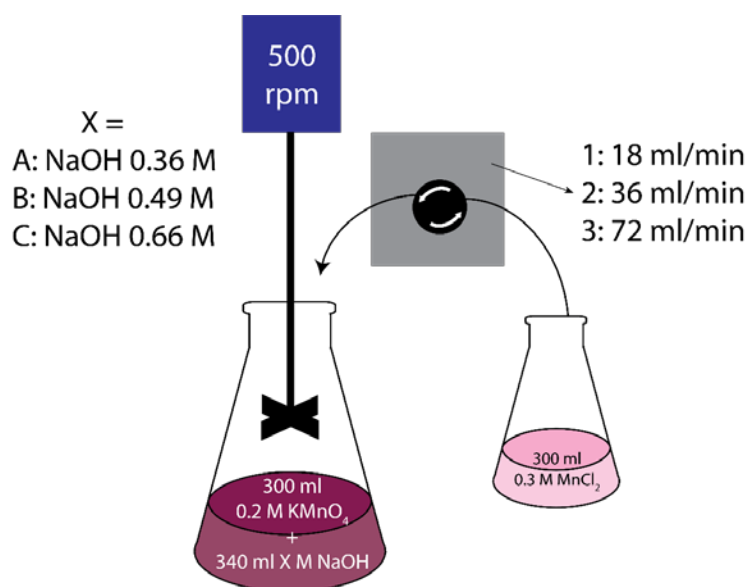


Figure S1: Schematic of the synthesis procedure and legend for sample names as a function of the parameters that were varied during the synthesis of the different samples.

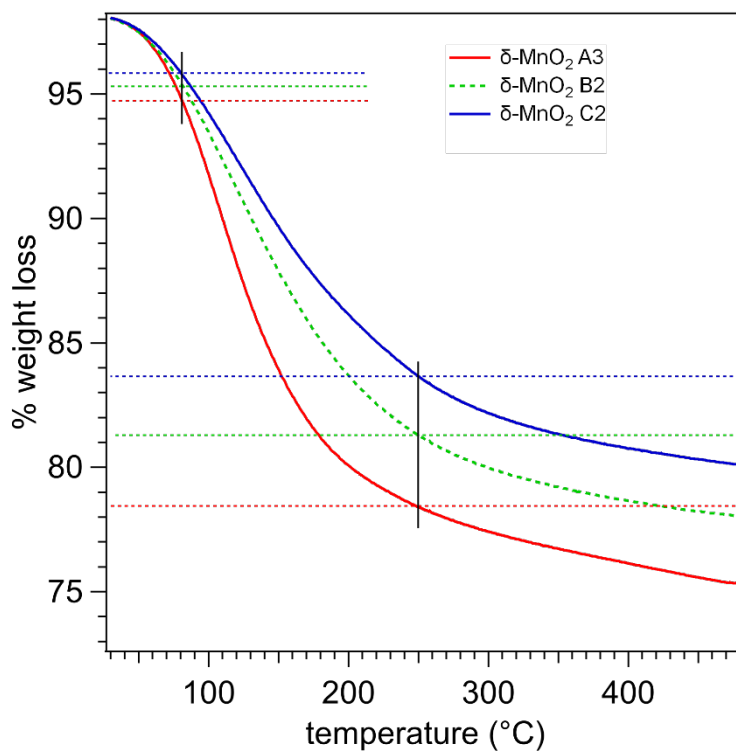


Figure S2: Thermogravimetric analysis weight loss curves normalized to sample weight at room temperature. The horizontal lines indicate the temperatures at which strongly bound water is lost.

ANNEX 3. Supporting information for Chapter 4

7.3. SI Materials and methods

Mineral synthesis and characterization. The Mn oxide phase, δ -MnO₂, was synthesized by combining stoichiometric amounts of MnCl₂ with KMnO₄ in excess NaOH under vigorous mixing (Villalobos et al., 2003). The solids were rinsed with water until the electrical conductivity of the supernatant was less than 30 μ S cm⁻¹. The washing procedure required 7 cycles of centrifuging the slurry (20 minutes at 27500 RCF and 25°C) and re-suspending the mineral paste in MQ water. After the final rinsing step, the mineral paste was re-suspended in MQ water and stored in the dark at 4°C. Mineral composition was characterized with respect to average Mn oxidation number and Na:Mn content. The average Mn oxidation number (AMON) was characterized by potentiometric titration (Grangeon et al., 2008) with a Metrohm 888 Titrand automatic titrator. Briefly, 15 mg of δ -MnO₂ were dissolved in a 0.01 M Mohr's salt [(NH₄)Fe(SO₄)₂•6H₂O] solution and residual Fe(II) was titrated with 0.01 M KMnO₄. The amount of Mn(II) generated was back titrated with 0.02 M KMnO₄ and all Mn(III) produced was trapped by complexation with excess sodium pyrophosphate (Na₄P₂O₇, abbreviated as PP) (Kostka et al., 1995; Klewicki and Morgan, 1998; Webb et al., 2005). A detailed description of the titration protocol is provided by Grangeon et al. (2008). The Na:Mn ratio was measured by inductively coupled plasma optical emission spectrometry (ICP-OES) on a Perkin Elmer Optima 8300 spectrometer on samples digested in 3% HNO₃ and 0.05 M H₂C₂O₄.

Structural characterization of δ -MnO₂ was carried out to determine specific surface area, mineral phase and intermediate-range structure (within 2 nm). Additionally, the light absorption spectrum of the mineral was measured by UV-vis spectrophotometry. Specific surface area was determined by a 5 point BET N₂ adsorption isotherm at 77 K on a Micromeritics Gemini 2375 instrument. Powder XRD patterns were collected on a Thermo Electron ARL X'TRA diffractometer with Cu K α radiation (λ =1.5418 Å) and a Peltier-cooled Si(Li) solid state detector, with a speed of 0.5° min⁻¹, a step size of 0.02° and an integration time of 2400 s. Both for XRD and BET powders were obtained by oven drying at 45° for 1 day pastes obtained by vacuum-filtering an aliquot of the stock suspension.

UV-vis absorption spectra from 200 – 800 nm were obtained on a Shimadzu UV-2600 spectrophotometer with 1 cm path length cuvettes or an Ocean Optics spectrophotometer with

0.5 mm path length cuvettes. High energy X-ray scattering data were collected at beamline 11-ID-B at the Advanced Photon Source (Argonne, USA). Atomic pair distribution functions [i.e., $G(r)$, **Figure S7b**] were obtained with the PDFgetX2 GUI utility following standard procedures (Qiu et al., 2004), which involve Fourier transformation of the reduced structure function, $F(Q) = Q[S(Q)-1]$ (**Figure S7a**). The reduced structure function is the total scattering pattern multiplied by the magnitude of the scattering vector, Q , and divided by the square of the atomic form factor, $|f_i|^2$.

Powder XRD patterns, high energy X-ray scattering data and UV-vis spectra were collected from both Na-MnO₂ and Ca-MnO₂, where Ca-MnO₂ was obtained by equilibrating a suspension of approximately 90 mM Na-MnO₂ with CaCl₂(aq) in a 3:1 Ca:Mn molar ratio from 12 h (LITR-XAS) to 2 months (optical TA). The effect of oxygen on the chemical composition of δ -MnO₂ upon the exchange of interlayer Na with Ca was evaluated by equilibrating an aliquot of Na-MnO₂ with Ca under N_{2(g)} purge. After equilibration, aliquots were filtered and digested for measurement of [Mn_{TOT}] and [Mn_(aq)] by ICP-OES; filtered pastes were oven dried at 40°C before collecting powder XRD patterns.

Quantum yield calculation. The apparent quantum yield for Mn(III) generation was calculated according to:

$$\Phi = \frac{f_{Mn(III),t} \times \text{moles of Mn}}{\varphi * t \times \frac{A_{400 \text{ nm, MnO}_2}}{A_{400 \text{ nm, ferrioxalate}}}}$$

where $f_{Mn(III),t}$, the fraction of photoreduced Mn after time, t , is multiplied by the total number of moles of Mn in the system; φ is the photon flux measured for the photoreactor; and $A_{400 \text{ nm MnO}_2}$ and $A_{400 \text{ nm ferrioxalate}}$ are the absorbances (in OD units) of Ca- or Na-MnO₂ and ferrioxalate at 400 nm (**Chapter 4**) measured in 1 cm path length quartz cuvettes with water as a blank. Due to the possible effect of birnessite aggregation on the measurement of optical extinction coefficients of the samples (see below), we use the term “apparent quantum yield”. The fraction of photoreduced Mn was calculated according to $([Mn(III)\text{-PP}_{\text{light}}] - [Mn(III)\text{-PP}_{\text{dark}}])/[Mn_{\text{TOT}}]$. The ratio of the absorbance values in the denominator accounts for the different absorptivity of δ -MnO₂ relative to ferrioxalate, where $\epsilon_{\text{Na-MnO}_2 \text{ pH } 6.5} = 2525 \text{ L mol}^{-1} \text{ cm}^{-1}$ and $\epsilon_{\text{Ca-MnO}_2} = 2300 \text{ L mol}^{-1} \text{ cm}^{-1}$, and $\epsilon_{\text{ferrioxalate}} = 110 \text{ L mol}^{-1} \text{ cm}^{-1}$. The molar absorptivity

of ferrioxalate was calculated from serial dilutions of stock solutions calibrated with ICP-OES measurements.

Optical transient absorption kinetic fits. A bleach signal on the microsecond timescale between 550 – 580 nm with the EOS spectrometer was observed for Ca-MnO₂ and Na-MnO₂ samples in Nafion, and Na-MnO₂ samples in water or terephthalic acid. The trends extracted at 580 nm were fitted by exponential decay functions with 2 time constants. The bleach appeared to return to baseline ($\Delta OD \sim 0$), however this could not be judged from the data due to the noise level inherent to the data acquisition. To evaluate whether or not the signal returned to baseline within sub-second timescales, the data were refitted using a third decay constant fixed to $10^6 \mu\text{s}$ (i.e., no decay to baseline within the $50 \mu\text{s}$ resolution of the experiment). An F-test showed only 67 % confidence that the model with three time constants returned a significantly better fit than the model with two time constants. Thus, we do not have 95 % confidence that the bleach persists over long time scales ($10^6 \mu\text{s}$).

7.4. SI Results and discussion

Mineral characterization. The δ -MnO₂ powder had a BET specific surface area of $141 \pm 3 \text{ m}^2 \text{ g}^{-1}$, an average Mn oxidation number (AMON) of 4.05 ± 0.05 and a Na:Mn ratio of 0.24. The XRD patterns collected from Na-MnO₂ and Ca-MnO₂, with a 5 day equilibration period under aerated and N_{2(g)}-purged conditions for Ca-MnO₂, were consistent with those reported for δ -MnO₂ (Villalobos et al., 2003). The UV-vis absorption spectra of Na-MnO₂ and Ca-MnO₂ are shown in **Figure S6a**. The UV-vis absorption spectrum of Ca-MnO₂ exhibits a significant red shift relative to that for Na-MnO₂. This red shift is accompanied by a change in line shape. Therefore, the redshift cannot be attributed simply to scattering from aggregated particles. Additional UV-vis spectra were acquired to test the effect of the background electrolyte and ionic strength on the observed red-shift. Only the CaCl₂-equilibrated sample showed a red shift (**Figure S6b**) that persisted after removing any excess CaCl_{2(aq)} electrolyte by rinsing the particles with MQ water. In addition, similar average Mn oxidation numbers were measured for Na-MnO₂ and Ca-MnO₂, indicating that the red-shift cannot be explained by a change in Mn valence. Thus the UV-vis spectra confirm that the red shift is caused by the presence of Ca as the interlayer cation, which may influence the ordering of interlayer water molecules (Cygan et al., 2012). The PDFs (**Figure S7**) match those reported for Mn(IV)-rich

birnessite nanoparticles with hexagonal sheet symmetry (Zhu et al., 2012). The PDFs show identical peak positions, while the amplitude of the first Mn-O (1.91 Å) and Mn-Mn (2.85 Å) distances are lower for Ca-MnO₂ than Na-MnO₂. However, there is no difference in the intermediate-range order (within 2 nm) of these two samples.

Photon flux comparison to natural environments. Our flow-through experiments were done using a photon flux of 0.77 μE/s. This photon flux can be compared to the photon flux delivered to the Earth's surface by integrating the area under the irradiance spectrum of natural sunlight. First, we converted solar irradiance from units of W m⁻² s⁻¹ to μE m⁻² s⁻¹ by normalizing the irradiance at each wavelength by the energy of the photons at that wavelength. Integration of the ASTM G173-03 reference solar irradiance spectrum between 280 nm and 900 nm yielded a photon flux equal to 3195 μE m⁻² s⁻¹. Once corrected to the surface area of the cuvette irradiated in our experiments (i.e., 0.0004 m²), we obtain a photon flux of 1.3 μE s⁻¹ with photons of wavelengths ranging from 280 – 900 nm, which include the UV-visible wavelengths of the light spectrum. However, since 42% of the irradiance spectrum of sunlight is between 400 nm and 600 nm, the photon flux delivered by the LED array to our photoreactor at 400 nm is comparable to the photon flux that would be delivered by sunlight between 400 and 600 nm.

Nature of red-shift in optical absorption spectra. Our optical transient absorption spectra show a new absorption feature upon laser excitation that we assigned to a Mn(III) excited state in the MnO₂ sheet. This feature is located at longer-wavelengths than the ground-state absorption of the initial birnessite (i.e., it is red-shifted). A similar red-shift was observed in the ground state UV-vis spectra from triclinic birnessite and c-disordered H⁺ birnessite (**Figure S5**), with triclinic birnessite showing a greater red shift relative to c-disordered H⁺ birnessite. These Mn(III)-bearing minerals contain significant proportions of Mn(III), but vary with respect to the distribution of Mn(III) within the octahedral layer and interlayer region and the extent of sheet stacking (Villalobos et al., 2003).

We expect that sheet stacking does not modify significantly the UV-vis absorption properties of birnessite. In their comparison between monolayer and multilayer MnO₂, Sakai et al. (2005) found that only the topmost layer was photosensitive and that the band gap was nearly identical between the two materials. Because the band gap can be correlated to the UV-

vis absorption, increased sheet stacking would not justify the observed red shift in our UV-vis absorption spectra.

Instead, we conclude that the red shift in the UV-vis spectra arises from the presence of Mn(III) in the octahedral layer. Based on solid-phase characterization (i.e., pyrophosphate extraction, potentiometric titration, and XRD), our triclinic birnessite contains up to 16 % Mn(III) located in the octahedral sheets, whereas *c*-disordered H⁺ birnessite contains about 19 % Mn(III) (Duckworth and Sposito, 2007). Based on the synthesis protocol for *c*-disordered H⁺ birnessite (Villalobos et al., 2003; Duckworth and Sposito, 2007) and structural characterization of the material synthesized according to this method (Villalobos et al., 2003; Manceau et al., 2013), we conclude that approximately half of the Mn(III) is situated in interlayer positions. Thus, our transient UV-vis spectra that reveal an absorption feature between 500 and 600 nm are consistent with the formation of Mn(III) located in the octahedral sheets.

Effects of aggregation on photoexcitation of birnessite. Light scattering due to particle aggregation may introduce Rayleigh scattering, which increases the observed optical extinction coefficient. If present and not accounted for, this effect could lead to an erroneous measurement of the true optical absorption coefficient, and hence an underestimation of the quantum yield. To minimize this potential source of error, we measured the UV-vis spectra of the samples prepared in water at the lowest possible concentrations (0.1 mM) at which we obtained visibly transparent suspensions with no noticeable aggregation. To investigate the consequences of aggregation, we added 10 mM of NaCl or CaCl₂ (*c.f.* **Figure S6**). At the higher concentrations used for the flow-through studies (0.5 mM) we also did not observe signs of aggregation. Only at the highest concentrations used for the transient absorption spectroscopy (3-6 mM) did we observe aggregation in all samples (with and without added electrolyte), leading us to add Nafion (see below).

Consequently, we do not believe that aggregation substantially altered our reported rate constants or quantum yield for photoreduction. However, because we do not have distinct measurements of scattering *vs* absorption, we now report the values as apparent quantum yield. If our reported absorbance at 400 nm of Ca-MnO₂ is an overestimate due to the presence of scattering, this would increase the effect of Ca *vs* Na, and would not change any of the

conclusions in the manuscript concerning the role of the counterions. We also note that while aggregation, when it occurs, can affect the apparent absorption coefficient, it does not alter peak position. We demonstrate this in **Figure S6**, which compares UV-vis spectra for our samples in water and in salt solutions sufficiently concentrated as to cause aggregation. Thus, aggregation does not affect the intrinsic strength of the absorption of 400-nm photons by either Na- or Ca-equilibrated birnessite.

Effects of aggregation on transient optical absorption kinetics. Aggregation interferes particularly strongly with the acquisition of kinetics data in time-resolved spectroscopy because it introduces non-statistical noise at each timepoint. Nafion reduced particle aggregation in time-resolved optical experiments, but the comparison of **Figures S8a, S8c** and **S9** for Na-MnO₂ shows that Nafion had a small effect on the observations. Slightly slower decays were observed for samples prepared without Nafion (**Table 1**), possibly indicating an effect of aggregation upon recombination rates. This could occur if recombination involved diffusion of soluble species, but this effect is impossible to explain confidently and is smaller than the influence of interlayer cation.

Calculation of Mn:photon ratio. We evaluated the likelihood that the LITR-XAS data were influenced by X-ray beam damage by estimating the number of X-ray photons that can interact with the sample. First, we assumed that a maximum of 5000 X-ray photons are delivered per camshaft (electron bunch) to the beamline endstation at 5 keV, with two consecutive camshafts separated by a period of 656 ns. Therefore, about 7.6×10^9 camshaft photons may interact with the sample each second. However, the camshaft photons represent only 1% of the total photons available from the storage ring (i.e., camshaft current is 5 mA and total storage ring current is 500 mA). Thus a total of 7.6×10^{11} camshaft and non-camshaft photons are delivered to the endstation per second. This total photon flux is attenuated 30 times by the X-ray chopper, a device designed to exclude non-camshaft photons, leading to a total exposure of 3.7×10^{14} photons to the sample during a 4 h experiment. Finally, a 250 mL suspension of 10 mM δ -MnO₂ contains approximately 1.5×10^{21} Mn atoms, thus the Mn to X-ray photon ratio is $1.5 \times 10^{21} : 3.7 \times 10^{14}$ or $10^6 : 1$.

A better estimate of the Mn:photon ratio can be obtained by modifying the above calculation to include more realistic estimates of photon flux and photon absorption by the

ANNEX 3

sample. First, fewer X-ray photons are actually delivered per camshaft to the beamline endstation at 5 keV: 3500 *vs* 5000 photons. Second, the photon flux drops anywhere from 10% - 90% when the monochromator is in motion because the motors move at different rates. Thus the sample exposure time is closer to 25% of the total experiment time. Third, about 50% of the photons are transmitted through the 600 μm jet. Of the photons that are absorbed by the sample, most are not absorbed by MnO_2 ($< 2\%$ for Mn and O combined). With these assumptions, a less conservative estimate of the Mn:X-ray photon ratio would be $1.5 \times 10^{21}:6.4 \times 10^{11}$ or on the order of $10^9:1$, lending strong support to our assumption that any long-term changes to the sample are not caused by X-ray exposure.

7.5. SI Figures

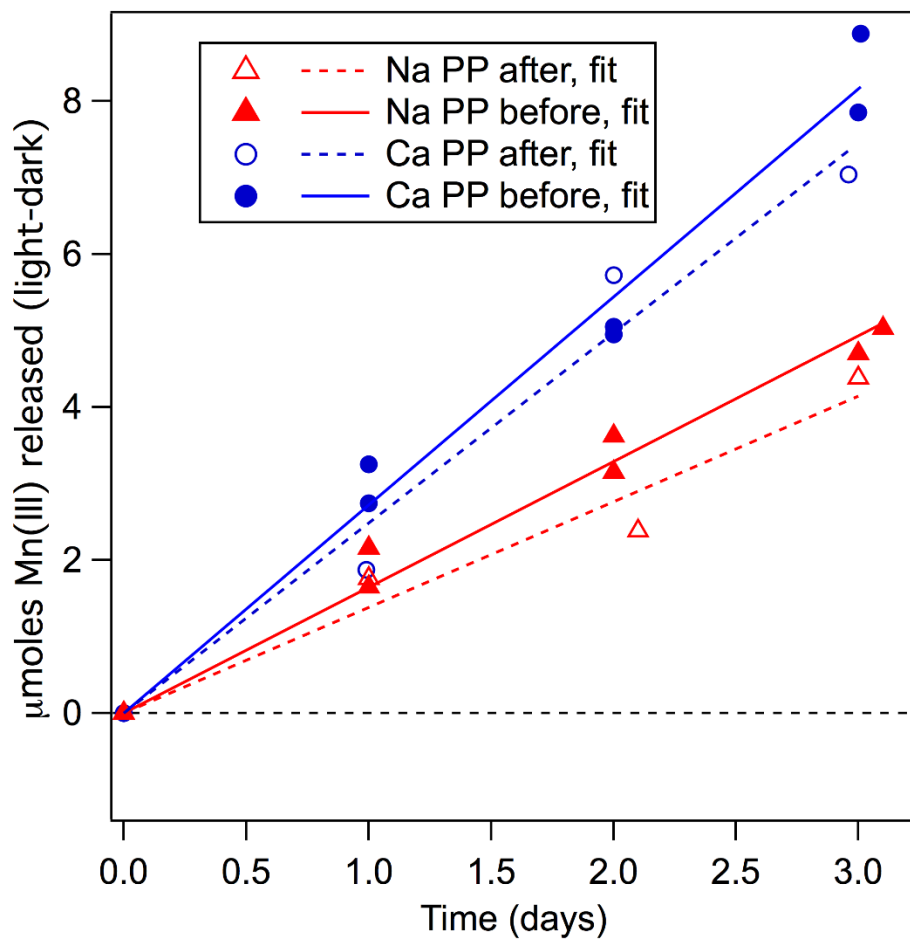


Figure S1. Time course plot showing Mn(III) generation upon 400 nm irradiation in flow through experiments at pH 6.5. Blue for Ca-MnO₂ and red for Na-MnO₂, filled symbols and solid lines for samples with sodium pyrophosphate (PP) added before irradiation, dashed lines and empty symbols for samples with PP added after irradiation. Aqueous Mn determined by ICP-OES is within 10% of Mn(III)-PP determined colorimetrically. No Mn was released to solution in experiments without PP.

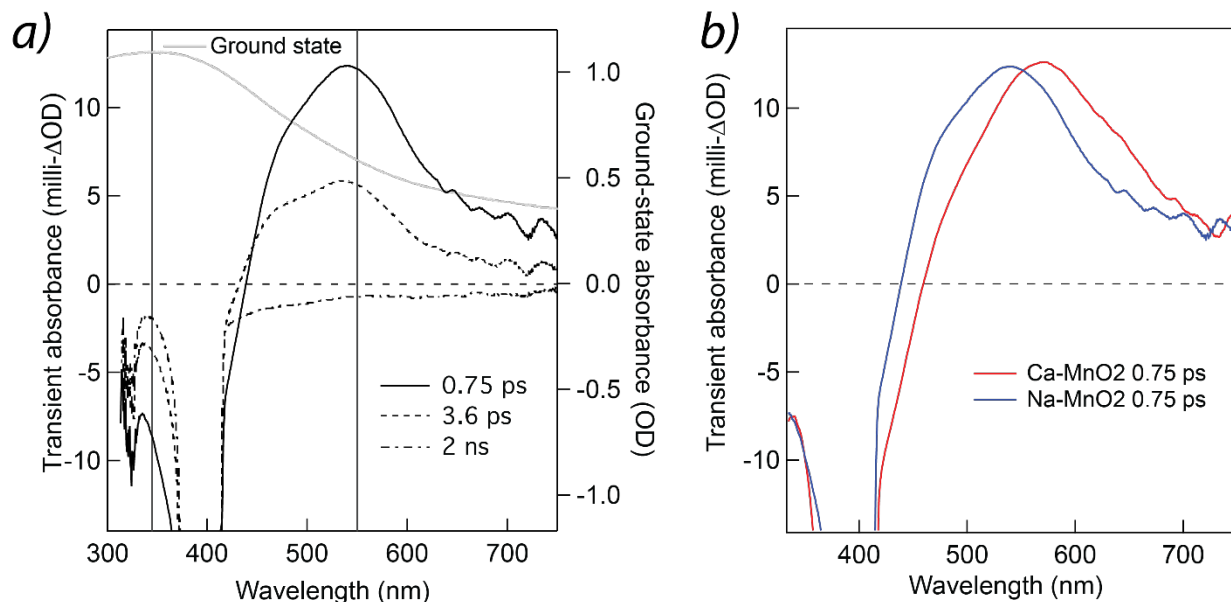


Figure S2. (a) Transient optical absorption spectra acquired on Na-MnO₂ in aqueous suspension with Nafion. Transient absorption difference spectra at 0.75 ps, 3.6 ps and 2 ns (ΔOD units; left axis) compared with the ground-state UV-vis absorption (OD units; right axis). The maximum intensity of the excited state absorption (ESA) is 550 nm. The data from 390 – 410 nm are affected by scattering of the pump beam; (b) Comparison between the transient absorption spectrum of Ca-MnO₂ and Na-MnO₂ in Nafion 0.75 ps after laser excitation show that the Ca-MnO₂ sample is red-shifted relative to the Na-MnO₂ sample (*cf.* Fig. S6a).

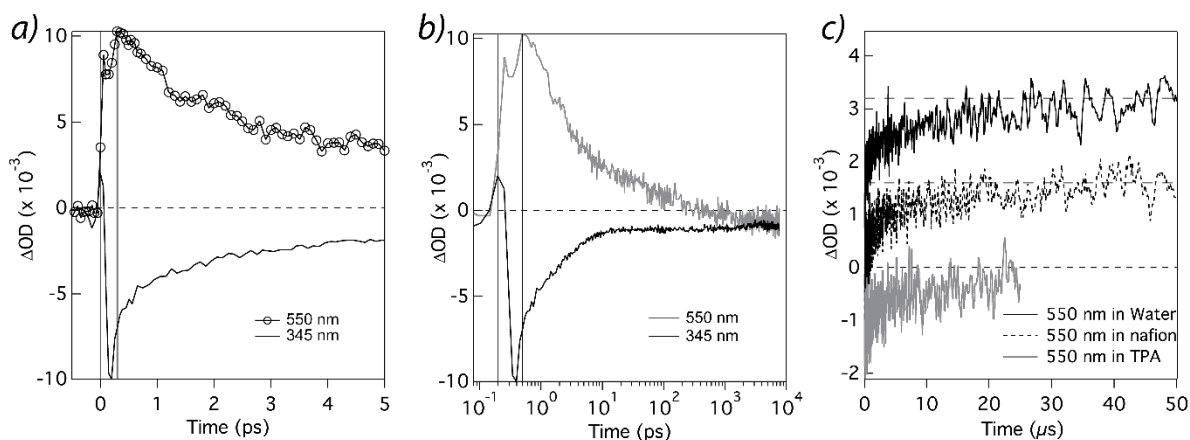


Figure S3. Summary of transient optical absorption kinetics acquired on Na-MnO₂ in aqueous suspension with Nafion. (a) Transient kinetic traces show that the onset of the ESA at 550 nm is slightly delayed relative to the bleach at 345 nm. (b) Decay kinetics of the ESA and bleach up to 8 ns. The time-zero was shifted by 0.2 ps to enable plotting on a logarithmic axis. (c) The decay of the bleach at 550 nm was recorded for up to 50 μs .

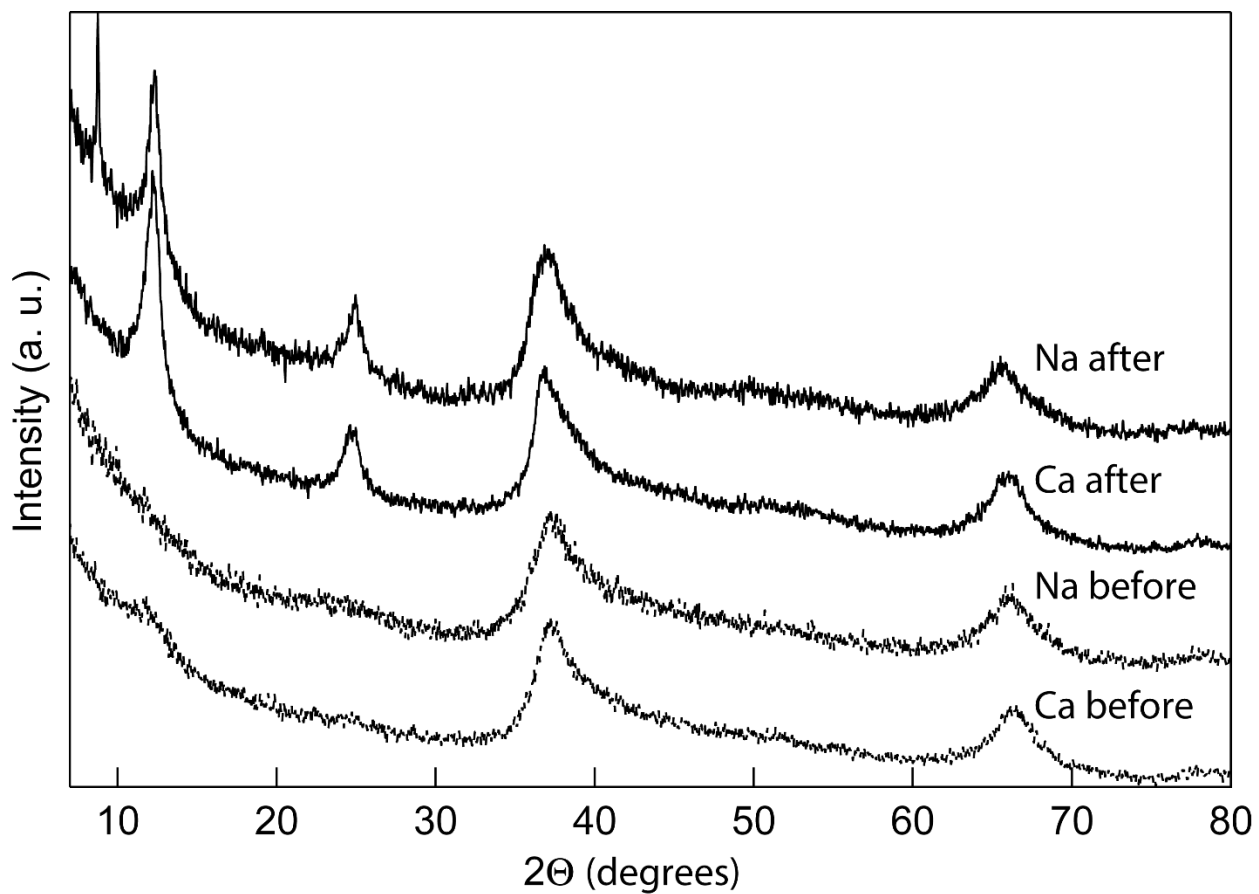


Figure S4. Powder X-ray diffraction patterns for selected samples before and after the light-initiated time-resolved XAS experiment. Samples after the LITR-XAS experiment show reflections of the 001 and 002 planes (reflection at $\sim 14^\circ$ and $\sim 25^\circ$ 2θ , respectively) due to increased stacking of MnO_2 sheets along the crystallographic c -axis.

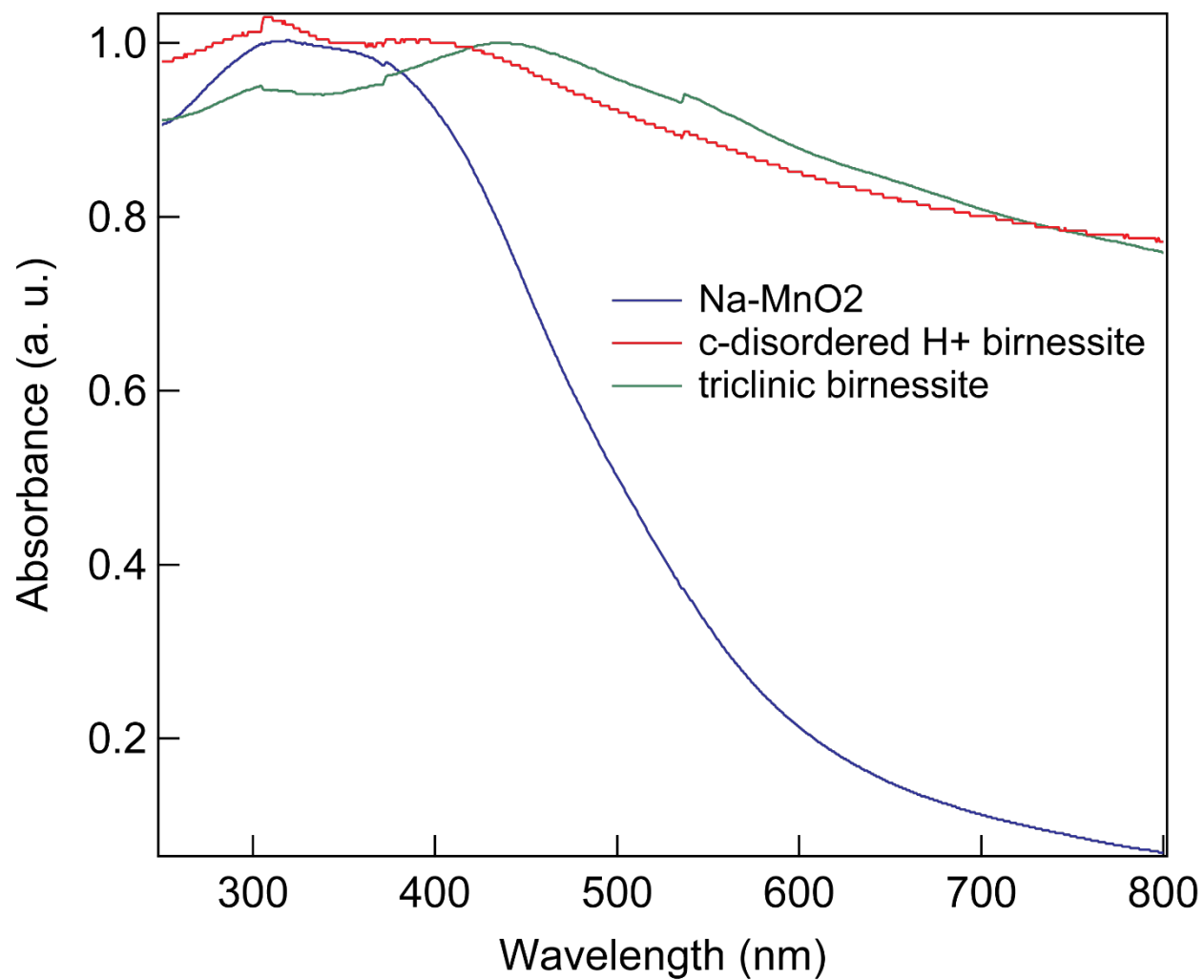


Figure S5. UV-vis absorption spectrum of Na-MnO₂, triclinic birnessite (ca. 16% Mn(III) in the octahedral sheet), and *c*-disordered H⁺ birnessite (ca. 19% Mn(III) distributed between the layer and interlayer positions in similar proportions).

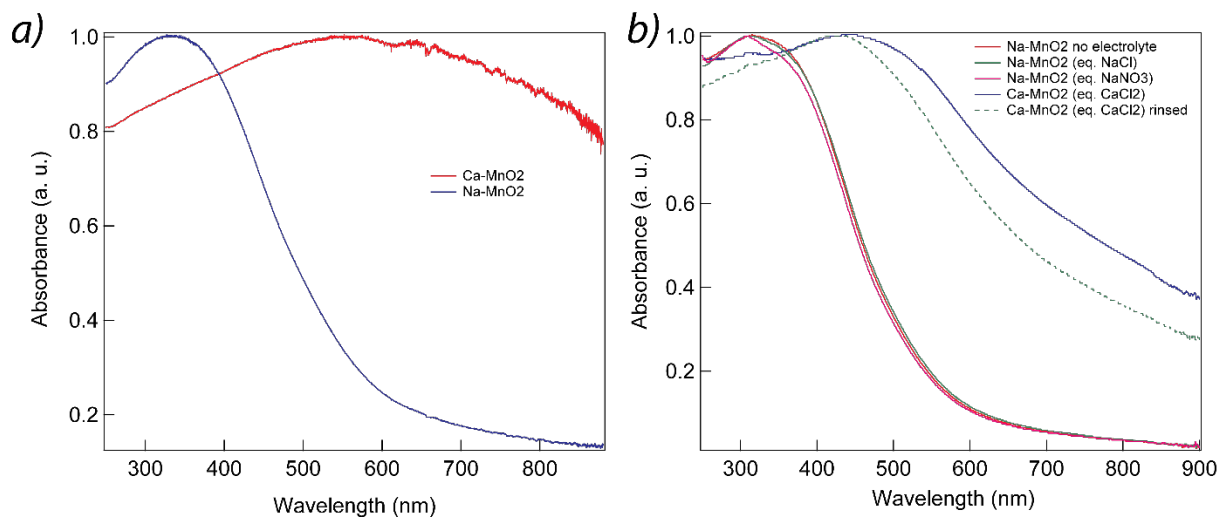


Figure S6: (a) UV-vis absorption spectra of Na-MnO₂ in water without background electrolyte (blue line) and Ca-MnO₂ with 10 mM background electrolyte (Cl⁻ -red line); (b) UV-vis absorption spectra of Na-MnO₂ with and without 10 mM NaCl and NaNO₃ as background electrolytes compared to Ca-MnO₂ with and without 10 mM CaCl₂ as the background electrolyte.

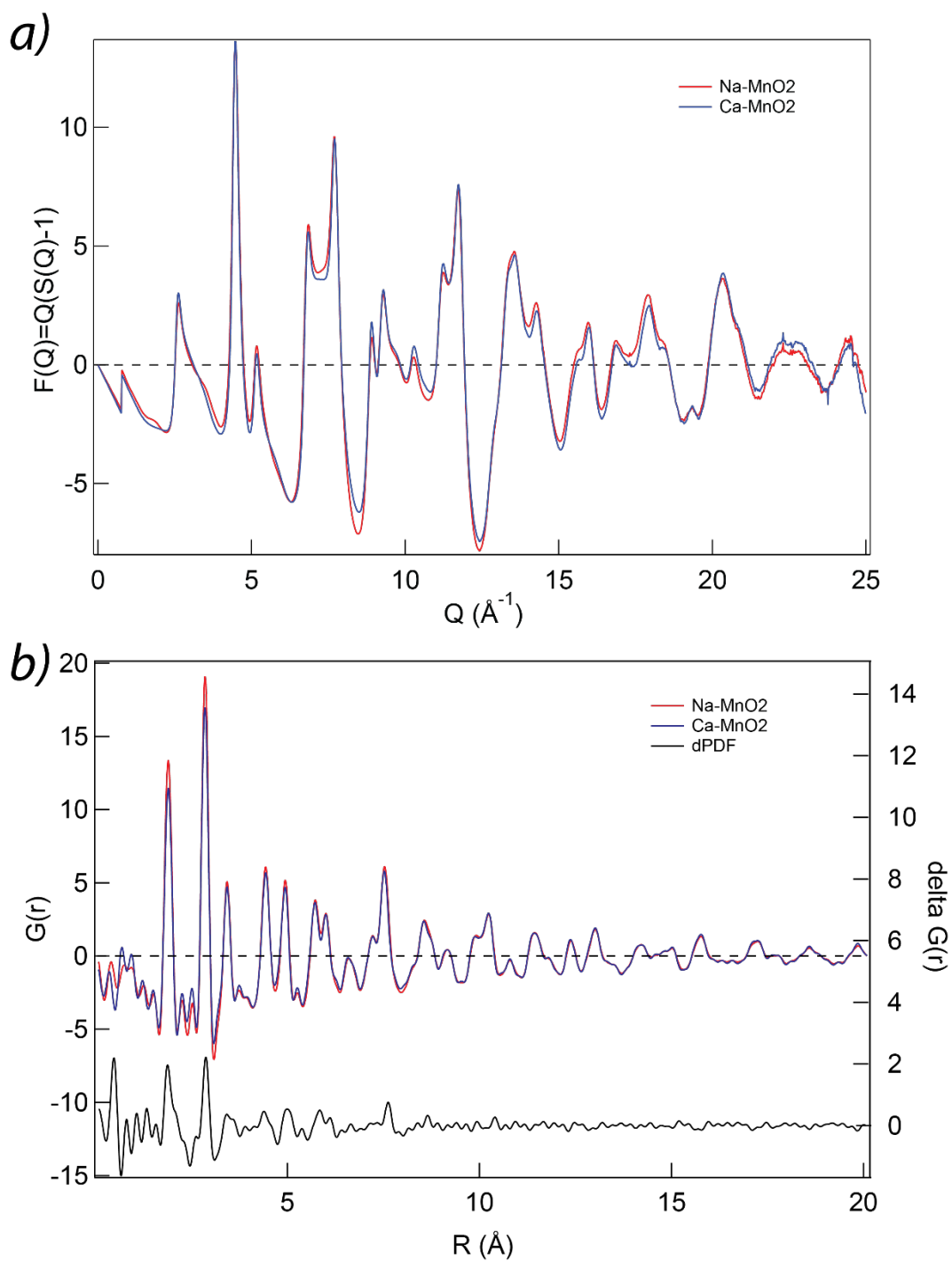


Figure S7. (a) reduced structure function, $F(Q) = Q[S(Q)-1]$, for Ca-MnO₂ and Na-MnO₂, respectively. (b) PDF data, obtained by Fourier transformation of the $F(Q)$, for Na-MnO₂ (blue line) and Ca-MnO₂ (red line), as well as difference PDF between the samples.

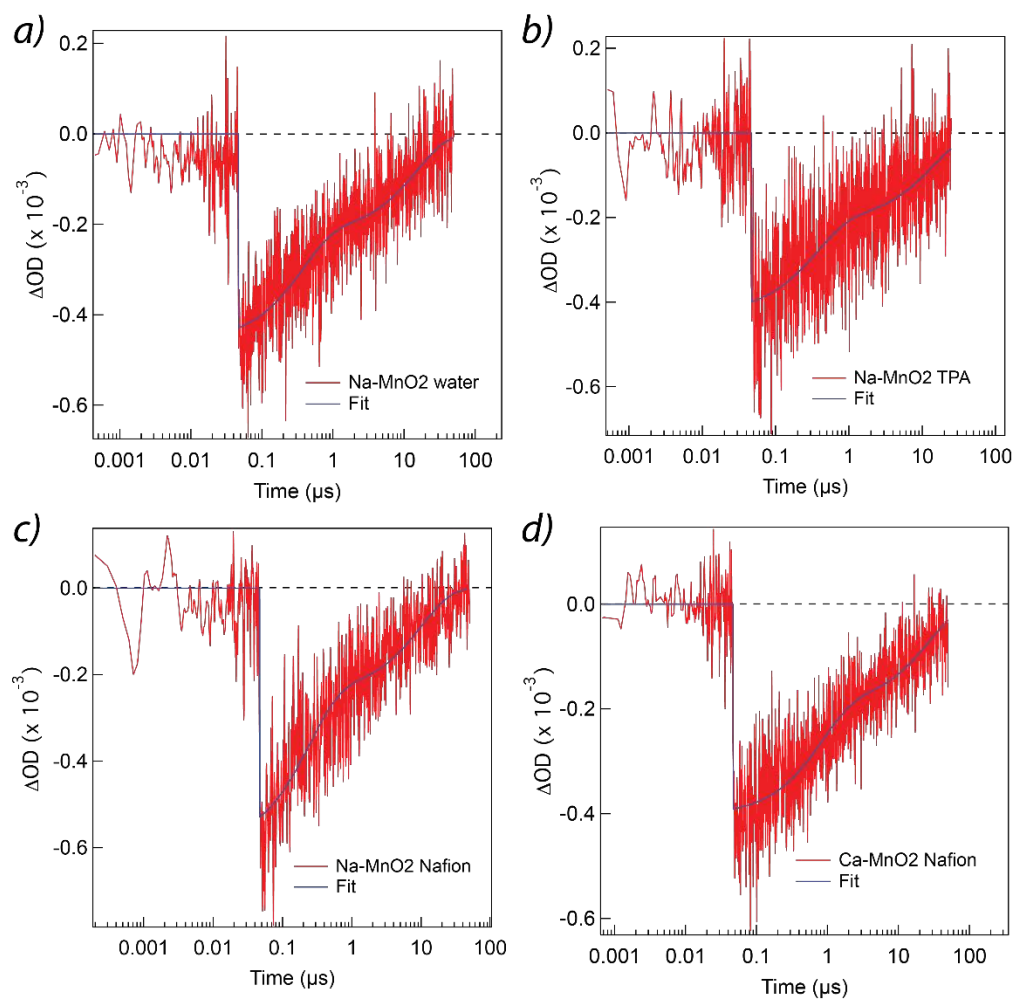


Figure S8. Comparison of the transient optical absorption kinetic data on the microsecond timescale extracted at 580 nm for Na-MnO₂ and Ca-MnO₂ in different aqueous solutions, overlain with the fits using 2 time constants (cf. **Table 1**): (a) Na-MnO₂ resuspended in water; (b) Na-MnO₂ resuspended in an 0.1 M terephthalic acid solution to trap any hydroxyl radical species formed during photoreduction; (c) Na-MnO₂ resuspended in an aqueous solution with Nafion to reduce particle aggregation; (d) Ca-MnO₂ resuspended in an aqueous solution with Nafion to reduce particle aggregation.

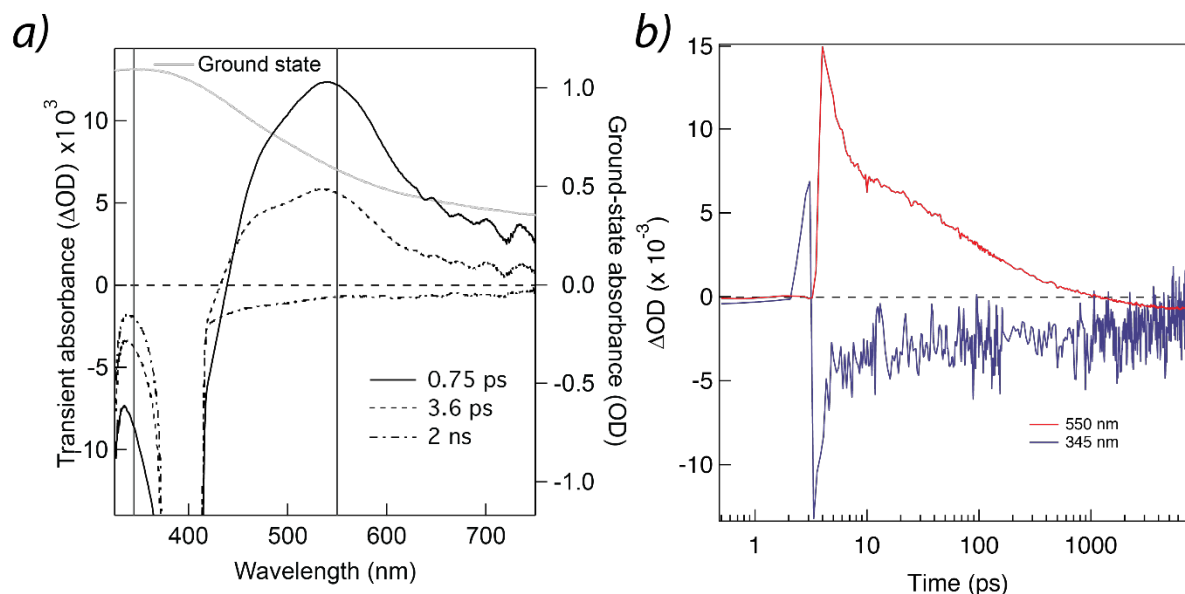


Figure S9. (a) Transient absorption spectra at different delay times for Na-MnO₂ in water; (b) transient absorption kinetic traces for Na-MnO₂ on pico- to nanosecond timescales extracted at 345 nm (blue) and 550 nm (red). The transient spectra and decay kinetics do not show differences on the pico- to nanosecond timescale with respect to Na-MnO₂ resuspended in Nafion.

7.6. References

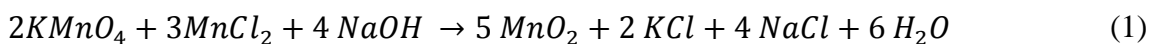
- Cygan, R.T., Post, J.E., Heaney, P.J., Kubicki, J.D., **2012**. Molecular models of birnessite and related hydrated layered minerals. *Am Mineral* 97, 1505-1514.
- Duckworth, O.W., Sposito, G., **2007**. Siderophore-promoted dissolution of synthetic and biogenic layer-type Mn oxides. *Chem Geol* 242, 497-508.
- Grangeon, S., Lanson, B., Lanson, M., Manceau, A., **2008**. Crystal structure of Ni-sorbed synthetic vernadite: a powder X-ray diffraction study. *Mineral Mag* 72, 1279-1291.
- Klewicki, J.K., Morgan, J.J., **1998**. Kinetic behavior of Mn(III) complexes of pyrophosphate, EDTA, and citrate. *Environ Sci Technol* 32, 2916-2922.
- Kostka, J.E., Luther, G.W., Nealson, K.H., **1995**. Chemical and Biological Reduction of Mn(III)-Pyrophosphate Complexes - Potential Importance of Dissolved Mn(II) as an Environmental Oxidant. *Geochim Cosmochim Acta* 59, 885-894.
- Manceau, A., Marcus, M.A., Grangeon, S., Lanson, M., Lanson, B., Gaillot, A.C., Skanthakumar, S., Soderholm, L., **2013**. Short-range and long-range order of phyllo-manganate nanoparticles determined using high-energy X-ray scattering. *J Appl Crystallogr* 46, 193-209.
- Qiu, X., Thompson, J.W., Billinge, S.J.L., **2004**. PDFgetX2: a GUI-driven program to obtain the pair distribution function from X-ray powder diffraction data. *J Appl Crystallogr* 37, 678-678.
- Sakai, N., Ebina, Y., Takada, K., Sasaki, T., **2005**. Photocurrent generation from semiconducting manganese oxide nanosheets in response to visible light. *J Phys Chem B* 109, 9651-9655.

- Villalobos, M., Toner, B., Bargar, J., Sposito, G., **2003**. Characterization of the manganese oxide produced by *Pseudomonas putida* strain MnB1. *Geochim Cosmochim Acta* 67, 2649-2662.
- Webb, S.M., Dick, G.J., Bargar, J.R., Tebo, B.M., **2005**. Evidence for the presence of Mn(III) intermediates in the bacterial oxidation of Mn(II). *Proc Natl Acad Sci U S A* 102, 5558-5563.
- Zhu, M.Q., Farrow, C.L., Post, J.E., Livi, K.J.T., Billinge, S.J.L., Ginder-Vogel, M., Sparks, D.L., **2012**. Structural study of biotic and abiotic poorly-crystalline manganese oxides using atomic pair distribution function analysis. *Geochim Cosmochim Acta* 81, 39-55.

ANNEX 4. Supporting information to Chapter 5

7.7. SI Text

Mineral Synthesis. Delta-MnO₂ minerals were synthesized in a previous study (**Chapter 3**). In particular, the mineral that was used for these studies was mineral B2 described in (**Chapter 3**). The synthesis of this mineral involves the reduction of Mn(VII) by Mn(II) in excess base according to the following reaction:



where NaOH is used to neutralize the acid formed during the reaction and to enhance the kinetics of Mn(II) oxidation.

The minerals obtained through this synthesis protocol were characterized with respect to specific surface area, Average Mn oxidation number (AMON), Mn(III) content, Na:Mn ratio as described in Chapter 3. The specific surface area, as calculated by Brunauer Emmet Teller (BET) theory on a standard 5-point N₂ sorption isotherm, was $163 \pm 8 \text{ m}^2/\text{g}$; the average Mn oxidation number, determined by potentiometric titration (initially described in (Gaillot et al., 2003)) was 4.03 ± 0.01 ; the Mn(III) content was 2.07 ± 0.52 and the Na:Mn ratio was 0.3.

Geometric constraints on the migration of Mn(III) out of the octahedral layer. To help evaluate which octahedral site is the most favorable for the transient Mn(III) to stabilize into, we rationalized the possible sites present in a δ -MnO₂ model and evaluated what structural requirements would be needed for Mn octahedrons in each singular site to accommodate an interlayer Mn(III). In the following hypotheses, we attempted to consider the effect of the Jahn teller distortion in Mn(III), which elongates the Mn-O bonds in the axial direction (z) and shrinks the Mn-O bonds on the equatorial plane (x - y) to accommodate the orbital degeneracy (Burns, 1993). We only considered sites that had oxygen atoms which were undersaturated, which are those that are likely to bind water molecules or protons. We excluded sites around an octahedral vacancy, since it is unlikely that Mn(III) will move out of the plane close to a vacancy, because this would be equivalent to forming two adjacent octahedral vacancies. With these conditions, there are 3 sites that were considered, all on the edges of the mineral (**Figure S4**):

- Site A, where the Mn octahedron is bound to the remaining sheet only through one edge, sharing one axial oxygen and one equatorial oxygen with the adjacent octahedron.

- Site B1 is an isolated corner site, which is bound to the remaining mineral in a double edge sharing configuration, sharing two equatorial and one axial oxygen atoms with the adjacent octahedrons.
- Site B2 is an edge site that is bound to the remaining mineral by sharing two edges and one corner (3 equatorial oxygens and one axial oxygen) with the remaining mineral.
- Site C is an edge site that has most of its coordinated oxygen atoms shared with adjacent octahedrons. Only one oxygen atom, an equatorial oxygen, is not shared with another octahedron and is the most undersaturated.

We then assumed that the stabilization of Mn(III) in the interlayer does not involve a complete detachment of the latter, but a rotation of the octahedron around one oxygen atom and detachment from the remaining oxygen atoms. The oxygen that is the most likely to remain bound to the mineral is the one that is the furthest away from the protons and the surface/edge of the mineral, being that it's charge is the least undersaturated by coordinating to the adjacent octahedrons. Below, we will describe how the 3 sites can possibly stabilize in the interlayer with a rotation around this oxygen out of the plane (rotation around an axis parallel to the mineral edge along the *ab* plane – **Figure S4**):

- Site A: The octahedron on site A may move out of the plane through the detachment of the equatorial oxygen, rotation around the axial oxygen, then binding through the equatorial oxygen. In this case, since the number of dangling oxygens does not change, the change in shape of the octahedron from the JT distortion would require a distortion of the adjacent octahedra to bind either along an edge or in a double corner sharing complex.
- Site B1: This Mn octahedron is bound by 3 oxygen atoms to the sheet. The octahedron remains bound through the axial oxygen, whereas the equatorial oxygens detach (they are singly undersaturated, so could be bound to protons or Na⁺). One of these oxygens then binds to the adjacent Mn octahedron, once the Mn(III) octahedron rotates around an axis parallel to the crystallographic *c* plane. The resulting octahedron now shares two edges with the remaining lattice, and has one less oxygen bound with respect to the previous configuration. It is likely that this vertex of the octahedron is now coordinated by a water molecule (either on the remaining surface or on the migrated octahedron). The dangling oxygen may become protonated from the proton that is released upon the hypothesized

formation of OH^\bullet from H_2O . Furthermore, the protonation of the oxygen atom may permit a reduction in rigidity, accommodating the Jahn-teller distortion of the Mn(III) octahedron. The out-of-plane Mn(III) octahedron results bound to the remaining surface in a double corner sharing configuration.

- Site B2: The Mn octahedron on this site is bound to the bulk by 4 oxygen atoms. Because of the JT distortion, it is likely that two oxygen atoms detach as a result of the steric strain as well as the reduction of Mn-O bond strength from protonation and reduction in ionic potential of Mn(III). The out-of-plane rotation is a combination of an *ab* rotation as in site A and an additional rotation around the *c* direction as for site B1. The resulting configuration has two dangling oxygens/coordinated water molecules, and is bound to the structure by a double corner sharing configuration. One of the remaining dangling oxygen atoms may protonate with the H^+ atom deriving from the OH^\bullet generation.
- Site C: The octahedron on this site is bound to the remaining bulk by sharing 5 oxygen atoms. An out-of-plane re-orientation of this octahedron would require the breaking of 4 Mn-O bonds and a rotation around the remaining axial oxygen atom. It would then bind in a double corner sharing configuration on either of the two adjacent octahedrons through the equatorial oxygen sites.

Among the different options described above, the one with least bonds breaking will likely be the most favourable. Furthermore, from the rate expressions described in the main text the photoreduction of Mn upon partial water oxydation to form a hydroxyl radical involves the release of a proton. Therefore, the B1 or B2 sites are favoured with respect to the other sites, since they involve the least amount of bonds broken and require an additional proton to balance the negative charge arising from the lowered saturation of the oxygen atom that remains unbound. Additionally, the B1 and B2 sites are also the most abundant on the surface, even more so with smaller particles, compared to the other sites.

7.8. SI Figures and tables

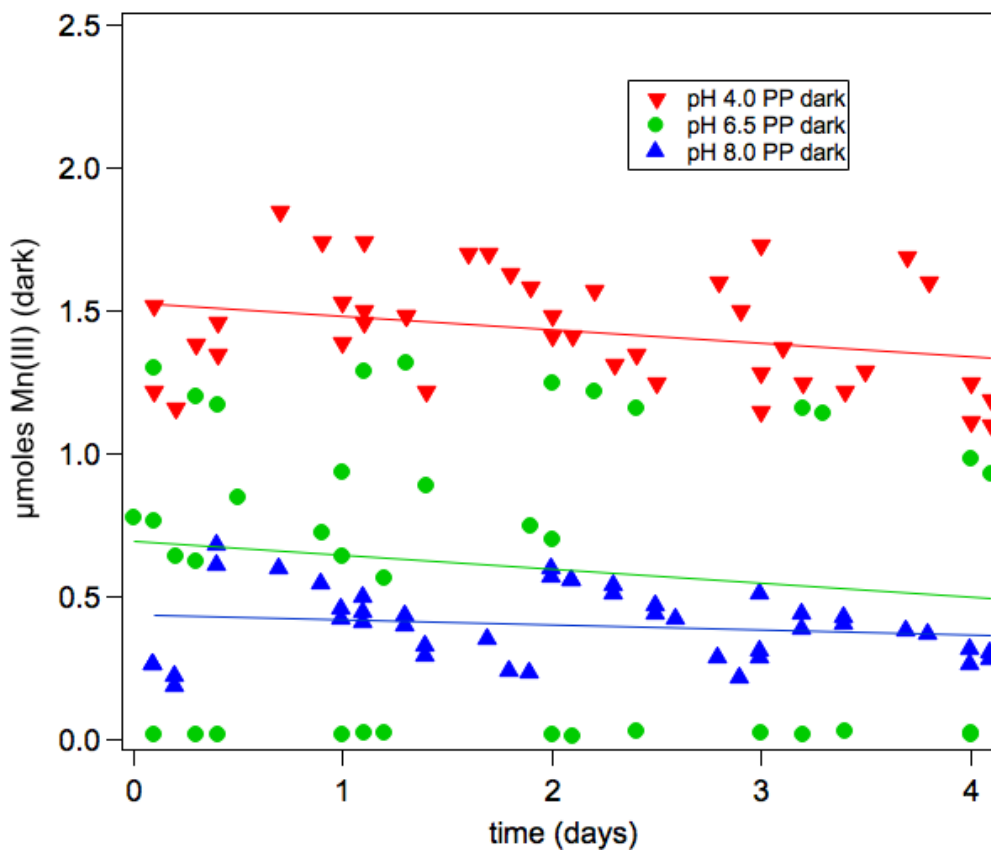


Figure S1: Release of Mn(III) in the dark as a function of pH. Lines are linear interpolations with free intercept.

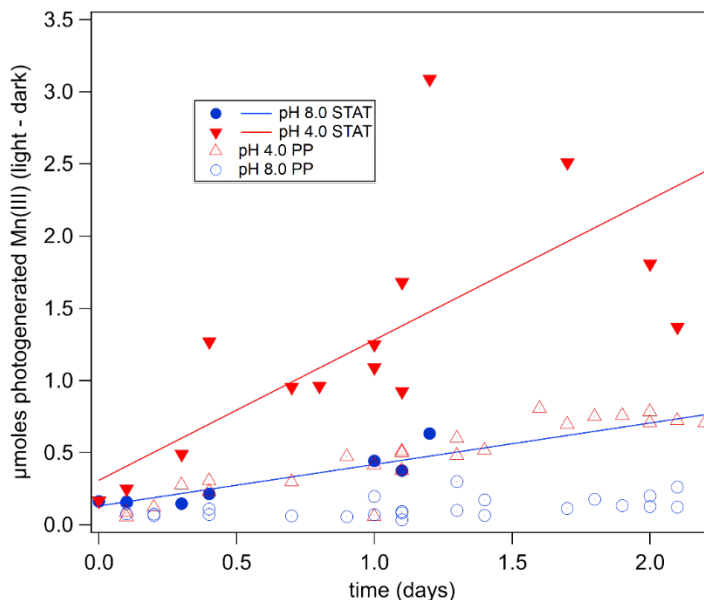


Figure S2. Comparison between the photoreduction rates on δ -MnO₂ suspensions with PP added before irradiation (empty symbols) and PP added after irradiation (full symbols) at pH 4.0 and pH 8.0. The pH was kept constant with a pH stat automatic titrator during irradiation. Fits are only shown for the pH STAT experiments, and were carried out only up to 2.2 days of irradiation, because of aggregation issues at longer timescales.

Table S1: experimental conditions for the flow-through photoreactor experiments

Reactor	Mn total [μ M]	pH/conditions	Duration	Date
3	221	4.0 STAT	4 days	May 16
3	223	4.0 STAT	2 days	May 16
2	218	8.0 STAT	4 days	May 16
1	255	6.5 PP	2 days	May 16
3	243	6.5 PP	2 days	May 16
1	239	6.5 PP	4 days	May 16
1	249	6.5 PP	4 days	May 16
3	252	4.0 PP	4 days	June 16
2	245	4.0 PP	4 days	June 16
1	249	4.0 PP	4 days	June 16
1	249	8.0 PP	4 days	June 16
2	252	8.0 PP	4 days	June 16
2	254	8.0 PP	4 days	June 16

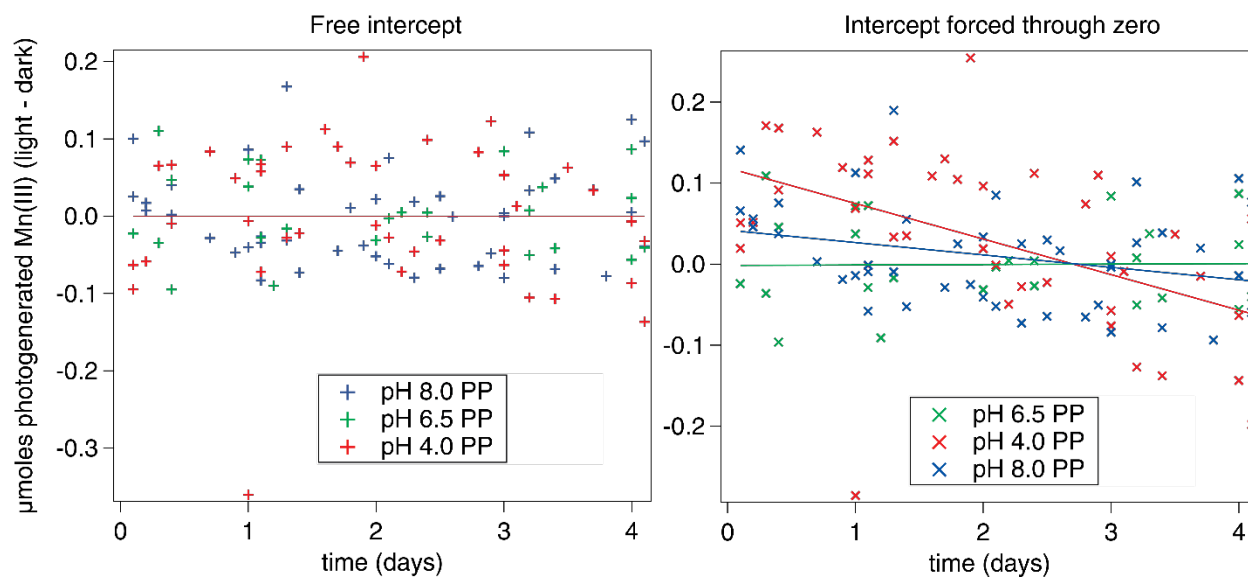


Figure S3: left – residuals of the linear interpolation without forcing through the origin, interpolations are superposed on the zero line; right – residuals of the linear interpolation forcing it through the origin. The homoscedasticity in the first plot is evident, whereas the second plot shows a trend, especially in the pH 4.0 data.

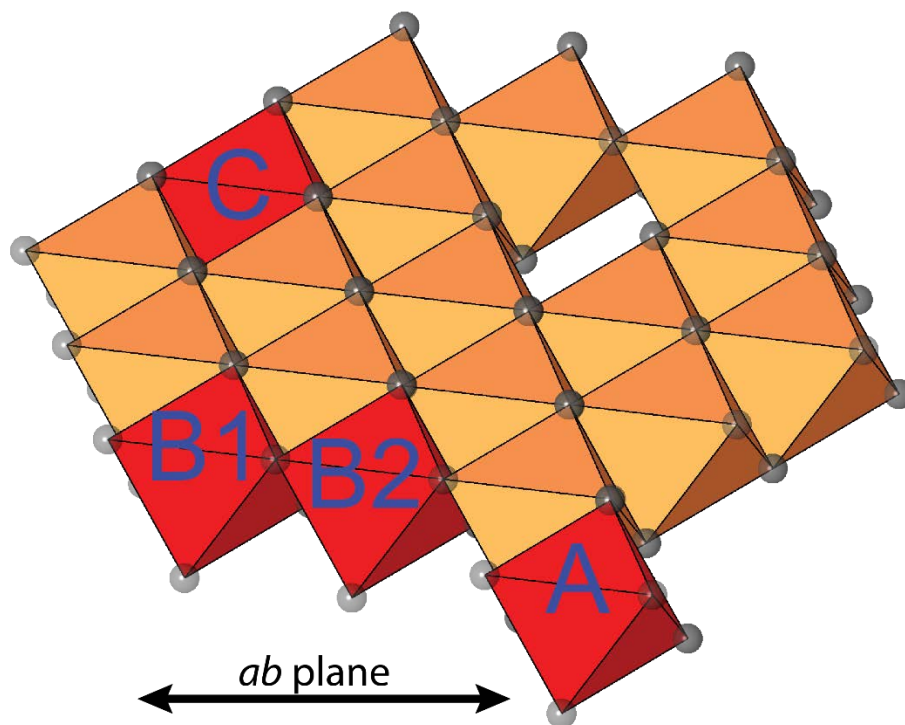


Figure S4: Visual representation of the edge sites that were chosen for the Mn(III) sites described in the SI text. The chosen cluster for the representation is much smaller than the actual mineral crystallite, for simplicity.

7.9. References

- Burns, R.G., **1993**. Mineralogical applications of crystal field theory, Second ed. *Cambridge University Press*, Cambridge.
- Gaillot, A.C., Flot, D., Drits, V.A., Manceau, A., Burghammer, M., Lanson, B., **2003**. Structure of Synthetic K-rich Birnessite Obtained by High-Temperature Decomposition of KMnO_4 . I. Two-Layer Polytype from 800 °C Experiment. *Chem Mater* 15, 4666-4678.

ANNEX 5. Supporting Information to Chapter 6

SI Text

Interaction between Ni and PP The photoreduction experiments carried out in the current work were different from our previous work in that the addition of sodium pyrophosphate (PP) was done after irradiation, to avoid interactions between PP and the adsorption of Ni on the mineral. Although the presence or absence of PP during Ni sorption did not lead to major differences in the surface loading of Ni in the dark (**Figure S1a**), the presence of PP during the irradiation experiment would have complexed any Mn(III) formed, preventing us to evaluate the effect of Mn(III) on the surface speciation of Ni. Additionally, the complexation between Ni and PP, which was observed measuring the UV-Vis spectrum of a filtered suspension of δ -MnO₂ with 5% Ni in excess PP, led to a broad shoulder between 300 nm and 500 nm, absent in a similar suspension without Ni (**Figure S1b**). The presence of this shoulder may have introduced artifacts during the irradiation of the suspension under 400 nm irradiation, therefore warranting experiments without PP during irradiation.

SI Figures

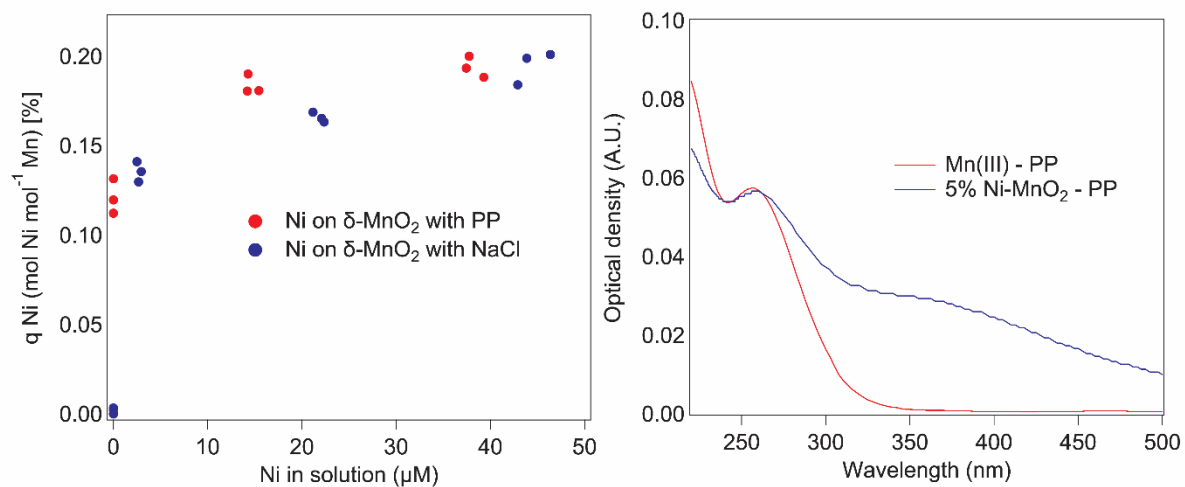


Figure S1 : A) q value for Ni sorbed on δ -MnO₂ in the presence of PP (red circles) compared to in the presence of NaCl (Blue circles) ; B) UV-Vis spectra of Mn(III)-PP (red line) and Mn(III)-PP with 5% Ni. It can be seen that with 5% Ni there is a broad absorption peak at 400 nm.

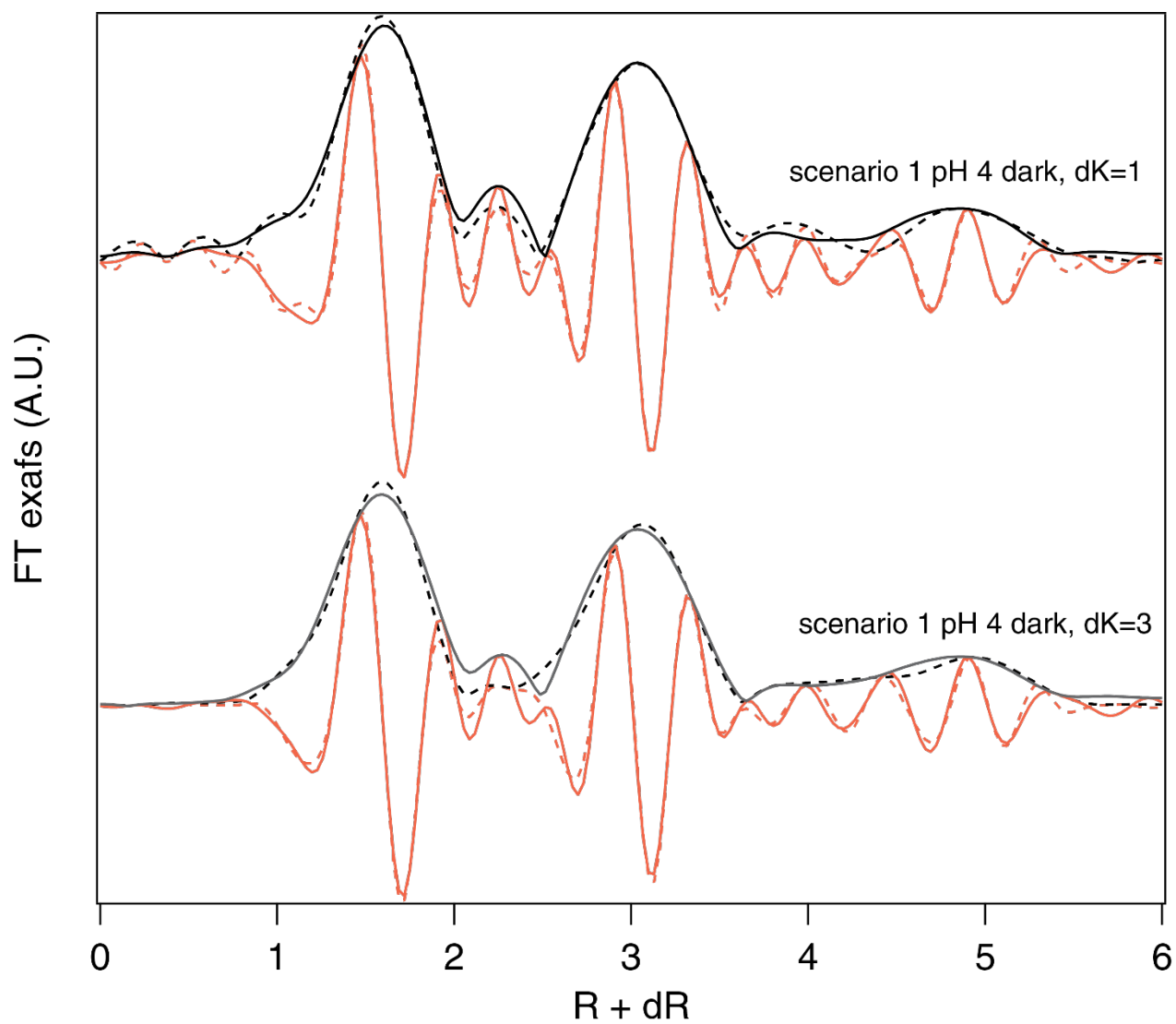


Figure S2 : Comparison between the fit of the pH 4 dark data under scenario 1 with a dK value of 1 (above) vs a dK value of 3 (below). As can be seen, the data is mismatched by the fit especially for the shoulder between an R value of 2 and 3 when a dK value of 3 is used.

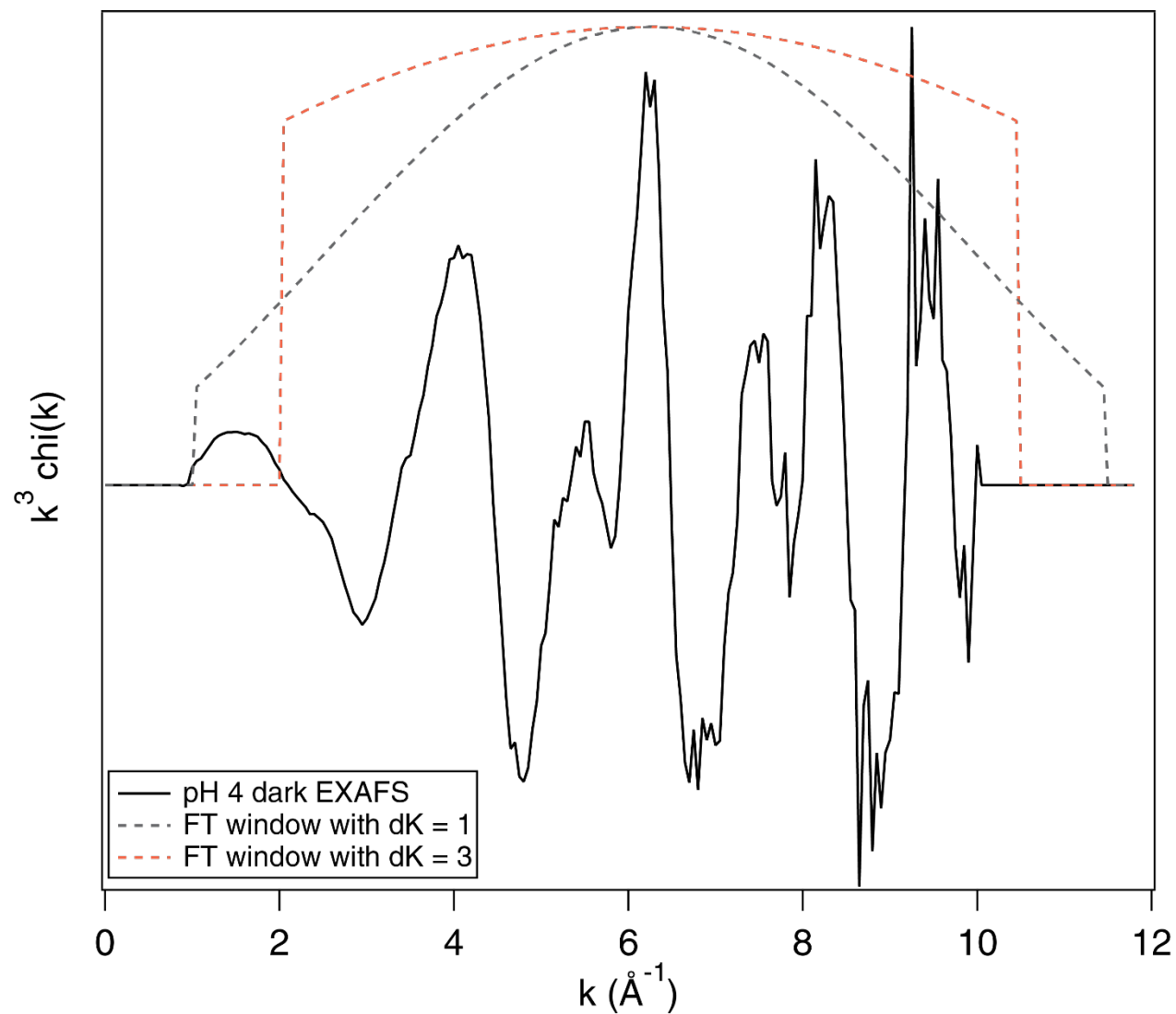


Figure S3: Comparison between the chi data for the pH 4 dark sample with an overlay of the FT transformation window with a dK of 1 (black dashed lines) and a dK of 3 (red dashed lines), respectively.

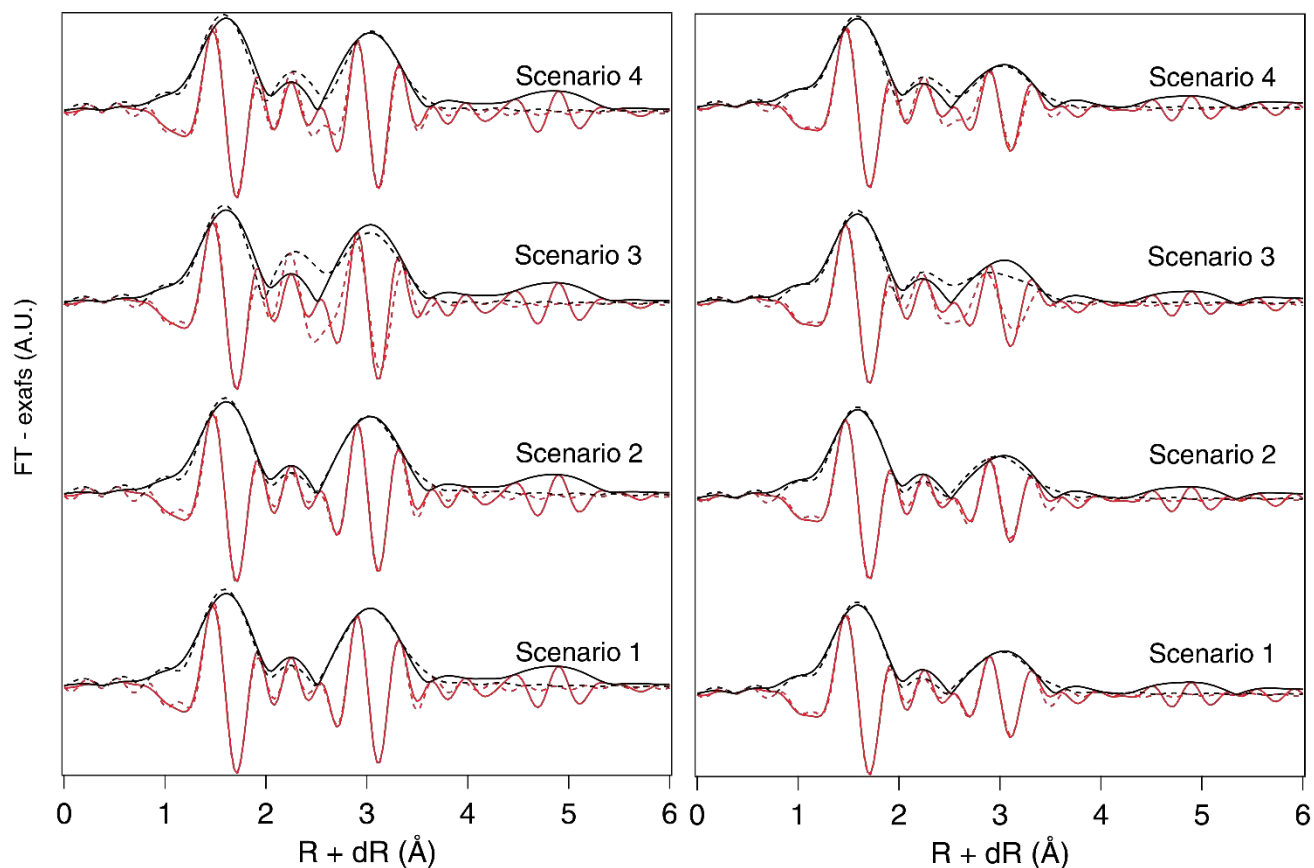


Figure S4. *a - left*) Plots of the different fit scenarios for the Ni-laden δ -MnO₂ pH 4 dark data; *b - right*) Plots of the different fit scenarios for the Ni-laden δ -MnO₂ pH 4 light data. The summary of the fit parameters are reported in **Tables S1** and **S2** for the Ni-laden δ -MnO₂ pH 4 dark and light data, respectively.

Table S1: Fit scenarios for the Ni-laden δ -MnO₂ pH 4 dark sample with the simplified 2-shell model (R range 1-4.1 Å) shown in **Figure S3**. A dK value of 0.96 was applied based on the work published by Pena et al. (2010). The amplitude (A) for the different shells is defined by the product of the CN and a scaling parameter (f), where f refers to the fraction of Ni in TCS complexes above vacancies and ($1-f$) refers to the fraction of Ni as incorporated in the nanosheet or in a double edge sharing complex at the particle edges.

Ni-laden δ -MnO ₂ pH 4 dark	Scenario 1	Scenario 2	Scenario 3	Scenario 4
Ni-O₁				
CN	6.05 ± 0.88	5.97 ± 0.80	6.10 ± 2.88	6.16 ± 1.44
R (Å)	2.05 ± 0.01	2.06 ± 0.01	2.05 ± 0.02	2.05 ± 0.01
σ^2 (Å ²)	0.003 ± 0.001	0.003 ± 0.001	0.003 ± 0.004	0.003 ± 0.002
Ni-O₂			Ni-Mn_{ES}	
A	6	3	6	2
R (Å)	3.54	3.45	2.86	2.86
σ^2 (Å ²)	0.05 ± 0.09	σ^2 Ni-O1	σ^2 Ni-Mn TCS	σ^2 Ni-Mn TCS
Ni-Mn_{TCS1}				
A	8.00 ± 1.79	6.62 ± 1.60	22.46 ± 11.50	11.93 ± 3.16
R (Å)	3.49 ± 0.01	3.49 ± 0.01	3.50 ± 0.03	3.48 ± 0.01
σ^2 (Å ²)	0.005 ± 0.002	0.005 ± 0.002	0.015 ± 0.005	0.008 ± 0.002
E0 (eV)	-1.44 ± 1.31	-0.98 ± 1.11	-1.81 ± 2.53	-2.25 ± 1.60
Red Chi2	4.37	3.74	44.86	11.31
R-factor	0.02	0.02	0.18	0.04
N vars/IDP	8/14	7/14	7/14	7/14

ANNEX 5

Table S2: Fit scenarios for the Ni-laden δ -MnO₂ pH 4 light sample with the simplified 2-shell model (R range 1-4.1 Å), shown in **Figure S3**. A dK value of 0.96 was applied based on the work published by Pena et al. (2010). The amplitude (A) for the different shells is defined by the product of the CN and a scaling parameter (*f*), where *f* refers to the fraction of Ni in TCS complexes above vacancies and (*1-f*) refers to the fraction of Ni as incorporated in the nanosheet or in a double edge sharing complex at the particle edges.

Ni-laden δ -MnO ₂ pH 4 light	Scenario 1	Scenario 2	Scenario 3	Scenario 4
Ni-O₁				
CN	6.15 ± 0.87	6.11 ± 0.83	5.95 ± 2.07	6.17 ± 1.23
R (Å)	2.05 ± 0.01	2.05 ± 0.01	2.05 ± 0.02	2.05 ± 0.01
σ^2 (Å ²)	0.004 ± 0.001	0.004 ± 0.001	0.004 ± 0.003	0.004 ± 0.002
Ni-O₂			Ni-Mn_{ES}	
A	6	3	6	2
R (Å)	3.54	3.45	2.86	2.86
σ^2 (Å ²)	0.08 ± 0.18	$\sigma^2_{\text{Ni-O1}}$	$\sigma^2_{\text{Ni-Mn TCS}}$	$\sigma^2_{\text{Ni-Mn TCS}}$
Ni-Mn_{TCS1}				
A	4.59 ± 1.69	3.22 ± 1.52	20.20 ± 19.34	8.31 ± 2.94
R (Å)	3.48 ± 0.01	3.48 ± 0.02	3.51 ± 0.05	3.48 ± 0.02
σ^2 (Å ²)	0.006 ± 0.003	0.005 ± 0.004	0.03 ± 0.01	0.01 ± 0.003
E0 (eV)	-1.82 ± 1.40	-1.44 ± 1.33	-2.04 ± 2.69	-2.26 ± 1.60
Red Chi2	10.46	9.78	61.61	21.03
R-factor	0.02	0.02	0.13	0.05
N vars/IDP	8/14	7/14	7/14	7/14

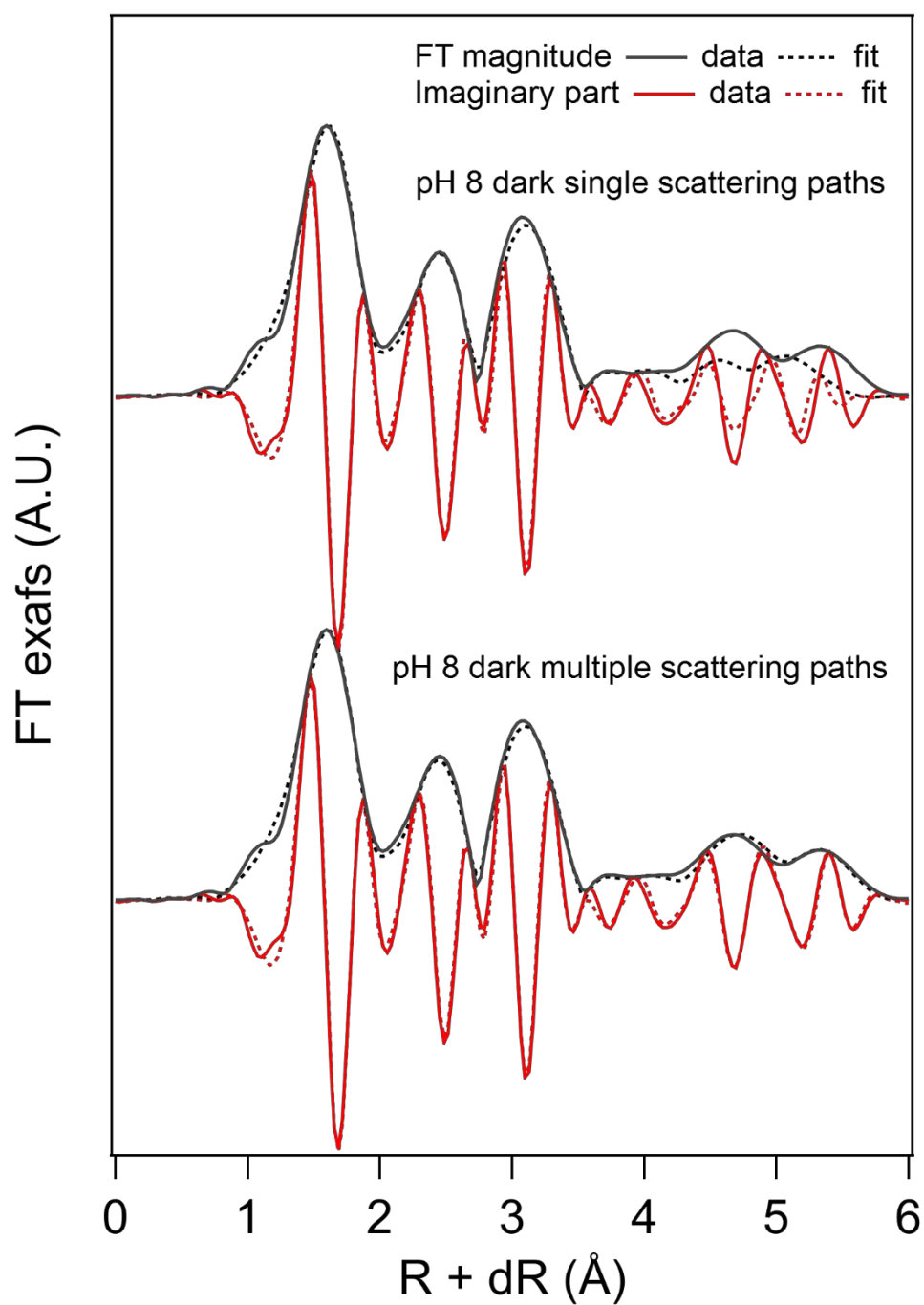


Figure S5: Plot of the fitted Ni-laden δ -MnO₂ pH 8 dark data without a multiple scattering path (above) and with a multiple scattering path (below).

7.10. References

Pena, J., Kwon, K.D., Refson, K., Bargar, J.R., Sposito, G., **2010**. Mechanisms of nickel sorption by a bacteriogenic birnessite. *Geochim Cosmochim Acta* 74, 3076-3089.

ANNEX 6. Chapter 4 as published in PNAS without modifications



Rate and mechanism of the photoreduction of birnessite (MnO₂) nanosheets

Francesco Femi Marafatto^a, Matthew L. Strader^{b,1}, Julia Gonzalez-Holguera^a, Adam Schwartzberg^c, Benjamin Gilbert^{d,2}, and Jasquelin Peña^{a,2}

^aInstitute of Earth Surface Dynamics, University of Lausanne, CH-1015 Lausanne, Switzerland; and ^bChemical Sciences Division, ^cMolecular Foundry, and ^dEarth Sciences Division, Lawrence Berkeley National Laboratory, Berkeley, CA 94720

Edited by François M. M. Morel, Princeton University, Princeton, NJ, and approved March 10, 2015 (received for review November 3, 2014)

The photoreductive dissolution of Mn(IV) oxide minerals in sunlit aquatic environments couples the Mn cycle to the oxidation of organic matter and fate of trace elements associated with Mn oxides, but the intrinsic rate and mechanism of mineral dissolution in the absence of organic electron donors is unknown. We investigated the photoreduction of δ -MnO₂ nanosheets at pH 6.5 with Na or Ca as the interlayer cation under 400-nm light irradiation and quantified the yield and timescales of Mn(III) production. Our study of transient intermediate states using time-resolved optical and X-ray absorption spectroscopy showed key roles for chemically distinct Mn(III) species. The reaction pathway involves (i) formation of Jahn–Teller distorted Mn(III) sites in the octahedral sheet within 0.6 ps of photoexcitation; (ii) Mn(III) migration into the interlayer within 600 ps; and (iii) increased nanosheet stacking. We propose that irreversible Mn reduction is coupled to hole-scavenging by surface water molecules or hydroxyl groups, with associated radical formation. This work demonstrates the importance of direct MnO₂ photoreduction in environmental processes and provides a framework to test new hypotheses regarding the role of organic molecules and metal species in photochemical reactions with Mn oxide phases. The timescales for the production and evolution of Mn(III) species and a catalytic role for interlayer Ca²⁺ identified here from spectroscopic measurements can also guide the design of efficient Mn-based catalysts for water oxidation.

manganese oxide | photoreduction | band-gap excitation | pump–probe spectroscopy | water oxidation

Manganese is a key element in environmental processes, catalytic materials, and biological systems due to its rich redox chemistry and ability to form species with a high oxidizing potential. Photochemical processes can enhance significantly the cycling of Mn between the +4, +3, and +2 valence states (1–3). Photoreduction of Mn(IV) is the first step in the reductive dissolution of birnessite minerals in the euphotic zone of marine and lacustrine environments (4–6). This process couples the biogeochemical cycle of Mn to the redox cycling of carbon and trace metals associated with Mn oxide phases. In addition, the greater role of Mn(IV) photoreduction relative to microbial Mn(II) oxidation leads to the predominance of dissolved over particulate Mn in the photic zone of natural waters (1). Thermodynamic calculations predict that direct photoexcitation of Mn oxides in water by visible light will lead to net metal reduction over a wide range of environmentally relevant pH values (7). However, experimental evidence of direct photoexcitation of MnO₂ and subsequent photoreduction of Mn(IV) in the absence of organic electron donors is currently lacking. Experimental studies on the photochemical cycling of Mn have incorporated natural organic ligands that can enhance metal reduction via multiple pathways (5, 8, 9). These studies have identified aqueous Mn(II) as a reaction end product but have not investigated the fate of Mn(III) in the dissolution process, even though Mn(III) is a necessary intermediate in the reduction of Mn(IV) to Mn(II) (10) and an important component of environmental systems (11).

The photochemistry of Mn also enables solar energy harvesting (12) and water oxidation catalysis in synthetic and biological systems (3, 13, 14). Mn-based cluster compounds (15, 16) and disordered birnessite nanoparticles (2) can exhibit analogous reactivity to the water-oxidizing center of photosystem II. Metal reduction is a key step in water oxidation using Mn oxide catalysts (2, 15, 17, 18) with evidence that Mn(III) plays an important role in O₂ generation (19). However, no information on the intrinsic kinetics or efficiency of Mn(IV) reduction has been reported to date. The structural and chemical constraints on the mechanism of Mn photoreduction are not known for any Mn phase (17, 18), although a recent study of MnO₂-based water oxidation showed that the substitution of Na with Ca in the interlayer of MnO₂ greatly enhances reactivity (15). The mineralogy literature suggests that the interlayer cations, which balance the excess charge in the MnO₂ sheet, may influence its photo-reactivity because the interlayer cations are known to bind water molecules to the neighboring MnO₂ octahedral sheets via hydrogen bonding, with the strength of the interactions dependent on the cation valence (20–22). However, the specific role of Ca in the photoreduction process is unknown (15).

The current work combines laboratory-based experiments and ultrafast pump–probe spectroscopy to investigate the photoreduction of δ -MnO₂, a fully oxidized synthetic analog of natural birnessites, which is comprised of randomly stacked MnO₂ nanosheets that extend only a few nanometers in the *ab* plane. The first objective was to measure the photoreduction efficiency of δ -MnO₂ in flow-through experiments by 400-nm illumination of aqueous

Significance

The photoreductive dissolution of Mn oxides governs the biogeochemical cycle of Mn and the fate of organic and inorganic species associated with Mn oxides in the euphotic zones of marine and freshwater systems. Mn oxide minerals also have garnered interest as water oxidation catalysts inspired by the Mn₄CaO₄ cluster of photosystem II. However, the mechanism of water oxidation by MnO₂ and the rate limiting steps for this reaction are unknown. In this study, we couple flow-through experiments and ultrafast pump–probe optical and X-ray absorption spectroscopy to develop a photoreduction model that includes the mechanism and timescales for the initial electron transfer steps in the oxidation of water by MnO₂.

Author contributions: F.F.M., M.L.S., A.S., B.G., and J.P. designed research; F.F.M., M.L.S., J.G.-H., A.S., B.G., and J.P. performed research; F.F.M., M.L.S., J.G.-H., A.S., B.G., and J.P. analyzed data; and F.F.M., B.G., and J.P. wrote the paper.

The authors declare no conflict of interest.

This article is a PNAS Direct Submission.

¹Present address: Beam Line Development, SLAC National Accelerator Laboratory, Menlo Park, CA 94025.

²To whom correspondence may be addressed. Email: bgilbert@lbl.gov or jasquelin.pena@unil.ch.

This article contains supporting information online at www.pnas.org/lookup/suppl/doi:10.1073/pnas.1421018112/-DCSupplemental.

suspensions of δ -MnO₂, with Na (Na-MnO₂) or Ca (Ca-MnO₂) as the interlayer cation. The second objective was to elucidate the mechanism of photoreduction by following the coupled changes in Mn valence and coordination that follow photon absorption over picosecond-to-microsecond timescales using time-resolved optical (23) and X-ray (24) absorption spectroscopy. Pyrophosphate was used in the flow-through experiments to quantitate Mn(III) but was not added during spectroscopic experiments because the timescale for Mn(III) production could be determined directly from the transient X-ray absorption data.

Results

Efficiency of MnO₂ Photoreduction. Flow-through experiments were carried out to evaluate the irreversibility of MnO₂ photoreduction, to identify the reduced Mn species, and to quantify the efficiency of the process. The irradiation of 500 μ M δ -MnO₂ suspensions at pH 6.5 ± 0.2 in 1-cm path length flow-through cuvettes showed irreversible Mn(III) generation upon 400 nm irradiation under a photon flux of $0.77 \mu\text{E s}^{-1}$, which is comparable to that of sunlight between 400 and 600 nm (calculations in *SI Text*). We measured the steady formation of Mn(III) at a rate of $2.20 \pm 0.27 \mu\text{mol Mn(III)}\cdot\text{d}^{-1}$ (95% confidence interval) in Ca-MnO₂ suspensions and $1.50 \pm 0.19 \mu\text{mol Mn(III)}\cdot\text{d}^{-1}$ in Na-MnO₂ suspensions containing pyrophosphate (PP) as a Mn(III) trapping agent (Fig. S1). These rates were corrected for any release of Mn(III) in dark controls (0.2 – $0.9 \mu\text{mol Mn(III)}\cdot\text{d}^{-1}$). The nonzero dark release is attributed to the extraction of residual Mn(III) not detectable by the method used to determine average Mn oxidation number (AMON). Apparent quantum yields of $8.2 \pm 0.1 \times 10^{-4}$ and $3.1 \pm 0.3 \times 10^{-4}$ (95% confidence interval) were calculated for Ca-MnO₂ and Na-MnO₂, respectively. Similar rates measured in suspensions where PP was added after irradiation (Fig. S1) indicate that PP does not influence photoreduction. Further evidence that PP and Mn(III)-PP do not influence Mn photoreduction comes from their UV-visible (UV-vis) spectra, which show no absorption at 400 nm (25).

Optical Transient Absorption Spectroscopy. Figs. 1 and 2 present optical transient absorption (TA) spectra and kinetics, respectively, for Ca-MnO₂ acquired at subpicosecond-to-microsecond timescales. Equivalent data for Na-MnO₂ are presented in Figs. S2 and S3. All samples were resuspended in 1.5% (mass/vol) Nafion to reduce particle aggregation. Following photoexcitation at 400 nm, the TA spectra acquired at a few picoseconds exhibited a broad excited-state absorption (ESA) feature with maximum intensity at 538 nm (Ca-MnO₂; Fig. 1) or 570 nm (Na-MnO₂; Fig. S24). The TA spectra also showed a ground-state bleach extending from the laser wavelength to the lowest wavelength measureable (\sim 335 nm); the bleach reflects the decrease in the population of valence band electrons that remain in the ground state. After correcting for the laser chirp, the comparison of the TA kinetics at 345 and 550 nm showed a rise in ESA intensity that was delayed relative to the prompt bleach signal. The maximum ESA intensity occurred at \sim 0.3 ps for Ca-MnO₂ (Fig. 24) and \sim 0.6 ps for Na-MnO₂ (Fig. S34). The ESA and bleach signals decayed with similar dynamics up to \sim 10 ps (Fig. 2B). The ESA then decayed completely within 1 ns, but the bleach signal remained detectable on the microsecond timescale. The decay kinetics of the bleach differed for Ca- vs. Na-MnO₂ (Fig. 1C), although both samples exhibited short (submicrosecond, τ_1) and long (10–30 μ s, τ_2) decay timescales (Table 1).

Direct comparison of the fitted first-order decay constants for Ca-MnO₂ and Na-MnO₂ in Nafion-stabilized suspensions reveals that the recombination rates are three- to fourfold slower in the presence of interlayer Ca. In particular, the τ_2 values indicate that the bleach returns to baseline within 50 μ s for Na-MnO₂ (five half-lives elapsed, 0.02% of initial signal remains), whereas for Ca-MnO₂ the bleach does not return to the baseline within

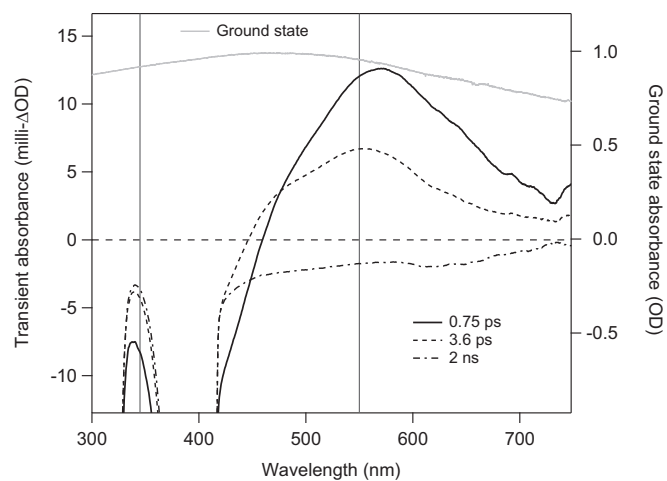


Fig. 1. Optical transient absorption (TA) spectra acquired from Ca-MnO₂ in an aqueous suspension containing Nafion at 0.75 ps, 3.6 ps, and 2 ns after photoexcitation at 400 nm. The TA spectra (milli- Δ OD units; left axis) are compared with the ground-state UV-vis absorption spectra (OD units; right axis). Vertical lines at 550 nm (the maximum intensity of the ESA) and at 345 nm (ground-state bleach) indicate wavelengths chosen for kinetics analysis. The data from 390–410 nm are affected by scattering of the excitation beam. Equivalent TA data for Na-MnO₂ are given in Fig. S24.

the resolution of the experiment (two half-lives elapsed, 8% of initial signal remains). Slightly slower decays were observed for samples prepared without Nafion, possibly indicating an effect of aggregation upon recombination rates. Slower decay could occur if recombination involved diffusion of soluble species, but this effect is impossible to explain confidently and is smaller than the influence of the interlayer cation (*SI Text*). The addition of the anionic hydroxyl radical scavenger, terephthalic acid (TPA), had no detectable effect on the decay kinetics for Na-MnO₂.

Light-Initiated Time-Resolved X-Ray Absorption Spectroscopy. Selected ground-state Mn K-edge spectra collected during a single 4-h light-initiated time-resolved X-ray absorption spectroscopy (LITR-XAS) experiment with Ca-MnO₂ are displayed in Fig. 3. The increase in the absorption intensity at 6,550 eV (Fig. 3, *Inset*) shows a shift of the Mn K-edge to lower energies, which is consistent with a decrease in the average oxidation state of Mn (26). Thus, 400-nm laser excitation causes the accumulation of reduced Mn. A difference X-ray absorption (Δ XA) spectrum, obtained by subtracting the initial ground-state spectrum from the 3-h ground-state spectrum, is included in Fig. 3 to emphasize the irreversible change in Mn valence and bonding environment after 3 h of irradiation.

Transient Δ XA spectra were obtained by subtracting the ground-state spectrum from the excited-state spectra at delay times of up to 10 ns (Fig. 4A). The first oscillation between 6,540 and 6,570 eV in the transient Δ XA spectrum at a 50-ps delay indicates a shift in the absorption edge position to lower energies that is consistent with the formation of reduced Mn (Fig. 3). The feature is approximately constant from 50 ps (the temporal resolution of the experiment) to 10 ns (the latest time point studied). As shown in Fig. 4B, transient kinetic data at 6,550 eV confirmed the prompt formation and negligible decay of the signal for reduced Mn. Within 600 ps, we observed modulations at energies above 6,570 eV, the fine-structure portion of the transient Δ XA spectrum, which reflect changes in the coordination environment of Mn. Finally, the close agreement between the transient Δ XA data at 10 ns and the Δ XA data associated with permanent photoreduction at 3 h indicates that at least a fraction of the reduced Mn species observed at 10 ns persists indefinitely.

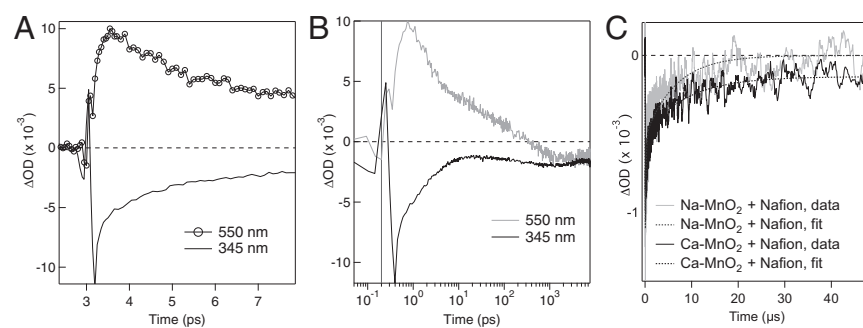


Fig. 2. Summary of optical transient absorption kinetics acquired from Ca-MnO₂ in an aqueous suspension containing Nafion. (A) Transient kinetic traces show a slight delay in the onset of the ESA at 550 nm relative to the bleach at 345 nm. (B) Decay kinetics of the ESA and bleach up to 8 ns. The time-zero was shifted by 0.2 ps to enable plotting on a logarithmic scale. Equivalent data for Na-MnO₂ are given in Fig. S3 A and B. (C) Comparison between the decay kinetics of the bleach recorded at 580 nm for Ca-MnO₂ and Na-MnO₂ in Nafion, fitted with two-component exponential decay functions.

The long-term effect of Mn(III) accumulation on the irradiated Mn oxide was assessed by characterization of the mineral structure. Powder X-ray diffraction (XRD) patterns acquired from samples before laser irradiation show broad $hk0$ peaks at 2.4 and 1.4 Å and no stacking peak at 7.2 Å (in d -spacing). This pattern is characteristic of δ -MnO₂ nanosheets with hexagonal sheet symmetry and fewer than three randomly stacked sheets (26). Following laser irradiation, the XRD patterns showed additional 001 and 002 Bragg reflections (Fig. S4) consistent with increased ordered stacking of the MnO₂ sheets (26).

Discussion

Efficiency of Mn(IV) Oxide Photoreduction. Our flow-through experiments show that the irreversible photoreduction of δ -MnO₂ to form Mn(III) occurs readily under environmentally relevant conditions in the absence of any electron donor other than water. In addition, our measurements show no production of Mn(II). The apparent quantum yield of the process at pH 6.5 is up to two orders of magnitude larger than the apparent quantum yield measured for γ -Fe₂O₃(s) at pH 3.0, $\sim 10^{-5}$ (27), and comparable to the value measured for γ -FeOOH(s) at pH 3.0, $\sim 10^{-3}$ (28). Furthermore, Fe photoreduction in water has only been observed at pH values below 5. These results emphasize the importance of photoreduction in the redox cycling of Mn oxides relative to Fe oxides and support the thermodynamic calculations presented by Sherman (7), which indicate that photoreduction may occur at higher pH values for Mn oxides than for Fe oxides.

Environmental Mn cycling is frequently coupled to the oxidation of dissolved organic matter (DOM). Manganese oxide photodissolution in the presence of 10–40 mg/L DOM has been reported to have a 5–10 times greater efficiency (9) than measured here for MnO₂ photoreduction without organics. DOM can increase the accumulation of reduced Mn by acting as the chromophore that either initiates electron transfer to the mineral (9) or photolyzes to generate reactive oxygen species (5); by acting as an electron donor to the photoexcited mineral; or by providing ligands that can complex intermediate Mn³⁺ as Mn(III)_(aq) species (11). Due to the optical properties of DOM, the first mechanism is only important under UV light, which is a minor component of the sun's irradiance spectrum on the Earth's surface and has a lower penetration depth (up to ~ 25 m) in natural waters than visible wavelengths (~ 100 m) (29). The complexation of reduced manganese by DOM is likely to occur independently from the photoreduction mechanism. Thus, our results indicate that Mn photoreduction in which water serves as electron donor must be a significant contributor to any overall environmental rate.

Manganese Redox Dynamics. We used the time-resolved optical and X-ray data to construct a model for the photoexcitation and evolution of Mn(III) states in δ -MnO₂ as visualized in Fig. 5.

A transient Jahn–Teller-distorted Mn(III) intermediate forms in the nano-sheet. We interpret the transient optical ESA that appears within 0.3–0.6 ps, and that has a lifetime less than 1 ns, as a transient intermediate Mn(III) state that is formed by ligand-to-metal charge-transfer that excites an oxygen-centered valence electron into the metal $3d$ state (7). This interpretation requires justification because transient electronic excitations observed in TA spectroscopy of metal oxides could be associated with either electrons (e.g., the transitions of electrons promoted to the conduction band) or holes (i.e., new excitations within the valence band). For example, band-gap excitation of hematite (α -Fe₂O₃) generates a prompt optical ESA centered at 580 nm attributed to hole excitations based on UV-vis spectra of a thin-film hematite electrode under oxidizing vs. reducing conditions (30). In the present case, however, the delayed onset of the ESA is consistent with electronic relaxation into a polaronic state, as observed for photoexcitation of manganites (31). Polaron formation would be expected for the creation of a Mn(III) state, for which Jahn–Teller (JT) distortion of the octahedron can lower the ground-state energy by adopting high-spin d^4 electron configuration and splitting of the e_g and t_{2g} orbitals (32). In this depiction, the ESA is caused by low-energy excitations of the extra electron localized in the JT state. Additionally, UV-vis spectra from well-characterized MnO_x phases show that Mn(III) located in the MnO₂ sheets confers absorption features in the visible range between 400 and 600 nm (Fig. S5).

The line shape of the ESA reported here closely matches a feature in the UV-vis spectrum reported for a birnessite anode poised at sufficiently positive potentials to oxidize water (19). Takashima et al. (19) assigned the optical feature between 400 and 600 nm to adsorbed Mn(III) based on pyrophosphate extractions. However, any Mn(III) extracted by pyrophosphate after the electrochemical oxidation of water reflects only the final Mn(III)

Table 1. Time constants obtained from fitting the EOS data with exponential decay functions (Fig. S8)

	τ_1 (μ s) \pm SD	τ_2 (μ s) \pm SD	χ^2
Na-MnO ₂			
Water	0.36 \pm 0.03	15.31 \pm 0.96	11.03
TPA	0.36 \pm 0.04	14.38 \pm 1.32	18.68
Nafion	0.24 \pm 0.02	10.14 \pm 0.63	12.68
Ca-MnO ₂			
Nafion	0.81 \pm 0.06	27.35 \pm 1.75	6.53

A time offset of 0.047 μ s was used for all data.

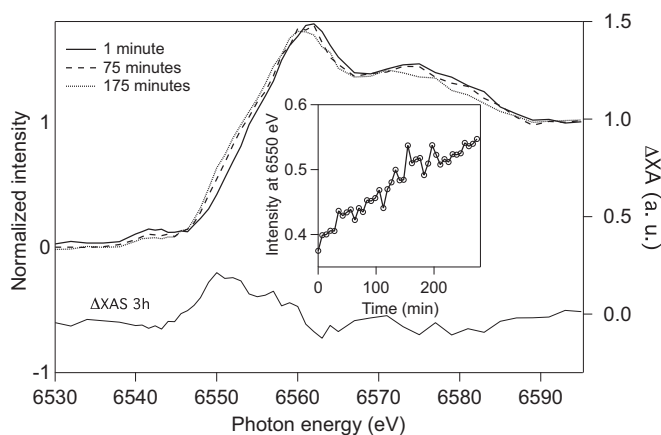


Fig. 3. Ground-state Mn K-edge X-ray absorption (XA) spectra show the steady reduction of Mn in a ~ 10 mM Ca-MnO₂ suspension at pH 6.5 during a ~ 4 -h laser pump/X-ray probe study. Spectra are shown for 1 min (solid line), 19 min (dashed line), and 175 min (dotted line) after the onset of the experiment (left vertical axis). The difference (Δ XA) spectrum obtained by subtracting the spectrum at 175 min from the spectrum at 1 min (right vertical axis) is included beneath the XA spectra. (Inset) XA intensity at 6,550 eV as a function of time, which indicates an increase in reduced Mn.

state. Our kinetic measurements demonstrate that the visible ESA is due to a transient state.

A long-lived interlayer Mn(III) adsorbate between the nanosheets. We propose that the loss of the optical ESA signal (i.e., the JT state) is caused by two processes occurring on different timescales. Within the first 10 ps, the ESA decay and that of the bleach were closely coupled, indicating electron-hole recombination. Further decay of the ESA signal, however, was not matched by further loss of the bleach. The LITR-XAS also showed that within ~ 600 ps there was a change in the Mn bonding environment but no loss of the reduced Mn state. We explain these trends by the displacement of Mn(III) from the nanosheet layer into the hydrated interlayer region, with the formation of a vacancy site beneath (Fig. 5C). Prior studies have established that Mn(III) cations can reside stably within the interlayer of birnessite nanosheets to reduce the sheet steric strain (33, 34). The JT distortion at the Mn(III) site could drive its migration into the interlayer, where it can act as an adsorbed cation that enhances the stacking of the negatively charged sheets (Fig. 5D). In addition, JT-distorted Mn(III) sites have been reported as key species for water oxidation (17). The migration of JT distorted Mn(III) from the MnO₂ sheet into the interlayer and change in Mn(III) bonding environment may decrease the overall reactivity of the material for multielectron water oxidation. Thus, our finding has implications regarding the mechanistic constraints on Mn oxide photocatalysis. The formation of new vacancy sites likely also alters the optical absorption properties of the modified nanosheet (35). Our model, however, requires that the putative interlayer Mn(III) ion lack an optical absorption signature in the 335- to 800-nm range; this could not be verified through published studies of the UV-vis absorption spectra of Mn³⁺ because this species is unstable in aqueous solution (11, 25).

Hole dynamics: Recombination vs. water oxidation chemistry. Photoexcitation of δ -MnO₂ and the generation of Mn(III) must be accompanied by the formation of valence band holes. Hole states in transition metal oxides are typically localized at oxygen sites, but holes that form close to surface sites may participate in reactions with water, including steps in the four-electron oxygen evolution reaction (36) or with aqueous ions such as Cl⁻ (37).

The bleach signal in the TA data shows complete return to the ground state after 50 μ s or longer, indicating that most of the hole states are able to recombine with the photoexcited electrons

in Mn(III) even after migration of the metal ion into the interlayer. Although we proved that net photoreduction occurs, the apparent quantum yield is too low for the irreversible fraction to be detectable above the statistical noise in the TA data. Recombination may involve exclusively solid-phase species, or the formation of chemical intermediates. Borer et al. (28) used a hydroxyl radical scavenger to demonstrate the generation of hydroxyl radicals (OH[•]) through hole reaction with surface hydroxyls on γ -FeOOH, but in that case only an anionic scavenger was able to react with the net positively charged surface of iron oxyhydroxides. In the present case, we were unable to identify a cationic hydroxyl scavenger that was stable against dark reaction with Mn(IV), and the anionic TPA may have been unable to interact with the net negatively charged δ -MnO₂ surface. Nevertheless, surface-bound hydroxyl groups on birnessite have been identified in a synthetic Mn(III)-bearing microcrystalline birnessite phase from the interpretation of thermogravimetric data (33). Reactions between OH[•] species could yield H₂O₂ or other reactive oxygen species that could oxidize Mn(III) back to Mn(IV) and thus reduce the net quantum yield of direct photoreduction by band-gap excitations. Our efforts are currently dedicated to identifying these radical species, which can also enhance microbial Mn oxidation (38) and induce cellular oxidative stress.

Influence of Interlayer Cation on MnO₂ Photoreduction. We observed that the interlayer cations, which balance the negative layer charge, influence the optical properties and photochemistry of layer-type MnO₂, as observed previously in water oxidation studies (15). The slower microsecond timescale kinetics for Ca- vs. Na-MnO₂ and greater apparent quantum yield, which cannot be explained by aggregation (*SI Text*), suggest a catalytic role for this ion that reduces the rate at which interlayer Mn(III) species and photoexcited hole states can recombine. Because Ca²⁺ has a greater hydration enthalpy (22) and slower water exchange rate than Na⁺ (10^8 s⁻¹ vs. 10^9 s⁻¹) (39), its catalytic role may reduce the mobility of water and other species in the interlayer. However, Ca also caused redshifts in both ground-state and transient UV-vis spectra (Figs. S3B and S6A), indicating that this ion has significant chemical interactions with the Mn oxide nanosheets. Further work will be required to fully determine the role of Ca, but the model proposed here provides a basis for future studies.

Environmental Implications

This work provides insight into the mechanism, rates, and chemical controls on the photoreduction of fully oxidized Mn oxide phases that are the initial products of biological manganese oxidation (6)

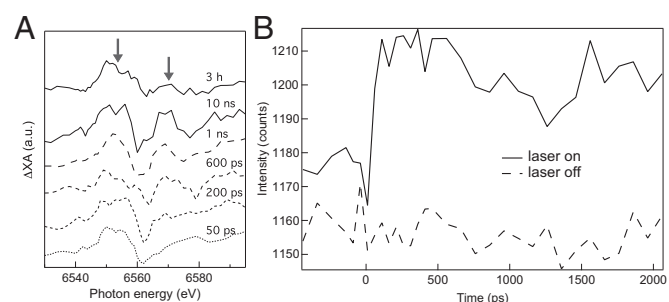


Fig. 4. (A) Δ XA spectra at various delay times reveal a prompt change in the Mn oxidation state (feature at 6,550 eV, left arrow) and evolution in fine structure within 1 ns (feature at 6,570 eV, right arrow). The ground-state Δ XA spectrum, obtained by subtracting the ground spectrum at 175 min from the ground spectrum at 1 min (Fig. 3), is shown for comparison with the transient Δ XA spectra. (B) Kinetic traces of the X-ray absorption intensity at 6,552 eV with (solid line) and without (dashed line) the laser pump confirm a prompt change in Mn valence and no decay within 2 ns.

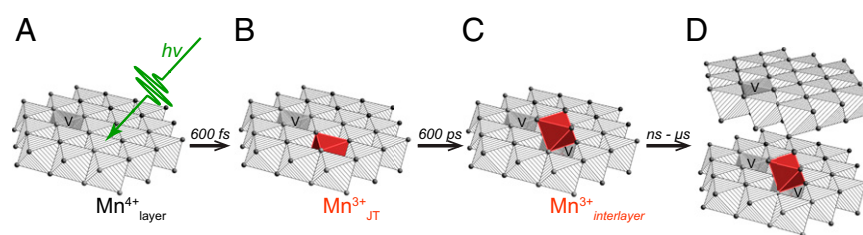


Fig. 5. Proposed model for the evolution of metal redox chemistry during δ -MnO₂ photoreduction. (A) Absorption of a photon ($h\nu$) by a single Mn(IV) oxide nanosheet that includes metal vacancy sites (V). (B) Formation within 600 fs of a Jahn–Teller distorted Mn(III) state within the nanosheet (dark red octahedron). (C) Migration within 1 ns of Mn(III) from the nanosheet to an adsorption site above a new vacancy. (D) Increased nanosheet stacking due to increased compensation of sheet negative charge by interlayer Mn(III). Water molecules are omitted for clarity.

and that may have been precursors to biological water oxidation catalysts (14). The evidence we provide for δ -MnO₂ photoreduction in the absence of organic electron donors establishes this pathway as an important component of the Mn cycle. That this reaction occurs at 400 nm indicates that it is important at all depths of the water column to which visible light penetrates, including depths where dissolved organic matter is not photoactive. The broad absorbance of MnO₂ suggests that photoreduction can occur across a wide spectrum of solar irradiation, although further experiments will be required to establish the wavelength dependence. Photoreduction creates Mn(III) states that are stabilized by adsorption at interlayer sites and increase nanosheet stacking. Our results also suggest that Mn(IV) photoreduction in sunlit environments may cause initial biogenic Mn(IV) oxides to transform to a phase with varying amounts of Mn(III) (6). We cannot generalize our conclusions to the many other phases of birnessite that can be found in nature, but we anticipate that photochemical transformations of these phases will retain similar mechanistic aspects, although the net rates may be influenced by Mn(III) content.

Materials and Methods

American Chemical Society-grade chemicals were purchased from Sigma-Aldrich or Merck; Nafion was purchased from Fuel Cell Earth LLC. All solutions were prepared with ultrapure water (18 M Ω · cm). The δ -MnO₂ phase used in flow-through photodissolution experiments and pump–probe experiments was synthesized according to Villalobos et al. (26). Synthesis and characterization of the mineral phase are described in *SI Text*. All experiments were carried out at ambient temperature, on suspensions under aerated conditions or purged with N_{2(g)} or He_{2(g)}.

Efficiency of MnO₂ Photoreduction. Flow-through experiments were carried out to verify whether δ -MnO₂ photoreduction by band-gap excitation generated reduced Mn ions irreversibly and to measure the rates and efficiency of the process. We prepared oxide suspensions containing 500 μ M Mn and 25 mM sodium pyrophosphate (PP) to trap Mn(III) with a final pH of 6.5 (no pH-adjustment was required). The Ca-MnO₂ suspensions were prepared by equilibrating the oxide with CaCl_{2(aq)} in a 3:1 molar ratio. All suspensions were equilibrated in the dark for 3 d before irradiation. The suspensions were then divided into two aliquots: one was used as a dark control and the second was recirculated through a flow-through quartz cuvette. Irradiation for 72 h was provided by an array of three 1-W light-emitting diodes at 400 nm (3.1 eV), close to the maximum UV-vis absorbance of a Na-MnO₂ suspension in water (Fig. S5A). The photoreactor was screened from ambient light.

Every 24 h, a sample aliquot was collected for inductively coupled plasma optical emission spectrometry (ICP-OES) measurement of [Mn_{TOT}] after digestion with 0.05 M H₂C₂O₄ and 3% (vol/vol) HNO₃ and another was filtered through a 0.2- μ m polyethersulfone syringe filter for ICP-OES measurement of [Mn_(aq)] and [Mn(III)-PP] quantification by UV-vis spectrophotometry ($\epsilon_{254\text{ nm}} = 6,562\text{ L}\cdot\text{mol}^{-1}\cdot\text{cm}^{-1}$) with 1-cm path-length quartz cuvettes using a 25-mM PP solution as a blank. Measurements of [Mn_(aq)] and [Mn(III)-PP] were within 10%, with concentrations ranging from 10 to 50 μ M. Experiments were conducted in duplicate; suspension pH was 6.5 \pm 0.2 before and after irradiation.

Complementary experiments were carried out to confirm that PP did not influence Mn photoreduction. Experiments were conducted as described

above but in the absence of PP and with Na-MnO₂ supplemented with 10 mM NaCl. After 0, 24, 48, and 72 h of irradiation, 10-mL sample aliquots were collected, mixed with 2 mL of a 100 mM PP stock solution (pH 6.5), and placed on an end-to-end shaker for 24 h in the dark. Measurements of [Mn_{TOT}], [Mn_(aq)], and [Mn(III)-PP_(aq)] were made as described above; suspension pH was 6.5 \pm 0.2 before and after irradiation.

The rate of Mn(III) production was determined from linear regression of Mn(III)-PP against time, after correction for any Mn(III) released in dark control experiments. We then calculated the apparent quantum yield for Mn(III) generation, which is defined as the amount of photoproduced Mn(III) per photon absorbed by the MnO₂ suspension. To calculate the number of photons absorbed, we measured the photon flux to the photoreactor by chemical actinometry using potassium ferrioxalate and then scaled the photon flux to the ratio of the absorbance of MnO₂ to ferrioxalate (*SI Text*).

Optical Transient Absorption Spectroscopy. Optical TA spectroscopy can be used to follow excited-state valence electron dynamics in semiconducting metal oxides (23). Optical TA experiments were carried out on a HELIOS femtosecond transient absorption spectrometer and on an EOS subnanosecond transient absorption spectrometer from Ultrafast Systems installed at the Molecular Foundry, Lawrence Berkeley National Laboratory. The laser source for both instruments was a Coherent Libra Amplified Femtosecond Laser System operating at 1 kHz with 45-fs pulse duration. The laser output was split, one arm passing through a Coherent OPerA optical parametric amplifier (OPA) to produce pump pulses at 400 nm, the other arm delivered to the transient absorption system where a white-light probe pulse was generated in a sapphire plate or by a fiber white-light source (Leukos-STM) for the HELIOS and EOS spectrometers, respectively. The intensity of the pump beam was measured to be 800 nJ·pulse⁻¹. Time delay was provided by a mechanical delay stage on the HELIOS setup and by instrument electronics on the EOS setup. Spectra were collected between 335 and 900 nm.

Samples of Ca-MnO₂ and Na-MnO₂ were either kept in their original aqueous suspension or resuspended in an aqueous solution of 1.5% (mass/vol) Nafion in 3% (vol/vol) isopropanol. The Nafion polymer reduced particle aggregation and there is no evidence that it influences the photochemical behavior of birnessite-based photocatalysts (2, 40). Furthermore, the comparison of TA data of Na-MnO₂ in water vs. in an aqueous Nafion solution showed no detectable differences on picosecond-to-nanosecond timescales (Fig. S9). The 3% (vol/vol) isopropanol was evaporated in air from the Nafion solution for 12 h before starting the measurements to ensure complete isopropanol evaporation. Additional Na-MnO₂ samples were resuspended in 0.1 M TPA, a hydroxyl radical trap (41), and measured on the EOS setup. The samples were measured in 1-mm path-length quartz cuvettes and stirred with a magnetic stir bar or recirculated in a flow-through cuvette. The optimum MnO₂ concentration for TA measurements ranged from 3 to 6 mM on a Mn molar basis, corresponding to an OD at 400 nm between 0.8 and 1.6 absorption units on 0.5-mm path-length quartz cuvettes. Spectra were collected from –10 ps to 8 ns (relative to laser pulse) on the HELIOS system and from 1 ns to 50 μ s on the EOS system. Custom user routines developed in the IGOR Pro software (WaveMetrics Inc.) were used to process the data, including correction of the time-dependent frequency modulation of the laser (laser chirp) on the signal to within ~0.15 ps and to extract transient kinetic data at 354 and 550 nm from 2D plots of spectra vs. time. IGOR Pro was also used to fit first-order exponential decay kinetics to the extracted data. Decay kinetics for all samples were adequately reproduced by fitting two exponential time constants (*SI Text*).

Laser-Initiated Time-Resolved X-Ray Absorption Spectroscopy. LITR-XAS excites core electrons and yields information on the oxidation state and local

bonding environment of the probed atoms following light excitation (24). LITR-XAS experiments were carried out at Beamline 6.0.1 at Advanced Light Source. At this beamline, the X-ray beam pulses are isolated with an X-ray chopper and combined with the output of a femtosecond Ti:Sapphire laser system with a power output of 800 mW measured at the sample position. The X-ray energy was scanned across the Mn K-edge (6,530–6,595 eV). Ground-state and transient X-ray absorption spectra were collected in fluorescence mode with an avalanche photodiode fitted with Soller slits and a Cr filter. The 400-nm laser pulse was obtained by converting the 800-nm output from the 4-kHz Ti:Sapphire laser system with an OPA. The laser pulse was synchronized to a single electron bunch by locking the 62.5-MHz repetition rate of the laser system oscillator to the 499.64-MHz of the synchrotron's radiofrequency cavity to an accuracy of less than 20 ps. The FWHM of the laser and X-ray pulses were 0.1 and 70 ps, respectively. Finally, the time 0 delay between X-ray and laser pulses was determined using an iron(II) Tris(2,2'-bipyridine) solution, which exhibits distinct changes in absorption at the Fe K-edge upon laser excitation.

The laser and X-ray beams intersected the sample in a closed He_{2(g)} purged chamber. Samples were recirculated from a bottle on a stir plate through a nozzle forming a 600- μ m diameter liquid jet. The size of the X-ray beam on the sample was 60 \times 60 μ m. To begin an experiment, 250-mL suspensions of \sim 10 mM Ca- and Na-MnO₂ were prepared. Before data acquisition, the chamber and sample were purged with He_{2(g)}. Each experimental condition was repeated in duplicate on suspensions recirculated for up to 4 h to obtain transient and kinetic data. For transient X-ray absorption experiments, spectra were collected at a fixed time delay and the monochromator was

scanned from 40 eV below to 70 eV above the Mn K-edge (6,539 eV). The transient spectra were three-point smoothed for plotting. Kinetic data were acquired by setting the monochromator at a fixed energy position and varying the time delay between laser and X-ray pulses. In both acquisition modes, data were collected before and after laser irradiation at the chosen time delay to extract ground-state and excited-state spectra. Following each LITR-XAS experiment, the samples were retained for analysis by X-ray diffraction. To assess the possibility of X-ray radiation damage, a conservative Mn:photon ratio was calculated. We estimated that 10¹⁴ X-ray photons are delivered to the sample over the 4-h timespan of the experiment, compared with \sim 10²¹ Mn atoms in the sample (SI Text). The Mn:photon ratio was thus estimated to be 10⁶:1, strongly suggesting that X-ray beam damage is negligible.

ACKNOWLEDGMENTS. We thank Drs. M. Hertlein and T. E. Glover for assistance with the X-ray measurements; Dr. R. W. Schoenlein for equipment and staff assistance; Drs. K. Sand and T. Adatte for the acquisition of high-energy X-ray scattering data and XRD patterns, respectively; and three anonymous reviewers for their valuable comments. F.F.M. and J.P. acknowledge support from the Swiss National Science Foundation (Proposal 200021_143742) and a grant from the Sandoz Family Foundation. B.G. was supported by the Director, Office of Science, Office of Basic Energy Sciences, of the US Department of Energy (BES-DOE) Contract DE-AC02-05CH11231. Research at the Molecular Foundry and the Advanced Light Source was supported by BES-DOE Contract DE-AC02-05CH11231. Pair distribution function data were acquired at the Advanced Photon Source, operated for BES-DOE by Argonne National Laboratory under Contract DE-AC02-06CH11357.

- Sunda WG, Huntsman SA (1990) Diel cycles in microbial manganese oxidation and manganese redox speciation in coastal waters of the Bahama Islands. *Limnol Oceanogr* 35(2):325–338.
- Hocking RK, et al. (2011) Water-oxidation catalysis by manganese in a geochemical-like cycle. *Nat Chem* 3(6):461–466.
- Armstrong FA (2008) Why did Nature choose manganese to make oxygen? *Philos Trans R Soc Lond B Biol Sci* 363(1494):1263–1270, discussion 1270.
- Morgan JJ (2000) Manganese in natural waters and earth's crust: Its availability to organisms. *Met Ions Biol Syst* 37:1–34.
- Sunda WG, Huntsman SA (1994) Photoreduction of manganese oxides in seawater. *Mar Chem* 46(1–2):133–152.
- Spiro TG, Bargar JR, Sposito G, Tebo BM (2010) Bacteriogenic manganese oxides. *Acc Chem Res* 43(1):2–9.
- Sherman DM (2005) Electronic structures of iron(III) and manganese(IV) (hydr)oxide minerals: Thermodynamics of photochemical reductive dissolution in aquatic environments. *Geochim Cosmochim Acta* 69(13):3249–3255.
- Kim K, Yoon HI, Choi W (2012) Enhanced dissolution of manganese oxide in ice compared to aqueous phase under illuminated and dark conditions. *Environ Sci Technol* 46(24):13160–13166.
- Waite TD, Wrigley IC, Szymczak R (1988) Photoassisted dissolution of a colloidal manganese oxide in the presence of fulvic acid. *Environ Sci Technol* 22(7):778–785.
- Luther GW (2005) Manganese(II) oxidation and Mn(IV) reduction in the environment—Two one-electron transfer steps versus a single two-electron step. *Geomicrobiol J* 22(3–4):195–203.
- Madison AS, Tebo BM, Mucci A, Sundby B, Luther GW, 3rd (2013) Abundant pore-water Mn(III) is a major component of the sedimentary redox system. *Science* 341(6148):875–878.
- Sakai N, Ebina Y, Takada K, Sasaki T (2005) Photocurrent generation from semiconducting manganese oxide nanosheets in response to visible light. *J Phys Chem B* 109(19):9651–9655.
- Kolling DR, Cox N, Ananyev GM, Pace RJ, Dismukes GC (2012) What are the oxidation states of manganese required to catalyze photosynthetic water oxidation? *Biophys J* 103(2):313–322.
- Johnson JE, et al. (2013) Manganese-oxidizing photosynthesis before the rise of cyanobacteria. *Proc Natl Acad Sci USA* 110(28):11238–11243.
- Wiechen M, Zaharieva I, Dau H, Kurz P (2012) Layered manganese oxides for water-oxidation: Alkaline earth cations influence catalytic activity in a photosystem II-like fashion. *Chem Sci* 3(7):2330–2339.
- Hsu YK, Chen YC, Lin YG, Chen LC, Chen KH (2012) Birnessite-type manganese oxides nanosheets with hole acceptor assisted photoelectrochemical activity in response to visible light. *J Mater Chem* 22(6):2733–2739.
- Robinson DM, et al. (2013) Photochemical water oxidation by crystalline polymorphs of manganese oxides: Structural requirements for catalysis. *J Am Chem Soc* 135(9):3494–3501.
- Birkner N, et al. (2013) Energetic basis of catalytic activity of layered nanophase calcium manganese oxides for water oxidation. *Proc Natl Acad Sci USA* 110(22):8801–8806.
- Takashima T, Hashimoto K, Nakamura R (2012) Mechanisms of pH-dependent activity for water oxidation to molecular oxygen by MnO₂ electrocatalysts. *J Am Chem Soc* 134(3):1519–1527.
- Johnson EA, Post JE (2006) Water in the interlayer region of birnessite: Importance in cation exchange and structural stability. *Am Mineral* 91(4):609–618.
- Drits VA, Lanson B, Gorshkov AI, Manceau A (1998) Substructure and superstructure of four-layer Ca-exchanged birnessite. *Am Mineral* 83(1–2):97–118.
- Cygan RT, Post JE, Heaney PJ, Kubicki JD (2012) Molecular models of birnessite and related hydrated layered minerals. *Am Mineral* 97(8–9):1505–1514.
- Gilbert B, et al. (2013) Ultrafast electron and energy transfer in dye-sensitized iron oxide and oxyhydroxide nanoparticles. *Phys Chem Chem Phys* 15(40):17303–17313.
- Katz JE, et al. (2012) Electron small polarons and their mobility in iron (oxyhydr)oxide nanoparticles. *Science* 337(6099):1200–1203.
- Wang Y, Stone AT (2008) Phosphonate- and carboxylate-based chelating agents that solubilize (hydr)oxide-bound Mn(II). *Environ Sci Technol* 42(12):4397–4403.
- Villalobos M, Toner B, Bargar J, Sposito G (2003) Characterization of the manganese oxide produced by *Pseudomonas putida* strain MnB1. *Geochim Cosmochim Acta* 67(14):2649–2662.
- Litter MI, Blesa MA (1992) Photodissolution of iron-oxides. 4. A comparative-study on the photodissolution of hematite, magnetite, and maghemite in EDTA media. *Can J Chem* 70(9):2502–2510.
- Borer P, Sulzberger B, Hug SJ, Kraemer SM, Kretzschmar R (2009) Photoreductive dissolution of iron(III) (hydr)oxides in the absence and presence of organic ligands: Experimental studies and kinetic modeling. *Environ Sci Technol* 43(6):1864–1870.
- Smith RC, Baker KS (1981) Optical properties of the clearest natural waters (200–800 nm). *Appl Opt* 20(2):177–184.
- Barroso M, Pendlebury SR, Cowan AJ, Durrant JR (2013) Charge carrier trapping, recombination and transfer in hematite (α -Fe₂O₃) water splitting photoanodes. *Chem Sci* 4(7):2724–2734.
- Wu KH, et al. (2009) Ultrafast optical probes of polaron dynamics in La_{0.7}Ca_{0.3}MnO₃ thin films. *J Appl Phys* 105(4).
- Burns RG (1993) *Mineralogical Applications of Crystal Field Theory* (Cambridge Univ Press, New York), 2nd Ed.
- Gaillot AC, et al. (2003) Structure of synthetic K-rich birnessite obtained by high-temperature decomposition of KMnO₄. I. Two-layer polytype from 800 °C experiment. *Chem Mater* 15(24):4666–4678.
- Manceau A, et al. (2013) Short-range and long-range order of phyllosilicate nanoparticles determined using high-energy X-ray scattering. *J Appl Cryst* 46(1):193–209.
- Kwon KD, Refson K, Sposito G (2009) On the role of Mn(IV) vacancies in the photo-reductive dissolution of hexagonal birnessite. *Geochim Cosmochim Acta* 73(14):4142–4150.
- Tang J, Durrant JR, Klug DR (2008) Mechanism of photocatalytic water splitting in TiO₂. Reaction of water with photoholes, importance of charge carrier dynamics, and evidence for four-hole chemistry. *J Am Chem Soc* 130(42):13885–13891.
- Grätzel M, Kiwi J, Morrison CL, Davidson RS, Tseung AC (1985) Visible-light-induced photodissolution of α -Fe₂O₃ powder in the presence of chloride anions. *J Chem Soc Faraday Trans 1* 81(8):1883–1890.
- Hansel CM, Zeiner CA, Santelli CM, Webb SM (2012) Mn(II) oxidation by an ascomycete fungus is linked to superoxide production during asexual reproduction. *Proc Natl Acad Sci USA* 109(31):12621–12625.
- Stumm W, Morgan JJ (1996) *Aquatic Chemistry: Chemical Equilibria and Rates in Natural Waters* (Wiley, New York).
- Young KJ, Gao Y, Brudvig GW (2011) Photocatalytic water oxidation using manganese compounds immobilized in Nafion polymer membranes. *Aust J Chem* 64(9):1221–1228.
- Barreto JC, Smith GS, Strobel NH, McQuillin PA, Miller TA (1995) Terephthalic acid: A dosimeter for the detection of hydroxyl radicals in vitro. *Life Sci* 56(4):PL89–PL96.

Supporting Information

Marafatto et al. 10.1073/pnas.1421018112

SI Materials and Methods

Mineral Synthesis and Characterization. The Mn oxide phase, δ -MnO₂, was synthesized by combining stoichiometric amounts of MnCl₂ with KMnO₄ in excess NaOH under vigorous mixing (1). The solids were rinsed with water until the electrical conductivity of the supernatant was less than 30 μ S·cm⁻¹. The washing procedure required seven cycles of centrifuging the slurry (20 min at 27,500 relative centrifugal force and 25 °C) and resuspending the mineral paste in Milli-Q (MQ) water. After the final rinsing step, the mineral paste was resuspended in MQ water and stored in the dark at 4 °C. Mineral composition was characterized with respect to average Mn oxidation number and Na:Mn content. The AMON was characterized by potentiometric titration (2) with a Metrohm 888 Titrand automatic titrator. Briefly, 15 mg of δ -MnO₂ were dissolved in a 0.01 M Mohr's salt [(NH₄)Fe(SO₄)₂·6H₂O] solution and residual Fe(II) was titrated with 0.01 M KMnO₄. The amount of Mn(II) generated was back-titrated with 0.02 M KMnO₄ and all Mn(III) produced was trapped by complexation with excess PP (Na₄P₂O₇) (3–5). A detailed description of the titration protocol is provided by Grangeon et al. (2). The Na:Mn ratio was measured by ICP-OES on a Perkin-Elmer Optima 8300 spectrometer on samples digested in 3% (vol/vol) HNO₃ and 0.05 M H₂C₂O₄.

Structural characterization of δ -MnO₂ was carried out to determine specific surface area, mineral phase, and intermediate-range structure (within 2 nm). Additionally, the light absorption spectrum of the mineral was measured by UV-vis spectrophotometry. Specific surface area was determined by a five-point Brunauer–Emmett–Teller (BET) N₂ adsorption isotherm at 77 K on a Micromeritics Gemini 2375 instrument. Powder XRD patterns were collected on a Thermo Electron ARL X'TRA diffractometer with Cu K α radiation ($\lambda = 1.5418$ Å) and a Peltier-cooled Si(Li) solid-state detector, with a speed of 0.5° min⁻¹, a step size of 0.02°, and an integration time of 2,400 s. Both for XRD and BET, powders were obtained by oven-drying at 45° for 1 d pastes obtained by vacuum-filtering an aliquot of the stock suspension.

UV-vis absorption spectra from 200 to 800 nm were obtained on a Shimadzu UV-2600 spectrophotometer with 1-cm path-length cuvettes or an Ocean Optics spectrophotometer with 0.5-mm path-length cuvettes. High-energy X-ray scattering data were collected at beamline 11-ID-B at the Advanced Photon Source. Atomic pair distribution functions [i.e., $G(r)$] (Fig. S7B) were obtained with the PDFgetX2 GUI utility following standard procedures (6), which involve Fourier transformation of the reduced structure function, $[F(Q) = Q[S(Q) - 1]]$ (Fig. S7A). The reduced structure function is the total scattering pattern multiplied by the magnitude of the scattering vector, Q , and divided by the square of the atomic form factor, $|f_i|^2$.

Powder XRD patterns, high-energy X-ray scattering data, and UV-vis spectra were collected from both Na-MnO₂ and Ca-MnO₂, where Ca-MnO₂ was obtained by equilibrating a suspension of ~90 mM Na-MnO₂ with CaCl₂(aq) in a 3:1 Ca:Mn molar ratio from 12 h (LITR-XAS) to 2 mo (optical TA). The effect of oxygen on the chemical composition of δ -MnO₂ upon the exchange of interlayer Na with Ca was evaluated by equilibrating an aliquot of Na-MnO₂ with Ca under N₂(g) purge. After equilibration, aliquots were filtered and digested for measurement of [Mn_{TOT}] and [Mn_(aq)] by ICP-OES; filtered pastes were oven-dried at 40 °C before collecting powder XRD patterns.

Quantum Yield Calculation. The photon flux, ϕ , to the photoreactor was characterized by ferrioxalate actinometry (7–9). Briefly, 20 mL of 0.012 M potassium ferrioxalate (K₃[Fe(C₂O₄)₃]) were

circulated through the photoreactor. Samples (0.4 mL) collected after 10, 25, 50, 75, and 100 s were added to BrandTech plastic UV-cuvettes previously filled with 0.8 mL 0.1% buffered 1.10-phenanthroline solution and 1.4 mL of ultrapure water, shaken, and left in the dark for 30 min. The extinction coefficient of the Fe(II)-phenanthroline complex was measured at 510 nm in a dark room ($\epsilon_{510} = 11,100$ L·mol⁻¹·cm⁻¹). The photon flux was then calculated according to

$$\phi = \frac{Nh\nu}{t} = \frac{\text{moles of Fe(II)-phenanthroline}}{\Phi_{400 \text{ nm}} \times t \times F},$$

where $\Phi_{400 \text{ nm}}$ is the quantum yield of the ferrioxalate at 400 nm (equal to 1.14) (9), t is the irradiation time, and F is the fraction of light absorbed by the ferrioxalate solution, which in this case was equal to unity (9).

The apparent quantum yield for Mn(III) generation was calculated according to

$$\Phi = \frac{f_{\text{Mn(III)}, t} \times \text{moles of Mn}}{\phi * t \times \frac{A_{400 \text{ nm, MnO}_2}}{A_{400 \text{ nm, ferrioxalate}}}},$$

where $f_{\text{Mn(III)}, t}$, the fraction of photoreduced Mn after time, t , is multiplied by the total number of moles of Mn in the system; ϕ is the photon flux measured for the photoreactor; and $A_{400 \text{ nm, MnO}_2}$ and $A_{400 \text{ nm, ferrioxalate}}$ are the absorbances (in OD units) of Ca- or Na-MnO₂ and ferrioxalate at 400 nm measured in 1-cm path-length quartz cuvettes with water as a blank. Due to the possible effect of birnessite aggregation on the measurement of optical extinction coefficients of the samples (see below), we use the term “apparent quantum yield.” The fraction of photoreduced Mn was calculated according to $([\text{Mn(III)-PP}_{\text{light}}] - [\text{Mn(III)-PP}_{\text{dark}}]) / [\text{Mn}_{\text{TOT}}]$. The ratio of the absorbance values in the denominator accounts for the different absorptivity of δ -MnO₂ relative to ferrioxalate, where $\epsilon_{\text{Na-MnO}_2} = 4,111$ L·mol⁻¹·cm⁻¹, $\epsilon_{\text{Ca-MnO}_2} = 2,300$ L·mol⁻¹·cm⁻¹, and $\epsilon_{\text{ferrioxalate}} = 110$ L·mol⁻¹·cm⁻¹. The molar absorptivity of ferrioxalate was calculated from serial dilutions of a stock solution calibrated with ICP-OES measurements.

Optical Transient Absorption Kinetic Fits. A bleach signal on the microsecond timescale between 550 and 580 nm with the EOS spectrometer was observed for Ca-MnO₂ and Na-MnO₂ samples in Nafion, and Na-MnO₂ samples in water or terephthalic acid. The trends extracted at 580 nm were fitted by exponential decay functions with two time constants. The bleach appeared to return to baseline ($\Delta\text{OD} \sim 0$); however, this could not be judged from the data due to the noise level inherent to the data acquisition. To evaluate whether the signal returned to baseline within subsecond timescales, the data were refitted using a third decay constant fixed to 10⁶ μ s (i.e., no decay to baseline within the 50- μ s resolution of the experiment). An F-test showed only 67% confidence that the model with three time constants returned a significantly better fit than the model with two time constants. Thus, we do not have 95% confidence that the bleach persists over long time scales (10⁶ μ s).

SI Results and Discussion

Mineral Characterization. The δ -MnO₂ powder had a BET-specific surface area of 141 ± 3 m²·g⁻¹, an AMON of 4.05 ± 0.05 , and a Na:Mn ratio of 0.24. The XRD patterns collected from Na-MnO₂

and Ca-MnO₂, with a 5-d equilibration period under aerated and N_{2(g)}-purged conditions for Ca-MnO₂, were consistent with those reported for δ-MnO₂ (1). The UV-vis absorption spectra of Na-MnO₂ and Ca-MnO₂ are shown in Fig. S6A. The UV-vis absorption spectrum of Ca-MnO₂ exhibits a significant redshift relative to that for Na-MnO₂. This redshift is accompanied by a change in line shape. Therefore, the redshift cannot be attributed simply to scattering from aggregated particles. Additional UV-vis spectra were acquired to test the effect of the background electrolyte and ionic strength on the observed redshift. Only the CaCl₂-equilibrated sample showed a redshift (Fig. S6B) that persisted after removing any excess CaCl_{2(aq)} electrolyte by rinsing the particles with MQ water. In addition, similar average Mn oxidation numbers were measured for Na-MnO₂ and Ca-MnO₂, indicating that the redshift cannot be explained by a change in Mn valence. Thus, the UV-vis spectra confirm that the redshift is caused by the presence of Ca as the interlayer cation, which may influence the ordering of interlayer water molecules (10). The pair distribution functions (PDFs; Fig. S7) match those reported for Mn(IV)-rich birnessite nanoparticles with hexagonal sheet symmetry (11). The PDFs show identical peak positions, whereas the amplitude of the first Mn-O (1.91 Å) and Mn-Mn (2.85 Å) distances are lower for Ca-MnO₂ than Na-MnO₂. However, there is no difference in the intermediate-range order (within 2 nm) of these two samples.

Photon Flux Comparison with Natural Environments. Our flow-through experiments were done using a photon flux of 0.77 μE/s. This photon flux can be compared with the photon flux delivered to the Earth's surface by integrating the area under the irradiance spectrum of natural sunlight. First, we converted solar irradiance from units of W·m⁻²·s⁻¹ to μE·m⁻²·s⁻¹ by normalizing the irradiance at each wavelength by the energy of the photons at that wavelength. Integration of the ASTM G173-03 reference solar irradiance spectrum between 280 and 900 nm yielded a photon flux equal to 3,195 μE·m⁻²·s⁻¹. Once corrected to the surface area of the cuvette irradiated in our experiments (i.e., 0.0004 m²), we obtain a photon flux of 1.3 μE·s⁻¹ with photons of wavelengths ranging from 280 to 900 nm, which include the UV-vis wavelengths of the light spectrum. However, because 42% of the irradiance spectrum of sunlight is between 400 and 600 nm, the photon flux delivered by the LED array to our photoreactor at 400 nm is comparable to the photon flux that would be delivered by sunlight between 400 and 600 nm.

Nature of Redshift in Optical Absorption Spectra. Our optical transient absorption spectra show a new absorption feature upon laser excitation that we assigned to a Mn(III) excited state in the MnO₂ sheet. This feature is located at longer wavelengths than the ground-state absorption of the initial birnessite (i.e., it is redshifted). A similar redshift was observed in the ground-state UV-vis spectra from triclinic birnessite and *c*-disordered H⁺ birnessite (Fig. S5), with triclinic birnessite showing a greater redshift relative to *c*-disordered H⁺ birnessite. These Mn(III)-bearing minerals contain significant proportions of Mn(III), but vary with respect to the distribution of Mn(III) within the octahedral layer and interlayer region and the extent of sheet stacking (1).

We expect that sheet stacking does not modify significantly the UV-vis absorption properties of birnessite. In their comparison between monolayer and multilayer MnO₂, Sakai et al. (12) found that only the topmost layer was photosensitive and that the band gap was nearly identical between the two materials. Because the band gap can be correlated to the UV-vis absorption, increased sheet stacking would not justify the observed redshift in our UV-vis absorption spectra.

Instead, we conclude that the redshift in the UV-vis spectra arises from the presence of Mn(III) in the octahedral layer. Based on solid-phase characterization (i.e., pyrophosphate extraction,

potentiometric titration, and XRD), our triclinic birnessite contains up to 16% Mn(III) located in the octahedral sheets, whereas *c*-disordered H⁺ birnessite contains ~19% Mn(III) (13). Based on the synthesis protocol for *c*-disordered H⁺ birnessite (1, 13) and structural characterization of the material synthesized according to this method (1, 14), we conclude that approximately half of the Mn(III) is situated in interlayer positions. Thus, our transient UV-vis spectra that reveal an absorption feature between 500 and 600 nm are consistent with the formation of Mn(III) located in the octahedral sheets.

Effects of Aggregation on Photoexcitation of Birnessite. Light scattering due to particle aggregation may introduce Rayleigh scattering, which increases the observed optical extinction coefficient. If present and not accounted for, this effect could lead to an erroneous measurement of the true optical absorption coefficient, and hence an underestimation of the quantum yield. To minimize this potential source of error, we measured the UV-vis spectra of the samples prepared in water at the lowest possible concentrations (0.1 mM) at which we obtained visibly transparent suspensions with no noticeable aggregation. To investigate the consequences of aggregation, we added 10 mM of NaCl or CaCl₂ (Fig. S6). At the higher concentrations used for the flow-through studies (0.5 mM), we also did not observe signs of aggregation. Only at the highest concentrations used for the transient absorption spectroscopy (3–6 mM) did we observe aggregation in all samples (with and without added electrolyte), leading us to add Nafion (see below).

Consequently, we do not believe that aggregation substantially altered our reported rate constants or quantum yield for photoreduction. However, because we do not have distinct measurements of scattering vs. absorption, we now report the values as apparent quantum yield. If our reported absorbance at 400 nm of Ca-MnO₂ is an overestimate due to the presence of scattering, this would increase the effect of Ca vs. Na, and would not change any of the conclusions in the manuscript concerning the role of the counterions. We also note that while aggregation, when it occurs, can affect the apparent absorption coefficient, it does not alter peak position. We demonstrate this in Fig. S6, which compares UV-vis spectra for our samples in water and in electrolytes sufficiently concentrated as to cause aggregation. Thus, aggregation does not affect the intrinsic strength of the absorption of 400-nm photons by either Na- or Ca-equilibrated birnessite.

Effects of Aggregation on Transient Optical Absorption Kinetics. Aggregation interferes particularly strongly with the acquisition of kinetics data in time-resolved spectroscopy because it introduces nonstatistical noise at each time point. Nafion reduced particle aggregation in time-resolved optical experiments, but the comparison of Figs. S8A and C and S9 for Na-MnO₂ show that Nafion had a small effect on the observations. Slightly slower decays were observed for samples prepared without Nafion (Table 1), possibly indicating an effect of aggregation upon recombination rates; this could occur if recombination involved diffusion of soluble species, but the effect is impossible to explain confidently and is smaller than the influence of interlayer cations.

Calculation of Mn:Photon Ratio. We evaluated the likelihood that the LITR-XAS data were influenced by X-ray beam damage by estimating the number of X-ray photons that can interact with the sample. First, we assumed that a maximum of 5,000 X-ray photons are delivered per camshaft (electron bunch) to the beamline end station at 5 keV, with two consecutive camshafts separated by a period of 656 ns. Therefore, $\sim 7.6 \times 10^9$ camshaft photons may interact with the sample each second. However, the camshaft photons represent only 1% of the total photons available from the storage ring (i.e., camshaft current is 5 mA and total storage

ring current is 500 mA). Thus, a total of 7.6×10^{11} camshaft and noncamshaft photons are delivered to the end station per second. This total photon flux is attenuated 30 times by the X-ray chopper, a device designed to exclude noncamshaft photons, leading to a total exposure of 3.7×10^{14} photons to the sample during a 4-h experiment. Finally, a 250-mL suspension of 10 mM δ - MnO_2 contains $\sim 1.5 \times 10^{21}$ Mn atoms; thus the Mn:X-ray photon ratio is $1.5 \times 10^{21}:3.7 \times 10^{14}$ or $10^6:1$.

A better estimate of the Mn:photon ratio can be obtained by modifying the above calculation to include more realistic estimates of photon flux and photon absorption by the sample. First, fewer X-ray photons are actually delivered per camshaft to the

beamline end station at 5 keV: 3,500 vs. 5,000 photons. Second, the photon flux drops anywhere from 10–90% when the monochromator is in motion because the motors move at different rates. Thus, the sample exposure time is closer to 25% of the total experiment time. Third, about 50% of the photons are transmitted through the 600- μm jet. Of the photons that are absorbed by the sample, most are not absorbed by MnO_2 (<2% for Mn and O combined). With these assumptions, a less conservative estimate of the Mn:X-ray photon ratio would be $1.5 \times 10^{21}:6.4 \times 10^{11}$ or on the order of $10^9:1$, lending strong support to our assumption that any long-term changes to the sample are not caused by X-ray exposure.

- Villalobos M, Toner B, Bargar J, Sposito G (2003) Characterization of the manganese oxide produced by *Pseudomonas putida* strain MnB1. *Geochim Cosmochim Acta* 67(14):2649–2662.
- Grangeon S, Lanson B, Lanson M, Manceau A (2008) Crystal structure of Ni-sorbed synthetic vernadite: A powder X-ray diffraction study. *Mineral Mag* 72(6):1279–1291.
- Klewicki JK, Morgan JJ (1998) Kinetic behavior of Mn(III) complexes of pyrophosphate, EDTA, and citrate. *Environ Sci Technol* 32(19):2916–2922.
- Kostka JE, Luther GW, Nealson KH (1995) Chemical and biological reduction of Mn(III)-pyrophosphate complexes - Potential importance of dissolved Mn(III) as an environmental oxidant. *Geochim Cosmochim Acta* 59(5):885–894.
- Webb SM, Dick GJ, Bargar JR, Tebo BM (2005) Evidence for the presence of Mn(III) intermediates in the bacterial oxidation of Mn(II). *Proc Natl Acad Sci USA* 102(15):5558–5563.
- Qiu X, Thompson JW, Billinge SJL (2004) PDFgetX2: A GUI-driven program to obtain the pair distribution function from X-ray powder diffraction data. *J Appl Cryst* 37(4):678.
- Hatchard CG, Parker CA (1956) A new sensitive chemical actinometer. II. Potassium ferrioxalate as a standard chemical actinometer. *P R Soc A* 235(1203):518–536.
- Parker CA (1953) A new sensitive chemical actinometer. 1. Some trials with potassium ferrioxalate. *P R Soc A* 220(1140):104–116.
- Montalti M, Credi A, Prodi L, Gandolfi MT (2006) *Handbook of Photochemistry* (CRC, Boca Raton, FL).
- Cygan RT, Post JE, Heaney PJ, Kubicki JD (2012) Molecular models of birnessite and related hydrated layered minerals. *Am Mineral* 97(8-9):1505–1514.
- Zhu MQ, et al. (2012) Structural study of biotic and abiotic poorly-crystalline manganese oxides using atomic pair distribution function analysis. *Geochim Cosmochim Acta* 81:39–55.
- Sakai N, Ebina Y, Takada K, Sasaki T (2005) Photocurrent generation from semi-conducting manganese oxide nanosheets in response to visible light. *J Phys Chem B* 109(19):9651–9655.
- Duckworth OW, Sposito G (2007) Siderophore-promoted dissolution of synthetic and biogenic layer-type Mn oxides. *Chem Geol* 242(3-4):497–508.
- Manceau A, et al. (2013) Short-range and long-range order of phyllosilicate nanoparticles determined using high-energy X-ray scattering. *J Appl Cryst* 46(1):193–209.

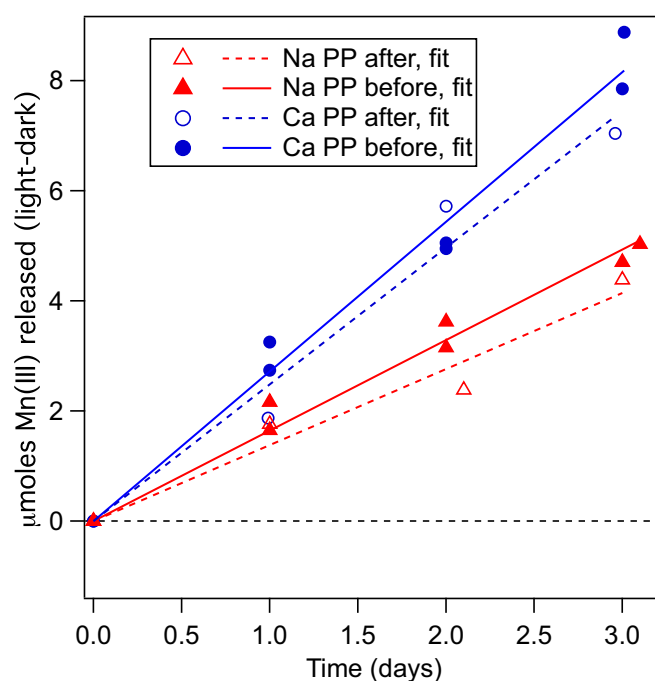


Fig. S1. Time course plot showing Mn(III) generation upon 400-nm irradiation in flow-through experiments at pH 6.5. Blue for Ca-MnO_2 and red for Na-MnO_2 , filled symbols and solid lines for samples with PP added before irradiation; dashed lines and empty symbols for samples with PP added after irradiation. Aqueous Mn determined by ICP-OES is within 10% of Mn(III)-PP determined colorimetrically. No Mn was released to solution in experiments without PP.

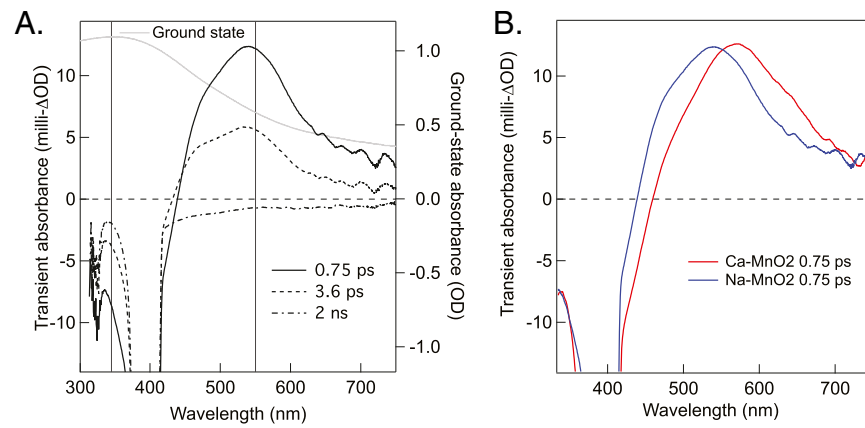


Fig. 52. (A) Transient optical absorption spectra acquired on Na-MnO₂ in aqueous suspension with Nafion. Transient absorption difference spectra at 0.75 ps, 3.6 ps, and 2 ns (ΔOD units; left axis) compared with the ground-state UV-vis absorption (OD units; right axis). The maximum intensity of the ESA is 550 nm. The data from 390–410 nm are affected by scattering of the pump beam. (B) Comparison between the transient absorption spectrum of Ca-MnO₂ and Na-MnO₂ in Nafion 0.75 ps after laser excitation show that the Ca-MnO₂ sample is redshifted relative to the Na-MnO₂ sample (Fig. S6A).

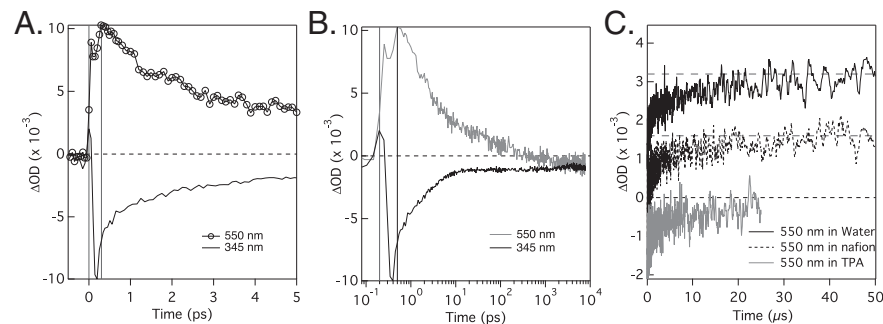


Fig. 53. Summary of transient optical absorption kinetics acquired on Na-MnO₂ in aqueous suspension with Nafion. (A) Transient kinetic traces show that the onset of the ESA at 550 nm is slightly delayed relative to the bleach at 345 nm. (B) Decay kinetics of the ESA and bleach up to 8 ns. The time 0 was shifted by 0.2 ps to enable plotting on a logarithmic axis. (C) The decay of the bleach at 550 nm was recorded for up to 50 μ s.

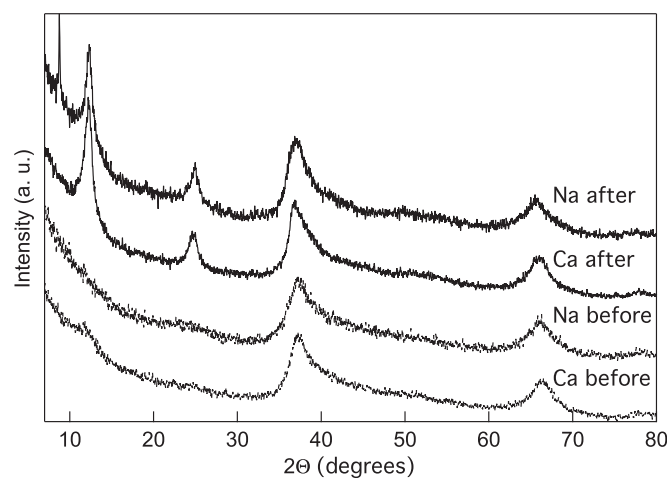


Fig. 54. Powder X-ray diffraction patterns for selected samples before and after the light-initiated time-resolved XAS experiment. Samples after the LITR-XAS experiment show reflections of the 001 and 002 planes (reflection at $\sim 14^\circ$ and $\sim 25^\circ$ 2θ , respectively) due to increased stacking of MnO₂ sheets along the crystallographic *c*-axis.

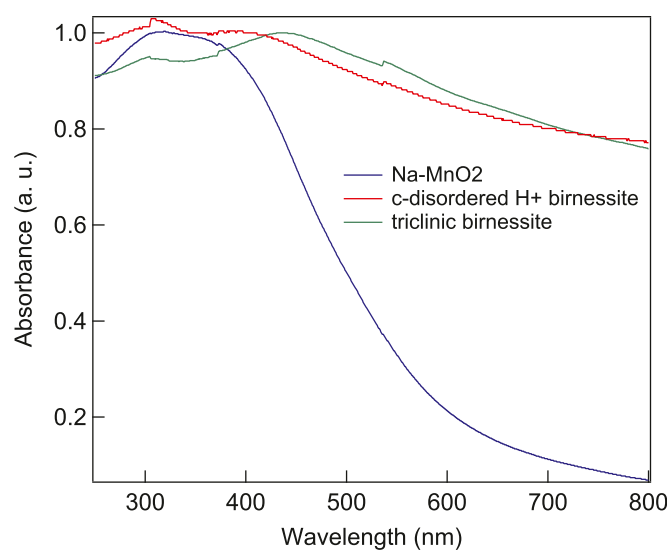


Fig. S5. UV-vis absorption spectrum of Na-MnO₂, triclinic birnessite (~16% Mn(III) in the octahedral sheet), and c-disordered H⁺ birnessite (~19% Mn(III) distributed between the layer and interlayer positions in similar proportions).

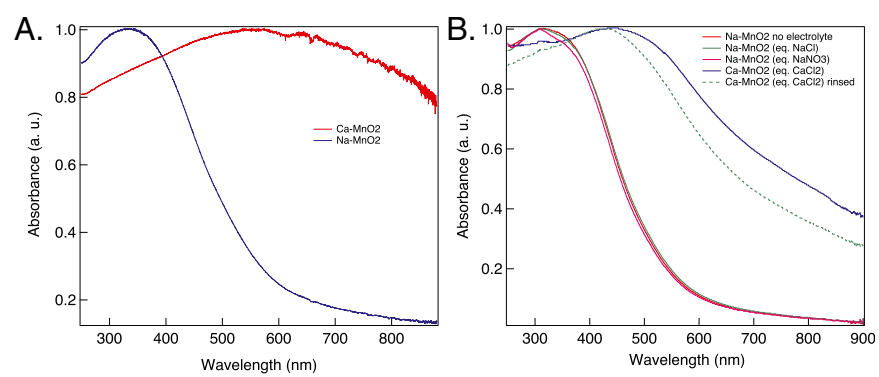


Fig. S6. (A) UV-vis absorption spectra of Na-MnO₂ in water without background electrolyte (blue line) and Ca-MnO₂ with 10 mM background electrolyte (Cl⁻, red line). (B) UV-vis absorption spectra of Na-MnO₂ with and without 10 mM NaCl and NaNO₃ as background electrolytes compared with Ca-MnO₂ with and without 10 mM CaCl₂ as the background electrolyte.

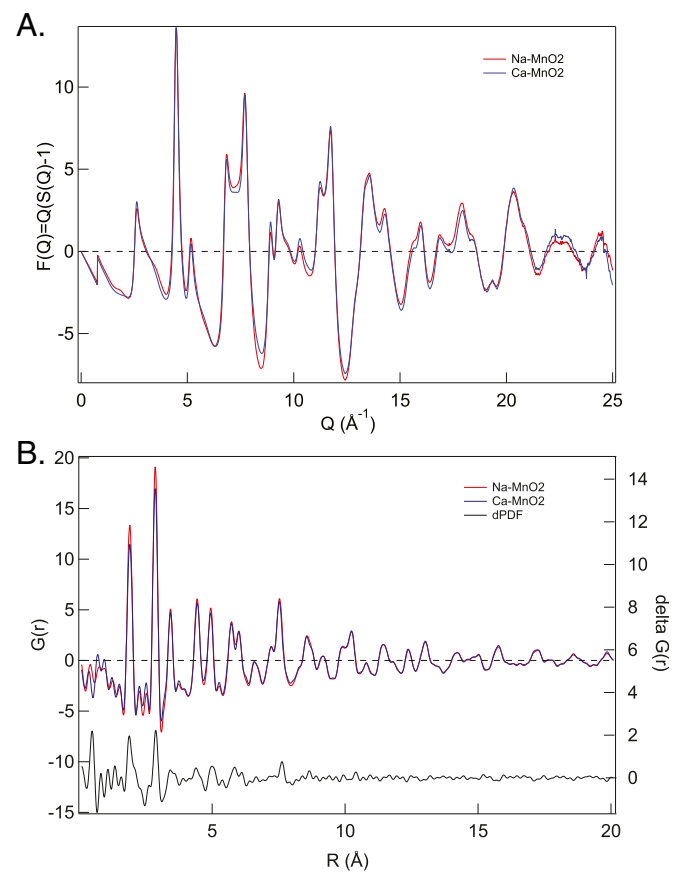


Fig. S7. (A) Reduced structure function, $F(Q) = Q[S(Q) - 1]$, for Ca-MnO₂ and Na-MnO₂, respectively. (B) PDF data, obtained by Fourier transformation of the $F(Q)$, for Na-MnO₂ (blue line) and Ca-MnO₂ (red line), as well as difference PDF between the samples.

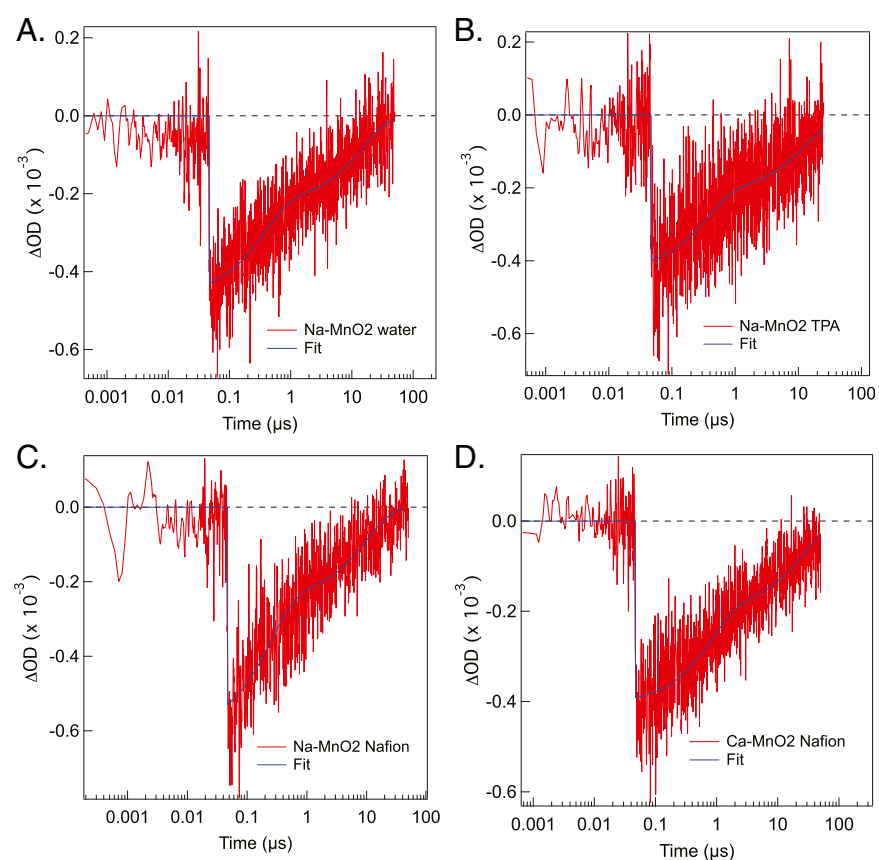


Fig. 58. Comparison of the transient optical absorption kinetic data on the microsecond timescale extracted at 580 nm for Na-MnO₂ and Ca-MnO₂ in different aqueous solutions, overlain with the fits using two time constants (Table 1): (A) Na-MnO₂ resuspended in water; (B) Na-MnO₂ resuspended in an 0.1 M terephthalic acid solution to trap any hydroxyl radical species formed during photoreduction; (C) Na-MnO₂ resuspended in an aqueous solution with Nafion to reduce particle aggregation; and (D) Ca-MnO₂ resuspended in an aqueous solution with Nafion to reduce particle aggregation.

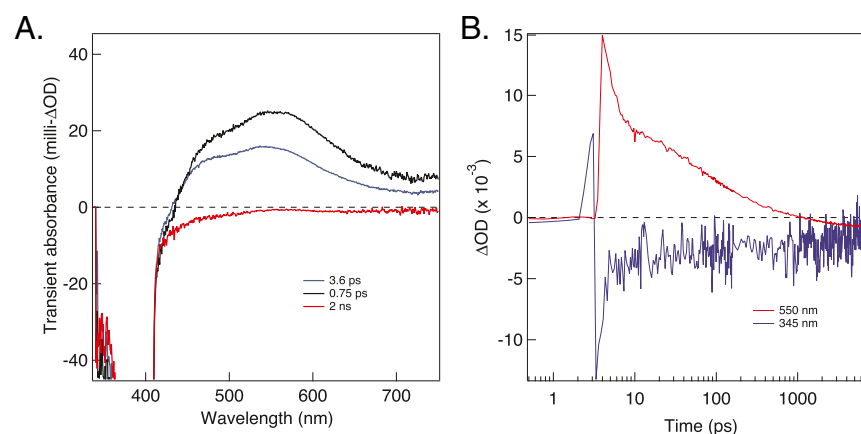


Fig. 59. (A) Transient absorption spectra at different delay times for Na-MnO₂ in water. (B) Transient absorption kinetic traces for Na-MnO₂ on picosecond-to-nanosecond timescales extracted at 345 nm (blue) and 550 nm (red). The transient spectra and decay kinetics do not show differences on the picosecond-to-nanosecond timescale with respect to Na-MnO₂ resuspended in Nafion.

ANNEX 7. Raw data from the flow through photoreduction experiments in Chapters 3 through 6

Table 1: Raw data for the time course plots shown in Chapter 4.

	time [days]	tot dk [uM]	% Mn(III) dark	tot lt [uM]	% Mn(III) light	Reduced μmol (light – dark)
CaMnO₂ pH 6.5	0.00	577.00	0.03	577.00	0.03	0.00
	1.00	593.28	0.04	533.34	0.05	1.14
	1.00	589.36	0.04	512.44	0.06	2.74
	2.00	637.16	0.04	635.24	0.05	3.58
	2.00	652.24	0.04	626.08	0.06	4.95
	3.00	746.70	0.04	654.98	0.07	7.85
	3.00	739.86	0.04	669.52	0.06	6.40
CaMnO₂ pH 6.5 rpt	0.00	460.07	0.02	463.47	0.01	-0.30
	1.00	473.93	0.02	377.40	0.04	3.25
	2.00	472.60	0.01	368.40	0.05	5.05
	3.01	470.13	0.01	354.13	0.07	8.88
	4.00	486.60	0.01	346.67	0.08	10.23
CaMnO₂ pH 6.5 N₂ purge	0.00	710.63	0.02	671.67	0.02	-0.52
	1.00	752.17	0.02	535.40	0.03	1.86
	2.00	685.50	0.02	620.77	0.04	2.95
CaMnO₂ pH 6.5 N₂ purge rpt	0.00	623.33	0.01	638.33	0.01	-0.30
	0.99	504.73	0.02	605.07	0.01	1.57
	2.00	570.77	0.04	613.60	0.02	5.41
	2.96	578.57	0.05	641.60	0.02	6.73
NaMnO₂ pH 6.5	0.00	765.60	0.03	779.13	0.02	-0.50
	1.00	832.40	0.02	666.60	0.04	1.65
	2.04	801.20	0.03	642.90	0.05	3.15
	3.05	791.33	0.02	598.10	0.07	5.03
	3.61	769.70	0.02	595.00	0.08	6.02
	5.00	805.27	0.03	560.00	0.12	8.69
NaMnO₂ pH 6.5	1.00	592.30	0.03	438.30	0.06	2.08
	2.00	591.40	0.03	390.10	0.08	3.54
	3.00	589.80	0.03	378.00	0.10	4.63
	4.00	562.70	0.03	359.73	0.12	5.22

ANNEX 7

NaMnO₂ pH 6.5	0.00	460.10	0.03	481.10	0.03	0.30
	1.01	457.10	0.04	409.60	0.06	1.76
	2.06	466.90	0.04	384.20	0.07	2.38
	3.02	459.50	0.04	369.20	0.10	4.38
	0.00	460.10	0.03	481.10	0.03	0.30
	1.01	457.10	0.04	409.60	0.06	1.76
	2.06	466.90	0.04	384.20	0.07	2.38
	3.02	459.50	0.04	369.20	0.10	4.38

Table 2: Data for the time-course plots of the pH study, described in Chapter 5.

	time [days]	tot dk [uM]	% Mn(III) dark	tot lt [uM]	% Mn(III) light	Reduced μmol (light – dark)
pH 4 stat	0.00	219.68	0.09	223.02	0.10	0.26
	0.10	216.80	0.10	222.50	0.10	0.41
	0.27	206.80	0.10	211.34	0.11	0.63
	0.42	214.92	0.12	193.82	0.15	0.62
	0.98	218.98	0.14	208.28	0.17	0.25
	1.07	208.84	0.13	194.40	0.16	1.74
	1.23	213.80	0.14	193.00	0.21	2.44
	2.01	218.24	0.14	206.52	0.18	1.02
	2.15	205.40	0.14	215.22	0.18	1.45
	2.42	258.70	0.14	134.36	0.21	1.87
	3.01	226.32	0.15	108.42	0.37	3.08
	3.22	233.18	0.15	158.12	0.55	4.76
	3.36	210.92	0.16	102.82	0.49	7.89
	3.99	231.60	0.25	241.92	0.58	0.36
4.05	295.84	0.14	107.72	0.28	4.07	
pH 4 stat rpt	0.00	223.50	0.07	223.35	0.07	-0.02
	0.08	141.18	0.08	176.40	0.08	-0.16
	0.67	178.77	0.07	175.02	0.09	0.95
	0.79	180.66	0.07	164.22	0.10	0.96
	0.96	154.35	0.08	143.40	0.12	1.25
	1.08	158.01	0.08	334.89	0.09	0.93
	1.71	178.14	0.02	130.50	0.11	2.51
pH 8 stat	0.00	229.08	0.01	222.88	0.01	0.16
	0.10	215.22	0.01	219.28	0.01	0.17
	0.27	220.58	0.01	211.78	0.01	0.16

	0.42	222.72	0.02	213.28	0.02	0.24
	0.98	221.32	0.02	208.28	0.03	0.49
	1.07	208.84	0.02	194.40	0.03	0.42
	1.23	222.16	0.02	215.36	0.03	0.70
	2.01	116.08	0.03	226.58	0.03	-0.11
	2.15	129.62	0.03	233.04	0.03	-0.11
	2.42	278.34	0.02	267.34	0.04	0.86
	3.01	238.78	0.02	258.56	0.03	0.60
	3.22	256.00	0.02	232.34	0.04	0.81
	3.36	261.66	0.02	264.34	0.04	0.97
	3.99	231.58	0.02	241.92	0.04	0.91
	4.05	295.84	0.01	107.72	0.04	1.19
pH 6.5 PP	0.00	255.47	0.01	255.47	0.01	0.08
	0.05	255.47	0.01	255.47	0.01	0.11
	0.09	255.47	0.01	255.47	0.01	0.11
	0.15	255.47	0.01	255.47	0.01	0.07
	0.28	255.47	0.01	255.47	0.01	0.17
	0.51	255.47	0.02	255.47	0.02	0.07
	0.90	255.47	0.01	255.47	0.02	0.36
	1.00	255.47	0.01	255.47	0.02	0.42
	1.19	255.47	0.01	255.47	0.02	0.50
	1.40	255.47	0.02	255.47	0.03	0.43
	1.89	255.47	0.01	255.47	0.03	0.72
	2.05	255.47	0.02	255.47	0.03	0.70
pH 6.5 PP rpt	0.00	243.03	0.01	243.03	0.02	0.15
	0.05	243.03	0.01	243.03	0.01	0.10
	0.09	243.03	0.01	243.03	0.01	0.06
	0.15	243.03	0.01	243.03	0.01	0.10
	0.28	243.03	0.01	243.03	0.01	0.09
	0.51	243.03	0.02	243.03	0.02	0.14
	0.90	243.03	0.01	243.03	0.02	0.20
	1.00	243.03	0.01	243.03	0.02	0.32
	1.19	243.03	0.01	243.03	0.02	0.38
	1.40	243.03	0.02	243.03	0.03	0.38
	1.89	243.03	0.02	243.03	0.03	0.55
	2.05	243.03	0.02	243.03	0.03	0.54
pH 6.5 PP trp	0.00	239.86	0.02	239.86	0.02	0.04
	0.10	239.86	0.02	239.86	0.02	0.00
	0.27	239.86	0.02	239.86	0.02	0.18
	0.42	239.86	0.02	239.86	0.02	0.14

ANNEX 7

	0.98	239.86	0.02	239.86	0.02	0.31
	1.07	239.86	0.02	239.86	0.02	0.24
	1.23	239.86	0.02	239.86	0.02	0.20
	2.01	239.86	0.02	239.86	0.03	0.45
	2.15	239.86	0.01	239.86	0.02	0.50
	2.42	239.86	0.02	239.86	0.04	0.58
	3.01	239.86	0.02	239.86	0.04	0.81
	3.22	239.86	0.02	239.86	0.04	0.73
	3.36	239.86	0.03	239.86	0.04	0.79
	3.99	239.86	0.02	239.86	0.05	1.01
	4.05	239.86	0.02	239.86	0.05	1.09
pH 6.5 PP rpt	0.00	249.84	0.02	249.84	0.02	0.04
	0.08	249.84	0.02	249.84	0.02	0.00
	0.25	249.84	0.02	249.84	0.02	0.04
	0.45	249.84	0.02	249.84	0.02	0.00
	1.00	249.84	0.02	249.84	0.02	0.28
	1.14	249.84	0.02	249.84	0.03	0.34
	1.35	249.84	0.02	249.84	0.03	0.30
	1.97	249.84	0.02	249.84	0.03	0.45
	2.15	249.84	0.02	249.84	0.03	0.53
	2.37	249.84	0.02	249.84	0.03	0.55
	3.16	249.84	0.02	249.84	0.04	0.81
	3.28	249.84	0.02	249.84	0.04	0.87
	4.00	249.84	0.02	249.84	0.04	0.95
	4.06	249.84	0.02	249.84	0.04	1.01
pH 4 PP	0.00	252.59	0.02	252.59	0.02	0.05
	0.08	252.59	0.02	252.59	0.03	0.05
	0.25	252.59	0.02	252.59	0.03	0.27
	0.45	252.59	0.02	252.59	0.03	0.31
	1.00	252.59	0.03	252.59	0.03	0.16
	1.14	252.59	0.03	252.59	0.04	0.51
	1.35	252.59	0.03	252.59	0.04	0.60
	1.97	252.59	0.03	252.59	0.04	0.78
	2.15	252.59	0.03	252.59	0.04	0.71
	2.37	252.59	0.03	252.59	0.04	0.94
	2.97	252.59	0.03	252.59	0.05	0.97
	3.14	252.59	0.03	252.59	0.05	1.10
	3.46	252.59	0.03	252.59	0.05	1.18
	4.00	252.59	0.03	252.59	0.06	1.26
	4.06	252.59	0.03	252.59	0.06	1.25

pH 4 PP rpt	0.00	245.53	0.02	245.53	0.02	0.13
	0.08	245.53	0.02	245.53	0.02	0.09
	0.20	245.53	0.02	245.53	0.02	0.12
	0.35	245.53	0.03	245.53	0.03	0.23
	0.99	245.53	0.02	245.53	0.03	0.41
	1.10	245.53	0.03	245.53	0.03	0.38
	1.25	245.53	0.03	245.53	0.04	0.48
	1.35	245.53	0.02	245.53	0.03	0.52
	2.00	245.53	0.03	245.53	0.04	0.71
	2.10	245.53	0.03	245.53	0.04	0.72
	2.28	245.53	0.03	245.53	0.04	0.76
	2.45	245.53	0.03	245.53	0.04	0.84
	2.99	245.53	0.03	245.53	0.05	0.95
	3.17	245.53	0.03	245.53	0.05	0.97
	3.35	245.53	0.03	245.53	0.05	1.03
	4.02	245.53	0.03	245.53	0.06	1.31
4.08	245.53	0.03	245.53	0.06	1.22	
pH 4 PP trp	0.00	249.27	0.03	249.27	0.03	0.04
	0.69	249.27	0.03	249.27	0.04	0.30
	0.90	249.27	0.03	249.27	0.04	0.47
	1.07	249.27	0.03	249.27	0.04	0.50
	1.67	249.27	0.03	249.27	0.04	0.69
	1.77	249.27	0.03	249.27	0.04	0.75
	1.95	249.27	0.03	249.27	0.04	0.76
	1.60	249.27	0.03	249.27	0.05	0.80
	2.76	249.27	0.03	249.27	0.05	1.07
	2.90	249.27	0.03	249.27	0.05	1.07
	3.04	249.27	0.04	249.27	0.06	1.14
	3.68	249.27	0.04	249.27	0.06	1.28
	3.75	249.27	0.03	249.27	0.06	1.29
pH 8 PP	0.00	249.32	0.01	249.32	0.01	0.00
	0.08	249.32	0.00	249.32	0.01	0.07
	0.20	249.32	0.00	249.32	0.00	0.07
	0.35	249.32	0.01	249.32	0.01	0.07
	0.99	249.32	0.01	249.32	0.01	0.07
	1.10	249.32	0.01	249.32	0.01	0.03
	1.25	249.32	0.01	249.32	0.01	0.10
	1.40	249.32	0.01	249.32	0.01	0.06
	2.00	249.32	0.01	249.32	0.01	0.13
	2.10	249.32	0.01	249.32	0.01	0.12
2.28	249.32	0.01	249.32	0.01	0.12	

ANNEX 7

	2.45	249.32	0.01	249.32	0.01	0.15
	2.99	249.32	0.01	249.32	0.01	0.17
	3.17	249.32	0.01	249.32	0.02	0.30
	3.35	249.32	0.01	249.32	0.01	0.21
	4.02	249.32	0.01	249.32	0.01	0.33
	4.08	249.32	0.01	249.32	0.01	0.30
pH 8 PP rpt	0.00	252.59	0.00	252.59	0.01	0.12
	0.08	252.59	0.00	252.59	0.01	0.15
	0.20	252.59	0.00	252.59	0.00	0.06
	0.35	252.59	0.01	252.59	0.01	0.11
	0.99	252.59	0.01	252.59	0.01	0.20
	1.10	252.59	0.01	252.59	0.01	0.08
	1.25	252.59	0.01	252.59	0.01	0.30
	1.40	252.59	0.01	252.59	0.01	0.17
	2.00	252.59	0.01	252.59	0.02	0.20
	2.10	252.59	0.01	252.59	0.02	0.26
	2.28	252.59	0.01	252.59	0.01	0.22
	2.45	252.59	0.01	252.59	0.01	0.24
	2.99	252.59	0.01	252.59	0.01	0.25
	3.17	252.59	0.01	252.59	0.02	0.38
	3.35	252.59	0.01	252.59	0.02	0.33
	4.02	253.59	0.01	253.59	0.02	0.46
	4.08	254.59	0.01	254.59	0.02	0.44
pH 8 PP trp	0.00	253.72	0.01	253.72	0.01	0.07
	0.69	253.72	0.01	253.72	0.01	0.06
	0.90	253.72	0.01	253.72	0.01	0.06
	1.07	253.72	0.01	253.72	0.01	0.09
	1.67	253.72	0.01	253.72	0.01	0.11
	1.77	253.72	0.00	253.72	0.01	0.17
	1.95	253.72	0.00	253.72	0.01	0.13
	2.60	253.72	0.01	253.72	0.01	0.15
	2.76	253.72	0.01	253.72	0.01	0.17
	2.90	253.72	0.00	253.72	0.01	0.19
	3.04	253.72	0.01	253.72	0.02	0.25
	3.68	253.72	0.01	253.72	0.01	0.33
	3.75	253.72	0.01	253.72	0.01	0.22

Table 3: raw data for the time course plots showed in Chapter 6

	time [days]	tot dk [uM]	tot lt [uM]	% Mn(III) dark	% Mn(III) light	photoreduced umol (light - dark)	time sorption (days)	Ni sorption dark (q %)	Ni sorption light (q %)	
pH 4 exafs	0.00	528.70	569.78	0.03	0.03	0.11	0.00	0.04	0.04	
	0.13	496.16	236.64	0.03	0.08	5.42				
	1.02	518.20	216.52	0.03	0.09	6.67	1.00	0.04	0.04	
	2.10	537.64	469.62	0.03	0.08	4.93				
	2.19	517.70	525.08	0.07	0.08	0.92				
	3.09	591.86	494.54	0.04	0.13	6.24	3.10	0.04	0.03	
	3.19	511.90	511.12	0.05	0.14	5.78				
	4.00	464.68	451.64	0.05	0.16	5.54	4.00	0.04	0.02	
	pH 4 rep	0.00	196.92	206.36	0.05	0.06	0.41	0.00	0.06	0.06
		0.35	153.14	192.92	0.06	0.08	1.24	0.15	0.06	0.06
0.96		133.52	172.76	0.06	0.10	2.25	0.35	0.06	0.06	
1.41		501.82	196.56	0.03	0.12	1.33	0.96	0.06	0.06	
2.25		60.76	347.34	0.09	0.09	5.50	1.08	0.06	0.06	
3.35		55.88	111.38	0.16	0.47	7.94	1.41	0.06	0.05	
4.01		46.52	79.72	0.16	0.93	11.50	1.99	0.06	0.05	
							2.25	0.06	0.04	
							3.02	0.06	0.05	
pH 4 dup		0.00	239.46	234.60	0.05	0.06	0.53	0.00	0.06	0.06
	0.17	233.31	233.67	0.05	0.06	1.06	0.17	0.06	0.06	
	0.39	219.72	203.34	0.04	0.08	1.73	0.39	0.06	0.06	
	1.40	206.01	200.34	0.05	0.10	2.24	0.97	0.05	0.05	
	1.98	209.94	145.02	0.11	0.16	0.16	1.40	0.06	0.05	
	2.40	215.58	217.17	0.08	0.11	1.51	1.98	0.06	0.04	
	2.90	201.06	183.24	0.08	0.13	1.29	2.40	0.06	0.04	
	3.93	198.51	153.33	0.05	0.16	2.56	2.90	0.06	0.03	
	3.99	199.08	191.73	0.05	0.23	5.12	3.93	0.07	0.02	

ANNEX 7

pH 4 trp	0.00	204.75	196.14	0.06	0.06	0.08	0.00	0.06	0.06	0.06
	0.14	195.78	133.11	0.04	0.08	0.47	0.14	0.06	0.06	0.06
	1.13	196.35	138.57	0.06	0.10	0.65	0.81	0.06	0.06	0.05
	1.69	213.72	132.21	0.05	0.12	1.22	1.13	0.05	0.05	0.05
	2.33	182.31	105.03	0.05	0.15	1.27	1.69	0.06	0.06	0.05
	2.77	179.76	104.79	0.07	0.18	1.18	2.33	0.06	0.06	0.04
	3.13	219.87	155.40	0.05	0.17	2.59	2.77	0.06	0.06	0.04
							3.13	0.06	0.06	0.04
							3.78	0.06	0.06	0.03
							3.86	0.06	0.06	0.05
pH 8 exafs	0.00	476.34	477.74	0.01	0.01	0.22	1.02	0.02	0.02	0.02
	1.02	504.74	413.96	0.01	0.01	0.54	2.08	0.02	0.02	0.02
	2.08	520.96	297.86	0.01	0.02	1.10	3.27	0.02	0.02	0.02
	3.27	511.74	370.60	0.01	0.02	1.18	3.99	0.02	0.02	0.02
	3.99	511.62	380.92	0.01	0.02	1.20				
pH 8 rpt	0.00	208.80	236.04	0.02	0.02	0.00	0.00	0.07	0.07	0.07
	0.17	193.80	227.28	0.02	0.02	0.17	0.17	0.07	0.07	0.07
	0.39	184.86	180.33	0.02	0.03	0.39	0.39	0.07	0.07	0.07
	1.40	161.67	140.58	0.03	0.04	0.97	0.97	0.07	0.07	0.07
	1.98	201.15	145.02	0.02	0.04	1.40	1.40	0.07	0.07	0.07
	2.40	215.58	217.17	0.02	0.04	1.98	1.98	0.07	0.07	0.07
	2.90	345.39	72.64	0.01	0.10	2.40	2.40	0.07	0.07	0.07
	3.93	166.89	45.80	0.02	0.17	2.90	2.90	0.07	0.07	0.07
	3.99	154.20	149.88	0.02	0.05	3.93	3.93	0.06	0.06	0.07
						3.99	3.99	0.07	0.07	0.07
pH 8 dup	0.00	191.61	206.43	0.02	0.02	0.17	0.00	0.06	0.06	0.06
	0.14	203.85	195.54	0.01	0.02	0.29	0.14	0.06	0.06	0.06
	1.13	200.37	195.69	0.01	0.02	0.44	0.81	0.06	0.06	0.06

